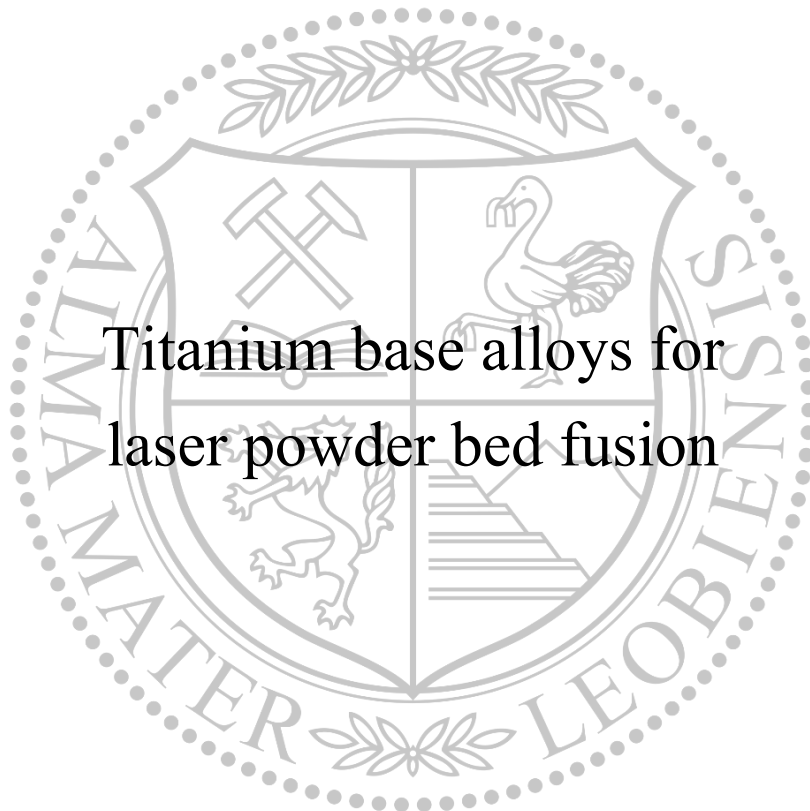




Chair of Physical Metallurgy and Metallic Materials

## Doctoral Thesis



Titanium base alloys for  
laser powder bed fusion

Dipl.-Ing. Christian Fleißner-Rieger, BSc

February 2022





**MONTANUNIVERSITÄT LEOBEN**

www.unileoben.ac.at

**AFFIDAVIT**

I declare on oath that I wrote this thesis independently, did not use other than the specified sources and aids, and did not otherwise use any unauthorized aids.

I declare that I have read, understood, and complied with the guidelines of the senate of the Montanuniversität Leoben for "Good Scientific Practice".

Furthermore, I declare that the electronic and printed version of the submitted thesis are identical, both, formally and with regard to content.

Date 20.02.2022

A handwritten signature in black ink, appearing to read 'Christian Fleißner-Rieger'.

---

*Christian Fleißner-Rieger*



“”

*There is no value in anything until it is finished.*

– Genghis Khan –

This dissertation was carried out at the **Department of Materials Science, Montanuniversität Leoben**, supervised by Univ.-Prof. Dr. mont. Helmut Clemens and assoc. Prof. Dr. mont. Svea Mayer. The work was supported by **voestalpine Böhler Edelstahl GmbH & Co KG** and **Pankl Racing Systems AG**, focusing on the characterization of titanium alloys for laser powder bed fusion.

---

# Contents

<b>Abstract</b>	<b>ix</b>
<b>Kurzfassung</b>	<b>x</b>
<b>List of abbreviations, acronyms and symbols</b>	<b>xi</b>
<b>1 Introduction, motivation and scope</b>	<b>1</b>
<b>2 State of the Art</b>	<b>3</b>
2.1 Titanium base alloys	3
2.1.1 Alloy classification	3
2.1.2 Phase transformations	4
2.1.3 Macro- and microstructure	5
2.1.4 Mechanical properties of $\alpha+\beta$ alloys	8
2.2 Additive manufacturing of titanium alloys	11
2.2.1 Working principle and process synergies	11
2.2.2 Melt pool and thermal behavior	12
2.2.3 Applications	14
2.3 Powder production and relations to LPBF	16
2.3.1 Electrode induction melting inert gas atomization	16
2.3.2 Morphology, particle size distribution and powder porosity	16
2.3.3 Powder reuse	19
<b>3 Relation of the current thesis to the state of the art</b>	<b>20</b>
<b>4 Experimental challenges during characterization</b>	<b>22</b>
4.1 Advanced sample preparation techniques	22
4.2 Characterization at macro, micro and nanoscale	24
4.3 X-ray diffraction methods	26
<b>5 Published content</b>	<b>27</b>
5.1 Focus of the research and published content	27
5.2 Conference contributions	29
5.3 Supervised theses	29
5.4 Summary of the published content and discussion	30
5.4.1 LPBF – A comparison of alloys	30

---

5.4.2	The impact of process parameter on phase transformations	32
5.4.3	Heat input and precipitation behavior	34
5.4.4	Optimization of post-process heat treatments	35
<b>6</b>	<b>Novel features</b>	<b>37</b>
<b>7</b>	<b>Outlook and open questions</b>	<b>38</b>
	<b>References</b>	<b>40</b>
	<b>Acknowledgments and closing remarks</b>	<b>47</b>
	<b>Appendix</b>	
	<b>Article A</b>	<b>49</b>
	An additively manufactured titanium alloy in the focus of metallography	
	<b>Article B</b>	<b>78</b>
	Selective laser melting of a near- $\alpha$ Ti6242S alloy for high performance automotive parts	
	<b>Article C</b>	<b>91</b>
	On the existence of orthorhombic martensite in a near- $\alpha$ titanium base alloy used for additive manufacturing	
	<b>Article D</b>	<b>102</b>
	Formation and evolution of precipitates in an additively manufactured near- $\alpha$ titanium base alloy	
	<b>Article E</b>	<b>109</b>
	Optimization of the post-process heat treatment strategy for a near- $\alpha$ titanium base alloy produced by laser powder bed fusion	



---

## Abstract

Ti base alloys are commercially used for various applications in almost all industrial sectors. The material-specific benefits, such as high strength, low density and high corrosion resistance, excellently suits the aerospace, automotive and medical industry requirements, which is why these industries are the prominent driving forces for the research and development activities in the Ti industry. The combination with the additive manufacturing technology enables to link the beneficial material specifics of Ti base alloys with the eco-design concept supporting low material waste and freeform fabrication ability. Although additively manufactured Ti base alloys are already used, the alloy portfolio is limited and almost reduced to the Ti-6Al-4V alloy. Hence, this thesis deals with the implementation of other Ti base alloys, such as the Ti-6Al-2Sn-4Zr-2Mo-Si alloy for laser powder bed fusion, and explores process limits and achievable mechanical properties. Via in-depth characterization techniques such as high-energy X-ray diffraction, transmission electron microscopy, differential scanning calorimetry and atom probe tomography, this thesis aims to enhance the fundamental understanding of the material response on the laser powder bed fusion process. Furthermore, it points out that analogies to well-investigated materials such as the Ti-6Al-4V alloy help to accelerate the implementation process based on a higher troubleshooting efficiency and already existing manufacturing know-how. In addition, martensitic phase transformations are investigated, displaying the potential use of a ‘softer’ martensite. Soft martensite was found to form in bulk materials when the solidification process is accelerated. Finally, the precipitation behavior of near- $\alpha$  and  $\alpha+\beta$  alloys was investigated in detail. The generated understanding of the decomposition of supersaturated phases enables the implementation of optimized post-process heat treatments.

---

## Kurzfassung

Ti-Basislegierungen werden für eine Vielzahl von Anwendungen in fast allen Industriezweigen kommerziell eingesetzt. Die werkstoffspezifischen Vorteile, wie hohe Festigkeit, geringe Dichte und hohe Korrosionsbeständigkeit, eignen sich besonders gut für die Anforderungen in der Luft- und Raumfahrt, der Automobilindustrie und der Medizintechnik, wodurch auch diese Branchen die treibenden Kräfte für die Forschungs- und Entwicklungsaktivitäten in der Ti Industrie sind. Die Kombination mit der additiven Fertigungstechnologie nutzt einerseits die Materialeigenschaften von Ti-Basislegierungen und unterstützt andererseits das Ökodesign-Konzept inklusive einer geringen Abfallerzeugung und der Fähigkeit zur Freiformfertigung. Obwohl es am Markt bereits additiv gefertigte Ti-Basislegierungen gibt, ist das Legierungsportfolio sehr begrenzt und in den meisten Fällen auf eine einzige Legierung, die Ti-6Al-4V Legierung, reduziert. Diese Arbeit befasst sich daher mit der Implementierung von anderen Ti-Basislegierungen, wie z. B. der Legierung Ti-6Al-2Sn-4Zr-2Mo-Si, für den Einsatz in einer additiven Fertigungstechnologie, dem Laser-Pulverbettenschmelzen, und untersucht die Prozessgrenzen und die erreichbaren mechanischen Eigenschaften. Basierend auf eingehenden Charakterisierungstechniken wie Hochenergie-Röntgenbeugung, Transmissions-Elektronenmikroskopie, dynamische Differenzkalorimetrie und Atomsonden-Tomographie können grundlegende Erkenntnisse über das Materialverhalten, hervorgerufen durch das selektive Laserschmelzen, gewonnen werden. Es hat sich gezeigt, dass Analogien zu gut untersuchten Werkstoffen, wie z.B. der Ti-6Al-4V-Legierung, helfen, den Implementierungsprozess aufgrund einer höheren Fehlerbehebungseffizienz und bereits vorhandenem Fertigungs-Know-how zu beschleunigen. Darüber hinaus wurden martensitische Phasenumwandlungen untersucht und es wurde festgestellt, dass die Bildung eines "weicheren" Martensits für den additiven Fertigungsprozess nützlich sein kann. Des Weiteren haben Untersuchungen über das Ausscheidungsverhalten von  $\alpha$  und  $\alpha+\beta$  Legierungen gezeigt, dass das Verständnis über den Zerfall von den übersättigten Phasen für die Implementierung optimierter Wärmebehandlungen eingesetzt werden kann.

---

## List of abbreviations, acronyms and symbols

$\alpha$	Ti hexagonal
$\alpha'$	Ti hexagonal martensite
$\alpha''$	Ti orthorhombic martensite
$\alpha_{GB}$	Grain boundary alpha
$\alpha_p$	Primary alpha grain
$\alpha_s$	Secondary alpha grain
$\beta$	Ti body-centered cubic
$\varepsilon_f$	Elongation at fracture
$\zeta$	(Ti,Zr) <sub>6</sub> Si <sub>3</sub> Intermetallic silicide phase
$\rho_c$	Conditioned bulk density
$\sigma_{0.2}$	Yield strength
$\sigma_m$	Ultimate tensile strength
AE	Aeration energy
Al <sub>eq.</sub>	Aluminum equivalent
AM	Additive manufacturing
APT	Atom probe tomography
ARPGE	Automatic reconstruction of parent grains from EBSD
at.%	Atom percent
bcc	Body-centered cubic
BFE	Basic flow energy
BOR	Burgers' orientation relationship
BSE	Backscattered-electron
$c_c$	Cohesion coefficient
CI	Compressibility
CP titanium	Commercially pure titanium
DED	Direct energy deposition
EBSD	Electron backscatter diffraction
EIGA	Electrode induction melting inert gas atomization
EPBF	Electron beam powder bed fusion
FIB	Focused ion beam
hex	Hexagonal
HEXRD	High-energy X-ray diffraction
HIP	Hot isostatic pressing
HTXRD	High-temperature X-ray diffraction
IPF	Inverse pole figure
IQ	Image quality
K <sub>IC</sub>	Fracture toughness

---

LOM	Light optical microscope
LPBF	Laser powder bed fusion
m.%	Mass percent
m.u.	measurement uncertainty
Mo <sub>eq.</sub>	Molybdenum equivalent
orth	Orthorhombic
PA	Produceability
PBF	Powder bed fusion
PE	Permeability
PSD	Particle size distribution
R&D	Research and development
RT	Room temperature
SE	Secondary-electron
S <sub>E</sub>	Specific energy
SEM	Scanning electron microscope
SRA	Stress relief annealing
Ti6242	Ti-6Al-2Sn-4Zr-2Mo-Si (m.%)
Ti6246	Ti-6Al-2Sn-4Zr-6Mo (m.%)
Ti64	Ti-6Al-4V (m.%)
vol.%	Volume percent
XRD	X-ray diffraction

# 1 Introduction, motivation and scope

Over the last 20 years, metal additive manufacturing (AM) processes significantly evolved due to advances in laser technology, affordable computer technologies, and the industrialization of metal powder production [1]. Starting as a prototyping technique for design purposes only, metal AM has become a state-of-the-art production technology for complex and high-performance components for the automotive, medical, energy, and aerospace industries [2–4]. Although the Covid19 pandemic substantially impacted the global AM sector in 2020, leading to an overall stagnation of the market revenue, especially in the automotive and aerospace sector, the expectations for the near future are positive. A yearly growth of 30 % for the next five years and an expected revenue of 18 billion EUR in 2025 justifies ongoing research and development activities in the metal AM industry [5, 6]. Moreover, the eco-design concept of AM holds great potential for environmentally friendly production with less raw material usage and material waste, reduced air pollution, and energy savings [7].

Titanium base alloys are a promising class of materials known to promote the eco-design concepts, especially in combination with AM. With regard to the low density of approximately  $4.5 \text{ g cm}^{-3}$ , titanium base alloys exhibit superior specific strength compared to other engineering alloys [8]. The combination of excellent corrosion resistance and highly tunable mechanical properties deriving from the allotropic phase transformation [9, 10] are major arguments for the intensive research and development (R&D) activities in the field of Ti base alloys.

Despite the background of a large Ti alloy portfolio for traditional process techniques, there is only a small selection of alloys applicable for metal AM techniques such as laser powder bed fusion (LPBF). In addition, most of them, besides the commonly used Ti-6Al-4V (Ti64, m.%) alloy, are modestly or minimally reported in terms of mechanical properties [11, 12]. Therefore, the present thesis is dedicated to implement already known and well-investigated titanium alloys for the LPBF process to increase the number of additively processible alloys. The successful implementation of new alloys also requires a deep understanding of material-specific characteristics. Therefore, this thesis starts with investigating AM Ti64 and subsequently applies the generated knowledge to analyze the practicability of other Ti base alloys for LPBF.

**Figure 1.1** schematically shows the workflow and the main scopes of this thesis. In the course of this work, it is essential to examine the entire AM product chain to obtain a profound image of the challenges and opportunities accompanying AM of a new alloy type. The investigations, therefore, start with a detailed analysis of the powder to evaluate the influence on the LPBF process and detect metastable phases occurring from the rapid cooling during atomization [13]. In the next step, the characterization of bulk components contributes to a deeper understanding of the material response during LPBF and helps to establish enhanced

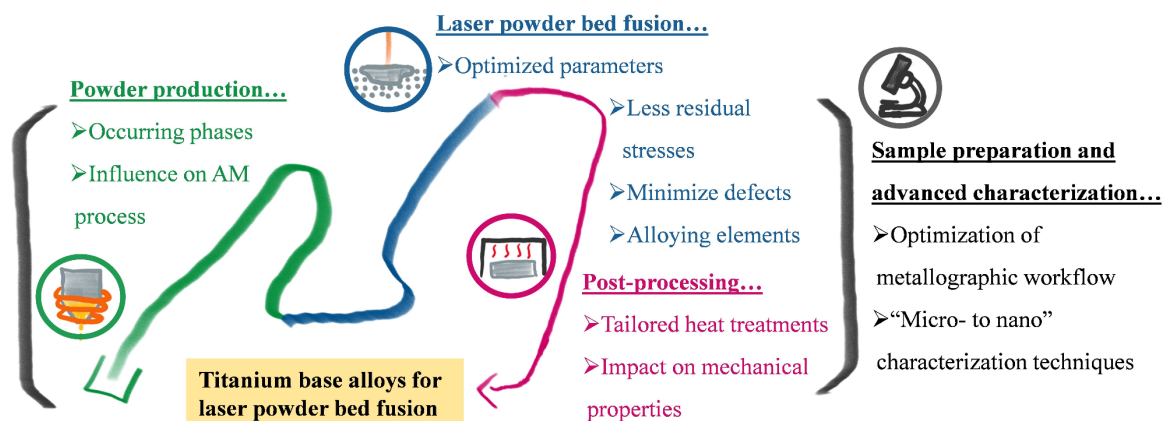


**Figure 1.1:** Schematic workflow diagram showing the main scopes of the present thesis. The investigations focus on the whole product chain, beginning with the powder production and the LPBF manufacturing process, and ending with the post process heat treatment supported by advanced sample preparation and characterization techniques.

process parameters. The adaptation of process parameters is essential to overcome typical defects related to AM, *e.g.*, pores and alloy specifics such as vulnerability for residual stresses [14, 15]. Moreover, understanding the influence of particular alloying elements helps to implement new alloys for the LPBF process to extend the alloy portfolio further.

In the last step, the fundamentals of post-processing are described. Post-processing assists in tuning the material properties with regard to the respective application. Furthermore, microstructure-properties relationships are examined and assist in determining potential applications that require high strength, high ductility or temperature resistance.

The workflow is guided by a newly developed and optimized metallographic sample preparation suited for the respective micro- or nano-characterization techniques. The optimized metallographic practice ensures reproducibility and focuses on particularities during the sample preparation of the metallic powder and the LPBF manufactured components.

The following sections provide an overview of the state of the art concerning titanium alloys, metal powder production, and additive manufacturing. Furthermore, the most important findings of the appended publications are summarized, and the remaining questions and future challenges regarding LPBF of titanium alloys are thematized.

## 2 State of the Art

### 2.1 Titanium base alloys

#### 2.1.1 Alloy classification

The two allotropic modifications of titanium are the body-centered cubic (bcc)  $\beta$  phase, which is also the high-temperature phase of titanium and its alloys, and the hexagonal close-packed (hcp)  $\alpha$  phase [16]. According to the concentration of  $\beta$  stabilizing elements in the alloy system, titanium alloys can be classified as depicted in the pseudo-binary phase diagram in **Figure 2.1** [9, 17]. The phase diagram shows the occurring phases as a function of the temperature and the amount of isomorphous alloying elements, based on an Al equivalent ( $Al_{eq.}$ )  $< 9$  m.%. The  $Al_{eq.}$  and Mo equivalent ( $Mo_{eq.}$ ), shown in **Equations (1) and (2)**, summarize the effect of  $\alpha/\beta$  stabilizing elements. Furthermore, the  $Al_{eq.}$  and  $Mo_{eq.}$  shift the  $\beta$  transus temperature to higher or lower temperatures as shown on the left side of **Figure 2.1** [9, 17]:

$$[Al]_{eq.} = [Al] + 0.33 [Sn] + 0.17 [Zr] + 10 [O] \quad (1)$$

$$[Mo]_{eq.} = [Mo] + 0.2 [Ta] + 0.28 [Nb] + 0.4 [W] + 0.67 [V] + 1.25 [Cr] \quad (2)$$

$$+ 1.25 [Ni] + 1.7 [Mn] + 1.7 [Co] + 2.5 [Fe]$$

Titanium alloys which exclusively contain  $\alpha$  stabilizers, neutral alloying elements, and only minor amounts of  $\beta$  stabilizers, are called  **$\alpha$  alloys**. These alloys are known for their high creep and corrosion resistance as well as low cytotoxicity and thus are often used in the chemical or biomedical industry [17, 18].

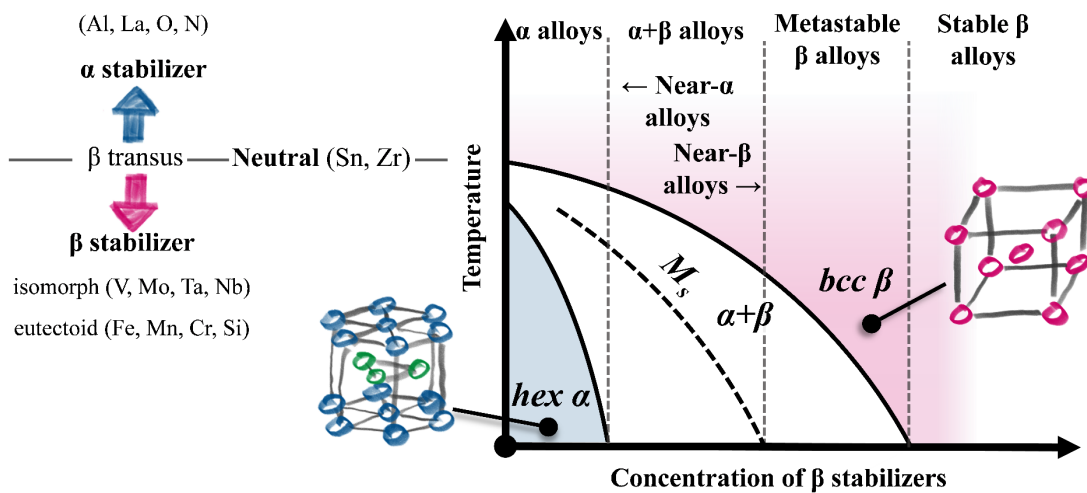


**Figure 2.1:** Pseudo-binary phase diagram showing the classification of titanium alloys depending on the concentration of  $\beta$  stabilizing elements (right side). The influence of particular elements on the  $\beta$  transus temperature is shown on the left side.

The class of  **$\alpha+\beta$  alloys** exists due to the simultaneous occurrence of both allotropic forms at room temperature (RT) if the concentration of  $\beta$  stabilizing elements is between 2 and 6 m.%. The simultaneous presence of both allotropic forms is decisive for the great variety of properties and assists in tailoring the mechanical properties to fit the application requirements [19]. The most important representative of this class is the “workhorse” alloy Ti64 which can be produced via various techniques, among them AM, and is broadly used in several industrial applications [20–26].  $\alpha+\beta$  alloys which contain only a small volume fraction of the  $\beta$  phase are often called **near- $\alpha$  alloys** [17]. These alloys combine a high creep resistance and strength and thus are mainly used for applications at high service temperatures [27]. In contrast, **near- $\beta$  alloys** contain a high concentration of  $\beta$  stabilizing elements and are known for their high strength [17].

Among the class of  $\beta$  alloys, **stable  $\beta$  alloys** are rarely used in the industry due to the relative high specific weight, unfavorable weldability and bad oxidation behavior. Therefore, only **metastable  $\beta$  alloys** are commercially used. In contrast to  $\alpha$  and  $\alpha+\beta$  alloys, quenching from the  $\beta$  phase-field of metastable  $\beta$  alloys does not lead to a martensitic transformation; hence close to 100 vol. % of the  $\beta$ -phase retain upon quenching. The combination of a good formability, arising from 12 possible slip systems in the bcc crystal, and high strength (>1400 MPa) makes these alloys suitable for various structural applications. Moreover, metastable  $\beta$  alloys exhibit excellent biocompatibility and thus are used for implants [9, 17, 18].

### 2.1.2 Phase transformations

The phase transformation from  $\beta$  to  $\alpha$  either takes place by diffusion-controlled nucleation and growth or by martensitic transformation for  $\alpha$  and  $\alpha+\beta$  alloys. During the  $\beta \rightarrow \alpha$  transformation, the bcc crystal can transform into 12 possible hexagonal (hex) variants, which is also known as the Burgers’ orientation relationship (BOR) given in **Equation (3)** [28, 29].

$$\{110\}_{\beta} \parallel \{0001\}_{\alpha} \text{ and } [111]_{\beta} \parallel [11\bar{2}0]_{\alpha} \quad (3)$$

Yellow planes in **Figure 2.2 (a)** schematically demonstrate the BOR and show the match between the  $\{110\}_{\beta}$  and  $\{0001\}_{\alpha}$  lattice planes appearing for both formation mechanisms; diffusion-controlled growth and martensitic transformation [9, 30]. The LPBF manufacturing process generates cooling rates up to  $10^4 - 10^6 \text{ K s}^{-1}$ , which most likely lead to martensitic phase transformations and martensitic microstructures [31, 32]. Apart from the basic principles of martensitic transformations, which will not be repeated here, the generation of martensite in titanium alloys involves three fundamental processes [10, 33]:

- The “Bain” distortion transforms the bcc lattice either into the hex or the orthorhombic (orth) lattice.
- Twinning or slip-induced shear processes generate an invariant plane.



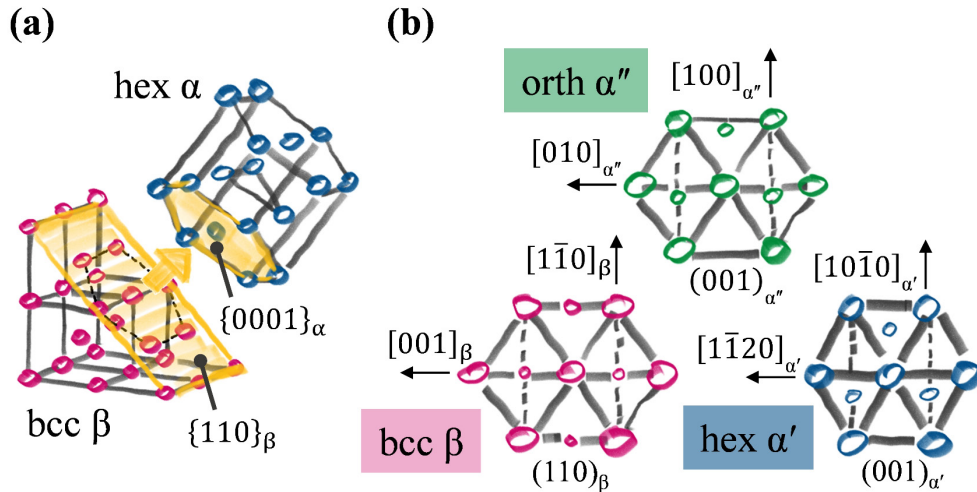


**Figure 2.2:** (a) The occurring variants during the phase transformations of titanium alloys are governed by the Burgers orientation relationship (BOR), which is schematically shown for a yellow-colored plane [30]. The atomic positions during the martensitic phase transformation from  $\beta$  (pink) to  $\alpha''$  (green) or  $\alpha'$  (blue) are presented in (b) and demonstrate the shuffle of atoms on the  $(110)_\beta$  planes in  $[1\bar{1}0]_\beta$  direction [10].

- Atom shuffling on  $(110)_\beta$  planes in  $[1\bar{1}0]_\beta$  direction takes place to locate the atoms in proper positions in the hex or the orth lattice structure. The shuffling process is shown in **Figure 2.2 b**, which highlights the atomic shift of the bcc  $\beta$  phase atoms (pink) towards the orth  $\alpha''$  (green) or the hex  $\alpha'$  (blue) lattice structure.

The atom movement and the specific atomic positions of the occurring phase during the athermal phase transformation strongly depend on the alloy's chemical composition [34]. The hex  $\alpha'$  martensite occurs for alloys with a low content of  $\beta$  stabilizers, whereas the orth  $\alpha''$  martensite forms in alloys with higher amounts of  $\beta$  stabilizers [9].

The LPBF manufacturing process and the rapid cooling of the molten pool lead to the supersaturation of substitutional alloying elements in the matrix phase. The resulting solid solution is, due to the rapid cooling, far away from thermodynamic equilibrium, and most likely only a single-phase –  $\alpha'$  or  $\alpha''$  – exists after the manufacturing process. These martensitic phases tend to be unstable and decompose during exposure to high temperatures. To avoid uncontrolled decomposition of the martensitic microstructure, which would lead to changes in the mechanical properties, LPBF post-process heat treatments are applied [9, 35–37].

### 2.1.3 Macro- and microstructure

The present section discusses the occurring microstructures of near- $\alpha$ , near- $\beta$  and  $\alpha+\beta$  titanium alloys with respect to the LPBF manufacturing process. Starting with the initial powder, **Figure 2.3** provides an overview of the occurring macro- and microstructures along the LPBF

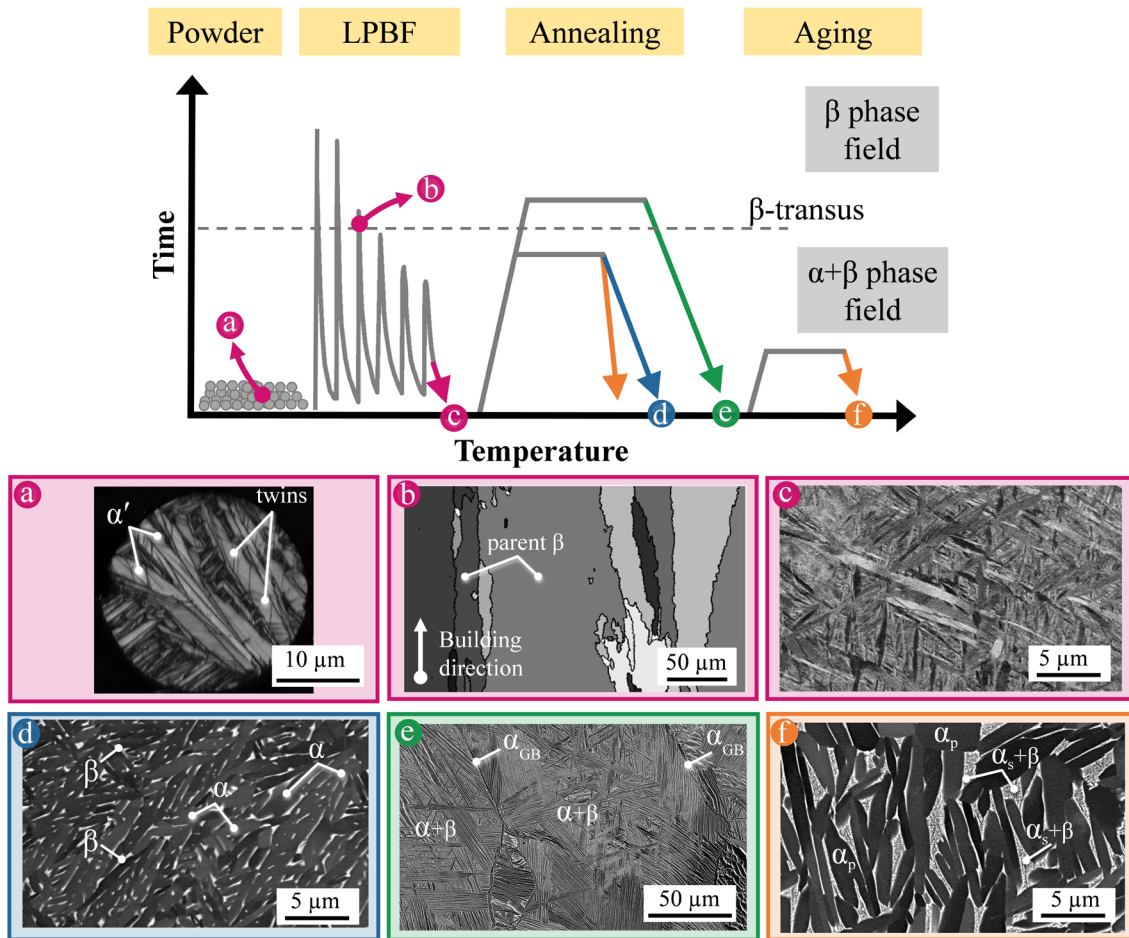


**Figure 2.3:** Microstructures of near- $\alpha$  and  $\alpha+\beta$  alloys along the processing route of a LPBF manufacturing process. The respective micro- and macrostructure of (a) and (b) are shown as EBSD images whereas the images of (c) – (f) are obtained via SEM in BSE mode.

processing route. Besides the “as-built” microstructure, **Figure 2.3** depicts the microstructure after common heat treatments.

The cooling rate during metallic powder production by gas atomization can reach up to  $10^8 \text{ K s}^{-1}$  [38–40] and thus is responsible for the martensitic microstructure in the powder material. The morphology of the martensite can either be massive [41–43] or acicular [17]. Massive martensite is typical for alloys with a low  $M_{0eq}$  and is defined by irregular regions containing parallel  $\alpha$  laths of  $0.5 - 1 \mu\text{m}$  size [9]. The acicular type is typical for alloys such as Ti64 and is shown in the electron backscatter diffraction (EBSD) image in **Figure 2.3 a**. However, no distinct differentiation exists between the massive and acicular martensitic microstructure. Both types can coexist in alloys with similar chemical compositions, as reported recently for a LPBF produced Ti64 alloy [44]. The powder microstructure in **Figure 2.3 a** also shows the occurrence of a high density of twins and dislocations, typical for acicular martensite [45–47].

During LPBF,  $\alpha+\beta$  alloys run through a  $\beta$  solidification pathway which leads to the formation of a  $\beta$  macrostructure – or often referred to as parent  $\beta$  microstructure – prior to the martensitic transformation. The typical parent  $\beta$  microstructure of a LPBF manufactured  $\alpha+\beta$

alloy (Ti64) is displayed in **Figure 2.3 b**. The visibility of the  $\beta$  grain morphology results from a parent grain reconstruction via a software-based tool called ARPGE (short for automatic reconstruction of parent grains from EBSD) [48, 49], which uses the BOR in **Equation (3)** to calculate the corresponding parent  $\beta$  grains. Several studies demonstrate a strong  $\langle 001 \rangle_{\beta}$  fiber texture along the additive manufacturing building direction, especially for electron beam powder bed fusion (EPBF) [50, 51] and other additively manufactured titanium base alloys [52–56]. The epitaxially grown elongated  $\beta$  grains lead, among other things, to anisotropic mechanical properties [23] and will be discussed in the next chapter. The size and morphology of the parent grains depend on the manufacturing parameters and the chemical composition, *i.e.*, the alloy's grain growth restriction factor [57].

**Figure 2.3 c** shows the RT microstructure via an scanning electron microscopic (SEM) image of an additively manufactured  $\alpha+\beta$  Ti64 alloy originating from the complex thermal cycles during the layer-by-layer additive manufacturing. The thermal cycles and the high cooling rates, *e.g.*,  $10^4 - 10^6 \text{ K s}^{-1}$  during LPBF [58–60], lead to a hierarchical martensitic  $\alpha'$  or  $\alpha''$  microstructure comprising primary, secondary, tertiary, etc. grain features [61, 62]. The size of the martensitic grains depends, equal to the parent  $\beta$ -grains, on the chemical composition, as the parent microstructure represents an expansion limitation of  $\alpha'$  or  $\alpha''$  features [9, 17]. Similar to the observations in titanium powder material, the as-built grains also reveal a high density of internal lattice defects such as twins and dislocations [63]. The as-built microstructures are supersaturated in alloying elements, and most likely, only a single phase is present at RT [10, 33]. The precipitation of additional equilibrium phases such as  $\beta$ ,  $\alpha_2$ , and silicide particles only occurs by adapting the manufacturing parameters or implementing a post-process heat treatment [9].

Post-process heat treatments are performed to shift the microstructure towards thermodynamic equilibrium and reduce residual stresses. **Figure 2.3 d** schematically shows the temperature-time control of a stress relief annealing (SRA) heat treatment, usually performed on an industrial scale due to moderate temperatures ( $< 900 \text{ }^\circ\text{C}$ ) and low heat treatment times ( $< 5 \text{ h}$ ). SRA leads to coarse  $\alpha$  grains and a minor amount of  $\beta$  phase, visible as the bright phase in the BSE image of a Ti-6Al-2Sn-4Zr-2Mo-Si (Ti6242, m.%) alloy in **Figure 2.3 d** [64]. The phase fraction of the equilibrium  $\beta$  phase depends on the chemical composition and especially the  $\text{Mo}_{\text{eq}}$  of the alloy. The final  $\alpha$  and  $\beta$  grain sizes can be modified by controlling the heat treatment temperature and time. However, in most cases, the temperature is limited as the material softens during high-temperature annealing. **Figure 2.3 e** displays the microstructure and the temperature profile of a super-transus heat treatment of a Ti64 alloy followed by moderate cooling rates. This super-transus heat treatment diminishes the LPBF manufactured morphology and results in lamellar  $\alpha+\beta$  microstructure. The size of the lamellas depends on the particular cooling rate applied. Nonetheless, it should be noted that annealing above the  $\beta$  transus temperature promotes the formation of grain boundary  $\alpha$  phase ( $\alpha_{\text{GB}}$ ), which negatively impacts the mechanical properties [9].

Furthermore, additional aging can be performed and leads to small secondary  $\alpha$  phase ( $\alpha_s$ ) precipitates within  $\beta$  areas, see SEM image of aged Ti6242S in **Figure 2.3 f**. However, additional aging is only reasonable if the first annealing step is followed by cooling rates high enough to originate a supersaturated  $\beta$  phase. The size and form of the large primary  $\alpha$  ( $\alpha_p$ ) grains, which substantially impact the mechanical properties, is influenced by the temperature-time control during annealing. Additionally, aging also promotes the formation of the intermetallic  $\text{Ti}_3\text{Al}$   $\alpha_2$  phase in regions where the Al content is high. According to literature [9, 17],  $\alpha_2$  precipitation hardening of the  $\alpha$  phase starts at a concentration of about 5 m.%.

#### 2.1.4 Mechanical properties of $\alpha+\beta$ alloys

In general, the mechanical properties of titanium alloys are affected by the material's chemical composition and microstructure. The solidification of the small melt pools during additive manufacturing is governed by high cooling rates, leading to a non-equilibrium microstructure. Such microstructures typically exhibit small grain sizes, saturated phases and residual stresses. Therefore, post-processing is required to transform the non-equilibrium material into a more stable form, resulting in an  $\alpha+\beta$  microstructure with improved mechanical properties. This chapter discusses the differences between the microstructure-property relationships of  $\alpha+\beta$  alloys manufactured via AM and  $\alpha+\beta$  alloys arising from traditional production methods.

For lamellar and bi-modal microstructures, the slip length across incoherent interfaces is the most crucial factor determining the strength, ductility, toughness and fatigue resistance [9, 17]. If the slip length is short, the strength increases and vice versa, a long slip length leads to a decreasing strength of the material. Typically, Ti alloys reveal incoherent  $\alpha/\beta$  interfaces ( $\sim 1 \mu\text{m}$ ), which are relatively close to each other. However, the effective slip length is usually given by the  $\alpha$  colony sizes (10 – 500  $\mu\text{m}$ ) with parallel slip systems, and thus slip can be transferred easily in lamellar microstructures. In contrast, the effective slip length in martensitic microstructures produced by AM is given by the individual widths of  $\alpha$  plates, resulting in a much higher yield strength up to 1300 MPa for LPBF Ti64 [65]. The application of post-process heat treatments significantly enhances the elongation at fracture up to 20 % for AM Ti64 [66] but, at the same time, increases the  $\alpha$  plate width and subsequently the effective slip length leading to reduced yield strength [9, 17].

For lamellar and bi-modal microstructures, the prior  $\beta$  grain structure is vital due to a continuous  $\alpha$  layer, *i.e.*, an  $\alpha_{\text{GB}}$  layer along parent  $\beta$  grain boundaries [9, 17]. Plastic deformation is known to accommodate at these  $\alpha_{\text{GB}}$  layers, leading to reduced ductility. This effect is diminished for AM typical microstructures with a fully martensitic transformation lacking  $\alpha_{\text{GB}}$  nucleation. Nonetheless, the elongated prior  $\beta$  grains in LPBF manufactured  $\alpha+\beta$  alloys result in anisotropic mechanical properties. Liu et al. [60], *e.g.*, reported that horizontal and vertical build tensile samples exhibit a difference of 30 MPa in yield strength and 2 % variation in the elongation at fracture. This is attributed to the elongation of grains in the building direction, originating from the AM process, which leads to reduced yield strength and an increase in elongation of vertical produced samples. In order to reduce the anisotropy in the material,

epitaxial grain growth of parent  $\beta$  grains must be limited. Yao et al. [67] and Zhang et al. [68] reported an alleviation of the anisotropy and less elongated  $\beta$  grains by adding boron to Ti-6Al-4V alloy. With boron, the grain growth is restricted and the microstructure becomes equiaxed. This results in reduced anisotropy and enhanced strength. However, the amount of boron must be limited ( $< 1$  m.%) to achieve a good balance of tensile strength and ductility along with a reduction of the anisotropy [67, 68]. Besides boron, trace elements such as carbon and silicon are also prominent for grain refinement and improved performance [67]. In addition to alloying, Zhang et al. [69] reported recrystallization of the parent  $\beta$  grains, caused by ultrasonic impact treatment on a common Ti-6Al-4V alloy. This method relies on the formation of dislocations on the surface through plastic deformation, which recrystallizes during the melting process of the next layer.

The high cycle fatigue strength is heavily impacted by the resistance to dislocation motion. The effective slip length, described in the previous lines, is of similar importance when considering the fatigue strength. In this context, higher cooling rates lead to smaller  $\alpha$  colony sizes and higher fatigue strength but deteriorate the fracture toughness [70]. However, additional aspects must be considered for AM-produced components as they are known to reduce the fatigue performance, *e.g.*, surface roughness, pores and residual stresses. In order to evaluate microstructural influences, surface machining is an efficient tool for diminishing the impact of surface roughness due to the minimization of crack initiation sites. In general, defect-free AM components would reveal even higher fatigue strength when compared to conventional manufactured (lamellar) parts [60]. However, the unavoidable presence of defects significantly deteriorates the fatigue properties and results in disadvantageous low fatigue strengths of AM components. In addition, hot-isostatic pressing (HIP) reduces internal defects such as pores and substantially enhances fracture toughness as well as fatigue strength ( $10^7$  cycles to failure) [71]. Zhao et al. [71] reported that a HIP treatment enhances the fatigue strength of AM produced samples up to 550 MPa compared to cast parts with an fatigue strength of about 450 MPa.

In contrast to tensile and fatigue properties, smaller  $\alpha$  grain sizes decrease the creep strength in  $\alpha+\beta$  titanium alloys [9]. Therefore, the cooling rate must be low to generate coarse grains and improve creep performance. However, additively manufactured components possess considerably fine microstructures inappropriate for sufficient creep performance and hence post-process heat treating is usually necessary. The limiting deformation mechanism which governs the creep resistance in  $\alpha+\beta$  alloys at application temperatures of 400 – 550 °C is lattice diffusion controlled dislocation climb [72, 73]. Slight amounts of Si are added in some Ti alloys, such as the Ti6242S alloy, to reduce dislocation motion via the formation of incoherent particles. Moreover, the presence of the coherent  $\alpha_2$ -Ti<sub>3</sub>Al phase is also an effective barrier for dislocation motion. The precipitation of this intermetallic phase is promoted by a higher Al content or the addition of Sn [9, 17].

The mentioned differences in the additively and conventionally manufactured Ti base alloys' mechanical properties are qualitatively summarized from various literature references [9, 17, 60, 66, 70–74] and displayed in **Figure 2.4**. More precisely, **Figure 2.4** visualizes the

as-built properties compared to the properties of heat-treated and conventional produced – lamellar – material conditions.

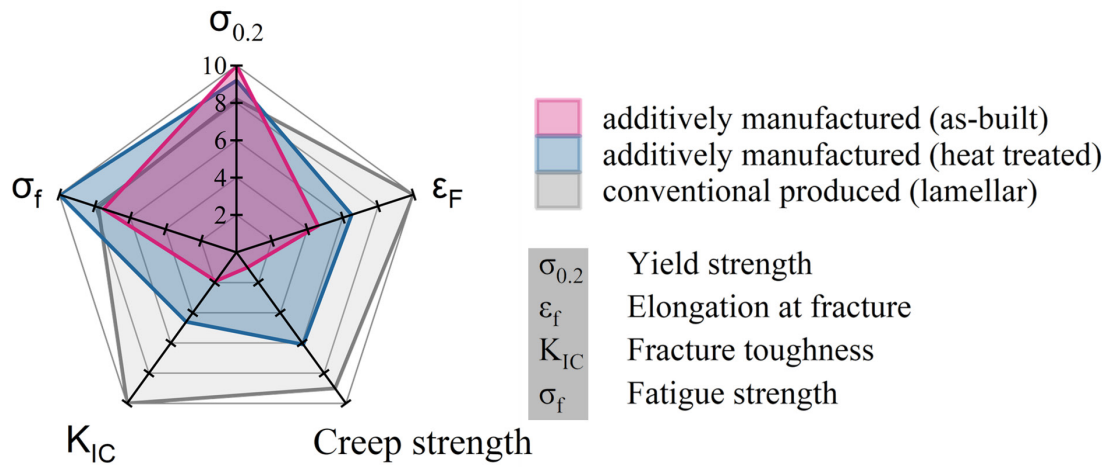


**Figure 2.4:** Radar diagram displaying qualitative trends of the mechanical properties of  $\alpha+\beta$  titanium alloys, revealing the difference between as-built, heat treated and lamellar microstructures.

## 2.2 Additive manufacturing of titanium alloys

### 2.2.1 Working principle and process synergies

AM is a complex manufacturing process whose outcome depends on multiple interacting process, material and system variables. In general, the primary goal of the AM process is to produce objects with high accuracy, surface quality and specific material properties, which is why it is often applied and heavily researched in industries such as aerospace and racing. Since the research of this thesis deals with additively manufactured Ti alloys applied for racing, **Figure 2.5** is related to this specific application field and schematically depicts the process synergies in the course of AM [75].

The process synergies have to be synchronized precisely to fulfill the racing industry's high demands. In the following paragraphs, the most critical process variables related to the field of Materials Science are described in detail.

AM allows the production of bulk components through progressively adding powder layers directed by a digital model of the final geometry. According to ASTM Standard F2792, AM can be categorized into two groups, namely the direct energy deposition (DED) and powder bed fusion (PBF) methods which can be further divided in terms of the primary heat source such as laser (DED-L), electron beam PBF (EPBF) or plasma arc (DED-PA) [76]. This work focuses on the LPBF manufacturing process, schematically depicted in **Figure 2.6** [77].

In the LPBF process, the process starts with a three-dimensional CAD model placed in a build volume. For geometries with insufficient bonding to the underneath layers, additional support structures are added. In the following steps, the desired geometry is sliced into planar

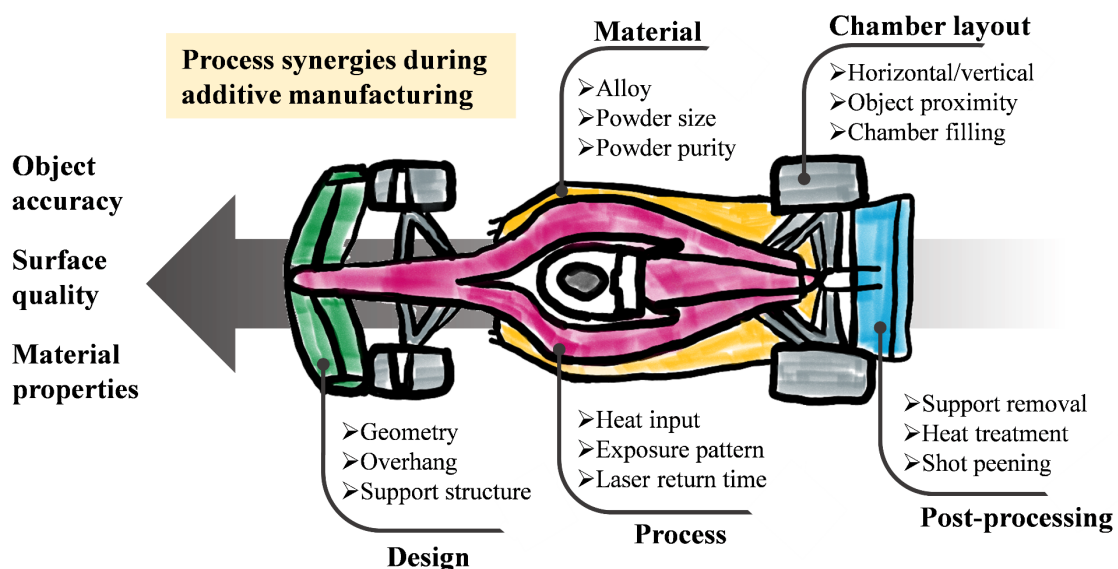


**Figure 2.5:** Schematic drawing depicting the synchronization of process synergies during additive manufacturing and demonstrates the interaction of process variables for the production of objects with high accuracy, surface quality and specific material properties for industries such as racing [75].

layers of equal thickness. Subsequently scan patterns are defined, and files are exported based on a material-specific parameter set, including machine configurations. During LPBF, components are built by fusing thin layers upon layer of spreaded powder on a building platform. After each layer, the building platform lowers and the process starts again [78–82].

### 2.2.2 Melt pool and thermal behavior

The heat transmission from the laser into the powder bed and the processes in the melt pool are multi-physics phenomena influenced by various process parameters [60]. The volumetric energy density  $E_d$  (in  $\text{J}\cdot\text{mm}^{-3}$ ) in Equation (4) summarizes the most important parameters to be considered by LPBF:

$$E_d = \frac{P}{v \cdot h \cdot t} \quad (4)$$

where  $P$  is the laser power (in  $\text{J}\cdot\text{s}^{-1}$ ),  $v$  is the scanning speed (in  $\text{mm}\cdot\text{s}^{-1}$ ),  $h$  is the hatch spacing (in mm), and  $t$  describes the layer thickness (in mm). Besides the mentioned parameters, multiple other parameters such as the scan pattern – also known as scan strategy-, powder properties, built plate temperature, laser turnaround control, laser spot size, track overlap and the process atmosphere have to be taken into account [83–89].

During PBF, the whole energy provided by the heat source is conducted immediately in the powder bed. A part of the energy is directly absorbed by single particles, while the residual energy is reflected and continues its path to the next absorption/reflection point [90]. In that way, many particles are heated simultaneously and a melt pool forms. Yin et al. [91] provided an overview of the dynamics in the melt pool, see schematic drawing in **Figure 2.7**. A high  $E_d$  can lead to the ejection of powder particles or molten droplets, also known as spattering [92]. Spattering is a critical value considering the formation of pores and typically occurs in the

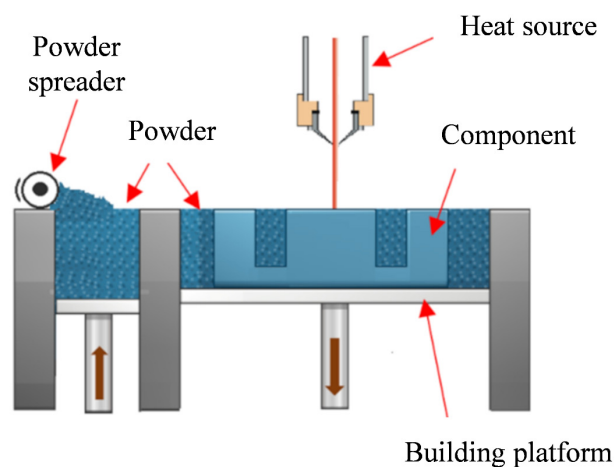


**Figure 2.6:** Schematic representation of the LPBF manufacturing process. Figure is redrawn from Ref. [77]



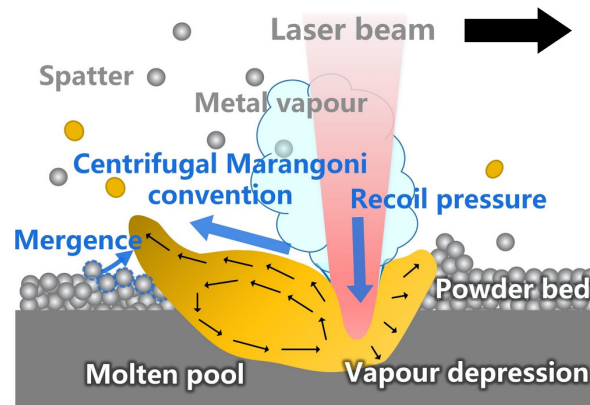


**Figure 2.7:** Hydrodynamic melt pool processes caused by the recoil pressure and the Marangoni force can result in spattering effects if the applied heat input, *i.e.* the energy density, is high. Figure is adapted from [91].

keyhole manufacturing mode, and not in the conduction mode [93], where the melt is relatively flat on the surface. Moreover, **Figure 2.7** visualizes that the combination of metal vapor-induced recoil pressure and the Marangoni effect leads to a head protrusion and a tail depression of the metal track. The backward surging of the melt is more pronounced for large melt pools, *i.e.*, a high  $E_d$ , promoting intensive droplet ejection at the end of the melt pool [91].

The whole LPBF process is performed in a chamber shielded by inert gas to prevent nitration and oxidation. Moreover, the gas flow is responsible for removing process by-products such as splattered melt and ejected powder, which would lead to spherical and non-spherical artefacts on the surface [94]. In this context, Ladewig et al. [94] recommend the following flow conditions of the shielding gas: (i) high gas velocity for enhanced removal of process by-products; (ii) homogeneous velocity in all areas; (iii) gas flow near the layer surface to reduce laser – spatter interactions and (iv) avoid turbulences in an upward direction for less laser – spatter interaction.

One of the key challenges for AM development is to control the defect structure, including porosity, high surface roughness, high affinity of Ti to oxygen and nitrogen, and residual stresses. Although, in theory, AM can provide fully dense structures with superior static and dynamic mechanical properties [60], it is very sensitive to process irregularities leading to inhomogeneities such as pores, even if the process parameters are finely tuned. However, the amount of pores should be minimized, as pores might limit mechanical properties, such as the fatigue strength by acting as nucleation sites for micro-cracks and adiabatic shear bands [60].

In general, two types of pores are typical in LPBF manufactured parts: Elliptical gas pores that are filled with trapped inert gas and are linked to collapsed keyholes [60, 91] and lack-of-fusion pores of irregular shape induced by insufficient laser energy [60, 91]. The latter is considered avoidable by simply increasing the  $E_d$  [95]. The size and the volume fraction of gas pores can only be reduced but not eliminated by applying additional HIP treatment [66, 96].

The roughness of the as-built components is considered [97] to be a result of three primary mechanisms: i) the stair-case effect and the related inclination angle, ii) the adhesion

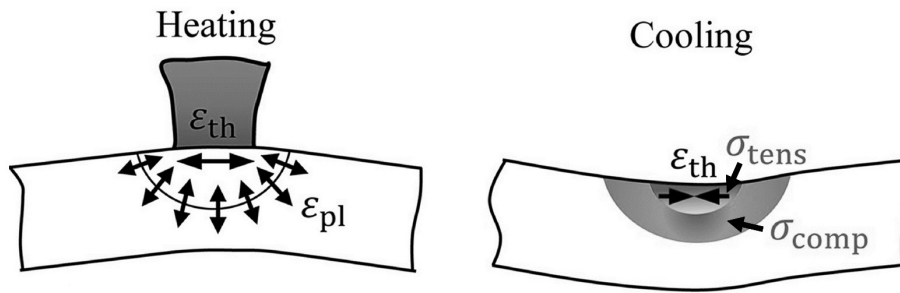


**Figure 2.8:** Formation of residuals stresses by the localized heating and cooling circle during LPBF.  $\epsilon_{th}$  is the thermal strain,  $\epsilon_{pl}$  is the plastic strain,  $\sigma_{tens}$  is the tensile and  $\sigma_{comp}$  compression stress. Figure is adapted with permission from Ref. [98].

of particles caused by partially melted powder, and iii) the surface porosity. It should be noted that the surface quality depends on AM process parameters such as layer thickness and laser power [60].

A common disadvantage, especially during LPBF of Ti alloys, is the occurrence of residual stresses, which might lead to distortions and cracks of the manufactured components. The main reason for residual stresses is the high-temperature gradient during AM. **Figure 2.8** schematically depicts the formation of residual stresses during a heating and cooling cycle where  $\epsilon_{th}$  is the thermal strain,  $\epsilon_{pl}$  is the plastic strain,  $\sigma_{tens}$  is the tensile and  $\sigma_{comp}$  compression stress [98]. Due to the small melt pool, the heated region is localized and surrounded by cooler areas. This induces compressive stresses in the hot regions, which transform into tensile stresses during the subsequent cooling. The contraction of these regions near the surface might ultimately lead to warped geometries. In addition, residual stresses accumulate with increasing number of layers, leading to peak stresses near or at the surface of the last applied layer [11, 60].

Typical approaches to reduce residual stresses during the manufacturing process are the application of a higher energy density, which is complicated because of the localized heat input of the laser, and *in situ* annealing during LPBF. Both methods focus on reducing the temperature gradient and a minimized temperature change [1, 99]. *In situ* annealing can be performed by increasing the pre-heating temperature of the building platform [100], by the implementation of a double exposure scan strategy [101], or via external devices such as diodes for large-area surface heating [99]. Contrarily, the application of higher temperature during LPBF might be accompanied with grain growth and microstructural changes and, therefore, must be tuned precisely [99, 101].

### 2.2.3 Applications

The production of complex parts and the freeform fabrication ability are the most significant advantages of AM when compared to traditional production methods [60]. Although the aerospace industry is the driving force for the usage of Ti alloys, recent developments, among

them AM, make these alloys also attractive for other industries such as the automotive sector and the biomedical industry [9, 11, 17, 60]. However, as mentioned before, the aerospace sector is still the main driving force for developing and adapting Ti alloys for AM applications. The aerospace industry is predicted to grow with an annual revenue of \$430 billion until 2025 [6]. However, only about \$3.1 billion of the global revenue is related to AM technologies. With an average annual growth rate of 20 % [6], AM is, nonetheless, one of the strongest growing techniques in this field.

**Figure 2.9** shows examples of additively manufactured Ti64 parts for different industrial sectors. **a-c)** presents LPBF manufactured aerospace parts like a door hinge, cabin brackets and a latch shaft [77, 102, 103]. **d)** and **e)** depict automotive components such as a brake caliper and a connecting element for the exhausting system produced by Pankl Racing Systems AG [77, 104]. Moreover, Ti alloys are used for manufacturing medical applications like an orthopedic device shown in **f)** and a porous spinal implant shown in **g)** [77].

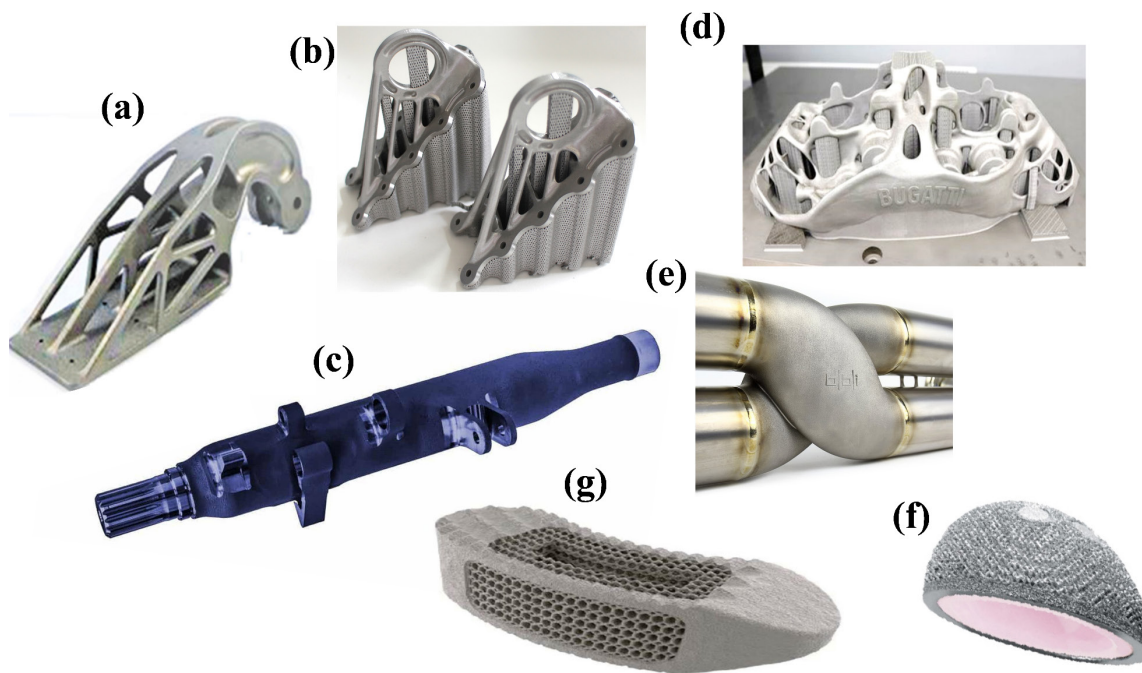


**Figure 2.9:** Additively manufactured components made of Ti64 for the aerospace: **a)** door hinge [77], **b)** cabin brackets [103], **c)** latch shaft [102]; the automotive industry: **d)** brake caliper [77], **e)** connecting element in the exhausting system [104]; medical applications: **f)** orthopedic device [77] and **g)** porous spinal implant [77].

## 2.3 Powder production and relations to LPBF

### 2.3.1 Electrode induction melting inert gas atomization

The initial material for metal additive manufacturing processes is metal powder. Gas atomization is a standard method on industrial scale for producing spherical powder particles to be used for LPBF [105]. **Figure 2.10 a** schematically depicts the crucible-free EIGA (electrode induction melting inert gas atomization) gas atomization technology, which is often used to produce titanium powder particles, see SEM image in **Figure 2.10 b**. During the EIGA process, the tip of a rotating ingot, used as an electrode, is heated by an induction coil and small amounts of melt drop into a gas nozzle [106–109]. The small melt droplets are atomized via high-pressure inert gas (e.g., Ar) and collected in a chamber for particle size fractioning. To ensure a high-quality titanium powder, the whole process is conducted under a shielding gas atmosphere for preventing oxidization and reducing the number of interstitial impurities like O, N and C [106, 110]. The amount of interstitials has to be limited as a high interstitial content increases the strength by solution strengthening and negatively impacts the manufactured components' ductility [105, 111].

### 2.3.2 Morphology, particle size distribution and powder porosity

Besides the chemical composition and interstitial impurities, titanium powder particles for LPBF application have additional requirements which must be considered and correlated to the bulk component properties. Essential characteristics of powder are the particle size distribution (PSD), the powder porosity and powder morphology properties like sphericity, as well as the presence of satellite particles. These powder characteristics are of crucial importance

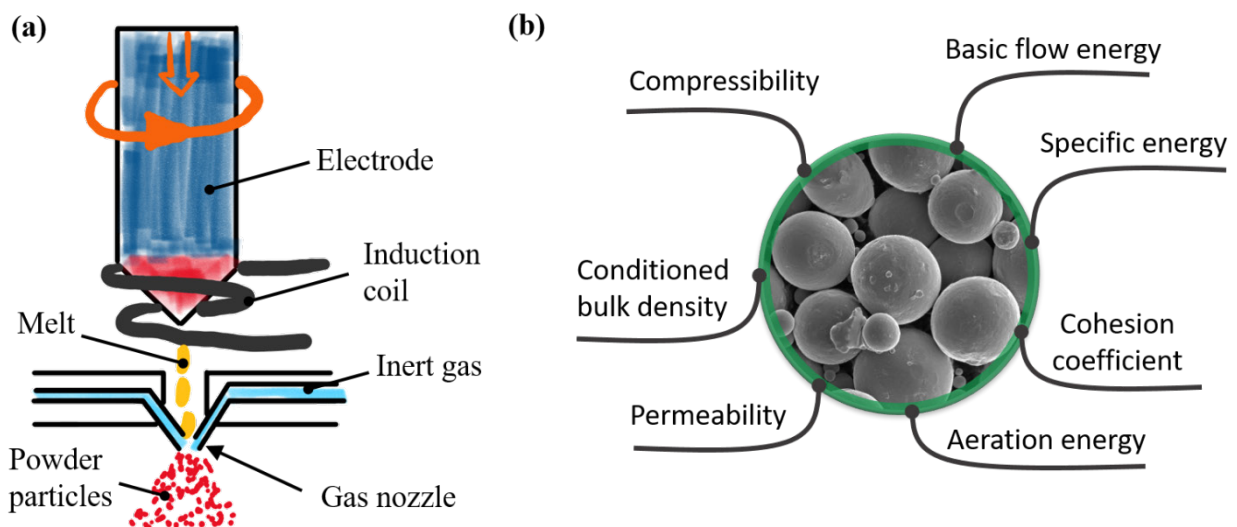


**Figure 2.10: a)** Schematic illustration of the EIGA (electrode induction melting gas atomization) process of Ref. [106] for the production of powder particles shown in the SEM image in **b)**. The rheological influencing factors (FT4) of the powder on the LPBF process are also depicted in **b)**.

for rheological aspects like flowability, apparent and tapped densities, and additionally, define the particle packing ability, which favors the formation of a dense powder bed leading to superior bulk densities after LPBF.

The PSD should be in the range of 10-60  $\mu\text{m}$  for the usage in an LPBF process, which is relatively low compared to 45-105  $\mu\text{m}$  for EPBF (electron powder bed fusion) applications. A smaller PSD reduces the electrostatic charging, repulsion and floating of single powder particles [112–115], whereas a wider PSD increases the packing density and decreases the flowability. As larger powder particles typically exhibit a higher amount of gas pores, the PSD also correlates with the internal porosity of the powder particles. Furthermore, besides the PSD, the amount of fine particles should be considered, as finer particles lead to higher inter-particle friction and thus negatively affect the rheological properties. [116–118].

### Rheological aspects correlated to LPBF

The rheological properties of additive manufacturing powders are severely influenced by the particle morphology (sphericity, satellite particles) and the PSD. Despite the complex interplay of powder morphology characteristics and rheological aspects, Brika et al. [118] managed to connect independent rheology-based criteria with the suitability for LPBF and determined measurable values for comparison. As the flowability is not an inherent property and depends on various variables, rheological FT4 metrics [119, 120] listed in **Figure 2.10 b** assist in collecting in-depth information about quantitative trends. The mentioned metrics and their influence on the LPBF process are shown in **Figure 2.11** and described in the following paragraphs.

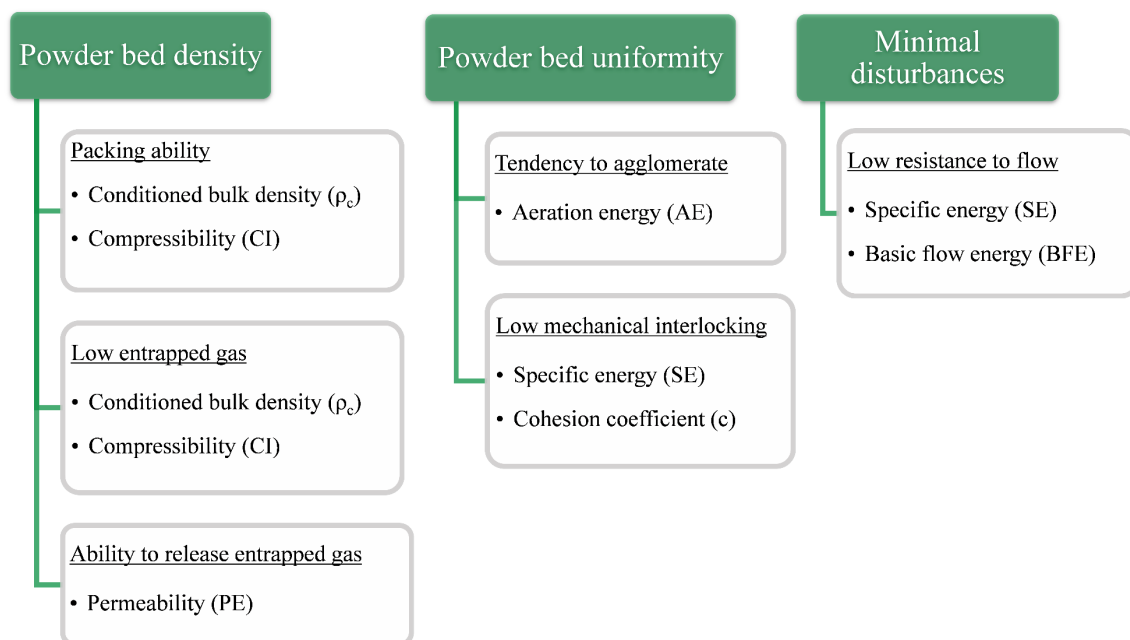


**Figure 2.11:** Rheological properties of metallic powder and their influence on the suitability for LPBF in terms of powder bed density, powder bed uniformity and recoating disturbances [118].

A maximized powder bed density improves the heat dissipation and powder absorptivity and enables a more stable interaction of the laser beam and the powder layer [118, 121–125]. Therefore, the powder particles should reveal a good packing ability and low entrapped gas to increase the powder bed density. This can be achieved by a high conditioned bulk density ( $\rho_c$ ) and low compressibility (CI). The CI value stands for the change in volume before and after the powder compression, *i.e.*, density of the compressed powder bed divided by  $\rho_c$ . The permeability (PE) represents the ability to release entrapped gas in the powder bed and thus should be high [118].

Furthermore, the quality of LPBF manufactured products depends on the powder bed uniformity, which is responsible for a steady laser-material dynamic [118]. To avoid variations in the powder bed, *e.g.*, differences in the thickness and curliness, the tendency for agglomeration should be low. The measurable quantity for agglomeration is the aeration energy (AE), which describes the energy barrier to overcome mechanical interlocking and cohesive forces. If the AE is low, the powder particles are less prone to mechanical interlocking, the cohesive force is low, and the powder bed reveals a high uniformity. Moreover, the specific energy ( $S_E$ ) should be minimized to minimize the mechanical interlocking and enhance the powder bed uniformity. A low cohesion coefficient ( $c_c$ ) ensures an easy transition from static to dynamic flow [118].

During the recoating process, uniform powder layers are applied to the building platform. Inconsistent powder layers may result in the formation of pores during the subsequent melting step. Recoating disturbances can be avoided by minimizing the energy for slicing through the powder bed, represented by the basic flow energy (BFE) and  $S_E$ , and thus ensuring thin and dense layers [118].

Although there are usually quantitative differences between specific powder batches, the influence of the rheological values on the LPBF process must be considered carefully. For example, a reduced BFE or a lower  $S_E$  does not necessarily improve the bulk components' properties quantitatively, and in many cases, the price of the powder might play a more critical role in the powder selection procedure [118].

### **Surface finishing and the influence of powder morphology**

The sphericity of the powder particles is essential for the surface finish and roughness of the bulk components and plays a crucial role for the geometrical accuracy [126–128]. It is reported by Ref. [118] that more spherical powder particles achieve a lower roughness due to increasing powder bed density. Because of the clear relation between the surface roughness and the powder bed density, the influence of the sphericity is superior to downsizing the layer thickness. Therefore, an increasing layer thickness and the usage of a powder with high sphericity allows to increase the building rate of the LPBF process [118].

The surface roughness should also be monitored with respect to the inclination angle. For example, the lowest surface roughness and the smoothest finish can be seen at the horizontal surfaces with an inclination angle around  $0^\circ$ . Higher inclined surfaces from  $45 - 90^\circ$  possess a

higher roughness due to the staircase effect, which becomes more problematic for down-faced surfaces with inclination angles around  $135^\circ$ . These unsupported surfaces show the highest roughness, resulting from poor heat dissipation and sintered particles on the surface [118].

### **2.3.3 Powder reuse**

The powder which has not been processed during the LPBF process is usually recycled, mixed with new powder, and reused in the follow-up printing jobs. Investigations on used powder particles [129, 130] indicate several changes described as follows.

The oxygen content of the powder increases with increasing powder reuse times as it is exposed to air before and after the manufacturing process and during the sieving. The shielding gas is also contaminated with slight amounts of oxygen [131], which diffuses into the surface of powder particles exposed to higher temperatures, *e.g.*, nearby the components on the building platform. Higher oxygen contents in the powder particles simultaneously increase the bulk components' oxygen content. Interstitial elements like oxygen are known [9] to promote strength but also lead to decreasing ductility and, thus, have to be limited and monitored to fulfill the requirements which are also set by the standards [105, 111, 132]. The exposure to vacuum and an inert gas atmosphere at high temperatures results in the removal of moisture, which contributes to a better flowability of the reused powder. Additionally, increasing reuse times leads to a narrower PSD and further improves the flowability due to a lower amount of small particles and the absence of satellites [130].

### 3 Relation of the current thesis to the state of the art

The total number of alloys applicable to AM is increasing but still limited. Engineers can choose from a series of metallic materials such as gold, silver, copper, platinum, palladium, tantalum, stainless and tool steel, nickel base superalloys, aluminum and titanium alloys. Moreover, research and development activities currently focus on the implementation of new types of alloys such as high-entropy alloys, bulk metallic glasses, magnetic alloys and novel metallic composite structures [77].

The limited choice of alloys for AM exists not only for overall alloy classes but also for specific alloys within a class. Despite the great number of Ti alloys for conventional production methods, only the alloy Ti64 is frequently applied by AM companies so far. Often designated as the workhorse alloy, Ti64 is by far the most researched and commonly used Ti base alloy. Although its invention dates back to the 1950s [9], no other Ti alloy has been as successful.

The development of Ti alloys with specific properties for applications beyond Ti64 is part of the continuing growth process of the AM industry. As the Ti64 alloy is well researched, even for LPBF applications, the available knowledge is helpful to adapt the AM process for the fabrication of other related Ti base alloys.

Besides the basic characterizations such as residual stress measurements, macro- and microstructure investigations as well as powder examinations, the investigation of fine LPBF microstructures requires analysis on the nanoscale to understand the physical-metallurgical processes fully. For example, Haubrich et al. [36] showed that the complex thermal impact of adjacent laser movements causes small  $\beta$  precursors, even in the as-built sample condition. The application of atom probe tomography (APT), assists in understanding the evolution of  $\beta$ , the role of lattice defects, and the diffusion behavior of elements, as shown in **Figure 3.1**. Complementary methods, such as high-energy X-ray diffraction, help to identify the occurring phases and reveal correlations with the applied LPBF heat input and the chosen post-process

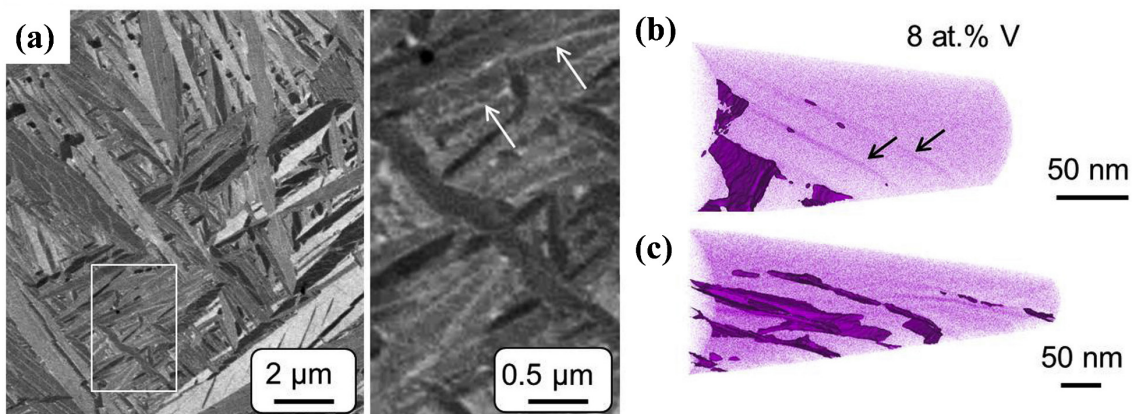


**Figure 3.1:** **a)** Acicular  $\alpha'$  microstructure of a Ti-6Al-4V alloy fabricated by LPBF revealing precursors of  $\beta$  and V enriched zones at lattice defects, which were validated by atom probe tomography in **b)**. Figure reprinted with permission from Ref. [36].



heat treatments. By combining standard with high-resolution methods, an improved understanding of the material's response during LPBF is gained. Moreover, the generated knowledge assists in improving the troubleshooting support for occurring defects and stresses, which are almost unavoidable for LPBF manufactured Ti base alloys.

In recent years, many researchers worked on expanding the alloy portfolio for LPBF processible Ti base alloys. For the first time, Fan et al. [133] managed to produce a near- $\alpha$  Ti6242S alloy via LPBF and provided the first basic characterization and mechanical properties. Carrozza et al. [134] presented the first studies of a near- $\beta$  Ti-6Al-2Sn-4Zr-6Mo (Ti6246, m.%) alloy manufactured by LPBF and revealed significant differences compared to other  $\alpha+\beta$  alloys related to the occurrence of orth martensite. However, there is still a gap between scientific proof-of-concept by the current literature and an in-depth understanding of the alloy's response to the LPBF process. Therefore, the main objective of this thesis is to close this gap and path the way for an extended application of Ti base alloys on an industrial scale.

## 4 Experimental challenges during characterization

This thesis deals with the comprehensive investigation of Ti alloys for AM via LPBF. To fully understand the mechanisms during the LPBF process and the AM material's response, the specimen preparation routine must be adapted. High cooling rates of up to  $10^6 \text{ K s}^{-1}$  produce an extremely fine microstructure that is not thermodynamically stable. Unintended variations of the sample environment, *e.g.*, higher temperatures during cutting or surface oxidation during heat treatment, could lead to irreversible changes of microstructural features impeding a proper investigation. Therefore, this thesis additionally focuses on the implementation of metallographic and analytical methods specifically for the preparation of LPBF produced Ti base alloys. In general, the investigation of AM alloys should always start with a powder characterization to reveal specific changes of different powder batches and end at the last part of the production chain to analyze the response of the solidified bulk components to the applied post-process heat treatments. The findings are documented in **Article A<sup>1</sup>** (Ref. [135]), which points out the importance of proper techniques for an optimized and reproducible and sample preparation. **Article A<sup>1</sup>** is appended at the end of this thesis.

### 4.1 Advanced sample preparation techniques

Ref. [135] describes the metallographic sample preparation, beginning with the powder material. It is recommended to conduct the powder extraction at different positions of the powder container to prevent misinterpretation due to accumulated particle fractions in a certain area of the container. Moreover, it was found that a mixture of powder and a fine fraction of sieved embedding media  $< 25 \mu\text{m}$  enhances the bonding of single particles in the metallographic specimen and thus improves the preparation quality.

In the next step, each metallographic specimen undergoes precise grinding and polishing steps, to produce scratch- and deformation-free plane surfaces. Ref. [135] provides precise preparation parameters for a fully automated grinding/polishing machine. The use of special chemicals such as hydrogen peroxide  $\text{H}_2\text{O}_2$  during grinding and polishing is recommended.  $\text{H}_2\text{O}_2$  increases the rate of material removal and suppresses the formation of surface layers, which is typical for Ti specimens. The reported sample preparation technique was successfully implemented, not only on Ti base alloys but also on commercially pure (CP) Ti and a variety of Ti-Al alloys such as the Ti-48Al-2Cr-2Nb (at.%) and the TNM alloy [136, 137].

For pore fraction analysis of the LPBF produced samples, light optical microscopy (LOM) was used. The analysis revealed that slight changes of the determination parameters significantly affect the pore fraction results, especially for samples with very low porosity. In

---

<sup>1</sup> C. Fleißner-Rieger et al., An additively manufactured titanium alloy in the focus of metallography. *Practical Metallography* **58**(1), 4–31 (2021) [135].

this context, the determination of the pore fraction should depend on the overall amount of pores, *e.g.*, above 1 vol.% or below 0.1 vol.%, and LOM parameters such as magnification and the size of the investigated area should be chosen accordingly.

Electron microscopy was found to be an effective tool for investigating the grain structure of Ti base alloys. However, the preparation has to be adjusted when using this characterization technique. Besides proper surface preparation via grinding and polishing, additional vibratory polishing should be applied to reduce the deformation zone in the last few microns of the surface and provide optimal conditions for electron microscopy.

The macro- and microstructural constituents of the LPBF produced Ti samples can also be visualized by applying additional preparation methods. Among all possible options for disclosing the crystal grain structure, electrochemical etching, electrolytic preparation and thermal etching are most relevant. For example, for investigations of the prior  $\beta$  structure – or sometimes referred to as parent grain structure –, special electrolytic etchants help to contrast the prior  $\beta$  grains [135]. **Figure 4.1** shows the electrolytically polished macrostructures of two Ti64 samples using a Ti Em3 electrolyte [135, 138]. By applying this specific etchant, it was possible to contrast the much smaller parent  $\beta$  grain size of components produced with a lower energy density ( $E_d$ ) in **(a)** compared to the high  $E_d$  sample in **(b)**.

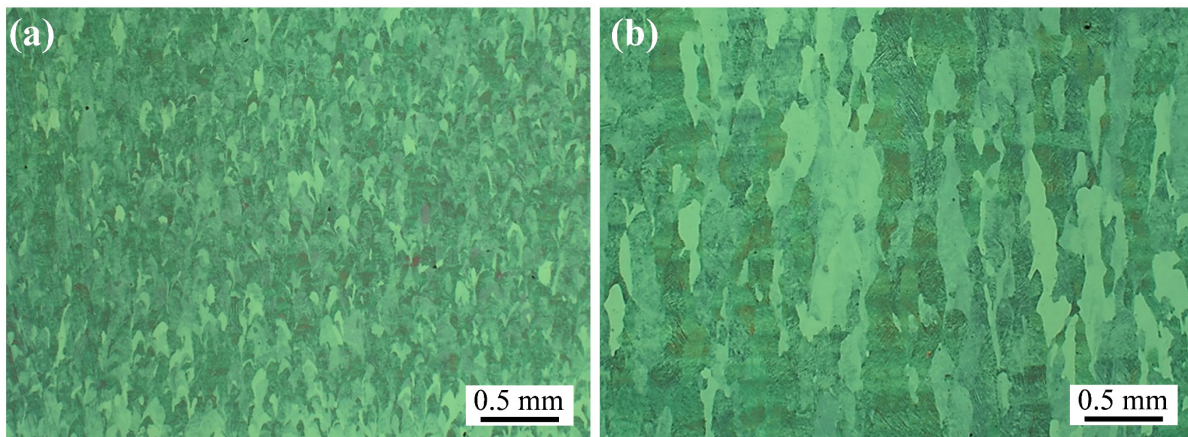


**Figure 4.1:** Electrolytically polished macrostructures of Ti-6Al-4V specimens manufactured with a low **(a)** and a high **(b)**  $E_d$ .

## 4.2 Characterization at macro, micro and nanoscale

Besides the mentioned LOM characterization, especially SEM methods are the most promising techniques for investigating the fine structure of the LPBF produced samples. The as-built samples as well as powder particles typically reveal highly supersaturated microstructures. Therefore, secondary electron (SE) imaging and chemical contrast imaging via backscattered electron diffraction (BSE) most likely do not provide much information about the macro- and microstructure. In contrast, with EBSD analysis it is possible to produce a clear image of the microstructure, even if SEM-BSE contrast imaging may not lead to the desired information. **Figure 4.2** depicts the differences of using SE, BSE and EBSD imaging techniques on Ti64 powder particles. In contrast to SE and BSE, EBSD provides information about the grain size, morphology, crystal orientation and the corresponding OR via the inverse pole figure (IPF) map [139]. The image quality (IQ) representation reveals lattice defects such as twins and

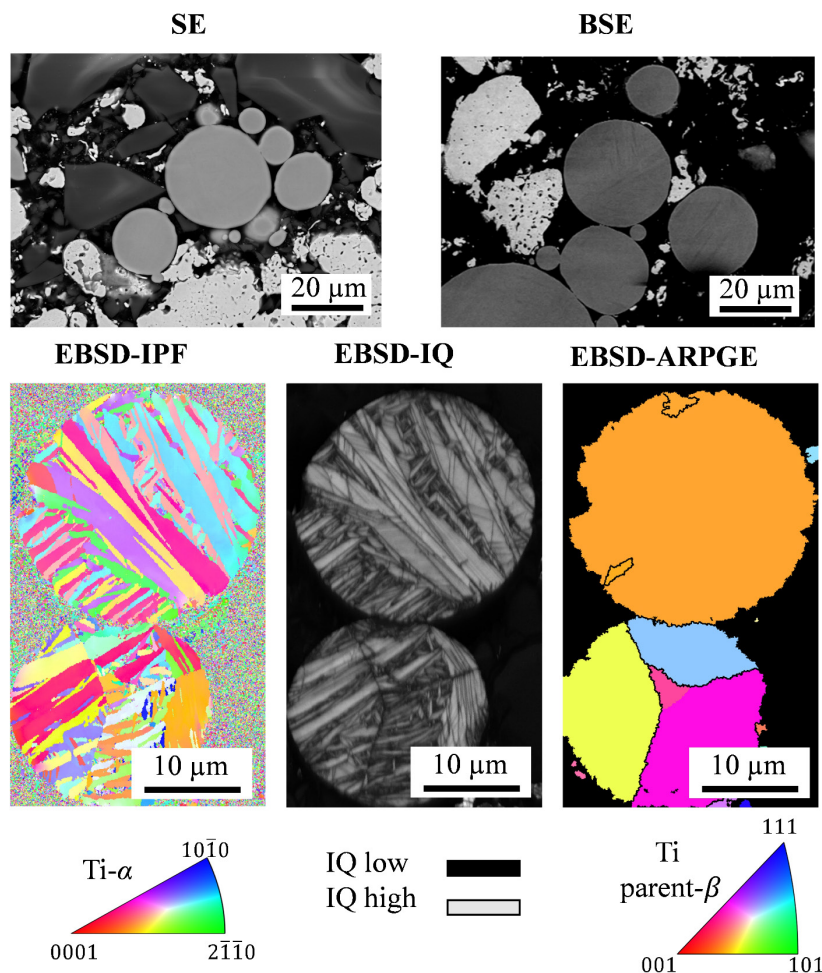


**Figure 4.2:** Representation of different SEM contrast methods to investigate supersaturated Ti-6Al-4V powder particles. SE and BSE imaging do not provide sufficient information when compared to EBSD characterization methods.

sub-grain structures, and the software program ARPGE [48, 49] can recalculate the parent  $\beta$  grain structure, which was present prior to the  $\beta \rightarrow \alpha$  phase transformation.

A more detailed analysis can be performed via APT, which allows to investigate small atom clusters. Furthermore, APT investigations are ideal to analyze the sub-microstructure of LPBF produced samples, which exhibit considerably fine microstructure and supersaturated phases. The tip-shaped specimens exhibit volumes in the  $\text{nm}^3$  range and tip radii  $< 100$  nm and are usually prepared via the focus ion beam (FIB) preparation method [140]. APT allows a 3-dimensional reconstruction of the tip geometry via collecting evaporated ions at a detector and cross-linking the coordinates with the mass-to-charge state, as schematically shown in **Figure 4.3** [141]. During the measurement, the specimen is cooled to cryogenic temperatures and positioned close to a counter electrode in a high vacuum chamber. Then a constant voltage that causes no ion evaporation is applied to the sample tip. Ions are solely evaporated by additionally applied laser or high-frequency voltage pulses and subsequently detected by a cross delay line detector [141, 142].

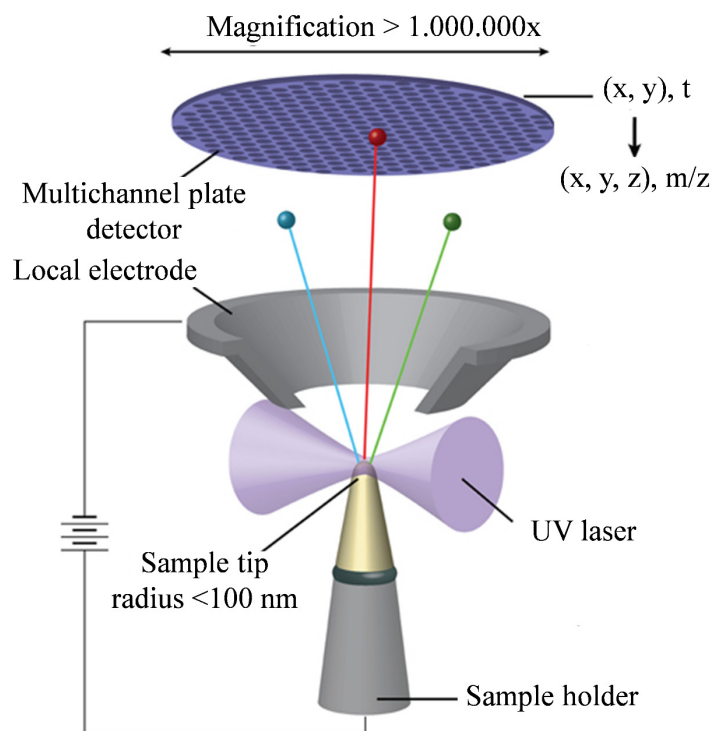


**Figure 4.3:** Schematic representation of the measurement principle of APT showing the most important components of a local electrode atom probe. Reprinted with permission from Ref. [141].

### 4.3 X-ray diffraction methods

X-ray diffraction (XRD) measurements offer the opportunity to investigate large sample areas with high statistical relevance when compared to direct imaging techniques like SEM and TEM. In contrast to these methods, XRD provides detailed information about occurring phases, residual stresses, grain sizes, defect density, and crystallographic textures [143]. In addition, *in situ* high-temperature XRD (HTXRD) experiments allow to determine phase fractions and the respective transformation temperatures directly during heating. Due to the high affinity of Ti alloys to oxygen [144], the specimens have to be shielded by inert gas or placed in a vacuum chamber. However, it has to be noted that the maximum operating temperature is limited as the vacuum stability decreases and the tendency for oxidation increases at higher temperatures.

In comparison to laboratory-scale X-ray sources, synchrotron radiation exhibits considerably higher energies around 100 keV (laboratory Cu anode 8.04 keV), which enables the analysis of large sample volumes in transmission mode. Due to the high brilliance of high-energy X-rays, even very low phase fractions are detectable. **Figure 4.4** schematically shows the setup of such a HEXRD experiment [145] in which the synchrotron X-ray beam is scattered at crystallographic planes and produces diffraction rings on the two-dimensional detector. The calculation of lattice spacings is possible according to Bragg's law given in **Equation 5**, where  $d_{hkl}$  is the lattice spacing,  $\theta_B$  is the Bragg angle,  $n$  is the diffraction order and  $\lambda_{hkl}$  the wavelength of the X-rays [146].

$$2 \cdot d_{hkl} \cdot \sin(\theta_B) = n \cdot \lambda_{hkl} \quad (5)$$

Via Rietveld refinement, which uses the azimuthal integrated diffraction pattern of the HEXRD experiments, volume fractions and crystallographic texture can be calculated through the height, width, position and area of certain peaks [147, 148].

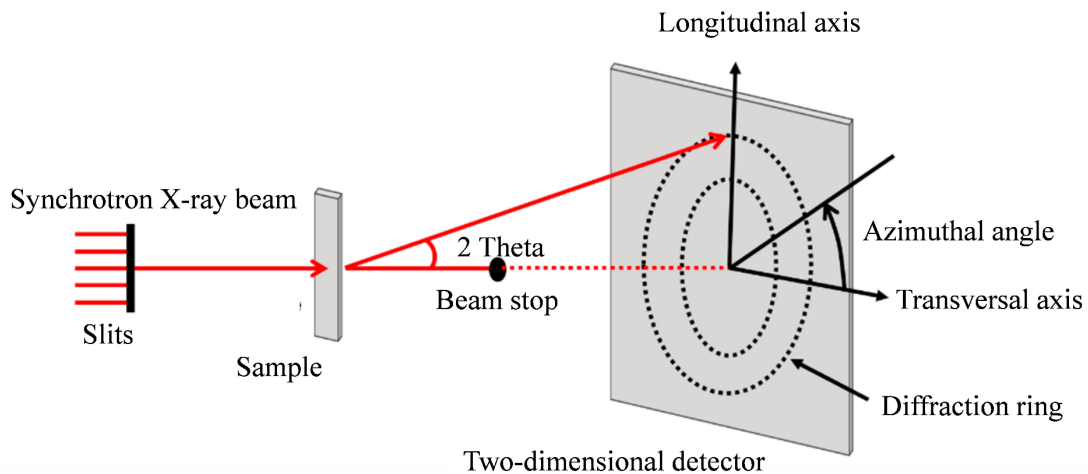


**Figure 4.4:** Schematic drawing of the HEXRD setup showing the synchrotron beam and the diffraction on the sample's lattice planes. The resulting diffraction pattern is collected on a two-dimensional detector. Figure is reused from Ref. [145].

## 5 Published content

### 5.1 Focus of the research and published content

Ti base alloys are already used in various structural applications due to their high specific strength in combination with tunable process-microstructure-property relationships. Especially the group of  $\alpha+\beta$  alloys gains a lot of attention due to their applicability for new production methods such as LPBF. In general, alloy design is used to adapt material properties with regard to the desired applications of the final components. For AM, the alloy portfolio is very limited and most likely reduced to Ti64 and, thus, prevents exploiting the full potential of Ti alloys in combination with AM.

This thesis is dedicated to improving the understanding of the implementation of Ti alloys to the LPBF production process and providing knowledge of the respective process limits and achievable mechanical properties. Although all of the studied alloys belong to the class of  $\alpha+\beta$  alloys, they respond differently to the AM process regarding microstructure and defect formation. Besides microstructure investigations in terms of morphology, grain size and lattice defects, particular focus is laid on determining the occurring phases in the powder and the bulk material.

The impact of post-processing was analyzed because it is an efficient tool for shifting the microstructure and subsequent mechanical properties towards desired properties. Therefore, investigations of the precipitation behavior of phases at the nanoscale help to understand the material response on larger scales. In addition, a metallographic preparation study supports the applied (high-resolution) investigation techniques to determine the microstructural constituents, which ensured reproducible sample conditions as described in **Chapter 4.1**.

**Figure 5.1** summarizes the scientific contributions and shows the workflow of the thesis in correlation with the appended peer-reviewed articles. The articles A-E can be found in the appendix of this thesis.

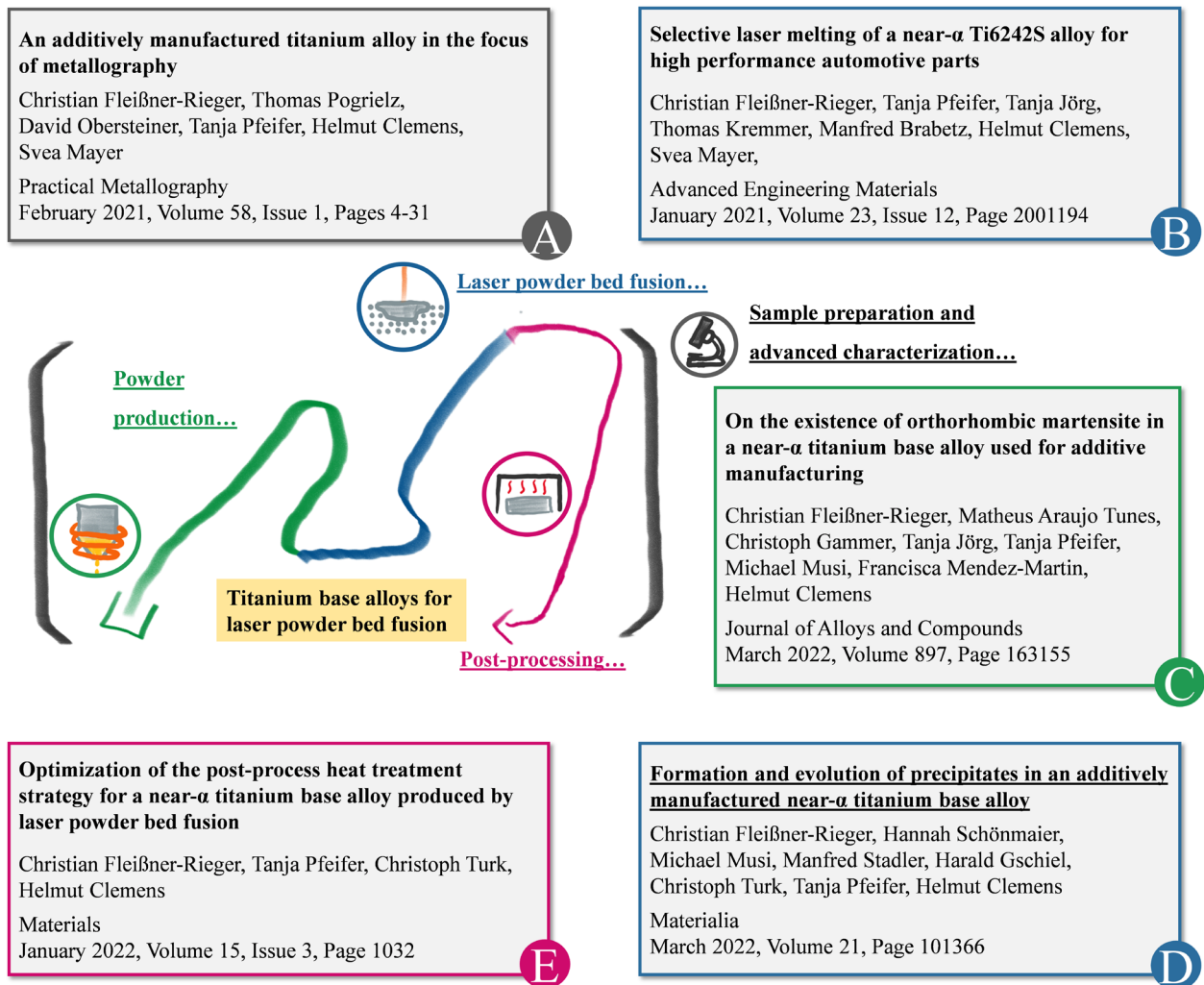


**Figure 5.1:** Schematic workflow diagram, as shown before in **Chapter 1**, that displays the correlation of the work packages with the publications emerged in this thesis.

### Remarks:

The production of the components by LPBF was carried out by Pankl Racing Systems AG, supervised by Tanja Pfeifer. Practical experiments, data analysis, conceptualization and writing of the appended articles A-E were performed by the author of this thesis or under his supervision, with the following exceptions:

- A** Thomas Pogrietz and David Obersteiner performed the metallographic preparation study and chemical etching.
- B** Manfred Brabetz and Thomas Kremmer conducted and evaluated the TEM experiments. Tensile tests were carried out by voestalpine Böhler Edelstahl GmbH & Co KG, supervised by Tanja Jörg.
- C** Christoph Gammer and Matheus Araujo Tunes conducted and evaluated the TEM experiments. Michael Musi performed and evaluated the HEXRD experiments. APT and corresponding data evaluation was conducted by Francisca Mendez-Martin.



**D** APT sample preparation and data evaluation was conducted by Hannah Schönmaier. Michael Musi performed and evaluated the HEXRD measurements.

## 5.2 Conference contributions

### 55. Materialographie-Tagung 2021 – Oral presentation and proceedings

Eine additiv gefertigte Titanlegierung im Fokus der Metallographie

Christian Fleißner-Rieger, Thomas Pogrietz, David Obersteiner, Tanja Pfeifer, Helmut Clemens and Svea Mayer

Conference and exhibition: Online, 2021

Awards: *Best contribution award, 3<sup>rd</sup> place*  
*Photo competition, 1<sup>st</sup> place*

### Euro PM2021 - Oral presentation and proceedings

Process-microstructure-property-relationship of the near-alpha Ti6242S alloy fabricated by laser powder bed fusion

Christian Fleißner-Rieger, Tanja Pfeifer, Tanja Jörg, Thomas Kremmer, Helmut Clemens and Svea Mayer

Proceedings in: European Powder Metallurgy Association (Ed.), Euro PM 2021 International Conference and exhibition: Online, 2021

### Remark

Other planned conferences were canceled in 2020 and 2021 due to the Covid-19 pandemic.

## 5.3 Supervised theses

Mikrostrukturelle Untersuchungen an additiv gefertigten Ti-6Al-4V Bauteilen, David Obersteiner, Bachelor thesis, Montanuniversität Leoben (2020).

Gegenüberstellung metallographischer Präparationsmethoden zur Anwendung an additiv gefertigten Ti-6Al-4V Bauteilen, Thomas Pogrietz, Bachelor thesis, Montanuniversität Leoben (2020).

Einfluss der Energiedichte auf die Mikrostruktur-Eigenschaftsbeziehungen einer additiv gefertigten Near- $\alpha$ -Titanlegierung, Jürgen Glettler, Bachelor thesis, Montanuniversität Leoben (2021).

About the productivity in laser powder bed fusion produced Ti-6Al-4V components, Thomas Pogrietz, Master thesis, Montanuniversität Leoben (2022).

## 5.4 Summary of the published content and discussion

### 5.4.1 LPBF – A comparison of alloys

Since the Ti64 alloy has been examined more profoundly than the other available Ti alloys, a comparison with Ti64 assists in accelerating the implementation of alloys for AM based on production analogies and troubleshooting similarities. However, the response of new Ti alloys in the LPBF process is not similar in all aspects, and thus, R&D is essential for an optimal implementation. According to **Article B<sup>2</sup>** (Ref. [149]), this chapter shows the differences between the investigated alloys.

In general, both alloys, Ti64 and Ti6242S, reveal a defect-rich acicular martensitic microstructure caused by the high cooling rates during LPBF. Based on similar production conditions such as layer thickness ( $t$ ), laser power, scanning speed and  $E_d$ , the solidified microstructure of Ti6242S is much smaller ( $\sim$ half of the grain size) compared to the Ti64 alloy, as shown in **Figure 5.2**. The decreased parent  $\beta$  and  $\alpha$  grain size is attributed to a higher growth restriction factor of the Ti6242S alloy. In addition, the heat treatment leads to precipitation of equilibrium  $\beta$  phase within the  $\alpha$  grains, caused by the lower diffusivity of the  $\beta$  stabilizing element Mo, compared to V in Ti64 [149].

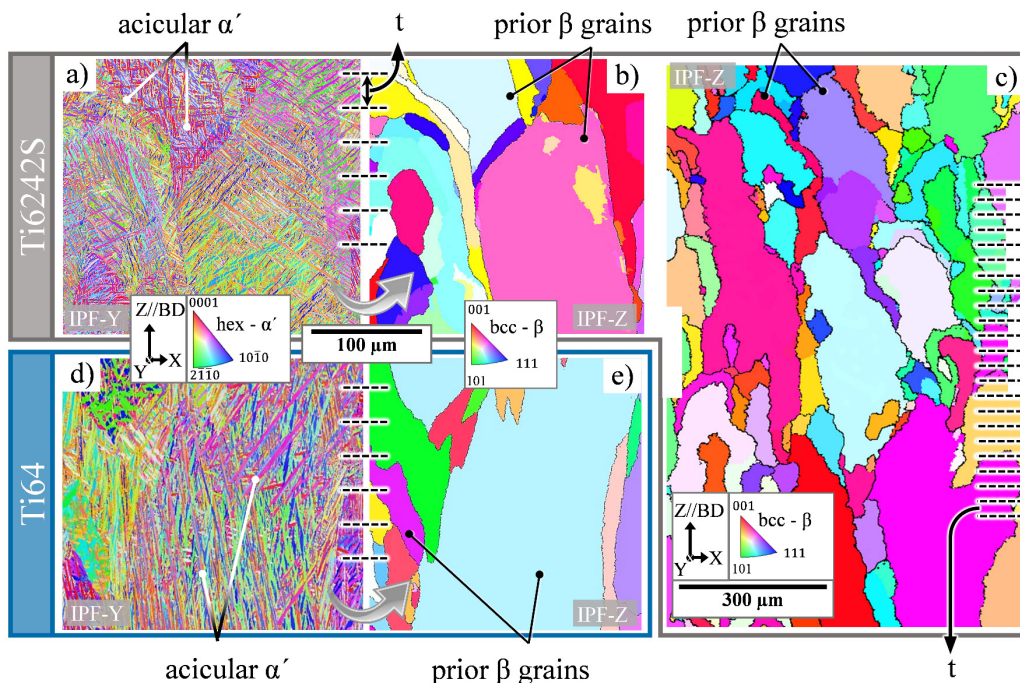


**Figure 5.2:** EBSD maps of **Article B<sup>2</sup>** showing the microstructures of the **a-c)** Ti6242S and **d-e)** Ti64 alloy in comparison [149].

<sup>2</sup> C. Fleißner-Rieger et al., Selective laser melting of a near- $\alpha$  Ti6242S alloy for high-performance automotive parts. *Advanced Engineering Materials*, **23**(12), 2001194, (2021) [149].

The enhanced tensile strength of Ti6242S, even at temperatures up to 500°C, is related to the complex interplay of grain refinement and the influence of the alloying elements Sn, Zr, Si and interstitial elements such as O and N. Simultaneously, the elongation at fracture in the stress relieved annealed (SRA) sample condition is lower for the Ti6242S alloy ( $A_5 = 11.3\%$ ) than for the Ti64 ( $A_5 = 14.6\%$ ) [149].

Differences in mechanical properties are referred to the general compositional differences of the Ti6242S and Ti64 alloy and to variations in the amount of interstitial elements. For example, there are two Ti64 Grades, namely Grade 5 and Grade 23, limiting the possible O/N content in the powder to 0.2/0.05 m.% and 0.13/0.03 m.%, respectively [150]. Interstitial elements of this kind are strong solid solution strengtheners [9, 17] and, therefore, substantially affect the mechanical properties of the supersaturated LPBF manufactured components. Slight changes in the chemical composition of the Ti6242S alloy, shown in **Table 5.1**, also lead to an enhanced hardness. These results show that although the Sn and Zr fraction in Powder 2 is reduced, the hardness of the as-built component 2 (produced with Powder 2) increases to 484 HV0.1 compared to 446 HV0.1 for the as-built component 1. This is attributed to a higher Si fraction, which is known to be a strong solid solution strengthening element and the formation of silicide particles in the Ti6242S alloy [9, 17]. However, the higher Si-containing as-built sample 2 reveals a higher vulnerability for residual stresses and cracks, and, therefore, tends to result in delamination and early crack formation during LPBF.

In addition, the O and N pickup was determined by comparing the chemical composition of the initial powder condition and the as-built components. The O and N enrichment is caused by the high affinity of Ti alloys to O and N and residual O/N contamination in the shielding gas atmosphere during manufacturing. Oxygen pickup, from the powder to the bulk material, is very common [151] and can barely be avoided during LPBF, but should be taken into account as these elements significantly influence the mechanical properties of the final components.

**Table 5.1:** Chemical analysis and corresponding measurement uncertainty (m. u.) of two Ti6242S powder batches; Microhardness (HV0.1) of the as-built samples and variations in chemical composition caused by the LPBF process is shown in comparison.

	Ti	Al	Sn	Zr	Mo	Si	O	N
	m.%	m.%	m.%	m.%	m.%	m.%	m.%	m.%
Powder 1	86.59	6.36	2.04	4.16	2.0	0.054	0.13	0.003
Powder 2	86.12	6.37	1.91	3.9	2.0	0.091	0.11	0.006
m. u.	1.385	0.336	0.054	0.174	0.2	0.0138		
	Hardness		LPBF parameters				O	N
	HV0.1						m.%	m.%
As-built 1	446 ± 10		Similar manufacturing parameters					
As-built 2	484 ± 10		according to Ref. [149]				+0.03	+0.01

### 5.4.2 The impact of process parameter on phase transformations

Near- $\alpha$  alloys are more sensitive to changes in the LPBF manufacturing parameters than  $\alpha+\beta$  alloys. The graphical abstract of **Article C**<sup>3</sup> (Ref. [152]), shown in **Figure 5.3**, displays how adapted process parameters evoke substantial changes in the phase transformation. It was found that high cooling rates lead to the occurrence of orth  $\alpha''$  martensite, which is very uncommon for the Ti6242S alloy. In addition, it was evidenced for the first time that two types of martensite exist in the same alloy, whereas the prevalent martensite type depends on the cooling rate.

The change in crystal structure from bcc to the hex lattice structure during the athermal phase transformation requires an atomic movement [152]. During the compression of the  $a$  axis and extension of the  $b$  axis, the atoms are located in an intermediate position between the equilibrium bcc and hex phases. As long as the final hex crystal structure cannot be reached, the atoms stay in this intermediate phase condition with an orth lattice structure. The orth phase is common for Ti alloys with a high fraction of  $\beta$  stabilizing elements such as Mo, V, Ta and Nb [9]. In the case of the Ti6242S alloy, the  $Mo_{eq}$  is low ( $Mo_{eq}=2.05$  m.%) compared to the lowest in literature ( $Mo_{eq}=4.45$  m.%, [153]), and thus, an orth phase was not expected to exist

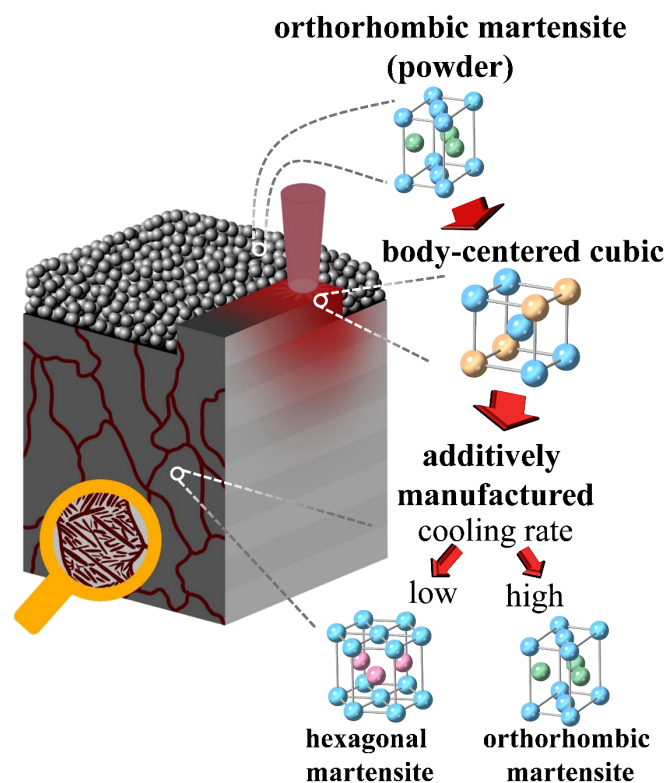


**Figure 5.3:** Graphical abstract of **Article C**<sup>3</sup> schematically depicting a LPBF manufactured sample and the lattice structures of the Ti6242S material during the stages of the production process. in this alloy [152].

<sup>3</sup> C. Fleißner-Rieger et al., On the existence of orthorhombic martensite in a near- $\alpha$  titanium base alloy used for additive manufacturing. *Journal of Alloys and Compounds*, **897**, 163155 (2022) [152].

The first evidence of the orth phase was found in the course of the HEXRD analysis of the Ti6242S powder, which showed the occurrence of characteristic double peaks, such as 110- $\alpha''$  and 020- $\alpha''$  compared to the single 100- $\alpha'/\alpha$  peak of the hex crystal pattern. HTXRD measurements of the Ti6242S powder material confirmed the phase transformation  $\alpha'' \rightarrow \alpha$  and assisted the conclusion of an intermediate atomic position which shifts from the metastable condition ( $\alpha''$ ) into the equilibrium ( $\alpha$ ) by additional heat input [152]. The difference between the  $\beta \rightarrow \alpha''$  and  $\beta \rightarrow \alpha'$  pathway is the complete atomic movement from bcc to hex for the latter one.

As the atomization process of the powder material generates cooling rates up to  $10^8 \text{ K s}^{-1}$ , and normal LPBF processes only reach  $10^4$ - $10^6 \text{ K s}^{-1}$ , it is evident that the cooling rate during LPBF must be adapted accordingly for producing this metastable phase. Higher cooling rates were achieved by reducing the heat input during LPBF, *i.e.*, a reduced  $E_d$ . Increasing the cooling rate ultimately led to the formation orth martensite in the as-built components, as experimentally confirmed in a HEXRD measurement presented in **Figure 5.4** of **Article D**<sup>4</sup> (Ref. [154]). In contrast, a higher heat input, *i.e.*, a higher  $E_d$ , and thus slower cooling led to the formation of classical hex martensite [152, 154]. It should be noted that too low  $E_d$  may result in a lack of fusion and increasing pore fractions. However, the pore fraction could be controlled and was below 0.5 vol.% [152].

According to described findings, it is evident that the appearance of the martensite variant can be controlled by adapting the manufacturing parameters without sacrificing a high density. The importance of the orth martensite formation for the LPBF process is related to the softer nature of the  $\alpha''$  phase in terms of mechanical strength. A softer orth phase might reduce the vulnerability for cracks due to less residual stresses [152].

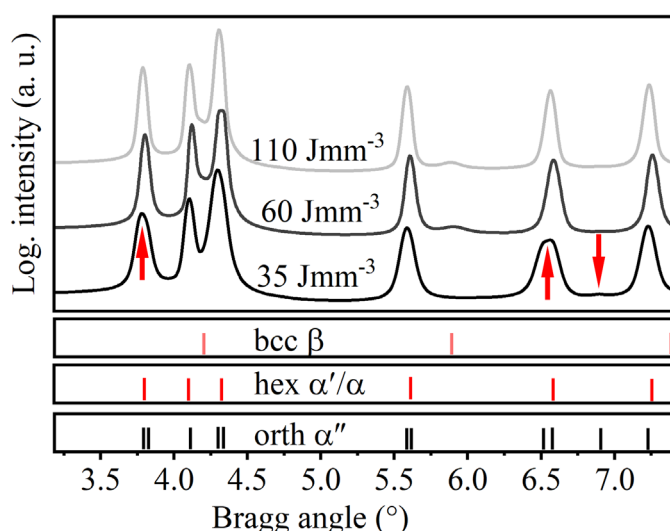


**Figure 5.4:** HEXRD diffraction pattern of Ti6242S components in as-built sample condition. The red arrows mark the characteristic peaks of the orthorhombic crystal structure. Figure is reused from Ref. [154].

<sup>4</sup> C. Fleißner-Rieger et al., Formation and evolution of precipitates in an additively manufactured near- $\alpha$  titanium base alloy. *Materialia*, **21**, 101366 (2022) [154].

### 5.4.3 Heat input and precipitation behavior

Fundamental knowledge of the precipitation behavior and the decomposition of supersaturated phases assists in predicting the material behavior and understanding the mechanical properties on all scales. In-depth microstructure characterization on the nanoscale utilizing APT experimentally confirmed that the diffusion of small elements such as Si in the supersaturated matrix phase is faster than the diffusion of other elements such as Mo and Zr and leads to early element clustering. The diffusion was found to impact the formation of the  $\beta$  phase and severely depends on the heat input of the LPBF process. As shown in **Figure 5.5**, a low  $E_d$  of  $35 \text{ J mm}^{-3}$  leads to rod-like Si segregations, whereas 60 or  $110 \text{ J mm}^{-3}$  enable sufficient heat input to overcome the activation energy for Mo diffusion [154]. An  $E_d$  of 60 or  $110 \text{ J mm}^{-3}$ , therefore, lead to the formation of early stages of  $\beta$  phase as well as Si clustering. After post-process heat treatment, the formation of  $\zeta\text{-(Ti,Zr)}_6\text{Si}_3$  silicide particles was determined and ascribed to additional Zr diffusion towards Si-rich areas. The resulting silicide particles are preferably located at  $\alpha/\beta$  phase boundaries and exhibit sizes of few nm to  $0.25 \mu\text{m}$ .

The precipitation of  $\beta$  phase is a result of the martensitic decomposition and diffusion processes related to the phase transformation pathway  $\alpha''/\alpha' \rightarrow \alpha + \beta$ . Mo clustering does not occur randomly and is more likely to take place at specific positions in the microstructure. Compared to Ti64, where  $\beta$  usually precipitates at  $\alpha$  grain boundaries,  $\beta$  also forms within grains in the Ti6242S alloy. TEM investigations in Refs. [152, 154] revealed Mo clusters at periodic

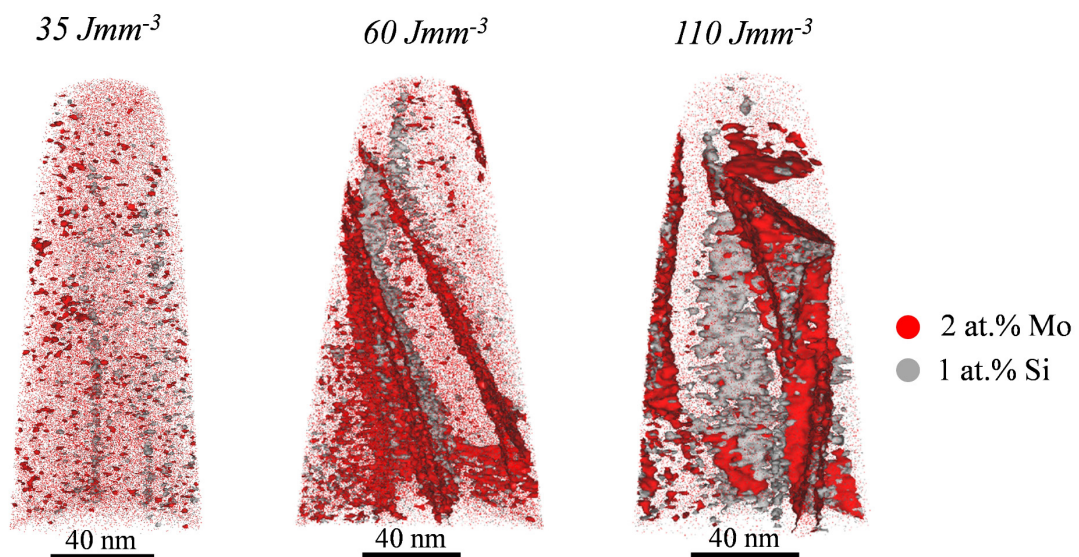


**Figure 5.5:** APT tips of as-built components manufactured with different  $E_d$ . The 2 at.% Mo isosurface and 1 at.% Si isosurface show Si clustering already with a low heat input whereas Mo needs additional heat, in form of a higher  $E_d$ , to enable diffusion. Figure is reused from Ref. [154].

dislocation structures at basal and prismatic planes in  $\sim 20\text{-}60 \text{ nm}$  distances. In addition, the effect of periodic  $\beta$  precipitation is more pronounced for intermediate cooling rates in industrial

heat treatment processes using air or nitrogen gas cooling compared to the furnace cooled samples which enable diffusion of Mo towards  $\alpha$  grain boundaries. The periodic  $\beta$  precipitates are effective barriers for dislocation motion and, thus, enhance the tensile strength of the Ti6242S alloy when compared to Ti64.

#### 5.4.4 Optimization of post-process heat treatments

Although  $\beta$  precipitates enhance the hardness of the LPBF manufactured components, post-process heat treatments should be adapted precisely to avoid a lack of ductility. **Article E<sup>5</sup>** (Ref. [155]) describes that duplex annealing at temperatures of 700 °C, on the one hand, leads to higher tensile strength but, on the other hand, diminishes the ductility. This is related to dislocation pile-ups, not only at  $\alpha/\alpha'$  grain boundaries but also at sub- $\mu\text{m}$  sized  $\beta$  precipitates. Therefore, in this particular case, annealing should be performed at higher temperatures to enable sufficient space for plastic deformation via dislocation movement. Proper heat treatments lead to a superior elongation at fracture ( $A_5$ ) of about 16 %, in combination with an ultimate tensile strength/yield strength ratio ( $\sigma_m/\sigma_{0.2}$ ) of 1155/1075 MPa for the LPBF manufactured Ti6242S alloy [155]. Moreover, Ref. [155] suggests specific heat treatments for particular application requirements such as high strength, high ductility and high creep resistance.

Ref. [155] also investigated the effect of aging on the mechanical properties and shows an enhanced strength of the aged compared to the stress relieved annealed sample condition. It should be noted that aging is only possible if supersaturated phases are present. Aging, *e.g.*, at 600 °C, leads to secondary  $\alpha$  ( $\alpha_s$ ) precipitates within the  $\beta$  areas, and a bi-lamellar microstructure with primary  $\alpha$  ( $\alpha_p$ ),  $\alpha_s$  and minor  $\beta$  phase fraction.

Near- $\alpha$  alloys are commonly used due to their high creep strength [9, 17]. Ref. [155] deals with the creep performance of samples after different post-process heat treatments. The results confirm that coarse microstructures result in higher creep strength compared to very fine microstructures. This is attributed to the creep mechanism of  $\alpha+\beta$  alloys for application temperatures of 500-600 °C and stress-loadings of about 200 – 250 MPa, which is lattice diffusion-controlled dislocation climb. Small grain sizes and a high density of lattice defects result in short slip lengths and early annihilation of dislocations and thus should be avoided for sufficient creep performance [155].

Generally, AM near- $\alpha$  and  $\alpha+\beta$  alloys in as-built condition exhibit higher strength than cast and wrought processed ones. The main difference of these alloys and near- $\beta$  alloys is that near- $\beta$  alloys typically form an orth martensite during rapid solidification [134]. This results in a dramatic strength loss with YS values in the range of 480 to 580 MPa, and the requirement of post-process heat treatments to enhance the YS [134] for LPBF manufactured components. On

---

<sup>5</sup> C. Fleißner-Rieger et al., Optimization of the post-process heat treatment strategy for a near- $\alpha$  titanium base alloy produced by laser powder bed fusion. *Materials*, **15**(3), 1032 (2022) [155].

the contrary, it is tempting to speculate that the formation of  $\alpha''$  martensite in the Ti6246 alloy contributes to an enhanced producibility (PA) related to lower residual stresses and less cracks.

**Figure 5.6** depicts the property profiles of near- $\alpha$ ,  $\alpha+\beta$  and near- $\beta$  alloys derived from the mechanical properties in the appended publications of this thesis [149, 152, 155] and from the Refs. [9, 17, 74, 134, 156–158]. As the LPBF manufactured components, in most cases, are used in a heat-treated sample condition, as-built and heat-treated property profiles are shown in comparison.

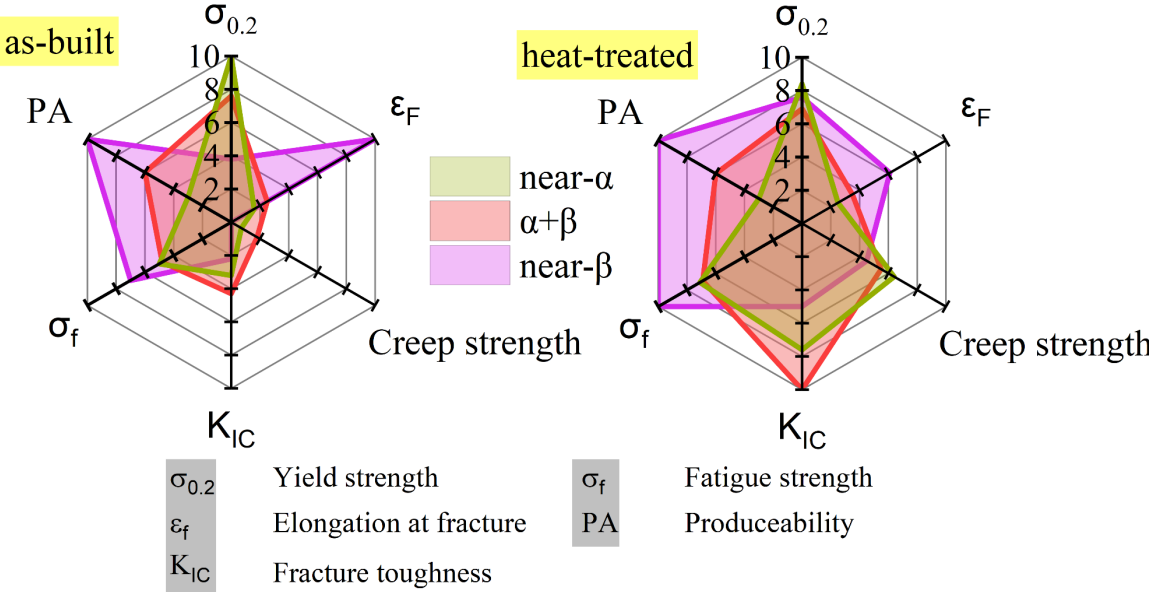


**Figure 5.6:** Mechanical properties of LPBF manufactured near- $\alpha$ ,  $\alpha+\beta$  and near- $\beta$  alloys in as-built and heat-treated sample condition.



## 6 Novel features

The following points outline the contributions to the scientific progress and provide answers to the main questions of this thesis in **Chapter 5.1**.

- Comparison of alloys produced by LPBF
  - The implementation of Ti alloys in the LPBF process is supported by analogies to well-investigated alloy systems such as Ti64. Near- $\alpha$  alloys like Ti6242S show similarities with Ti64 but reveal a higher tensile and creep strength related to the effect of alloying elements, especially Si and Mo, and a smaller grain structure.
  - Material characteristics of the Ti6242S alloy tend to generate residual stresses and might lead to delamination of the building platform and cracks.
  - The martensitic transformation in the near- $\beta$  alloys Ti6246 generate an orth  $\alpha''$  martensite. This results in a significant deterioration of the mechanical properties in terms of tensile strength but might reduce the vulnerability for crack formation and propagation.
- Process limits
  - Near- $\alpha$  alloys are sensitive to changes in the LPBF manufacturing parameters. Standard LPBF parameters with an  $E_d$  of about  $60 \text{ J mm}^{-3}$  generate hex  $\alpha'$  martensite in both alloys, Ti64 and Ti6242S. In comparison, a reduced  $E_d$ , and thus, an increasing cooling rate, results in the formation of an uncommon orth  $\alpha''$  martensite in the Ti6242S alloy.  $\alpha''$  can reduce the vulnerability for cracks due to the softer nature of this martensitic type.
- Achievable mechanical properties
  - The periodic dislocation structure at basal and prismatic planes of the  $\alpha''/\alpha'$  microstructure acts as nucleation sites for  $\beta$  precipitation. The low diffusivity of Mo in the matrix phase leads to the formation of sub- $\mu\text{m}$   $\beta$  precipitates, which are effective barriers for dislocation motion.
  - Post-processes heat treatments are suitable for tailoring the microstructure to the final applications. This work presents heat treatment suggestions for applications aimed for high strength, high ductility, or high creep resistance. It was found that the as-built sample condition or a duplex annealing suits best for high strength applications, whereas a triplex heat treatment fulfills high ductility requirements. For high creep resistance, super-transus  $\beta$  annealing is recommended.
- Sample preparation
  - A reproducible high specimen quality is crucial for the proper interpretation of experimental results. The detailed preparation guide, evolved in the course of this work, allows the automatized and reproducible production of scratch- and deformation-free plane surfaces, applicable to Ti base alloys, pure titanium and TiAl alloys.

## 7 Outlook and open questions

This thesis focuses on the implementation of Ti alloys, beyond Ti64, for fabrication via LPBF. It is shown that the Ti6242S alloy is a promising candidate for special applications that require enhanced mechanical properties in terms of tensile strength and creep performance. The high mechanical strength of the Ti6242S alloy, on the downside, goes along with an increased vulnerability for cracks caused by residual stresses. In the following, various approaches for producing crack-free components are proposed. Moreover, the development of post-process heat treatment strategies and their implementation on real products is discussed in further detail.

Furthermore, besides Ti6242S, the Ti6246 alloy is also a promising candidate for the LPBF manufacturing technique as its responses to the complex layer-by-layer process by forming a very soft orth martensite. However, additional investigations are necessary to uncover the full potential of this alloy.

For future research on AM Ti alloys, the application of in-depth investigation methods such as HEXRD, TEM and APT is recommended to obtain a comprehensive image of the fine microstructure constituents resulting from LPBF and their correlation with the mechanical properties.

### Approaches to reduce residual stresses during LPBF

The comparison of the two Ti6242S alloys with compositional differences in **Chapter 5.4.1** clearly displays the effect of Si as a solid solution strengthening element. A reduced Si fraction in combination with less interstitial elements such as O, N decreases the mechanical strength and is believed to reduce residual stresses and crack formation.

Moreover, it was found that  $\alpha''$  martensite can be obtained by adjusting the LPBF manufacturing parameters to reduce the  $E_d$  [152].  $\alpha''$  is known to soften the material due to its orth crystal structure.

Besides the reduction of  $E_d$ , a higher  $E_d$  might also reduce the residual stresses in the components by enabling longer times at higher temperatures and thus *in situ* relaxation of the martensitic microstructure. However, the implementation of the proposed strategies has to be investigated on components with varying geometries to obtain detailed information about the actual potential for reducing residual stresses.

### Selection of post-process heat treatment parameters

Since the Ti6242S alloy is commonly used due to its superior creep resistance, the formation mechanism of the  $(\text{Ti,Zr})_6\text{Si}_3$  silicide particles is of particular interest. On the one hand, silicide particles act as effective barriers for dislocation motion if they are small in size and equally distributed through the microstructure. On the other hand, coarse lamellar microstructures are preferred for enhancing the creep resistance as the plastic strain is governed by lattice self-diffusion-controlled dislocation climb [155]. This contravenes the typical microstructures obtained by the LPBF process, which will be discussed as follows.

The formation of silicide particles in the LPBF manufactured Ti6242S alloy requires Zr diffusion, which can be enabled by additional heat input during post-processing. It was found that small silicide particles already form during heat treatment at 600 °C. In this condition, the AM-produced microstructure is still very fine, which is detrimental to the creep performance; hence the heat treatment temperature should be increased for grain coarsening. However, higher heat treatment temperatures increase the size of the silicide particles making them too large to act as effective dislocation barriers.

In contrast to sub-transus annealing mentioned before, super-transus  $\beta$  annealing diminishes the microstructure obtained by the LPBF process and significantly enhances the creep performance. However, super-transus  $\beta$  annealing goes along with a dramatic loss of tensile properties. To summarize, no annealing strategy covers all disciplines such as strength, ductility and creep performance and thus, the requirements of the final product should always be taken into account during the selection of proper heat treatments.

### **Analysis of the fatigue performance**

The current thesis almost entirely investigated the process-microstructure-property relationships on the basis of a machined and smooth surface. However, LPBF produced components typically reveal a high surface roughness, which is known to negatively affect the fatigue performance of the near-net-shape components by causing stress concentrations and, thus, crack initiation at critical defects [11, 55, 60]. Since fatigue strength is essential for various applications, future research should also cross-link the influence of the surface on fatigue properties and determine the effect of post-process heat treatments and fatigue life.

## References

- [1] T. DebRoy, H. L. Wei, J. S. Zuback, T. Mukherjee, J. W. Elmer, J. O. Milewski, A. M. Beese, A. Wilson-Heid, A. De, W. Zhang, Additive manufacturing of metallic components – process, structure and properties. *Prog. Mater. Sci.* **92**, 112–224 (2018).
- [2] D. D. Gu, W. Meiners, K. Wissenbach, R. Poprawe, Laser additive manufacturing of metallic components: Materials, processes and mechanisms. *Int. Mater. Rev.* **57**, 133–164 (2012).
- [3] W. J. Sames, F. A. List, S. Pannala, R. R. Dehoff, S. S. Babu, The metallurgy and processing science of metal additive manufacturing. *Int. Mater. Rev.* **61**, 315–360 (2016).
- [4] D. Herzog, V. Seyda, E. Wycisk, C. Emmelmann, Additive manufacturing of metals. *Acta Mater.* **117**, 371–392 (2016).
- [5] AMPOWER Report 2021: Meta (2021), (accessed December 21, 2021, available at <https://additive-manufacturing-report.com/report-2021/metal-am-market-by-technology-2021/>).
- [6] B. Blakey-milner, P. Gradl, G. Snedden, M. Brooks, J. Pitot, E. Lopez, M. Leary, F. Berto, A. du Plessis, Metal additive manufacturing in aerospace: A review. *Mater. Des.* **209**, 110008 (2021).
- [7] T. Peng, K. Kellens, R. Tang, C. Chen, G. Chen, Sustainability of additive manufacturing: An overview on its energy demand and environmental impact. *Addit. Manuf.* **21**, 694–704 (2018).
- [8] R. Boyer, G. Welsch, E. W. Collings, *Materials properties handbook: titanium alloys* (ASM International, Materials Park, Novelty, Ohio, 4<sup>th</sup> ed., 1994).
- [9] G. Lütjering, J. C. Williams, *Titanium* (Springer Science & Business Media, Berlin Heidelberg, ed. 1, 2007).
- [10] D. Banerjee, J. C. Williams, Perspectives on titanium science and technology. *Acta Mater.* **61**, 844–879 (2013).
- [11] Z. Liu, B. He, T. Lyu, Y. Zou, A Review on Additive Manufacturing of Titanium Alloys for Aerospace Applications: Directed Energy Deposition and Beyond Ti-6Al-4V. *JOM.* **73**, 1804–1818 (2021).
- [12] A. T. Clare, R. S. Mishra, M. Merklein, H. Tan, I. Todd, L. Chechik, J. Li, M. Bambach, Alloy design and adaptation for additive manufacture. *J. Mater. Process. Technol.* **299** (2022).
- [13] C. F. Yolton, F. H. Froes, in *Titanium Powder Metallurgy* (Butterworth-Heinemann, Waltham, MA, 2015), pp. 21–32.
- [14] N. C. Levkulich, S. L. Semiatin, J. E. Gockel, J. R. Middendorf, A. T. DeWald, N. W. Klingbeil, The effect of process parameters on residual stress evolution and distortion in the laser powder bed fusion of Ti-6Al-4V. *Addit. Manuf.* **28**, 475–484 (2019).
- [15] A. du Plessis, Effects of process parameters on porosity in laser powder bed fusion revealed by X-ray tomography. *Addit. Manuf.* **30**, 100871 (2019).
- [16] A. D. McQuillan, Allotropic Transformations in Titanium. *Nature.* **164**, 24 (1949).
- [17] C. Leyens, M. Peters, *Titanium and Titanium Alloys: Fundamentals and Applications* (Wiley-VCH, Weinheim, 1<sup>st</sup> ed., 2003).
- [18] R. P. Kolli, Arun Devaraj, A Review of Metastable Beta Titanium Alloys. *Metals (Basel).* **8**, 1–41 (2018).
- [19] A. P. Mouritz, in *Introduction to aerospace materials* (Woodhead Publishing, Cambridge, 2012), pp. 202–223.
- [20] P. A. Kobryn, S. L. Semiatin, Mechanical Properties of Laser-Deposited Ti-6Al-4V P.A. Kobryn and S.L. Semiatin Air Force Research Laboratory, AFRL/MLLMP, Wright-Patterson Air Force Base, OH 45433-7817. *Int. Solid Free. Fabr. Symp.*, 179–186 (2001).
- [21] L. E. Murr, E. V. Esquivel, S. A. Quinones, S. M. Gaytan, M. I. Lopez, E. Y. Martinez, F. Medina, D. H. Hernandez, E. Martinez, J. L. Martinez, S. W. Stafford, D. K. Brown, T. Hoppe, W. Meyers, U. Lindhe, R. B. Wicker, Microstructures and mechanical properties of electron beam-rapid manufactured Ti-6Al-4V biomedical prototypes compared to wrought Ti-6Al-4V. *Mater. Charact.* **60**, 96–105 (2009).
- [22] L. Facchini, E. Magalini, P. Robotti, A. Molinari, Microstructure and mechanical properties of Ti-6Al-4V produced by electron beam melting of pre-alloyed powders. *Rapid Prototyp. J.* **15**,

- 171–178 (2009).
- [23] B. E. Carroll, T. A. Palmer, A. M. Beese, Anisotropic tensile behavior of Ti-6Al-4V components fabricated with directed energy deposition additive manufacturing. *Acta Mater.* **87**, 309–320 (2015).
- [24] V. Cain, L. Thijs, J. Van Humbeeck, B. Van Hooreweder, R. Knutsen, Crack propagation and fracture toughness of Ti6Al4V alloy produced by selective laser melting. *Addit. Manuf.* **5**, 68–76 (2015).
- [25] S. L. Sing, J. An, W. Y. Yeong, F. E. Wiria, Laser and electron-beam powder-bed additive manufacturing of metallic implants: A review on processes, materials and designs. *J. Orthop. Res.* **34**, 369–385 (2016).
- [26] S. Palanivel, A. K. Dutt, E. J. Faierson, R. S. Mishra, Spatially dependent properties in a laser additive manufactured Ti-6Al-4V component. *Mater. Sci. Eng. A.* **654**, 39–52 (2016).
- [27] J. C. Williams, A. F. Belov, Eds., *Titanium and Titanium Alloys: Scientific and Technological Aspects Volume 3* (Springer Science & Business Media, New York, 1982).
- [28] W. G. Burgers, On the process of transition of the cubic-body-centered modification into the hexagonal-close-packed modification of zirconium. *Physica.* **1**, 561–586 (1934).
- [29] J. B. Newkirk, A. H. Geisler, Crystallographic aspects of the beta to alpha transformation in titanium. *Acta Metall.* **1** (1953).
- [30] P. Barriobero-Vila, *Phase transformation kinetics during continuous heating of  $\alpha+\beta$  and metastable  $\beta$  titanium alloys*, PhD Thesis, TU Vienna, Austria (2015).
- [31] L. Qian, J. Mei, J. Liang, X. Wu, Influence of position and laser power on thermal history and microstructure of direct laser fabricated Ti-6Al-4V samples. *Mater. Sci. Technol.* **21**, 597–605 (2005).
- [32] J. Yu, M. Rombouts, G. Maes, F. Motmans, Material properties of Ti6Al4V parts produced by laser metal deposition. *Phys. Procedia.* **39**, 416–424 (2012).
- [33] S. Banerjee, P. Mukhopadhyay, *Phase transformations: Examples from titanium and zirconium alloys* (Elsevier, 1<sup>st</sup> ed., 2007).
- [34] S. Banumathy, R. K. Mandal, A. K. Singh, Structure of orthorhombic martensitic phase in binary Ti-Nb alloys. *J. Appl. Phys.* **106** (2009).
- [35] M. J. Donachie, *Titanium - A technical guide* (ASM International, Ohio, 2<sup>nd</sup> ed., 2000).
- [36] J. Haubrich, J. Gussone, P. Barriobero-Vila, P. Kürnsteiner, E. A. Jäggle, D. Raabe, N. Schell, G. Requena, The role of lattice defects, element partitioning and intrinsic heat effects on the microstructure in selective laser melted Ti-6Al-4V. *Acta Mater.* **167**, 136–148 (2019).
- [37] G. M. Ter Haar, T. H. Becker, Low temperature stress relief and martensitic decomposition in selective laser melting produced Ti6Al4V. *Mater. Des. Process. Commun.* **3**, e138 (2021).
- [38] K. Guo, C. Liu, S. Chen, H. Dong, S. Wang, High pressure EIGA preparation and 3D printing capability of Ti – 6Al – 4V powder. *Trans. Nonferrous Met. Soc. China.* **30**, 147–159 (2020).
- [39] P. Fang, Y. Xu, X. Li, Y. Chen, Influence of Atomizing Gas and Cooling Rate on Solidification Characterization of Nickel-based Superalloy Powders. *Rare Met. Mater. Eng.* **47**, 423–430 (2018).
- [40] He Shiwen, Liu Yong, Guo Sheng, Cooling rate calculation of non-equilibrium aluminum alloy powders prepared by gas atomization. *Rare Met. Mater. Eng.* **38**, 353–356 (2009).
- [41] M. R. Plichta, J. C. Williams, H. I. Aaronson, On the existence of the  $\beta \rightarrow \alpha m$  transformation in the alloy systems Ti-Ag, Ti-Au, and Ti-Si. *Metall. Trans. A.* **8**, 1885–1892 (1977).
- [42] M. R. Plichta, H. I. Aaronson, J. H. Perepezko, The thermodynamics and kinetics of the  $\beta \rightarrow \alpha m$  transformation in three Ti-X systems. *Acta Metall.* **26**, 1293–1305 (1978).
- [43] M. R. Plichta, J. H. Perepezko, H. I. Aaronson, W. F. Lange, Nucleation kinetics of the  $\beta \rightarrow \alpha m$  transformation in Ti-Ag and Ti-Au alloys. *Acta Metall.* **28**, 1031–1040 (1980).
- [44] S. L. Lu, M. Qian, H. P. Tang, M. Yan, J. Wang, D. H. StJohn, Massive transformation in Ti-6Al-4V additively manufactured by selective electron beam melting. *Acta Mater.* **104**, 303–311 (2016).
- [45] J. C. Williams, B. S. Hickman, Tempering behavior of orthorhombic martensite in titanium alloys. *Metall. Trans.* **1**, 2648–2650 (1970).
- [46] R. Davis, H. M. Flower, D. R. F. West, Martensitic transformations in Ti-Mo alloys. *J. Mater. Sci.* **14**, 712–722 (1979).
- [47] H. M. Flower, R. Davis, D. R. F. West, in *Titanium and titanium alloys* (Springer, 1982), vol. 3,

- pp. 1703–1715.
- [48] C. Cayron, B. Artaud, L. Briottet, Reconstruction of parent grains from EBSD data. *Mater. Charact.* **57**, 386–401 (2006).
- [49] C. Cayron, ARPGE: a computer program to automatically reconstruct the parent grains from electron backscatter diffraction data. *J. Appl. Crystallogr.* **40**, 1183–1188 (2007).
- [50] S. S. Al-Bermani, M. L. Blackmore, W. Zhang, I. Todd, The origin of microstructural diversity, texture, and mechanical properties in electron beam melted Ti-6Al-4V. *Metall. Mater. Trans. A Phys. Metall. Mater. Sci.* **41**, 3422–3434 (2010).
- [51] A. A. Antonysamy, J. Meyer, P. B. Prangnell, Effect of build geometry on the  $\beta$ -grain structure and texture in additive manufacture of Ti6Al4V by selective electron beam melting. *Mater. Charact.* **84**, 153–168 (2013).
- [52] L. Thijs, F. Verhaeghe, T. Craeghs, J. Van Humbeeck, J. P. Kruth, A study of the microstructural evolution during selective laser melting of Ti-6Al-4V. *Acta Mater.* **58**, 3303–3312 (2010).
- [53] B. Vrancken, L. Thijs, J. P. Kruth, J. Van Humbeeck, Heat treatment of Ti6Al4V produced by selective laser melting: microstructure and mechanical properties. *J. Alloys Compd.* **541**, 177–185 (2012).
- [54] Y. Zhu, X. Tian, J. Li, H. Wang, The anisotropy of laser melting deposition additive manufacturing Ti-6.5Al-3.5Mo-1.5Zr-0.3Si titanium alloy. *Mater. Des.* **67**, 538–542 (2015).
- [55] M. Strantza, R. Vafadari, D. De Baere, B. Vrancken, W. Van Paepegem, I. Vandendael, H. Terryn, P. Guillaume, D. Van Hemelrijck, Fatigue of Ti6Al4V structural health monitoring systems produced by selective laser melting. *Materials (Basel)*. **9**, 1–15 (2016).
- [56] P. Barriobero-Vila, J. Gussone, A. Stark, N. Schell, J. Haubrich, G. Requena, Peritectic titanium alloys for 3D printing. *Nat. Commun.* **9**, 1–9 (2018).
- [57] M. J. Bermingham, S. D. McDonald, M. S. Dargusch, D. H. St. John, Grain-refinement mechanisms in titanium alloys. *J. Mater. Res.* **23**, 97–104 (2008).
- [58] P. K. Gokuldoss, S. Kolla, J. Eckert, Additive manufacturing processes: Selective laser melting, electron beam melting and binder jetting-selection guidelines. *Materials*. **10**, 672 (2017).
- [59] C. Qiu, M. Al Kindi, A. S. Aladawi, I. Al Hatmi, A comprehensive study on microstructure and tensile behaviour of a selectively laser melted stainless steel. *Sci. Rep.* **8**, 1–16 (2018).
- [60] S. Liu, Y. C. Shin, Additive manufacturing of Ti6Al4V alloy: A review. *Mater. Des.* **164**, 107552 (2019).
- [61] J. Yang, H. Yu, J. Yin, M. Gao, Z. Wang, X. Zeng, Formation and control of martensite in Ti-6Al-4V alloy produced by selective laser melting. *Mater. Des.* **108**, 308–318 (2016).
- [62] G. Ter Haar, T. Becker, Selective laser melting produced Ti-6Al-4V: post-process heat treatments to achieve superior tensile properties. *Materials*. **11**, 146 (2018).
- [63] M. T. Tsai, Y. W. Chen, C. Y. Chao, J. S. C. Jang, C. C. Tsai, Y. L. Su, C. N. Kuo, Heat-treatment effects on mechanical properties and microstructure evolution of Ti-6Al-4V alloy fabricated by laser powder bed fusion. *J. Alloys Compd.* **816**, 152615 (2020).
- [64] X. Y. Zhang, G. Fang, S. Leeftang, A. J. Böttger, A. A. Zadpoor, J. Zhou, Effect of subtransus heat treatment on the microstructure and mechanical properties of additively manufactured Ti-6Al-4V alloy. *J. Alloys Compd.* **735**, 1562–1575 (2018).
- [65] B. Wysocki, P. Maj, R. Sitek, J. Buhagiar, K. J. Kurzydłowski, W. Świeszkowski, Laser and electron beam additive manufacturing methods of fabricating titanium bone implants. *Appl. Sci.* **7**, 1–20 (2017).
- [66] G. Kasperovich, J. Hausmann, Improvement of fatigue resistance and ductility of TiAl6V4 processed by selective laser melting. *J. Mater. Process. Technol.* **220**, 202–214 (2015).
- [67] M. Yao, Z. Yao, X. Tao, C. Huang, S. Zhang, Alleviating plastic anisotropy of boron modified titanium alloy by constructing layered structure via electron beam directed energy deposition. *Addit. Manuf.* **50**, 102561 (2022).
- [68] K. Zhang, X. Tian, M. Bermingham, J. Rao, Q. Jia, Y. Zhu, X. Wu, S. Cao, A. Huang, Effects of boron addition on microstructures and mechanical properties of Ti-6Al-4V manufactured by direct laser deposition. *Mater. Des.* **184** (2019).
- [69] M. Zhang, C. Liu, X. Shi, X. Chen, C. Chen, J. Zuo, J. Lu, S. Ma, Residual stress, defects and grain morphology of Ti-6Al-4V alloy produced by ultrasonic impact treatment assisted selective laser melting. *Appl. Sci.* **6**, 304 (2016).
- [70] J. O. Peters, G. Lütjering, R. K. Nalla, I. Altenberger, R. O. Ritchie, High-cycle fatigue of beta

- titanium alloys. *Fatigue 2002* (2002).
- [71] X. Zhao, S. Li, M. Zhang, Y. Liu, T. B. Sercombe, S. Wang, Y. Hao, R. Yang, L. E. Murr, Comparison of the microstructures and mechanical properties of Ti-6Al-4V fabricated by selective laser melting and electron beam melting. *Mater. Des.* **95**, 21–31 (2016).
- [72] R. W. Hayes, G. B. Viswanathan, M. J. Mills, Creep behavior of Ti-6Al-2Sn-4Zr-2Mo: I. The effect of nickel on creep deformation and microstructure. *Acta Mater.* **50**, 4953–4963 (2002).
- [73] L. Badea, M. Surand, J. Ruau, B. Viguier, Creep behavior of Ti-6Al-4V from 450 ° C to 600 ° C. *Sci. Bull. Ser. B.* **76**, 185–196 (2014).
- [74] S. G. Ivanova, R. R. Biederman, R. D. Sisson, Investigation of fatigue crack initiation in Ti-6Al-4V during tensile-tensile fatigue. *J. Mater. Eng. Perform.* **11**, 226–231 (2002).
- [75] Roland Berger Strategy Consultants, *Additive manufacturing. A game changer for the manufacturing industry?* (Munich, 2013).
- [76] ASTM F2792-12a, Standard terminology for additive manufacturing technologies. *ASTM Int. West Conshohocken* (2013).
- [77] A. Vafadar, F. Guzzomi, A. Rassau, K. Hayward, Advances in metal additive manufacturing: A review of common processes, industrial applications, and current challenges. *Appl. Sci.* **11**, 1–33 (2021).
- [78] C. Kamath, B. El-dasher, G. F. Gallegos, W. E. King, A. Sisto, Density of additively-manufactured, 316L SS parts using laser powder-bed fusion at powers up to 400W. *Int J Adv Manuf Technol.* **74**, 65–78 (2014).
- [79] V. Bhavar, P. Kattire, V. Patil, S. Khot, K. Gujar, R. Singh, in *4th International conference and exhibition on additive manufacturing technologies* (2014), pp. 1–2.
- [80] K. S. Jamshidinia M, Sadek A, Wang W, Additive Manufacturing of Steel Alloys Using Laser Powder-Bed Fusion. *Adv Mater Process.* **173**, 20–4 (2015).
- [81] S. A. Khairallah, A. T. Anderson, A. Rubenchik, W. E. King, Laser powder-bed fusion additive manufacturing: Physics of complex melt flow and formation mechanisms of pores, spatter, and denudation zones. *Acta Mater.* **108**, 36–45 (2016).
- [82] T. M. Mower, M. J. Long, Mechanical behavior of additive manufactured, powder-bed laser-fused materials. *Mater. Sci. Eng. A.* **651**, 198–213 (2016).
- [83] M. Simonelli, Y. Y. Tse, C. Tuck, On the texture formation of selective laser melted Ti-6Al-4V. *Metall. Mater. Trans. A.* **45**, **6**, 2863–2872 (2014).
- [84] B. Dutta, F. H. Froes, *Additive manufacturing of Titanium alloys: state of the art, challenges and opportunities* (Butterworth-Heinemann, Oxford, UK, 2016).
- [85] B. Vrancken, S. Buls, J.-P. Kruth, J. Van Humbeeck, in *Proceedings of the 13th World Conference on Titanium* (The Minerals, Metals & Materials Society, 2016), pp. 1269–1277.
- [86] S. Wang, Y. Liu, W. Shi, B. Qi, J. Yang, F. Zhang, D. Han, Y. Ma, Research on high layer thickness fabricated of 316L by selective laser melting. *Materials (Basel)*. **10** (2017).
- [87] M. Neikter, A. Huang, X. Wu, Microstructural characterization of binary microstructure pattern in selective laser-melted Ti-6Al-4V. *Int. J. Adv. Manuf. Technol.* **104**, 1381–1391 (2019).
- [88] A. A. Martin, N. P. Calta, S. A. Khairallah, J. Wang, P. J. Depond, A. Y. Fong, V. Thampy, G. M. Guss, A. M. Kiss, K. H. Stone, C. J. Tassone, J. Nelson Weker, M. F. Toney, T. van Buuren, M. J. Matthews, Dynamics of pore formation during laser powder bed fusion additive manufacturing. *Nat. Commun.* **10**, 1987 (2019).
- [89] N. P. Calta, V. Thampy, D. R. C. Lee, A. A. Martin, R. Ganeriwala, J. Wang, P. J. Depond, T. T. Roehling, A. Y. Fong, A. M. Kiss, C. J. Tassone, K. H. Stone, J. Nelson Weker, M. F. Toney, A. W. Van Buuren, M. J. Matthews, Cooling dynamics of two titanium alloys during laser powder bed fusion probed with in situ X-ray imaging and diffraction. *Mater. Des.* **195**, 108987 (2020).
- [90] X. C. Wang, T. Laoui, J. Bonse, J. P. Kruth, B. Lauwers, L. Froyen, Direct selective laser sintering of hard metal powders: Experimental study and simulation. *Int. J. Adv. Manuf. Technol.* **19**, 351–357 (2002).
- [91] J. Yin, D. Wang, L. Yang, H. Wei, P. Dong, L. Ke, G. Wang, H. Zhu, X. Zeng, Correlation between forming quality and spatter dynamics in laser powder bed fusion. *Addit. Manuf.* **31**, 100958 (2020).
- [92] S. Pal, N. Gubeljak, R. Hudak, G. Lojen, V. Rajtukova, J. Predan, V. Kokol, I. Drstvensek, Tensile properties of selective laser melting products affected by building orientation and energy

- density. *Mater. Sci. Eng. A*. **743**, 637–647 (2019).
- [93] J. Yang, J. Han, H. Yu, J. Yin, M. Gao, Z. Wang, X. Zeng, Role of molten pool mode on formability, microstructure and mechanical properties of selective laser melted Ti-6Al-4V alloy. *Mater. Des.* **110**, 558–570 (2016).
- [94] A. Ladewig, G. Schlick, M. Fisser, V. Schulze, U. Glatzel, Influence of the shielding gas flow on the removal of process by-products in the selective laser melting process. *Addit. Manuf.* **10**, 1–9 (2016).
- [95] N. Hrabe, T. Gnäupel-Herold, T. Quinn, Fatigue properties of a titanium alloy (Ti-6Al-4V) fabricated via electron beam melting (EBM): Effects of internal defects and residual stress. *Int. J. Fatigue*. **94**, 202–210 (2017).
- [96] S. Leuders, M. Thöne, A. Riemer, T. Niendorf, T. Tröster, H. A. Richard, H. J. Maier, On the mechanical behaviour of titanium alloy TiAl6V4 manufactured by selective laser melting: fatigue resistance and crack growth performance. *Int. J. Fatigue*. **48**, 300–307 (2013).
- [97] P. Li, D. H. Warner, A. Fatemi, N. Phan, Critical assessment of the fatigue performance of additively manufactured Ti-6Al-4V and perspective for future research. *Int. J. Fatigue*. **85**, 130–143 (2016).
- [98] L. Zhao, J. G. Santos Macías, A. Dolimont, A. Simar, E. Rivière-Lorphèvre, Comparison of residual stresses obtained by the crack compliance method for parts produced by different metal additive manufacturing techniques and after friction stir processing. *Addit. Manuf.* **36**, 101499 (2020).
- [99] J. D. Roehling, W. L. Smith, T. T. Roehling, B. Vrancken, G. M. Guss, J. T. McKeown, M. R. Hill, M. J. Matthews, Reducing residual stress by selective large-area diode surface heating during laser powder bed fusion additive manufacturing. *Addit. Manuf.* **28**, 228–235 (2019).
- [100] D. Schimbäck, J. Braun, G. Leichtfried, H. Clemens, S. Mayer, Laser powder bed fusion of an engineering intermetallic TiAl alloy. **201**, 7–12 (2021).
- [101] X. Miao, M. Wu, J. Han, H. Li, X. Ye, Effect of laser rescanning on the characteristics and residual stress of selective laser melted titanium Ti6Al4V alloy. *Materials (Basel)*. **13** (2020).
- [102] V. Anusci, Airbus Helicopters to begin 3D printing metal A350 components. *3D Print. Media Netw.* (2018), (accessed November 26, 2021, available at <https://www.3dprintingmedia.network/airbus-helicopters-a350/%0A>).
- [103] T. Childerhouse, M. Jackson, Near net shape manufacture of titanium alloy components from powder and wire: A review of state-of-the-art process routes. *Metals (Basel)*. **9** (2019).
- [104] BBi Autosport, Porsche GT2 RS 3D Printed Titanium Exhaust System, (accessed December 13, 2021, available at <https://bbiautosport.com/collections/991-gt2-rs>).
- [105] J. Dawes, R. Bowerman, R. Trepleton, Introduction to the additive manufacturing powder metallurgy supply chain. *Johnson Matthey Technol. Rev.* **59**, 243–256 (2015).
- [106] R. Gerling, H. Clemens, F. P. Schimansky, Powder metallurgical processing of Intermetallic Gamma Titanium Aluminides. *Adv. Eng. Mater.* **6**, 23–38 (2002).
- [107] G. Chen, S. Y. Zhao, P. Tan, J. Wang, C. S. Xiang, H. P. Tang, A comparative study of Ti-6Al-4V powders for additive manufacturing by gas atomization, plasma rotating electrode process and plasma atomization. *Powder Technol.* **333**, 38–46 (2018).
- [108] A. Lawley, Atomization of Specialty Alloy Powders. *JOM*. **33**, 13–18 (1981).
- [109] W. Schatt, K.-P. Wieters, B. Kieback, *Pulvermetallurgie: Technologien und Werkstoffe* (Springer, Berlin Heidelberg, 2. Auflage., 2007).
- [110] A. Allimant, M. P. Planche, Y. Bailly, L. Dembinski, C. Coddet, Progress in gas atomization of liquid metals by means of a De Laval nozzle. *Powder Technol.* **190**, 79–83 (2009).
- [111] P. Sun, Z. Z. Fang, Y. Zhang, Y. Xia, Review of the methods for production of spherical Ti and Ti alloy powder. *JOM*. **69**, 1853–1860 (2017).
- [112] M. Fousová, D. Vojtěch, K. Doubrava, M. Daniel, C. F. Lin, Influence of inherent surface and internal defects on mechanical properties of additively manufactured Ti6Al4V alloy: Comparison between selective laser melting and electron beam melting. *Materials (Basel)*. **11** (2018).
- [113] W. Zhang, P. Qin, Z. Wang, C. Yang, L. Kollo, D. Grzesiak, P. K. Gokuldoss, Superior wear resistance in EBM-processed TC4 alloy compared with SLM and forged samples. *Materials (Basel)*. **12**, 2–12 (2019).
- [114] S. A. Khairallah, A. A. Martin, J. R. I. Lee, G. Guss, N. P. Calta, J. A. Hammons, M. H. Nielsen,



- K. Chaput, E. Schwalbach, M. N. Shah, M. G. Chapman, T. M. Willey, A. M. Rubenchik, A. T. Anderson, Y. Morris Wang, M. J. Matthews, W. E. King, Controlling interdependent meso-nanosecond dynamics and defect generation in metal 3D printing. *Science*. **368**, 660–665 (2020).
- [115] T. Achee, G. Guss, A. Elwany, M. Matthews, Laser pre-sintering for denudation reduction in the laser powder bed fusion additive manufacturing of Ti-6Al-4V alloy. *Addit. Manuf.* **42**, 101985 (2021).
- [116] A. M. Master, M. E. Rodriguez, M. E. Kenney, N. L. Oleinick, A. Sen Gupta, Delivery of the photosensitizer Pc 4 in PEG–PCL micelles for in vitro PDT studies. *J. Pharm. Sci.* **99**, 2386–2398 (2010).
- [117] A. G. Stavrou, C. Hare, A. Hassanpour, C. Y. Wu, Investigation of powder flowability at low stresses: Influence of particle size and size distribution. *Powder Technol.* **364**, 98–114 (2020).
- [118] S. E. Brika, M. Letenneur, C. A. Dion, V. Brailovski, Influence of particle morphology and size distribution on the powder flowability and laser powder bed fusion manufacturability of Ti-6Al-4V alloy. *Addit. Manuf.* **31**, 100929 (2020).
- [119] R. Freeman, Measuring the flow properties of consolidated, conditioned and aerated powders - A comparative study using a powder rheometer and a rotational shear cell. *Powder Technol.* **174**, 25–33 (2007).
- [120] R. Freeman, X. Fu, Characterisation of power bulk, dynamic flow and shear properties in relation to die filling. *Powder Metall.* **51**, 196–201 (2008).
- [121] S. Kolossov, E. Boillat, R. Glardon, P. Fischer, M. Locher, 3D FE simulation for temperature evolution in the selective laser sintering process. *Int. J. Mach. Tools Manuf.* **44**, 117–123 (2004).
- [122] M. Matsumoto, M. Shiomi, K. Osakada, F. Abe, Finite element analysis of single layer forming on metallic powder bed in rapid prototyping by selective laser processing. *Int. J. Mach. Tools Manuf.* **42**, 61–67 (2002).
- [123] R. B. Patil, V. Yadava, Finite element analysis of temperature distribution in single metallic powder layer during metal laser sintering. *Int. J. Mach. Tools Manuf.* **47**, 1069–1080 (2007).
- [124] A. V. Gusarov, I. Yadroitsev, P. Bertrand, I. Smurov, Model of radiation and heat transfer in laser-powder interaction zone at selective laser melting. *J. Heat Transfer.* **131**, 1–10 (2009).
- [125] G. Jacob, C. U. Brown, A. Donmez, The influence of spreading metal powders with different particle size distributions on the powder bed density in laser-based powder bed fusion processes. *NIST Adv. Manuf. Ser.*, 100–17 (2018).
- [126] N. P. Karapatis, G. Egger, P.-E. Gyax, R. Glardon, in *10th Solid Freeform Fabrication Symposium* (1999), pp. 255–263.
- [127] A. Strondl, O. Lyckfeldt, H. Brodin, U. Ackelid, Characterization and control of powder properties for additive manufacturing. *JOM.* **67**, 549–554 (2015).
- [128] G. Spierings, A.B. & Levy, Comparison of density of stainless steel 316L parts produced with selective laser melting using different powder grades. *Rev. Lit. Arts Am.*, 342–353 (2009).
- [129] E. Uhlmann, R. Kersting, T. B. Klein, M. F. Cruz, A. V. Borille, Additive manufacturing of titanium alloy for aircraft components. *Procedia Cirp.* **35**, 55–60 (2015).
- [130] H. P. Tang, M. Qian, N. Liu, X. Z. Zhang, G. Y. Yang, J. Wang, Effect of powder reuse times on additive manufacturing of Ti-6Al-4V by selective electron beam melting. *JOM.* **67**, 555–563 (2015).
- [131] X. Li, J. Xie, Y. Zhou, Effects of oxygen contamination in the argon shielding gas in laser welding of commercially pure titanium thin sheet. *J. Mater. Sci.* **40**, 3437–3443 (2005).
- [132] AMS4999A, Titanium Alloy Direct Deposited Products 6Al - 4V Annealed. *SAE Int.* (2016).
- [133] H. Fan, S. Yang, Effects of direct aging on near-alpha Ti–6Al–2Sn–4Zr–2Mo (Ti-6242) titanium alloy fabricated by selective laser melting (SLM). *Mater. Sci. Eng. A.* **788**, 139533 (2020).
- [134] A. Carrozza, A. Aversa, P. Fino, M. Lombardi, A study on the microstructure and mechanical properties of the Ti-6Al-2Sn-4Zr-6Mo alloy produced via Laser Powder Bed Fusion. *J. Alloys Compd.* **870**, 159329 (2021).
- [135] C. Fleißner-Rieger, T. Pogrietz, D. Obersteiner, T. Pfeifer, H. Clemens, S. Mayer, An additively manufactured titanium alloy in the focus of metallography. *Pract. Metallogr.* **58**, 4–31 (2021).
- [136] D. Wimler, J. Lindemann, T. Kremmer, H. Clemens, S. Mayer, Microstructure and mechanical properties of novel TiAl alloys tailored via phase and precipitate morphology. *Intermetallics.* **138**, 107316 (2021).
- [137] M. Musi, B. Galy, J. P. Monchoux, A. Couret, H. Clemens, S. Mayer, In-situ observation of the

- phase evolution during an electromagnetic-assisted sintering experiment of an intermetallic  $\gamma$ -TiAl based alloy. *Scr. Mater.* **206**, 114233 (2022).
- [138] G. Petzow, *Metallographisches, Keramographisches, Plastographisches Ätzen* (Borntraeger Gebraueder, Stuttgart, Germany, 7. Auflage., 2015).
- [139] A. J. Schwartz, M. Kumar, B. L. Adams, D. P. Field, Eds., *Electron Backscatter Diffraction in Materials Science* (Springer US, Boston, MA, 2009).
- [140] M. K. Miller, K. F. Russell, K. Thompson, R. Alvis, D. J. Larson, Review of atom probe FIB-based specimen preparation methods. *Microsc. Microanal.* **13**, 428–436 (2007).
- [141] L. M. Gordon, D. Joester, Mapping residual organics and carbonate at grain boundaries and the amorphous interphase in mouse incisor enamel. *Front. Physiol.* **6**, 1–10 (2015).
- [142] M. K. Miller, R. G. Forbes, *Atom-probe tomography: The local electrode atom probe* (Springer US, Boston, MA, 2014; <http://link.springer.com/10.1007/978-1-4899-7430-3>).
- [143] R. E. Dinnebier, S. J. L. Billinge, Eds., *Powder Diffraction* (Royal Society of Chemistry, Cambridge, 2008).
- [144] A. Casadebaigt, D. Monceau, J. Hugues, I. R. T. Saint Exupery, B. Bâtiment, in *The 14 th World Conference on Titanium* (2020), vol. 03006, pp. 4–7.
- [145] Q. Meng, H. Li, K. Wang, S. Guo, F. Wei, J. Qi, Y. Sui, B. Shen, X. Zhao, In Situ Synchrotron X-ray Diffraction Investigations of the Nonlinear Deformation Behavior of a Low Modulus  $\beta$ -Type Ti<sub>36</sub>Nb<sub>5</sub>Zr Alloy. *Metals (Basel)*. **10** (2020).
- [146] P. Staron, A. Schreyer, H. Clemens, S. Mayer, Eds., *Neutrons and Synchrotron Radiation in Engineering Materials Science* (Wiley-VCH, Weinheim, Germany, 2<sup>nd</sup> ed., 2017).
- [147] B. H. Toby, R factors in Rietveld analysis: How good is good enough? *Powder Diffr.* **21**, 67–70 (2006).
- [148] L. B. Mccusker, R. B. Von Dreele, D. E. Cox, D. Louër, P. Scardi, Rietveld refinement guidelines. *J. Appl. Crystallogr.* **32**, 36–50 (1999).
- [149] C. Fleißner-Rieger, T. Pfeifer, T. Jörg, T. Kremmer, M. Brabetz, H. Clemens, S. Mayer, Selective laser melting of a near- $\alpha$  Ti6242S alloy for high-performance automotive parts. *Adv. Eng. Mater.* **23**, 2001194 (2021).
- [150] Continental Steel & Tube Co, Chemical composition chart (2016), (accessed December 6, 2021, available at <https://continentalsteel.com/titanium/grades/>).
- [151] M. Velasco-Castro, E. Hernández-Nava, I. A. Figueroa, I. Todd, R. Goodall, The effect of oxygen pickup during selective laser melting on the microstructure and mechanical properties of Ti–6Al–4V lattices. *Heliyon*. **5**, e02813 (2019).
- [152] C. Fleißner-Rieger, M. A. Tunes, C. Gammer, T. Jörg, T. Pfeifer, M. Musi, F. Mendez-Martin, H. Clemens, On the existence of orthorhombic martensite in a near- $\alpha$  titanium base alloy used for additive manufacturing. *J. Alloys Compd.* **897**, 163155 (2022).
- [153] P. Barribero-Vila, V. Biancardi Oliveira, S. Schwarz, T. Buslaps, G. Requena, Tracking the  $\alpha''$  martensite decomposition during continuous heating of a Ti-6Al-6V-2Sn alloy. *Acta Mater.* **135**, 132–143 (2017).
- [154] C. Fleißner-Rieger, H. Schönmaier, M. Musi, M. Stadler, H. Gschiel, C. Turk, T. Pfeifer, H. Clemens, Formation and evolution of precipitates in an additively manufactured near- $\alpha$  titanium base alloy. *Materialia*. **21**, 101366 (2022).
- [155] C. Fleißner-Rieger, T. Pfeifer, C. Turk, H. Clemens, Optimization of the post-process heat treatment strategy for a near- $\alpha$  titanium base alloy produced by laser powder bed fusion. *Materials (Basel)*. **15**, 1032 (2022).
- [156] H. Chandler (Eds.), *Heat Treater's Guide Practices and Procedures for Nonferrous Alloys* (ASM International, Ohio, 2006).
- [157] F. Cao, T. Zhang, M. A. Ryder, D. A. Lados, A Review of the Fatigue Properties of Additively Manufactured Ti-6Al-4V. *JOM*. **70**, 349–357 (2018).
- [158] S. Rajan, P. Wanjara, J. Gholipour, A. S. Kabir, Fatigue behavior of linear friction welded ti-6al-4v and ti-6al-2sn-4zr-2mo-0.1si dissimilar welds. *Materials (Basel)*. **14**, 1–18 (2021).

## Acknowledgments and closing remarks

This dissertation was supported by many personalities that demand my greatest acknowledgments. A lot of individual contributions, which helped me stay focused over the past years and motivated me to conduct this work, deserve special mention

- First and foremost, to Univ.-Prof. Dr. mont. Helmut Clemens and assoc. Prof. Dr. mont. Svea Mayer from the Department of Materials Science for providing the opportunity to conduct this thesis and the professional guidance from the Masters up to this point. I was pleased to have had advisors who allowed me to explore my own ideas and, at the same time, offered guidance that I needed to focus and stay on course. *Lieber Helmut und liebe Svea: Vielen Dank für alles!*
- To the industrial partners voestalpine Böhler Edelstahl GmbH & Co KG and Pankl Racing Systems AG for the financial and material assistance without whom it would not have been possible to conduct this research. Personally, I would like to thank T. Pfeifer, T. Jörg and C. Turk for the scientific exchange and essential discussions within and outside of project meetings.
- To my mentor Univ.-Prof. Dr. tech. Jürgen Eckert, who supported me and my work and for his contributions to this thesis.
- To the HEAT group members, who encouraged me, not only scientifically, but also to non-work related exchanges. I was privileged to benefit from scientific discussions ‘at its best’, which helped me to look outside the box and find something that is not meant to be found. Moreover, I value the numerous talks about the ‘little joys of life’, which filled one day or the other. In this context, M. Musi, D. Wimler, A. Janda, G. Graf, S. Kardos and R. Wartbichler – all members of the HEAT group – deserve special mention.
- To scientific partners in Leoben and around the world at the Department of Materials Science, the Department of Nonferrous Metallurgy, the Erich Schmid Institute of Materials Science and the Los Alamos National Laboratory for the scientific expertise and countless discussions. Especially F. Mendez-Martin, M.A. Tunes, C. Gammer, T. Kremmer and M. Brabetz are gratefully acknowledged.
- To student assistants, bachelor and master students. Special thanks go to T. Pogrietz, D. Obersteiner and J. Glettler. It was a pleasure to guide these highly motivated personalities.
- Finally, but not less important, is the contribution of my family and close friends in Austria, Germany and Italy, who supported me and always had an open ear for the ramblings about the topic additive manufacturing and titanium alloys.
- To my dear fiancée Hannah, who supported me throughout the entire time of my studies. Without her assistance, both professionally and personally, I would not have come this far. *Liebste Hannah, ich bin überglücklich eine solch starke und charismatische Persönlichkeit an meiner Seite zu wissen.*

Closing remarks

This book intends to provide information about the implementation of Ti alloys in the LPBF process. In combination with this thesis, the appended articles provide much data, which can be helpful for engineers and materials scientists interested in the AM production technology and Ti alloys in general. However, it is noteworthy to say that the scientific discourse is ongoing, and still, much R&D is needed to overcome the obstacles occurring during the manufacturing of new alloys by LPBF.

## Article A

---

# An additively manufactured titanium alloy in the focus of metallography

Christian Fleißner-Rieger<sup>1,\*</sup>, Thomas Pogrietz<sup>1</sup>, David Obersteiner<sup>1</sup>, Tanja Pfeifer<sup>2</sup>,  
Helmut Clemens<sup>1</sup> and Svea Mayer<sup>1</sup>

<sup>1</sup> Department Werkstoffwissenschaft, Montanuniversität Leoben, Franz-Josef Straße 18, 8700 Leoben,  
Österreich

<sup>2</sup> Pankl Systems Austria GmbH, Additive Manufacturing Technologies, Industriestraße Ost 4, 8605  
Kapfenberg, Österreich

\* Corresponding author

Practical Metallography, **58**(1), 4–31 (2021)

<https://doi.org/10.1515/pm-2020-0001>

open access: CC BY 4.0



C. Fleißner-Rieger, T. Pogrietz, D. Obersteiner, T. Pfeifer, H. Clemens, S. Mayer

# An Additively Manufactured Titanium Alloy in the Focus of Metallography

## Eine additiv gefertigte Titanlegierung im Fokus der Metallographie

Received: June 05, 2020  
Accepted: August 26, 2020  
Translation: E. Engert

Eingegangen: 05. Juni 2020  
Angenommen: 26. August 2020

### Abstract



Additive manufacturing processes allow the production of geometrically complex lightweight structures with specific material properties. However, by contrast with ingot metallurgy methods, the manufacture of components using this process also brings about some challenges. In the field of microstructural characterization, where mostly very fine structures are analyzed, it is thus indispensable to optimize the classic sample preparation process and to furthermore implement additional preparation steps. This work focuses on the metallography of additively manufactured Ti-6Al-4V components produced in a selective laser melting process. It offers a guideline for the metallographic preparation along the process chain of additive manufacturing from the metal powder characterization to the macro- and microstructural analysis of the

### Kurzfassung

Additive Fertigungsprozesse ermöglichen die Herstellung von geometrisch komplexen Leichtbaustrukturen mit spezifischen Werkstoffeigenschaften. Die Bauteilfertigung über diesen Prozess bringt aber, im Vergleich zu den schmelzmetallurgischen Verfahren, einige Herausforderungen mit sich. So auch im Bereich der Mikrostrukturcharakterisierung des meist sehr feinen Gefüges, wobei es unumgänglich ist, die klassische Probenpräparation zu optimieren sowie darüber hinaus zusätzliche Präparationsschritte zu implementieren. Diese Arbeit beschäftigt sich mit der Metallographie von additiv gefertigten Ti-6Al-4V-Bauteilen, hergestellt durch selektives Laserschmelzen. Beginnend bei der Metallpulvercharakterisierung bis hin zur makro- und mikrostrukturellen Analyse der lasergeschmolzenen Probenkörper bietet diese Arbeit einen Leitfaden für die metallographische Präparation entlang der

### Authors:

**Christian Fleißner-Rieger, Thomas Pogrietz, David Obersteiner, Helmut Clemens, Svea Mayer** Department Werkstoffwissenschaft, Montanuniversität Leoben, Franz-Josef Straße 18, 8700 Leoben, Österreich; e-mail: christian.fleissner-rieger@unileoben.ac.at  
**Tanja Pfeifer** Pankl Systems Austria GmbH, Additive Manufacturing Technologies, Industriestraße Ost 4, 8605 Kapfenberg, Österreich

 Open Access. © 2020 Christian Fleißner-Rieger, published by De Gruyter.  This work is licensed under the Creative Commons Attribution 4.0 International License.

laser melted sample. Apart from developing preparation parameters, selected etching methods were examined with regard to their practicality.

## 1. Introduction

The production of metallic structural components by additive manufacturing, AM, has become established in the last two decades. Universities and research institutions have considerably contributed to its use in industrial applications. This method is also already established in the manufacture of lightweight construction materials such as titanium and titanium alloys. It is used in the aviation sector, in medical technology, and in the automotive and ship building industry in the production of partially complex components that are, for instance, subjected to elevated temperatures and corrosive media [1]. Titanium alloys are classified as  $\alpha$ , near- $\alpha$ ,  $\alpha+\beta$  and  $\beta$  alloys depending on their alloying elements [2]. The  $\alpha+\beta$  alloy Ti-6Al-4V (m.%) is the most frequently used titanium alloy [3, 4]. Components made of this alloy are, for instance, manufactured using a powder bed-based selective laser melting technique (Laser Powder Bed Fusion, LPBF). Against the backdrop of a process and product quality assurance process, the material is characterized – from the initial metallic powder to the additively manufactured solid material sample. The quality of the end product is closely linked with the powder quality. Parameters such as chemical composition, flow behavior, tap and bulk density, sphericity, porosity, and particle size distribution are therefore analyzed [5]. The main focus of the examination of the additively manufactured Ti-6Al-4V samples is on microstructural characteristics such as structural homogeneity, appearance of the hexagonal (hex) martensitic  $\alpha'$  phase, and phase fractions [6, 7]. The AM process generates microstructures that differ fundamentally from those generated based on

Prozesskette der additiven Fertigung. Neben der Entwicklung von Präparationsparameter wurden ausgewählte Ätzmethoden auf ihre Durchführbarkeit untersucht.

## 1. Einleitung

Die Herstellung von metallischen Strukturbauteilen über additive Fertigungsverfahren (engl.: Additive Manufacturing, AM) ist in den letzten 20 Jahren etabliert worden. Universitäten und Forschungseinrichtungen haben wesentlich dazu beigetragen, dass AM in industriellen Anwendungen zum Einsatz kommt. Auch im Bereich der Leichtbauwerkstoffe, wie Titan und Titanlegierungen, ist AM bereits ein etabliertes Fertigungsverfahren und wird in der Luftfahrt, Medizintechnik, Automobil- und Schifffahrtindustrie für die Herstellung von zum Teil komplexen Bauteilen verwendet, die dann z. B. bei erhöhten Temperaturen und in korrosiven Medien eingesetzt werden [1]. Titanlegierungen werden in Abhängigkeit der Legierungselemente in  $\alpha$ -, Near- $\alpha$ -,  $\alpha+\beta$ - und  $\beta$ -Legierungen eingeteilt [2]. Die am häufigsten eingesetzte Titanlegierung ist die  $\alpha+\beta$ -Legierung Ti-6Al-4V (m.%) [3, 4]. Bauteile daraus werden bspw. über das pulverbettbasierte selektive Laserschmelzen (engl.: Laser Powder Bed Fusion, LPBF) hergestellt. Dabei erstreckt sich die Materialcharakterisierung, vor dem Hintergrund der Qualitätssicherung von Prozess und Produkt, von metallischen Ausgangspulver bis hin zur additiv gefertigten dichten Materialprobe. Da die Qualität des Pulvers eng mit der Qualität des Endprodukts verknüpft ist, werden Parameter, wie die chemische Zusammensetzung, das Fließverhalten, die Klopff- und Füllichte, die Sphärizität, der Porenanteil und die Partikelgrößenverteilung analysiert [5]. Bei der Untersuchung der additiv gefertigten Ti-6Al-4V Proben wird das Hauptaugenmerk auf mikrostrukturelle Charakteristika, wie z. B. Gefügehomoogenität, Aussehen der hexagonalen (hex) martensitischen  $\alpha'$ -Phase sowie auf die Phasenanteile gelegt [6, 7]. Durch den AM-Fertigungsprozess entstehen Gefügestrukturen, welche sich grundlegend vom

classical melting metallurgy manufacturing processes. For instance, a layered structure with so-called “layer bands” is formed when Ti-6Al-4V is additively manufactured. This layered structure forms owing to segregations of the alloy constituents during the solidification process and the reaction of the surface with the ambient atmosphere and thus represents the molten pool boundaries of the manufacturing process [8, 9]. This work also discusses how these layer structures are contrasted.

From a microstructural point of view, SLM manufactured  $\alpha+\beta$  alloys, such as Ti-6Al-4V, exhibit an epitaxially  $\beta$  solidification process through several applied layers inducing an anisotropic material behavior [8]. During the solidification process, the body-centered cubic (bcc)  $\beta$  phase, the high temperature phase of Ti and its alloys, is characterized by a preferred orientation in  $\langle 100 \rangle$  direction. Given that the size and shape of this columnar  $\beta$  grain structure are a function of the SLM manufacturing parameters and subsequently impact on the component properties, it is particularly relevant to reveal this process-microstructure-property relationship. Knowing these relationships, SLM manufacturing parameters can be optimally adapted in order to achieve desired mechanical properties [8]. The  $\beta$  grain structure formed from the melt in the epitaxial solidification process can either be visualized by etching (owing to the allotropic phase transformation ( $\beta \rightarrow \alpha'$ )) or by reconstruction using a program-based process. The program-based back-calculation is based on data from backscatter diffraction experiments. The data analysis is, for instance, performed based on ARPGE data [10, 11] (Automatic Reconstruction of Parent Grains from EBSD).

Once the additive manufacturing processes completed, the component is most often

klassischen schmelzmetallurgischen Herstellprozess unterscheiden. Beispielsweise kommt es bei der additiven Fertigung von Ti-6Al-4V zu sogenannten „Layer-Bands“ bzw. zur Ausbildung einer schichtartigen Struktur. Diese Schichtstruktur entsteht durch Segregationen der Legierungsbestandteile während des Erstarrungsprozesses sowie der Reaktion der Oberfläche mit der Umgebungsatmosphäre und repräsentiert somit die Schmelzbadgrenzen des Fertigungsprozesses [8, 9]. Im Rahmen dieser Arbeit wird auf die Kontrastierung dieser Schichtstrukturen eingegangen.

Aus mikrostruktureller Sicht erstarren SLM gefertigte  $\alpha+\beta$ -Legierungen, wie z. B. Ti-6Al-4V, epitaktisch in Form der primären  $\beta$ -Phase über mehrere aufgebrauchte Schichten, was zu anisotropen Materialverhalten führt [8]. Die kubisch raumzentrierte (krz)  $\beta$ -Phase, die Hochtemperaturphase des Ti und seiner Legierungen, zeigt beim Erstarrungsprozess eine Vorzugsorientierung in  $\langle 100 \rangle$ -Richtung. Da Größe und Form dieser kolumnaren  $\beta$ -Kornstruktur von den SLM-Fertigungsparametern abhängen und in weiterer Folge die Bauteileigenschaften beeinflussen, ist das Erfassen dieser Prozess-Mikrostruktur-Eigenschaftsbeziehung von besonderer Bedeutung. Die Kenntnis dieser Beziehungen macht es möglich, optimale Einstellung der SLM Fertigungsparameter und dadurch der mechanischen Eigenschaften zu erzielen [8]. Die visuelle Darstellung der  $\beta$ -Kornstruktur, welche sich im epitaktischen Erstarrungsprozess aus der Schmelze bildet, ist aufgrund der allotropen Phasenumwandlung ( $\beta \rightarrow \alpha'$ ) entweder über Ätzen, oder durch eine Rekonstruktion über eine programm-basierte Rückrechnung möglich. Die programm-basierte Rückrechnung basiert auf Daten aus Experimenten der Elektronenrückstreuung und die Auswertung erfolgt z. B. mit ARPGE [10, 11] (engl.: Automatic Reconstruction of Parent Grains from EBSD).

Nach Abschluss des additiven Fertigungsprozesses wird das Bauteil meist einem Nach-



subjected to a post-processing step [12]. Post-processing steps such as Hot Isostatic Pressing, HIP, can induce further changes to the microstructure within the component or in surface-near layers [13]. In order to analyze the effectiveness and efficiency of the additive manufacturing process and/or post-processing, the metallographic preparation for the respective material characterization must therefore imperatively take into account process-microstructure relationships.

Components made of titanium alloys are usually prepared in a multi-stage grinding and polishing process subsequent to which they are directly examined or etched. In this context, Kroll etching is a frequently applied method for revealing the microstructure of the castings and forgings [7, 14–17]. The suitability of this preparation technique for additively manufactured titanium components is assessed in this work and the optimization of the metallographic preparation along the process chain, from the powdery raw material to the additively manufactured component, is outlined taking the example of the two-phase alloy Ti-6Al-4V.

## 2. Experimental Procedure

The metallographic preparation was carried out on additively manufactured components made of gas-atomized titanium alloy powder Ti-6Al-4V, grade 23 ELI (Extra Low Interstitials). For comparison purposes, the powder's particle size determination was performed applying two different methods. In addition to dry screening with mesh widths of 100, 63, 40, and 25  $\mu\text{m}$ , a Sympatec HELOS laser diffraction spectrometer was used to determine the grain size. The chemical composition of the powder was determined by atomic emission spectroscopy for the elements Al (6.27 m.%), V (3.9 m.%), and Fe (0.2 m.%), and by carrier gas hot extraction for the ele-

bearbeitungsschritt, dem Postprocessing, unterzogen [12]. Das Postprocessing, wie z. B. heiß-isostatisches Pressen (engl.: Hot Isostatic Pressing, HIP), kann darüber hinaus Veränderungen der Mikrostruktur innerhalb des Bauteils oder in den randnahen Schichten hervorrufen [13]. Um die Effektivität und Effizienz des additiven Fertigungsprozesses bzw. des Postprocessings zu analysieren, ist es daher unabdingbar, bei der metallographischen Präparation im Zuge der Materialcharakterisierung auf die Prozess-Mikrostrukturbeziehungen einzugehen.

In der Regel werden Bauteile aus Titanlegierungen über einen mehrstufigen Schleif- und Polierprozess präpariert und in weiterer Folge direkt untersucht oder geätzt. Die Ätzung nach Kroll ist dabei eine häufig angewandte Methode, um die Mikrostruktur der Guss- und Schmiedeteile zu visualisieren [7, 14–17]. Die Eignung dieser Präparationstechnik für additiv gefertigte Titanbauteile wird in dieser Arbeit beleuchtet. So wird am Beispiel der zweiphasigen Ti-6Al-4V-Legierung die Optimierung der metallographischen Präparation entlang der Prozesskette, beginnend vom pulverförmigen Ausgangsprodukt bis zum additiv gefertigten Bauteil, gezeigt.

## 2. Experimentelles

Die metallographische Präparation erfolgte an additiv gefertigten Bauteilen, hergestellt aus gasverdüstertem Pulver der Titanlegierung Ti-6Al-4V Grade 23 ELI (engl.: Extra Low Interstitials). Die Partikelgrößenbestimmung des Pulvers erfolgte aus Vergleichszwecken mittels zweier unterschiedlicher Verfahren. Zusätzlich zu einer Trockensiebanalyse mit den Maschenweiten 100, 63, 40 und 25  $\mu\text{m}$  wurde ein HELOS Laserbeugungsspektrometer der Fa. Sympatec GmbH zur Korngrößenbestimmung eingesetzt. Die Bestimmung der chemischen Zusammensetzung des Pulvers erfolgte mittels Atomemissionspektroskopie für die Elemente Al (6,27 m.%), V (3,9 m.%) und Fe (0,2 m.%) bzw. einer Trägergas-Heiß-

ments O (0.083 m.%) and N (0.0205 m.%), respectively. To characterize the powder, the powder flowability was determined by measuring the flow rate (ASTM B964 [18]) using a Carney funnel, while the powder bulk density was measured according to ASTM B212 [19] using a Hall flow meter. The sphericity measurements were carried out using a Retsch Technology particle size analyzer CAMSIZER XT.

The samples for the test series were manufactured on an EOS machine of the type M290. SLM manufactured density cubes with the dimensions  $22 \times 22 \times 25 \text{ mm}^3$  were manufactured for the characterization of the microstructure. Not just the as-built condition, i. e. the condition immediately subsequent to the manufacturing process, but also a heat-treated variant was analyzed. The heat treatment was performed by applying temperatures ranging from  $800 \text{ }^\circ\text{C}$  to  $850 \text{ }^\circ\text{C}$  for 1–3 hours in Ar atmosphere. Due to non-disclosure agreements, the exact parameters of the heat treatment must not be specified. The samples were cut in a cutting machine ATM Brillant 221 using a resin-bonded, abrasive diamond cut-off wheel of the type BOD13 (Struers). It should be noted here that more detailed information about the preparation methods and parameters can be found in the next chapter. Subsequent to the cutting process, the sample material was embedded using the Struers hot mounting press CitoPress-20. For the sample mounting process, we had the bakelite-based mounting resin PolyFast (Struers) and the Cu-based mounting compound ProbeMet (Buehler) at our disposal. Grinding and polishing of the mounted samples were performed on a semi-automatic grinding and polishing machine Struers Tegramin-30. The vibratory polishing machine VibroMet-2 was used in combination with a chemically resistant polishing cloth of the type MicroCloth (Buehler) for further polishing. Electrolytic polishing and etching steps were performed on a

extraktion für die Elemente O (0,083 m.%) und N (0,0205 m.%). Im Zuge der Pulvercharakterisierung wurde die Pulver-Fließfähigkeit mittels Messung der Durchflussrate (ASTM B964 [18]) unter Verwendung eines Carney-Trichters bestimmt und die Pulver-Schüttdichte nach ASTM B212 [19] mit einem Hall-Flussmesser gemessen. Die Sphärizitätsmessungen erfolgten an einem Partikelmessgerät CAMSIZER XT der Fa. Retsch Technology GmbH.

Die Fertigung der Proben für die Versuchsreihe wurden an einer EOS-Maschine des Typs M290 vollzogen. Für die Mikrostrukturcharakterisierung wurden SLM gefertigte Dichtewürfel mit den Maßen  $22 \times 22 \times 25 \text{ mm}^3$  hergestellt. Neben dem as-built Zustand, d.h. direkt nach dem Fertigungsprozess, wurde auch eine wärmebehandelte Variante analysiert. Die Wärmebehandlung erfolgte in einem Temperaturbereich von  $800 \text{ }^\circ\text{C}$  –  $850 \text{ }^\circ\text{C}$  für 1–3 Stunden unter Ar-Atmosphäre. Die exakten Parameter der Wärmebehandlung dürfen aufgrund von Vertraulichkeitsvereinbarungen nicht angegeben werden. Der Zuschnitt der Proben erfolgte an einer Trennmaschine ATM Brillant 221 unter Verwendung einer harzgebundenen, abrasiv wirkenden Diamant-trennscheibe des Typs BOD13 der Fa. Struers. An dieser Stelle sei angemerkt, dass detaillierte Informationen der Präparationsmethoden und Parameter im nächsten Kapitel zu finden sind. Das Probenmaterial wurde im Anschluss an den Trennvorgang mit der Warmeinbettpresse CitoPress-20 der Fa. Struers eingefasst. Als Einbettmittel standen die kunststoffbasierte Variante Polyfast der Fa. Struers und die Cu-basierte Variante ProbeMet der Fa. Buehler zur Verfügung. Die Schleif- und Polierschritte der eingebetteten Proben erfolgte an einem semiautomatischen Schleif- und Polierautomat Tegramin-30 der Fa. Struers. Für weiteres Polieren wurde das Vibrationspoliergerät VibroMet-2 mit einem chemisch beständigen Poliertuch des Typs MicroCloth der Fa. Buehler verwendet. Die elektrolytischen Polier- sowie Ätzschritte erfolgten an einem Gerät vom Typ LectroPol-5 der Fa. Struers unter Verwendung der in Tab. 1 angeführten Elektrolyte. Des Weiteren sind im unteren Teil der Tabelle

Struers LectroPol-5 machine using the electrolytes listed in Tab. 1. The lower part of the table also lists the etchants used to reveal the macro and microstructure. The present phases were also analyzed in X-ray diffraction experiments (XRD). For this purpose, a Bruker D8 Advance diffractometer was used in Bragg-Brentano geometry with a parallel beam configuration applying Cu-K<sub>α</sub> radiation ( $\lambda=1.54 \text{ \AA}$ ). The diffractograms were acquired using a Sol-X detector applying the following measurement parameters: step size of  $0.02^\circ$ , measuring time of 2 s.

The light microscope examinations were performed on a Zeiss AXIO Imager.M2 light microscope (LM) equipped with an AxioCam HRc.5 camera. A Versa 3D Dual Beam type FEI scanning electron microscope (SEM) with a field emission cathode and a

auch die verwendeten Ätzmittel zur Darstellung der Makro- bzw. Mikrostruktur aufgelistet. Die Analyse der vorliegenden Phasen wurden auch mittels Röntgenbeugungsexperimente (engl.: X-Ray Diffraction, XRD) vorgenommen. Hierzu wurde ein Diffraktometer des Typs D8 Advance der Fa. Bruker in Bragg-Brentano-Anordnung und Parallelstrahl-Konfiguration eingesetzt, wobei mit Cu-K<sub>α</sub>-Strahlung ( $\lambda=1,54 \text{ \AA}$ ) gearbeitet wurde. Die Diffraktogramme wurden mit einem Sol-X Detektor aufgenommen, wobei als Messparameter eine Schrittweite von  $0,02^\circ$  und eine Messzeit von 2 s eingestellt wurden.

Die lichtmikroskopischen Untersuchungen wurden am Lichtmikroskop (LM) des Typs AXIO Imager.M2, ausgestattet mit einer AxioCam-HRc.5 Kamera der Fa. Zeiss, durchgeführt. Für hochauflösende Untersuchungen wurde ein Rasterelektronenmikroskop (REM) vom Typ

Name	Composition / Zusammensetzung
Electrolyte A3 (Struers) / Elektrolyt A3 der Fa. Struers	Mixture of methanol CH <sub>3</sub> OH and 2-butoxyethanol / Gemisch aus Methanol CH <sub>3</sub> OH und 2-Butoxy-Ethanol
Electrolyte Ti Em3 / Elektrolyt Ti Em3	35 ml distilled water, 60 ml methanol CH <sub>3</sub> OH-99.8%, 10 ml lactic acid C <sub>3</sub> H <sub>6</sub> O <sub>3</sub> -32%, 5 ml phosphoric acid H <sub>3</sub> PO <sub>4</sub> -85%, 5 g citric acid C <sub>6</sub> H <sub>8</sub> O <sub>7</sub> , and 5 g oxalic acid C <sub>2</sub> H <sub>2</sub> O <sub>4</sub> [31] / 35 ml destilliertes Wasser, 60 ml Methanol CH <sub>3</sub> OH-99,8%, 10 ml Milchsäure C <sub>3</sub> H <sub>6</sub> O <sub>3</sub> -32%, 5 ml Phosphorsäure H <sub>3</sub> PO <sub>4</sub> -85%, 5 g Zitronensäure C <sub>6</sub> H <sub>8</sub> O <sub>7</sub> und 5 g Oxalsäure C <sub>2</sub> H <sub>2</sub> O <sub>4</sub> [31]
Wet etching according to Kroll / Nassätzung nach Kroll	100 ml distilled water, 2–6 ml nitric acid HNO <sub>3</sub> -65%, and 1–3 ml hydrofluoric acid HF-40% [31] / 100 ml destilliertes Wasser, 2–6 ml Salpetersäure HNO <sub>3</sub> -65% und 1–3 ml Flusssäure HF-40% [31]
Wet etching according to Weck / Nassätzung nach Weck	100 ml distilled water, 50 ml ethanol C <sub>2</sub> H <sub>5</sub> OH-50%, 2 g ammonium bifluoride NH <sub>4</sub> HF <sub>2</sub> [31] / 100 ml destilliertes Wasser, 2–6 ml Salpetersäure HNO <sub>3</sub> -65% und 1–3 ml Flusssäure HF-40% [31]
Thermal etching according to Barnes / Thermische Ätzung nach Barnes	30 and 120 min heat treatment at 540 °C, respectively [29] / Wärmebehandlung bei 540 °C für 30 bzw. 120 min [29]

**Tab. 1:** List of the electrolytes used for electrolytic polishing and of etchants used to reveal the macro and microstructure.

**Tab. 1:** Auflistung der für das elektrolytische Polieren verwendeten Elektrolyte sowie die verwendeten Ätzmittel zur Sichtbarmachung der Makro- und Mikrostruktur.

secondary electron detector was used for high resolution examinations. The electron backscatter diffraction (EBSD) measurements for a determination of the crystallographic structure and the orientation of the crystalline phases were also performed on the above-mentioned FEI device using a Hikari XP EBSD camera and an EDAX EBSD detector. Data were acquired and analyzed using the EDAX software OIM Data Collection and OIM Analysis 7 based on the following EBSD measurement parameters: accelerating voltage of 20 kV, step size of 100 nm and a 4×4 binning mode of the EBSD camera.

Versa 3D Dual Beam der Fa. FEI unter Verwendung einer Feldemissionskathode und eines Sekundärelektronendetektors herangezogen. Die Elektronenrückstreubeugungs-Messungen (engl.: Electron Backscatter Diffraction, EBSD), zur Ermittlung der kristallographischen Struktur und Orientierung der kristallinen Phasen, erfolgten ebenfalls an dem zuvor erwähnten FEI-Gerät mittels einer EBSD-Kamera vom Typ Hikari XP und einem EBSD-Detektor der Fa. EDAX. Die Datenerfassung sowie -auswertung wurde mit der Software OIM Data Collection und OIM Analysis 7 der Fa. EDAX vorgenommen, wobei die Parameter der EBSD-Messung wie folgt waren: Beschleunigungsspannung 20 kV, Schrittweite 100 nm und ein 4×4 Binning Modus der EBSD-Kamera.

### 3. Results and Discussion

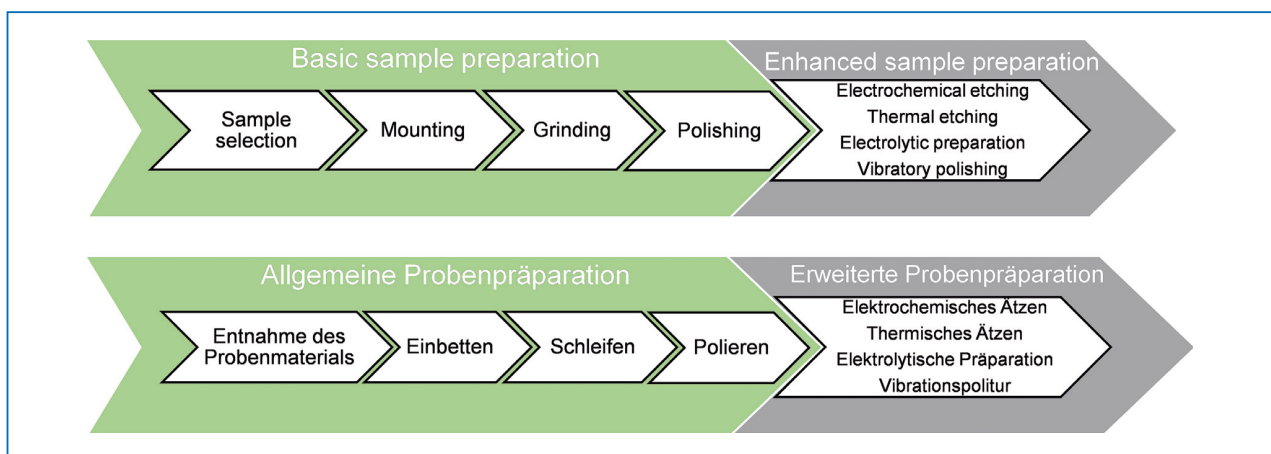
#### 3.1 Material Sampling and Mounting

Fig. 1 shows the metallographic sample preparation workflow. In a first step, the sample material is taken. First, the powder is sampled. It should preferably be taken at several container positions. It is thus ensured that no individual powder fractions of a particular particle size are preferably examined, such as due to segregations.

### 3. Ergebnisse und Diskussion

#### 3.1 Entnahme des Probenmaterials und Einbetten

In Bild 1 ist der Verlauf der metallographischen Probenpräparation dargestellt. Der erste Schritt dabei ist die Entnahme des Probenmaterials. Beginnend beim Pulver sollte die Entnahme an mehreren Stellen des Behälters erfolgen. Hierdurch wird vermieden, dass bezüglich der Partikelgröße, z. B. aufgrund von Entmischungen, einzelne Pulverfraktionen bevorzugt untersucht werden.



**Fig. 1:** Metallographic sample preparation workflow.

**Bild 1:** Verlauf der metallographischen Probenpräparation.

Subsequent to the powder sampling process, the particles are characterized. For this purpose, particle size distribution, morphology, sphericity, flow rate, and bulk density are determined. In the diagram in Fig. 2, the cumulative powder particle distribution is plotted against the particle size. As is apparent from the diagram, there is a significant difference between the particle size distribution determined by laser diffraction and the distribution determined by sieve analysis. It should be taken into consideration that the sieve analysis was performed with a limited number of mesh sizes. As compared to the distribution obtained by laser diffraction-based particle sizing which allows for a finer gradation, this limited number of mesh sizes as well as sieve clogging by fine particles therefore resulted in a coarser distribution and over-estimated d values ( $d_{10}$ ,  $d_{50}$ ,  $d_{90}$ ). Due to the mentioned problem, dry sieving should therefore be dispensed with for an examination of particles with a diameter of  $< 40 \mu\text{m}$ .

Fig. 3a) shows the powder particle morphology in a secondary electron SEM image. The SEM images reveal that the particles have a smaller fraction of satellites and

Im Anschluss an die Pulverentnahme erfolgt die Partikelcharakterisierung. Dazu werden Partikelgrößenverteilung, Morphologie, Sphärizität, Fließrate und Schüttdichte ermittelt. In dem in Bild 2 gezeigten Diagramm ist die Verteilungssumme der Pulverpartikel über der Partikelgröße aufgetragen. Es ist ersichtlich, dass ein deutlicher Unterschied zwischen der mit Laserdiffraktion und der mit Siebanalyse ermittelten Partikelgrößenverteilung gegeben ist. Zu beachten ist, dass die Siebanalyse mit einer limitierten Anzahl an Maschenweiten erfolgte. Diese limitierte Anzahl an Maschenweiten sowie das Verkleben der Siebe durch feine Partikel führten dazu, dass die Partikelgrößenverteilung im Vergleich zur Laserdiffraktion, bei der eine feinere Abstufung möglich ist, entsprechend gröber war und die ermittelten d-Werte ( $d_{10}$ ,  $d_{50}$ ,  $d_{90}$ ) überschätzt werden. Wegen der erwähnten Problematik sollte deshalb bei der Untersuchung von Partikel mit Durchmessern  $< 40 \mu\text{m}$  davon abgesehen werden eine Trockensiebung durchzuführen.

Die Partikelmorphologie des Pulvers ist in Bild 3a) durch eine REM-Aufnahme im Sekundärelektronen-Modus dargestellt. Anhand der REM-Aufnahmen ist ersichtlich, dass die Par-

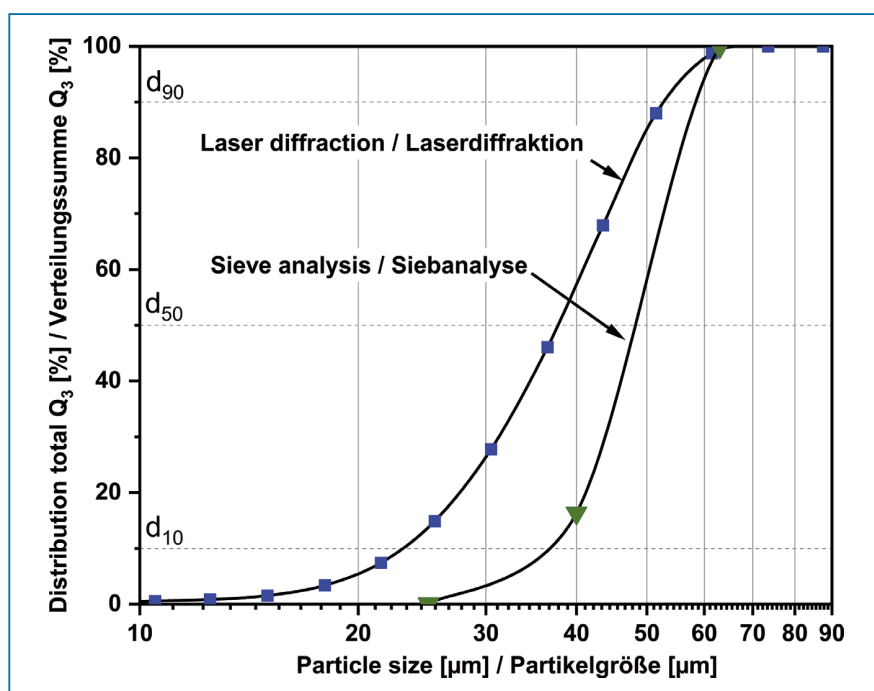


**Fig. 2:** Powder particle distribution results using two different analysis methods. The blue data points show the particle size distribution determined by laser diffraction. The green data points on a thin line illustrate the result of dry sieving (see text).

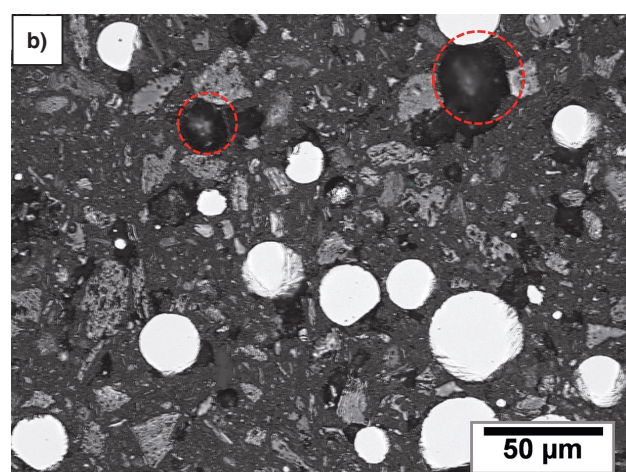
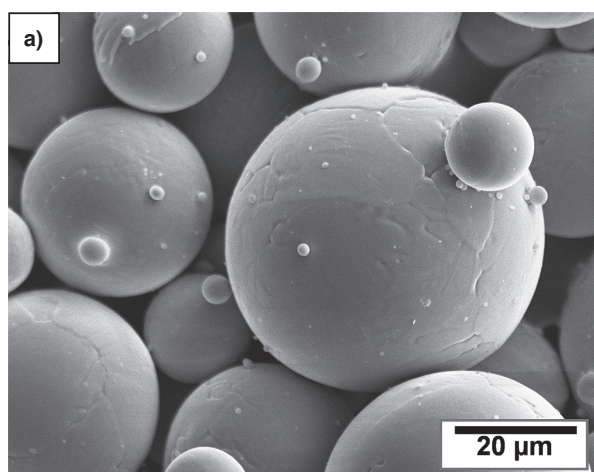
**Bild 2:** Ergebnis der Pulverpartikelverteilung mit zwei unterschiedlichen Analyseverfahren. Die blauen Datenpunkte zeigen die mittels Laserdiffraktion bestimmte Partikelgrößenverteilung. Die grünen Datenpunkte, verbunden mit einer dünnen Linie, stellen das Ergebnis aus der Trockensiebung dar (siehe Text).

are very spherical which is reflected by a high sphericity value (0.95) according to ISO 9276 [20]. The bulk density of the powder is  $2.49 \text{ g/cm}^3$ . It thus amounts to 56% of the theoretical density of Ti-6Al-4V [21]. The Carney flow rate of the powder according to ASTM B964 [18] is 6.4 s/50 g.

A metallographic section of the powder has to be prepared for the purpose of examining any existing gas pores within the powder particles and for the structural analysis. As is apparent from Fig. 3b), individual powder particles may be removed during the metal powder mounting process (marked in red). To avoid this, it is recommended to either mix the metal powder particles with a sieved fine fraction ( $< 25 \mu\text{m}$ ) of the mounting medium before mounting or to use a very fine mounting material with a low grain size. The use of a fine mounting material allows for reducing the fraction of removed powder particles.

tikel einen geringen Satellitenanteil aufweisen und sphärisch sind, was sich in einem hohen Sphäritätswert (0,95) nach ISO 9276 [20] widerspiegelt. Die Schüttdichte des Pulvers beträgt  $2,49 \text{ g/cm}^3$  und liegt somit bei 56% der theoretischen Dichte von Ti-6Al-4V [21]. Die Carney-Durchflussrate des Pulvers nach ASTM B964 [18] beträgt 6,4 s/50 g.

Für die Untersuchung von eventuell vorliegenden Gasporen im Inneren der Pulverpartikel sowie der Gefügeanalyse ist es nötig einen metallographischen Schliff des Pulvers anzufertigen. Wie in Bild 3b) gezeigt, kann es beim Einbetten des metallischen Pulvers zur Herauslösung einzelner Pulverpartikel kommen (in Rot markiert). Um dies zu vermeiden, ist es empfehlenswert, entweder das einzubettende Metallpulver vor dem Einfassvorgang mit einem gesiebten Feinanteil ( $< 25 \mu\text{m}$ ) des Einbettmittels zu mischen oder ein sehr feines Einbettmittel mit einer geringen Korngröße zu verwenden. Durch die Verwendung eines feinen Einbettmittels kann der Anteil an herausgelösten Pulverpartikeln deutlich reduziert werden.



**Figs. 3a and b:** a) The SEM image (secondary electron mode) of the Ti-6Al-4V powder's particle morphology is characterized by very spherical shapes with a small proportion of satellites; b) LM image of the powder section, embedded in the bakelite-based mounting resin PolyFast. The dashed red circles mark positions where powder particles have been removed.

**Bilder 3a und b:** a) Die REM-Aufnahme (Sekundärelektronen-Modus) der Partikelmorphologie des Ti-6Al-4V Pulvers zeigt eine sphärische Form mit einem geringen Anteil an Satelliten; b) LM-Aufnahme des Pulverschliffs, eingebettet in das kunststoffbasierte Einbettmittel Polyfast. Die rot strichlierten Kreise markieren die Positionen, aus denen sich Pulverteilchen herausgelöst haben.

The solid material samples are taken by sample cutting with the aid of abrasive cut-off wheels. They offer the advantage of being able to cut a wide range of materials and furthermore ensure a good surface quality after the cutting process [16]. However, in case of insufficient cooling or when the feed rate of the cut-off wheel is too high, the material may overheat. Such sample damages may lead to a misinterpretation of the microstructures and, once they have occurred, it is rather complicated to remove them. Sufficient cooling and the appropriate feed rate should therefore be ensured during the cut-off process. At a feed rate of 1 mm/min, it is appropriate to maintain a rotational speed of the cut-off wheel of 2500–3600 min<sup>-1</sup>. The used coolant should be composed of water, lubricant, and an anticorrosive agent additive. The additively manufactured solid material samples were either mounted in a bakelite mounting resin or a Cu-based mounting compound. The difference in hardness between the sample and the mounting medium is smaller using the Cu-based ProbeMet compound, thus allowing an enhanced mechanical preparation, including the surface layers. The examination of the surface and the surface layer is particularly important when analyzing additively manufactured components. During the electron microscope examination, the good electrical conductivity of copper additionally ensures a high and stable flow of secondary electrons (and thus a good contrast). However, longer curing times and higher acquisition costs are the drawbacks of this mounting material. For this work, the Cu-based mounting compound ProbeMet was used for SEM examinations. For all other examinations, the bakelite-based mounting resin was used. The sections were manufactured applying the following mounting press settings:

Die Entnahme der Vollmaterialproben erfolgt über einen Probenzuschnitt durch abrasiv wirkende Schneidscheiben. Diese bieten den Vorteil ein breites Spektrum an Werkstoffen trennen zu können und darüber hinaus eine gute Oberflächenqualität nach dem Trennprozess zu gewährleisten [16]. Bei unzureichender Kühlung oder durch einen zu hohen Vorschub der Trennscheibe kann es jedoch zum Überhitzen des Werkstoffs kommen. Während des Schneidvorgangs sollte daher stets auf eine ausreichende Kühlung sowie die richtige Vorschubgeschwindigkeit geachtet werden, da derartige Probenschädigungen nur sehr aufwendig wieder entfernt werden können bzw. zu Fehlinterpretationen des Gefüges führen können. Bei einer Vorschubgeschwindigkeit von 1 mm/min ist es zweckmäßig eine Umdrehungsgeschwindigkeit der Trennscheibe von 2500–3600 min<sup>-1</sup> einzuhalten. Das verwendete Kühlmittel sollte eine Mischung aus Wasser, Schmiermittel und einem Korrosionsschutz in Form eines Additivs sein. Das Einbetten der additiv gefertigten Vollmaterialproben erfolgte entweder durch ein kunststoff- oder ein Cu-basiertes Einbettmittel. Bei der Verwendung des Cu-basierten ProbeMet ist der Härteunterschied zwischen Probe und Einbettmittel geringer, was eine bessere mechanische Präparation, auch im Bereich der Randschichten, ermöglicht. Gerade bei additiv gefertigten Bauteilen ist eine Oberflächen- und Randschichtuntersuchung von besonderer Bedeutung. Aufgrund der guten elektrischen Leitfähigkeit des Kupfers ist zusätzlich für einen hohen und stabilen Sekundärelektronenstrom (und damit einem guten Kontrast) im Zuge der elektronenmikroskopischen Untersuchung gesorgt. Nachteile dieses Einbettmittels sind jedoch eine höhere Aushärtezeit sowie höhere Materialkosten bei der Anschaffung. Im Zuge dieser Arbeit wurde für Untersuchungen im REM das Cu-basierte Einbettmittel ProbeMet verwendet. Für alle anderen Untersuchungen fand das kunststoffbasierte Einbettmittel seine Anwendung. Zur Herstellung der Schiffe wurden folgende Einstellungen an der Einbettpresse vorgenommen:

- Bakelite mounting resin PolyFast: 3 minute heating phase at 180 °C and 250 bar followed by 1.5 min water rinsing,
- Cu mounting compound ProbeMet: 7.5 minute heating phase at 180 °C and 300 bar followed by 4.5 min water rinsing.

### 3.2 Grinding and Polishing

Subsequent to cutting and mounting, the sample preparation workflow involves a wet grinding and polishing step. The rough and deformed zone resulting from the cut-off process is unfavorable for the analysis. It is removed by plane grinding ensuring a plane-parallel sample surface [16, 17]. Subsequently, successive fine grinding steps are performed using progressively finer grits. It should be taken into consideration here, that severe damages such as scratches, relief, break-offs, and cracks cannot be removed anymore in the following polishing steps [16, 17].

The dense, thin, and stable oxide layer on the surface with its high affinity for oxygen presents a challenge in the preparation of Ti alloys. Although it provides effective corrosion protection [22], it needs to be removed in the course of sample preparation. A chemical-mechanical polishing process is appropriate to suppress the formation of an oxide layer, especially during the last polishing steps. The formation of a surface layer is suppressed, i. e. the removal rate is increased and the formation of a cover layer is prevented by adding hydrogen peroxide  $H_2O_2$  to the colloidal silicon dioxide  $SiO_2$  polishing suspension (OPS) [16, 23]. Tab. 2 shows the parameters of the grinding and polishing steps applied based on which reproducible results and an optimal metallographic sample preparation providing excellent surface quality could be achieved. The difference in hardness between the investment material and the sample and the thus generated sample elevation may provoke an undesired rocking motion of the sample

- Kunststoffeinbettmittel Polyfast: Heizphase bei 180 °C, 250 bar für 3,0 min, gefolgt von 1,5 min Wasserspülung.
- Cu-Einbettmittel ProbeMet: Heizphase bei 180 °C, 300 bar für 7,5 min, gefolgt von 4,5 min Wasserspülung.

### 3.2 Schleifen und Polieren

Nach dem Trenn- und Einbettvorgang stellen Nassschleifen und Polieren die nächsten Schritte der Probenpräparation dar. Während des Planschleifens wird die durch den Trennvorgang entstandene, aber für die Analyse ungeeignete, Rauigkeits- und Deformationszone entfernt und eine planparallele Oberfläche der Probe erzeugt [16, 17]. Folgend werden aneinander gereihte Feinschleifschritte mit jeweils abnehmender Körnung des Schleifens durchgeführt. Es sollte dabei beachtet werden, dass schwerwiegende Schädigungen (Kratzer, Relief, Ausbrüche, Risse) in den nachfolgenden Polierschritten nicht mehr entfernt werden können [16, 17].

Eine Herausforderung bei der Präparation von Ti-Legierungen stellt aufgrund der hohen Affinität zu Sauerstoff die dichte, dünne und stabile Oxidschicht auf der Oberfläche dar. Diese Schicht ist ein effektiver Korrosionsschutz [22], muss jedoch im Rahmen der Probenpräparation abgetragen werden. Um die Bildung der Oxidschicht zu unterdrücken, ist speziell bei den letzten Polierschritten ein chemisch-mechanischer Poliervorgang zweckmäßig. Durch Zugabe von Wasserstoffperoxid  $H_2O_2$  zu der kolloidalen Siliziumdioxid  $SiO_2$  Poliersuspension (OPS) wird die Deckschichtbildung auf der Oberfläche unterdrückt, d.h. die Abtragsrate erhöht sowie eine Schmier-schichtbildung verhindert [16, 23]. Tab. 2 zeigt die angewandten Parameter der Schleif- und Polierschritte, welche zu reproduzierbaren Ergebnissen und einer optimalen metallographischen Probenpräparation mit einer hervorragenden Oberflächenqualität führten. Durch den Härteunterschied zwischen Einbettmasse und Probe sowie der dadurch entstehenden Probenüberhöhung kann es im Schleifprozess



Step / Stufe	Grinding/ polishing pad / Schleif-/Polier- auflage	Time [min] / Zeit [min]	Force per Sample [N] / Kraft pro Probe [N]	Rotational speed / Drehgeschwindigkeit		Cooling/ polishing agent / Kühl-/ Poliermittel
				Pad [rpm] / Auflage [U/min]	Sample holder [rpm] / Probenhal- ter [U/min]	
1	Diamond grinding wheel MD-Piano 220 / Diamant- schleifscheibe MD-Piano 220	03:00–04:00	40	300	150	H <sub>2</sub> O
2	SiC paper #1200 / SiC-Papier #1200	00:15–00:20	40	140	150	H <sub>2</sub> O
3	SiC paper #2000 / SiC-Papier #2000	00:15–00:20	40	140	150	H <sub>2</sub> O
4	SiC paper #2000 / SiC-Papier #2000	00:15–00:20	40	140	150	H <sub>2</sub> O
5	SiC paper #2000 / SiC-Papier #2000	00:15–00:20	40	140	150	H <sub>2</sub> O
6	Polishing cloth MD-Chem / Polier- tuch MD-Chem	up to / bis zu 08:00	40	140	150	OPS/H <sub>2</sub> O <sub>2</sub> 90 ml:15 ml

**Tab. 2:** Metallographic sample preparation parameters using the grinding and polishing machine Struers Tegramin-30 with a fixed sample holder.

**Tab. 2:** Parameter der metallographischen Probenpräparation am Schleif- und Polierautomat Tegramin-30 der Fa. Struers unter Verwendung eines fixierten Probenhalters.

during the grinding process [24]. It is particularly important to counter these rocking motions. Therefore, after the mounting process, all sample surfaces to be ground were given a chamfered edge. The sample motion can further be reduced by firmly fixing all samples in a sample holder instead of using a non-fixing sample holder with single piston force transmission. However, it should be taken into consideration here, that, owing to the fact that an uneven force application can occur induced by the central contact pressure, at least three samples are prepared simultaneously when using a fixing sample holder. In the course of the preparation optimization process, the removal of scratches was also analyzed with regard to the rotational motion of the sample holder relative to

zu einer unerwünschten Wippbewegung der Probe kommen [24]. Da es von besonderer Bedeutung ist diesen Wippbewegungen entgegenzuwirken, wurden alle Proben nach dem Einbettprozess an der Schleiffläche mit einer Randfase versehen. Eine weitere Reduktion der Probenbewegung ist möglich, indem anstelle eines nicht fixierenden Probenhalters mit Kraftübertragung über Einzelkolben, alle Proben in einem Probenhalter fest eingespannt werden. Es sollte aber dabei beachtet werden, dass durch Verwendung eines fixierenden Probenhalters mindestens drei Proben gleichzeitig präpariert werden, da es aufgrund des Zentralandruckes zu einer ungleichmäßigen Kraftauftragung kommen kann. Im Zuge der Präparationsoptimierung wurde auch die Kratzerentfernung im Hinblick auf die Relativedreh-

the grinding and polishing pad. It was found that the deformation zone was smaller when sample holder and working disk work in synchronization than when they are configured in counter rotation. Synchronism of the sample and the working disk reduces the relative speed and simultaneously suppresses rocking motions of the sections.

As is shown in Tab. 2, the plastic bonded diamond grinding wheel MD-Piano 220 (Struers) was used in preparation step 1 to provide plane-parallelism and to ensure the flatness of the section's surface. As this procedure may take up to 4 minutes, it is advantageous to use a manually resharpenable grinding wheel. It ensures a consistent removal rate and causes less wear as compared to SiC paper. When using SiC paper, the material removal rate is significantly reduced within a very short time. Therefore, the grinding time was limited to 15 to 20 seconds for the preparation steps 2 to 5, respectively. The last preparation step, step 6, is an OPS polishing process. For this procedure, a mixture of OPS and  $H_2O_2$  with a ratio of 90 ml OPS:15 ml  $H_2O_2$  is applied to a chemically resistant polishing cloth (Struers). It may take up to 8 minutes to remove the deformation zone of step 5 by OPS polishing.

It is equally important to perform intermediate sample cleaning after each preparation step. This ensures that no particles dislodged from the roughness and deformation zone are transferred to the next preparation step and, as a result, damage the surface. The sample cleaning processes during the preparation were carried out by thoroughly washing the sample holder and the clamped samples with soap. Once the preparation steps are completed, it is appropriate to remove the metallographic samples from the sample holder in order to clean them in an ultrasonic bath, for instance in ethanol solution, for several minutes. Subsequent to the ultrasonic bath, highly volatile substances

bewegung des Probenhalters zur Schleif- und Polieraufgabe untersucht. Es zeigte sich, dass durch Gleichlauf von Probenhalter und Arbeitsscheibe die Verformungszone geringer war als bei einer Schaltung im Gegenlauf. Durch den Gleichlauf von Probe und Arbeitsscheibe wird die Relativgeschwindigkeit reduziert und auch Wippbewegungen der Schlitze unterdrückt.

Wie in Tab. 2 dargestellt, wurde im Präparationsschritt 1 die kunststoffgebundene Diamantschleifscheibe MD-Piano 220 der Fa. Struers verwendet, um eine Planparallelität herzustellen und die Ebenheit der Schlitsoberfläche zu gewährleisten. Da dieser Vorgang bis zu 4 Minuten dauern kann, ist der Einsatz einer manuell nachschärfbaren Diamantschleifscheibe von Vorteil. Diese sorgt für eine gleichbleibende Abtragsleistung bei einem geringeren Verschleiß im Vergleich zu SiC-Papier. Da der Materialabtrag bei Verwendung eines SiC-Papiers innerhalb kürzester Zeit signifikant abnimmt, wurde bei den Präparationsschritten 2 bis 5 die Zeit auf 15 bis 20 Sekunden begrenzt. Im letzten Präparationsschritt 6 erfolgte die Politur mittels OPS. In diesem Schritt wird ein OPS- $H_2O_2$ -Gemisch im Verhältnis 90 ml-OPS:15 ml- $H_2O_2$  auf ein chemisch beständiges Poliertuch der Fa. Struers aufgebracht. Die Entfernung der Deformationszone aus Stufe 5 mit Hilfe der OPS-Politur kann bis zu 8 Minuten dauern.

Von besonderer Bedeutung ist darüber hinaus die Zwischenreinigung der Probe nach jedem Präparationsschritt. Durch diese wird vermieden, dass herausgelöste Partikel aus der Rauigkeits- und Deformationszone in den nächsten Präparationsschritt übertragen werden und so die Oberfläche schädigen. Die Probenreinigung während den Präparationsschritten wurde durch ein gründliches seifenbasiertes Waschen des Probenhalters und der eingespannten Proben sichergestellt. Am Ende der Präparationsschritte ist es sinnvoll die metallographischen Schlitze aus dem Probenhalter zu entfernen und in einem Ultraschallbad, z. B. in einer Ethanolösung, für wenige Minuten zu reinigen. Des Weiteren wird nach dem Ultraschallbad

such as isopropyl or petroleum ether are furthermore applied to avoid the formation of drying artifacts on the final, glassy surface.

### Microstructural Examination by Light Microscopy

In the SLM process, powder layers are selectively heated and molten. Once the molten pool is solidified, further cooling results in  $\alpha$  lamellae growth at the  $\beta$  grain boundaries from the moment of reaching the  $\beta$ -transus temperature. Given sufficient undercooling, a diffusion-less martensitic transformation to acicular  $\alpha'$  martensite takes place induced by Umklapp processes once the temperature falls below the martensite start temperature. Moreover, the repeated thermal cycles of the AM process lead to an epitaxial growth of the  $\beta$  grains induced by the steep temperature gradient in the molten pool and the resulting lower nucleation rate, as is described in [6]. The aforementioned microstructure formation can be evidenced after the basic sample preparation. The crystallographic orientations of the material can be revealed as early as after preparation step 6 by using a polarization filter in the LM without recourse to specific surface-modifying methods such as for selective etching. Fig. 4a) is a LM image of an additively manufactured Ti-6Al-4V sample in the as-built condition using a polarization filter combined with increased light intensity. Not only the acicular  $\alpha'$  martensite structure, but also the former  $\beta$  grain boundaries can be recognized (dashed lines). It is apparent that the columnar  $\beta$  grains extend over several hundred micrometers in the build direction, BD.

### Pore Analysis

Fig. 4b) presents a LM image of the surface of an as-built sample prepared for the pore

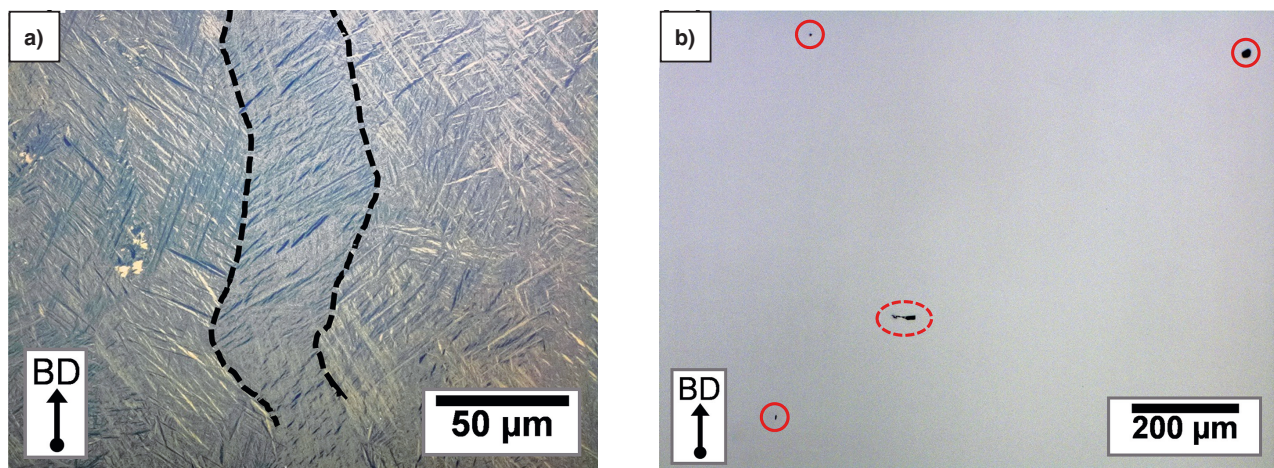
durch Aufbringung von hochflüchtigen Substanzen, wie z. B. Isopropanol oder Petrolether, verhindert, dass sich Trocknungsartefakte auf der finalen, spiegelglatten Oberfläche bilden.

### Mikrostrukturuntersuchung mittels Lichtmikroskopie

Durch den SLM-Herstellungsprozess werden Pulverschichten selektiv erwärmt und aufgeschmolzen. Nach der Erstarrung des Schmelzbades beginnen bei weiterer Abkühlung ab Erreichen der  $\beta$ -Transustemperatur an den  $\beta$ -Korngrenzen  $\alpha$ -Lamellen zu wachsen. Bei ausreichender Unterkühlung kommt es nach Unterschreiten der Martensit-Start-Temperatur durch Umklappprozesse zu einer diffusionslosen martensitischen Umwandlung in nadeligen  $\alpha'$ -Martensit. Die wiederholten thermischen Zyklen des AM Prozesses führen darüber hinaus zu einem epitaktischen Wachstum der  $\beta$ -Körner, welches durch den steilen Temperaturgradient im Schmelzbad und der daraus resultierenden geringen Keimbildungsrate hervorgerufen wird, wie es in [6] beschrieben ist. Der Nachweis der soeben beschriebenen Gefügeentstehung ist bereits nach der allgemeinen Probenpräparation möglich. Ohne Anwendung von speziellen oberflächenverändernden Methoden, wie z. B. für eine selektive Ätzung, können bereits nach Präparationsschritt 6 durch den Einsatz eines Polarisationsfilters im LM die kristallographischen Orientierungen des Materials sichtbar gemacht werden. Bild 4a) zeigt eine LM-Aufnahme einer additiv gefertigten Ti-6Al-4V-Probe im as-built Zustand unter Verwendung eines Polarisationsfilters in Kombination mit einer erhöhten Lichtstärke. Neben der nadeligen  $\alpha'$ -Martensitstruktur sind auch die ehemaligen  $\beta$ -Korngrenzen anhand der gestrichelten Linien erkennbar. Es ist ersichtlich, dass sich die columnaren  $\beta$ -Körner über mehrere hundert Mikrometer in Baurichtung (engl.: Build direction, BD) erstrecken.

### Porenanalyse

Bild 4b) zeigt eine für die Porenanalyse präparierte Aufnahme der Oberfläche einer as-built



**Figs. 4 a and b:** a) Light microscope image of the martensitic microstructure of an additively manufactured Ti-6Al-4V sample in the as-built condition using a polarization filter. The dashed lines mark the epitaxial growth of a  $\beta$  grain in the build direction (BD) of the SLM process; b) light microscope BF image of the sample surface used to determine the porosity. The circles with solid lines mark gas pores, while the dashed ellipse indicates a lack of fusion defect.

**Bilder 4 a und b:** a) Lichtmikroskopische Aufnahme der martensitischen Mikrostruktur einer additiv gefertigten Ti 6Al 4V-Probe im as-built Zustand unter Verwendung eines Polarisationsfilters. Die gestrichelten Linien markieren das epitaktische Wachstum eines  $\beta$  Korns in Baurichtung BD des SLM Prozesses; b) Lichtmikroskopische HF-Aufnahme der Probenoberfläche zur Bestimmung der Porosität. Die durchgehenden Kreise markieren Gasporen, die gestrichelte Ellipse zeigt einen Anbindefehler.

analysis at a magnification of  $200\times$ . Not only gas pores (continuous red circles), but also a lack of fusion defect (dashed red ellipse) could be detected in this sample during the 2D pore analysis. It is important to make sure the section's surface is dust-free, especially when determining the porosity in AM manufactured samples of a very high density ( $> 99.95\%$ ), as otherwise the result may be distorted. In addition to that, a preferably large part of the surface should be considered and evaluated in order to ensure a statistically relevant result. The magnification for the LM images should not be less than  $200\times$  to ensure that smaller pores can be detected. The porosity was evaluated by phase fraction analysis using the software Olympus Stream Motion 1.9.3. The pores must additionally be manually sorted as a function of the surface area, and smaller pores ( $< 5 \mu\text{m}^2$ ) must be removed to avoid that pixels appearing dark are erroneously assigned to the pore fraction. By adhering to the mentioned process steps, a very precise

Probe im LM unter 200-facher Vergrößerung. Im Rahmen der 2D-Porenanalyse konnten bei dieser Probe neben Gasporen (durchgehende rote Kreise) auch Anbindefehler (gestrichelte rote Ellipse) detektiert werden. Speziell bei der Bestimmung des Porenanteils von AM gefertigten Proben, welche eine sehr hohe Dichte ( $> 99,95\%$ ) aufweisen, muss auf eine staubfreie Schliifffläche geachtet werden, da sonst das Ergebnis verfälscht werden kann. Des Weiteren sollte ein möglichst großer Anteil der Oberfläche erfasst und ausgewertet werden, um ein statistisch relevantes Ergebnis sicherzustellen. Die Vergrößerung bei den LM-Aufnahmen sollte nicht kleiner als 200 sein, um auch kleinere Poren detektieren zu können. Die Auswertung des Porenanteils erfolgte mittels Phasenanteilsanalyse der Software Olympus Stream Motion 1.9.3. Bei der Auswertung ist es überdies erforderlich, eine manuelle Sortierung von Poren als Funktion der Fläche durchzuführen und kleine Poren ( $< 5 \mu\text{m}^2$ ) zu entfernen, um zu verhindern, dass dunkel erscheinende Pixel fälschlicherweise den Poren-

and reproducible porosity can be represented. In this work, a surface area of at least 100 mm<sup>2</sup> covering different positions of the section represented in different images was accounted for during the pore analysis. For this purpose, a section from the center of the component was taken for examination. Care should be taken that the examined site is not located too near the component's edge, as, due to the high roughness in the edge areas, a non-representative porosity may be accounted for. A porosity of 0.028 vol.% was measured for the as-built sample shown in Fig. 4b). By comparison, the heat-treated variant has an even lower porosity of 0.008 vol.%, i. e. the sample is virtually completely dense.

### Phase Analysis

One of the methods used to determine the phases and phase fractions, is the X-ray diffraction examination. As it is a surface sensitive method, a deformed sample surface may lead to distorted measurement results and thus to misinterpretations. Turk et al. [25] showed that preparation-related residual compressive stresses induced by the grinding and polishing processes result in shifted and broadened XRD peaks. It is thus indispensable to ensure a deformation-free plane surface.

Fig. 5 shows an extract of XRD measurements performed on laser melted samples and on the powder sample. The solid material samples were treated following the preparation method presented in Tab. 2, removed from the mounting material, and analyzed. The powder samples were poured on a monocrystalline Si wafer plate for their examination and, as opposed to the solid material samples, the measurement was carried out without sample rotation.

anteil zugerechnet werden. Bei Beachtung der erwähnten Verfahrensschritte ist es möglich, einen genauen und reproduzierbaren Porenanteil wiederzugeben. Im Zuge dieser Arbeit wurde durch mehrere Aufnahmen von unterschiedlichen Stellen des Schliffes, eine Fläche von mindestens 100 mm<sup>2</sup> für die Porenanalyse erfasst. Es wurde dazu ein Schliff aus der Bauteilmitte für die Untersuchung herangezogen. Es ist zu beachten, dass die untersuchte Stelle nicht zu nahe am Bauteilrand liegt, da es aufgrund der hohen Rauigkeit an den Randbereichen zu einem nicht repräsentativen Porenanteil kommen kann. Bei der in Bild 4b) gezeigten as-built Probe wurde ein Porenanteil von 0,028 vol.% gemessen. Im Vergleich dazu weist die wärmebehandelte Variante einen noch geringeren Porenanteil von 0,008 vol.% auf, d. h. eine nahezu vollständig dichte Probe liegt vor.

### Phasenanalyse

Die Röntgenbeugungsuntersuchung ist eine Untersuchungsmethode, welche z. B. zur Bestimmung von auftretenden Phasen und Phasenanteilen eingesetzt wird. Da es sich hierbei um eine oberflächensensitive Methode handelt, kann eine verformte Probenoberfläche zu einer Verfälschung der Messergebnisse und somit zu einer Fehlinterpretation führen. Turk et al. [25] zeigte, dass präparationsbedingte Druckeigenspannungen, hervorgerufen durch den Schleif- und Polierprozess, zu einer Verschiebung und Verbreiterung der XRD-Peaks führen, wodurch unbedingt darauf geachtet werden muss, dass die Oberfläche verformungsfrei und plan ist.

In Bild 5 ist der Auszug aus XRD-Messungen an lasergeschmolzenen Proben sowie an der Pulverprobe dargestellt. Die Vollmaterialproben wurden nach der in Tab. 2 angegebenen Präparationsmethode behandelt und im ausgebetteten Zustand analysiert. Die Pulverproben wurden für die Untersuchung auf eine einkristalline Si-Waferplatte aufgeschüttet und die Messung erfolgte im Gegensatz zu den Vollmaterialproben ohne Probenrotation.

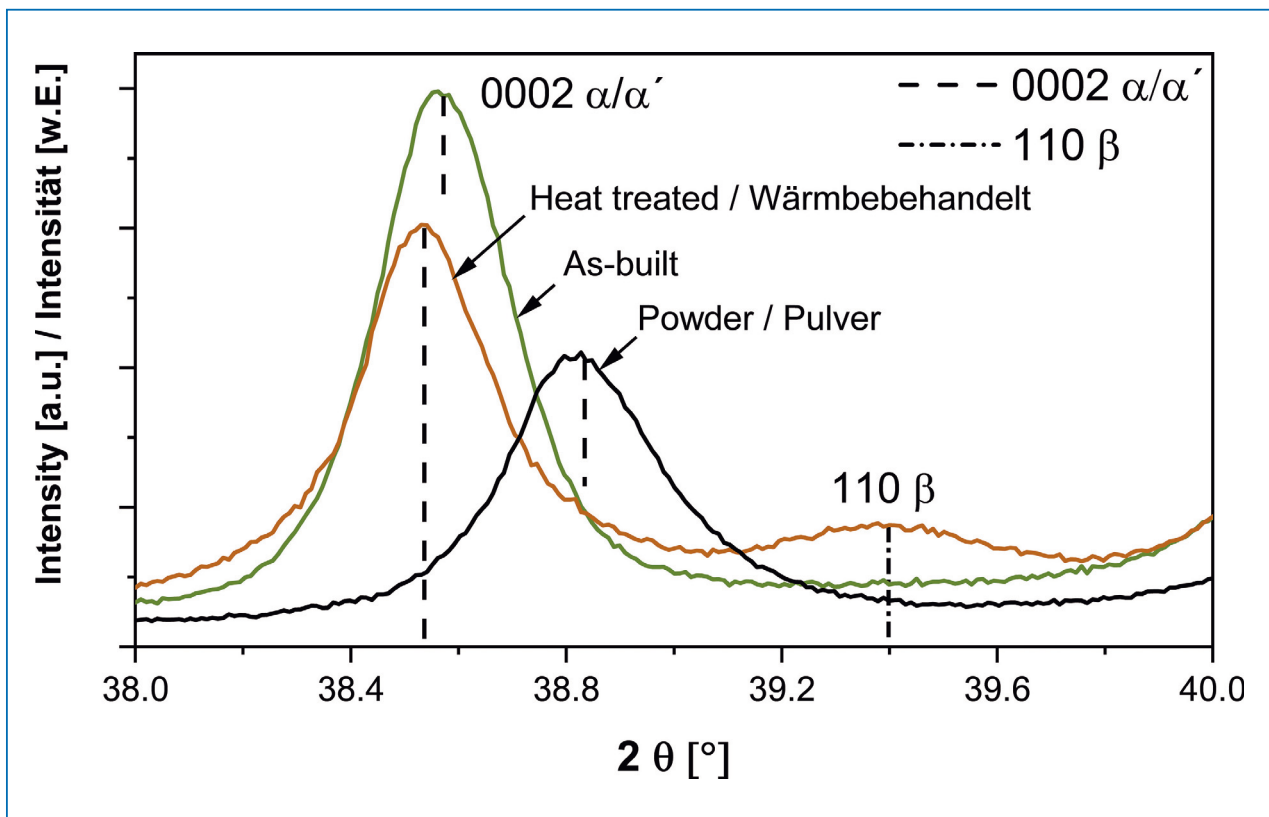


**Fig. 5:** XRD diffraction spectrum of the laser-melted samples and the examined powder indicating the angular range in which the 0002  $\alpha/\alpha'$  and the 110  $\beta$  peak occur. The shift of the  $\alpha/\alpha'$  peak position (dashed line) from the powder sample to the heat-treated sample and the formation of the bcc  $\beta$  phase (dash-dotted line) indicate a phase transformation ( $\alpha' \rightarrow \alpha+\beta$ ) towards the thermodynamic equilibrium [7].

**Bild 5:** XRD-Beugungsspektren der lasergeschmolzenen Proben sowie des untersuchten Pulvers. Dargestellt ist der Winkelbereich, wo der 0002  $\alpha/\alpha'$ - und der 110  $\beta$ -Peak auftreten. Die Verschiebung der  $\alpha/\alpha'$ -Peakposition (gestrichelte Linie) vom Pulver bis zur wärmebehandelten Probe und die Entstehung der krz  $\beta$ -Phase (strichpunktiierte Linie) deuten auf eine Phasenumwandlung ( $\alpha' \rightarrow \alpha+\beta$ ) in Richtung des thermodynamischen Gleichgewichts hin [7].

The obtained diffraction spectra show that the  $\alpha/\alpha'$  peaks (dashed peak position) are shifted from the powder samples to the heat-treated sample via the as-built sample. The diagram furthermore reveals that the bcc  $\beta$  phase (dash-dotted position) occurs in the heat-treated condition. The shift of the hex 0002 peak and the precipitation of the  $\beta$  phase are an indication of a phase transformation towards the thermodynamic equilibrium ( $\alpha' \rightarrow \alpha+\beta$ ). The atomic radii of Al (0.143 nm) and V (0.132 nm), smaller as compared to those of Ti (0.147 nm), thus lead to an increasing  $\alpha$  lattice parameter (decreasing  $2\theta$  angle) for an enrichment of V in the  $\beta$  phase [7].

Die erhaltenen Beugungsspektren zeigen, dass es zu einer Verschiebung des  $\alpha/\alpha'$ -Peaks (gestrichelte Peakposition) von den Pulverproben über die as-built Probe bis zur wärmebehandelten Probe kommt. Darüber hinaus tritt im wärmebehandelten Zustand die krz  $\beta$ -Phase (strichpunktiierte Position) auf. Die Verschiebung des hex 0002 Peaks sowie die Ausscheidung der  $\beta$ -Phase deuten auf eine Phasenumwandlung in Richtung des thermodynamischen Gleichgewichts ( $\alpha' \rightarrow \alpha+\beta$ ) hin. Die kleineren Atomradien von Al (0,143 nm) und V (0,132 nm) im Vergleich zu Ti (0,147 nm) führen dementsprechend bei Anreicherung von V in der  $\beta$ -Phase zu einem größer werdenden  $\alpha$ -Gitterparameter (abnehmender  $2\theta$ -Winkel) [7].

### 3.3 Enhanced Sample Preparation

#### Electrochemical Etching

Electrochemical etching is a corrosive process generating a metallographic microstructural contrast based on a potential difference of different surface areas [26]. Potential differences occur owing to physical, structural, and chemical inhomogeneities such as those generated by the presence of multiple phases of varying density, with varying crystallographic orientations, or segregations [16]. At room temperature, the hex  $\alpha$  phase and the bcc  $\beta$  phase are present in the thermodynamic equilibrium in Ti-6Al-4V. A potential difference is already present here due to the different chemical compositions of these phases. An etchant frequently used for Ti-6Al-4V is the so-called Kroll's reagent. It contains hydrofluoric acid for a selective attack of the less noble Al-rich  $\alpha$ -phase, and nitric acid to brighten the surface [16]. The exact composition of Kroll's reagent is given in Tab. 1. Fig. 6 is a LM image of a laser-molten Ti-6Al-4V sample after ten-second Kroll etching. For the purpose of representing this 3D cube, three metallographic

### 3.3 Erweiterte Probenpräparation

#### Elektrochemisches Ätzen

Eine elektrochemische Ätzung ist ein korrosiver Prozess, in welchem durch eine Potentialdifferenz verschiedener Oberflächenbereiche eine metallographische Gefügekontrastierung generiert wird [26]. Potentialunterschiede entstehen durch physikalische, strukturelle und chemische Inhomogenitäten, wie z. B. durch Mehrphasigkeit unterschiedlicher Dichte, unterschiedliche kristallographische Orientierungen oder Seigerungen [16]. Im Fall von Ti-6Al-4V liegt bei Raumtemperatur im thermodynamischen Gleichgewicht sowohl die hex  $\alpha$ -Phase als auch die krz  $\beta$ -Phase vor. Hier besteht bereits ein Potentialunterschied aufgrund der unterschiedlichen chemischen Zusammensetzung dieser Phasen. Ein häufig eingesetztes Ätzmittel für Ti-6Al-4V ist die sogenannte Kroll-Ätzung. Dieses Reagenz enthält Fluorwasserstoffsäure zum selektiven Angriff der unedleren, Al-reichen  $\alpha$ -Phase und Salpetersäure zum Aufhellen der Oberfläche [16]. Die genaue Zusammensetzung des Kroll-Ätzmittels ist in Tab. 1 angeführt. Bild 6 zeigt eine LM-Aufnahme einer lasergeschmolzenen Ti-6Al-4V-Probe nach einer 10-sekündigen

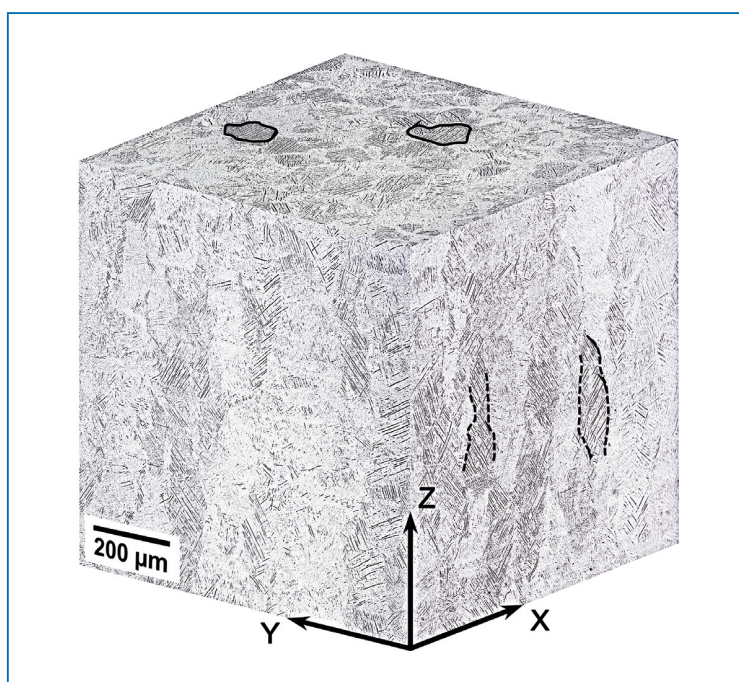


**Fig. 6:** Three-dimensional representation of a contrasted and laser-melted Ti-6Al-4V sample etched using Kroll's etching solution, acquired in the LM (BF mode). The dashed lines indicate the epitaxial growth of a  $\beta$  grain, while the black circles mark individual  $\beta$  grains in the X-Y cross section. The Z direction represents the BD of the SLM process.

**Bild 6:** Dreidimensionale Darstellung einer mit der Ätzlösung nach Kroll kontrastierten lasergeschmolzenen Ti-6Al-4V-Probe, aufgenommen im LM (HF-Modus). Die gestrichelten Linien zeigen das epitaktische Wachstum eines  $\beta$ -Korns und die schwarzen Kreise markieren einzelne  $\beta$ -Körner im X-Y-Querschnitt. Die Z-Richtung repräsentiert die BD des SLM Prozesses.

sections were prepared, where the Z axis represents the BD of the SLM process. This three-dimensional representation provides an overview of different areas of the additively manufactured components. The columnar grain structure (dashed lines) can be recognized in the X-Z cross section, while the  $\beta$  grain structure can be seen in the X-Y cross section.

Another way of representing the microstructure is Weck's etching [27]. Figs. 7a–c) show the results of etching by immersion according to Weck. During the test series, it was found that an optimal microstructural contrast is achieved after a period of 35 seconds. Fig. 7a) shows the LM image (BF mode) of an as-built sample. This magnification reveals the layer structure (marked by black arrows). Owing to their different coloration, columnar grain structures (dashed lines) can also be observed normal to the BD. Fig. 7b) is a light microscope image of the same image detail at a higher magnification. It is apparent that this etching method provides an excellent contrast revealing the martensitic  $\alpha'$  needles.

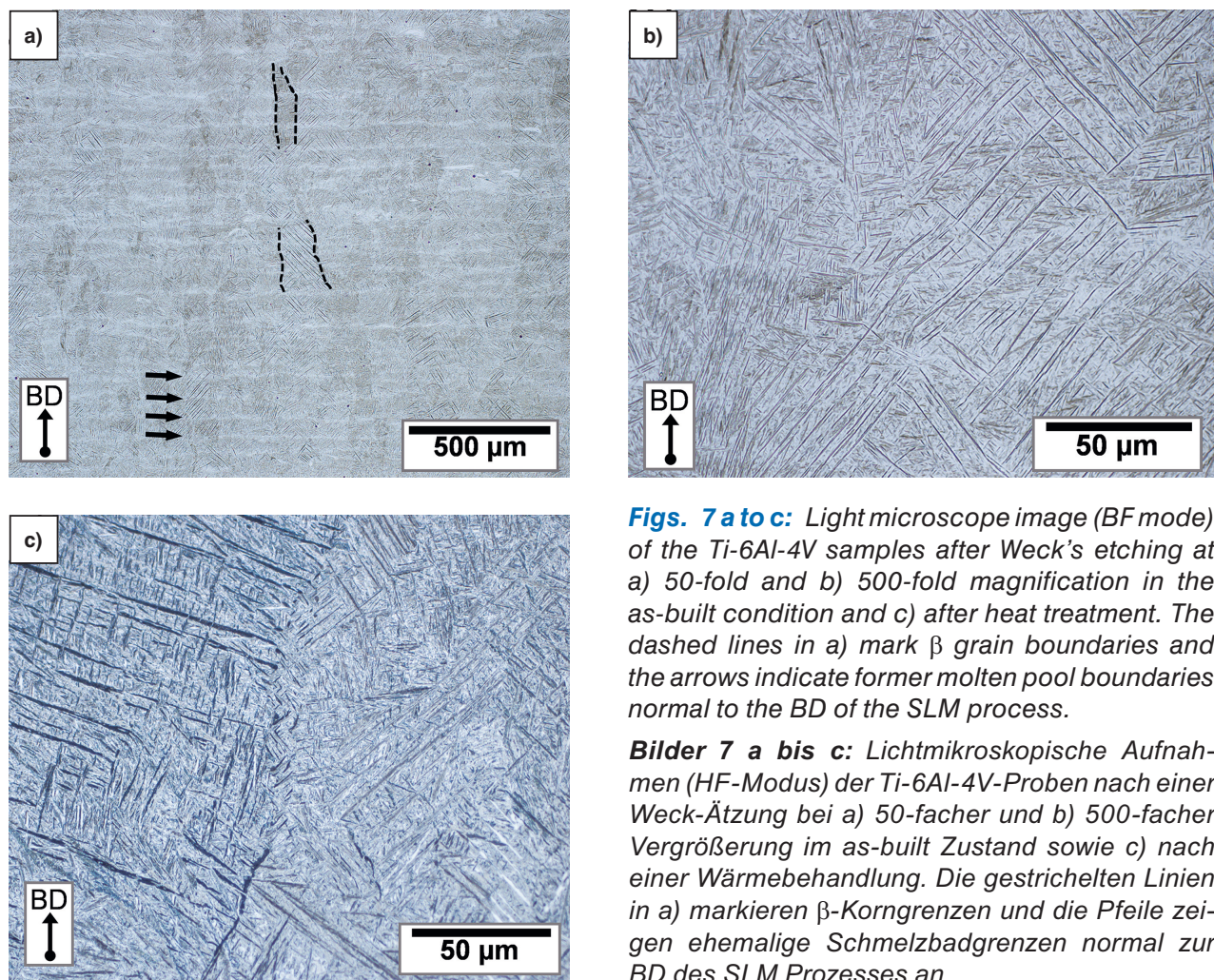
In order to compensate the microstructural defects induced by the manufacturing process, components are subjected to a heat-treatment or to HIP [28]. HIP reduces the porosity of the components and increases their density. Fig. 7c) shows the structure after Weck's etching of a heat-treated sample (1–3 hours at 800–850 °C). Compared to the as-built sample, the needles appear broader, indicating a transformation of the martensite towards the thermodynamic equilibrium ( $\alpha' \rightarrow \alpha + \beta$ ). The gray and black appearance of the  $\alpha'$  needles in Fig. 7c) indicates, moreover, that the needles belong to the former mother phase, the  $\beta$  phase.

Kroll-Ätzung. Zur Darstellung dieses 3D-Würfels wurden drei metallographische Schlitze angefertigt, wobei die Z-Achse die BD im SLM-Prozess repräsentiert. Durch diese dreidimensionale Darstellung kann ein Überblick über verschiedene Bereiche des additiv gefertigten Bauteils geschaffen werden. Neben der kolumnaren Kornstruktur (gestrichelte Linien) im X-Z-Querschnitt ist auch die  $\beta$ -Kornstruktur im X-Y-Querschnitt zu erkennen.

Eine andere Möglichkeit um die Mikrostruktur abzubilden ist die Ätzmethode nach Weck [27]. Die Ergebnisse der Tauchätzung nach Weck sind in den Bildern 7a–c) dargestellt. Im Rahmen der Versuchsreihe zeigte sich, dass nach einer Dauer von 35 Sekunden die Mikrostruktur optimal kontrastiert wird. In Bild 7a) ist die LM-Aufnahme (HF-Modus) einer as-built Probe dargestellt. In dieser Vergrößerung sind die Schichtstruktur (markiert durch schwarze Pfeile) und, aufgrund unterschiedlicher Färbung, auch kolumnare Kornstrukturen (gestrichelte Linien) normal zur BD zu erkennen. Bild 7b) zeigt eine lichtmikroskopische Aufnahme desselben Bildausschnitts bei höherer Vergrößerung. Es ist zu erkennen, dass sich diese Ätzmethode durch eine deutliche Kontrastierung der martensitischen  $\alpha'$ -Nadeln auszeichnet.

Um mikrostrukturelle Defekte, hervorgerufen durch den Herstellungsprozess, auszugleichen, werden Bauteile einer Wärmebehandlung oder HIP unterzogen [28]. Beim HIPen wird die Porosität des Bauteils reduziert und die Dichte erhöht. Des Weiteren ermöglicht HIPen die Minimierung des Anteils an geschlossenen Poren, welche durch Gaseinschlüsse entstehen. In Bild 7c) ist die Ätzung nach Weck an einer wärmebehandelten Probe (1–3 Stunden bei 800–850 °C) gezeigt. Im Vergleich zur as-built Probe erscheinen die Nadeln breiter, was auf eine Umwandlung des Martensits in Richtung des thermodynamischen Gleichgewichts ( $\alpha' \rightarrow \alpha + \beta$ ) hindeutet. Aufgrund der grau bzw. schwarz erscheinenden  $\alpha'$ -Nadeln in Bild 7c) ist auch die Zugehörigkeit dieser zur ehemaligen Mutterphase, der  $\beta$ -Phase, zu erkennen.





**Figs. 7 a to c:** Light microscope image (BF mode) of the Ti-6Al-4V samples after Weck's etching at a) 50-fold and b) 500-fold magnification in the as-built condition and c) after heat treatment. The dashed lines in a) mark  $\beta$  grain boundaries and the arrows indicate former molten pool boundaries normal to the BD of the SLM process.

**Bilder 7 a bis c:** Lichtmikroskopische Aufnahmen (HF-Modus) der Ti-6Al-4V-Proben nach einer Weck-Ätzung bei a) 50-facher und b) 500-facher Vergrößerung im as-built Zustand sowie c) nach einer Wärmebehandlung. Die gestrichelten Linien in a) markieren  $\beta$ -Korngrenzen und die Pfeile zeigen ehemalige Schmelzbadgrenzen normal zur BD des SLM Prozesses an.

### Thermal Etching

Another possibility to visualize the microstructure is a thermal etching process. During thermal etching, a physical etching method, an oxide layer is generated on the surface by elevated temperatures. In the LM, this layer appears in colors varying as a function of the present phases and their respective crystallographic orientation. The colors vary from brown (for shorter etching times) to red and blue (for longer etching times) [29]. Fig. 8 shows the result of a 120 min thermal etching process at 540 °C in air atmosphere. The image detail clearly shows the  $\alpha$  needles. Given that elevated temperatures are required to generate the oxide layers, it must be noted at this point that thermal

### Thermisches Ätzen

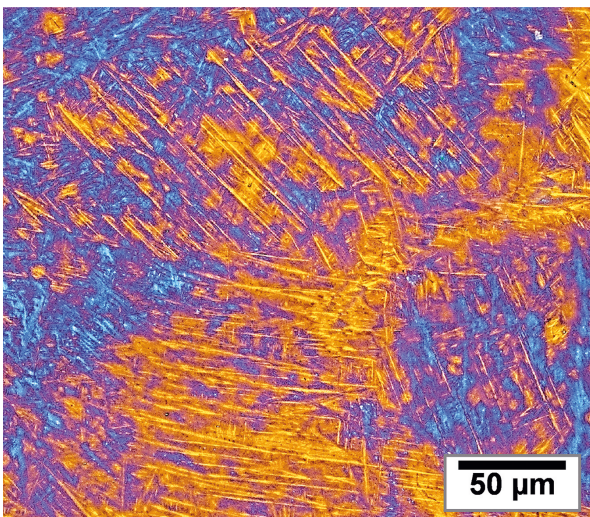
Eine weitere Möglichkeit die Mikrostruktur zu visualisieren ist das Durchführen einer thermischen Ätzung. Bei dieser zu den physikalischen Ätzungen zählenden Methode, wird durch erhöhte Temperaturen eine Oxidschicht auf der Oberfläche erzeugt. Diese erscheint im LM in verschiedenen Farben in Abhängigkeit der auftretenden Phasen und deren kristallographischer Orientierung. Die Farben variieren dabei von braun bei kürzeren Ätzzeiten bis rot und blau bei längeren Ätzzeiten [29]. Das Ergebnis einer 120 min andauernden thermischen Ätzung unter Luftatmosphäre bei 540 °C wird in Bild 8 gezeigt. In diesem Bildausschnitt sind deutlich die  $\alpha$ -Nadeln zu erkennen. An dieser Stelle muss aber auch darauf hingewiesen werden, dass bei An-

etching may, however, bring about microstructural changes.

### Electrolytic Preparation

Owing to an electric current flow between the sample (anode) and the counter electrode (cathode) and the use of an electrolyte, the surface is anodically dissolved during the electrolytic preparation. In addition, the potential difference results in precipitations and a varying surface layer thickness caused by the electrolyte [26, 30]. Fig. 9 shows the results of an electrolytic sample preparation using the electrolyte Ti Em3 on an as-built component. Owing to the varying surface layer coverage, the columnar  $\beta$  grain structure is particularly well contrasted applying a voltage of 100 V and a polishing time of 10 s. As shown in Fig. 9a), it is also possible to capture a large number of  $\beta$  grains, thus subsequently allowing a quantitative evaluation. The higher magnification of Fig. 9b) furthermore reveals the martensitic  $\alpha'$  needles, marked by arrows. They appear considerably brighter.

As opposed to anodic etching, where a surface layer is produced, a surface layer formation must be suppressed in case of a



wendung einer thermischen Ätzung mikrostrukturelle Veränderungen auftreten können, da erhöhte Temperaturen zur Erzeugung der Oxidschichten notwendig sind.

### Elektrolytische Präparation

Bei einer elektrolytischen Präparation wird aufgrund eines Stromes zwischen Probe (Anode) und Gegenelektrode (Kathode) und durch die Verwendung eines Elektrolyten die Oberfläche anodisch aufgelöst. Wird bei diesem Verfahren ein Elektrolyt verwendet, der zusätzlich zur Auflösung einen Niederschlag bzw. eine Deckschicht verursacht, werden aufgrund der Potentialunterschiede Kornflächen unterschiedlich stark belegt [26, 30]. Bild 9 zeigt eine elektrolytische Probenpräparation unter Verwendung des Elektrolyt Ti Em3 an einem as-built Bauteil. Bei Anlegung einer Spannung von 100 V und einer Polierzeit von 10 s kann durch die variierende Deckschichtbelegung besonders die kolumnare  $\beta$ -Kornstruktur kontrastiert werden. Wie aus Bild 9a) hervorgeht, ist es hierbei möglich, auch eine große Anzahl von  $\beta$ -Körnern zu erfassen, was in weiterer Folge eine quantitative Auswertung zulässt. Des Weiteren zeigt eine höhere Vergrößerung in Bild 9b) die martensitischen  $\alpha'$ -Nadeln, angedeutet durch Pfeile, welche deutlich heller erscheinen.

Im Gegensatz zur anodischen Ätzung mit Deckschichtbildung muss bei der Präparation für die Elektronenrückstreubeugung eine

**Fig. 8:** Light microscope image (BF mode) of an additively manufactured Ti-6Al-4V sample thermally etched at 540 °C for 2 hours (see text).

**Bild 8:** Lichtmikroskopische Aufnahme (HF-Modus) einer bei 540 °C für 2 Stunden wärmegeätzten additiv gefertigten Ti-6Al-4V-Probe, siehe Text.

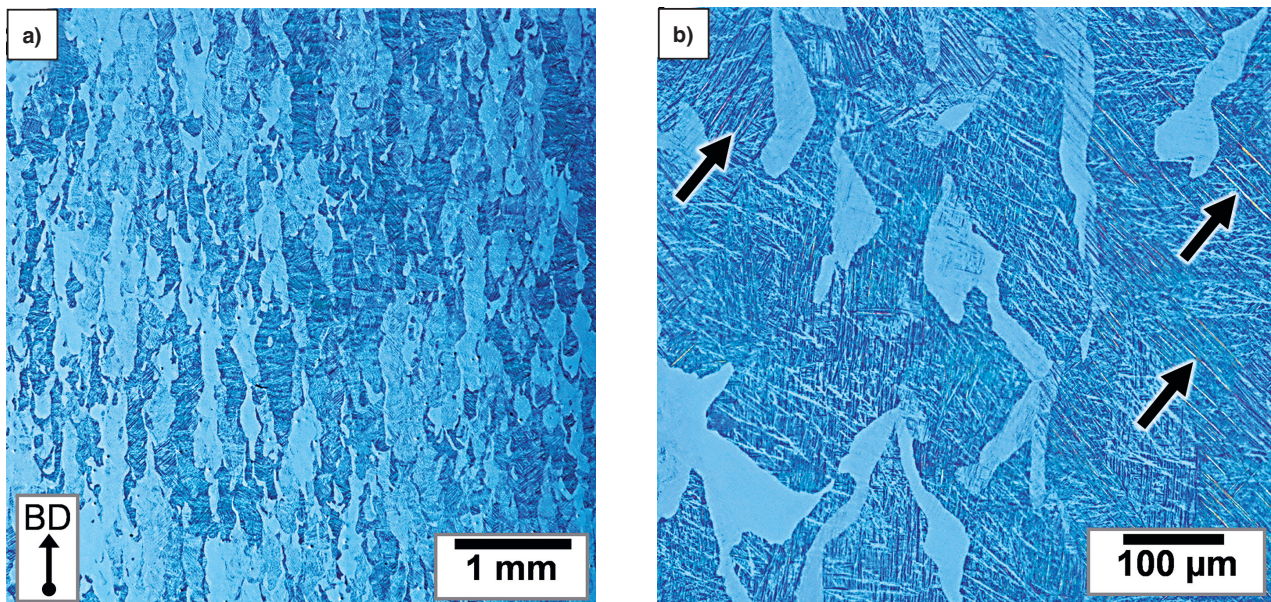


**Fig. 9 a and b:** Light microscope images in the BF mode: a) 25-fold and b) 200-fold magnification of an electrolytically polished as-built sample. The electrolyte Ti Em3 forms a surface layer as a function of the grain orientations. It is thus particularly suited to reveal the columnar  $\beta$  grain structure, while also contrasting the martensitic  $\alpha'$  needles (see arrows).

**Bilder 9 a und b:** Lichtmikroskopische Aufnahmen im HF-Modus: a) 25-fache und b) 200-fache Vergrößerung einer elektrolytisch polierten as-built Probe. Der Elektrolyt Ti Em3 bildet eine Deckschicht in Abhängigkeit der Kornorientierungen und eignet sich daher besonders gut zur Visualisierung der kolumnaren  $\beta$ -Kornstruktur. Die martensitischen  $\alpha'$ -Nadeln werden ebenfalls kontrastiert (siehe Pfeile).

preparation intended for electron backscatter diffraction, as the layer acts passively and impedes an emission of electrons from the surface. When samples are prepared for EBSD measurements, it should therefore be ensured that no surface layers are present on the surface and that the material removal process leaves a deformation-free surface [15]. Polishing parameters such as voltage, flow rate, and polishing time, were therefore varied aiming at improving the preparation result. Providing constant environmental conditions in the SEM such as sample type, accelerating voltage, sample current, and magnification, an average Confidence Index, CI, was determined for the respective EBSD measured area using the evaluation software OIM. The CI indicates the level of accuracy of crystallographic orientation indexing. In this work, this value is used as a reference value to evaluate the preparation outcome. Given

Deckschichtbildung unterdrückt werden, da diese passiv wirkt und ein Austreten von Elektronen aus der Oberfläche erschwert. Bei der Probenvorbereitung für EBSD-Messungen sollte deshalb sichergestellt werden, dass die Oberfläche frei von Oberflächenschichten ist sowie eine durch den Materialabtrag geschaffene verformungsfreie Oberfläche entsteht [15]. In dieser Arbeit wurden deshalb gezielt Polierparameter, wie z. B. Spannung, Flussrate und Polierzeit, variiert, um das Präparationsergebnis zu verbessern. Bei gleichbleibenden Umfeldbedingungen im REM, wie Probentyp, Beschleunigungsspannung, Probenstrom und Vergrößerung, wurde mittels der Auswertesoftware OIM ein durchschnittlicher Vertrauensindex (engl.: Confidence Index, CI) für die jeweilige EBSD gemessene Fläche ermittelt. Der CI ist ein Wert für die Richtigkeit der Indizierung einer kristallographischen Orientierung. In dieser Arbeit wird dieser Wert als Vergleichswert für den Präpa-

the same environmental conditions, higher CI values indicate a better sample surface quality. The preparation studies have shown that the best surface quality could be obtained using the electrolyte A3 at a voltage of 30 V and a flow rate of 10 for a polishing time of 40 s. The highest CI values were reached based on these parameters for both, the as-built samples and the heat-treated samples.

### Vibratory Polish

Apart from the described electrolytic preparation methods, it is also possible to prepare the surface of a sample for an EBSD measurement by subjecting it to a vibratory polish. However, in this case, the polishing rate is very low and the polishing process generally takes several hours [16]. For vibratory polishing, the mounted samples are clamped into a sample holder, thus providing the required contact pressure on the polishing disk. The holder is subsequently placed on a polishing cloth moistened with a polishing suspension and moved over the cloth by vibrations. For the vibratory polish, a chemically resistant MicroCloth polishing cloth (Buehler) was used in combination with an OPS. It was found that the highest CI index for as-built samples was obtained after a polishing time of 8 hours. Owing to their lower hardness, the vibratory polishing time was reduced to 4 hours for the heat-treated Ti-6Al-4V samples.

### EBSD Examinations

Figs. 10 a) and b) show the grain orientation and the Image-Quality map (IQ) of an EBSD measurement on an as-built sample after 8 hours of vibratory polishing, respectively. The Z axis of the EBSD coordinate system runs parallel to the BD. The martensitic microstructure's  $\alpha'$  needles and their crystallographic orientations can clearly be recognized, whereas, due to the heat-treat-

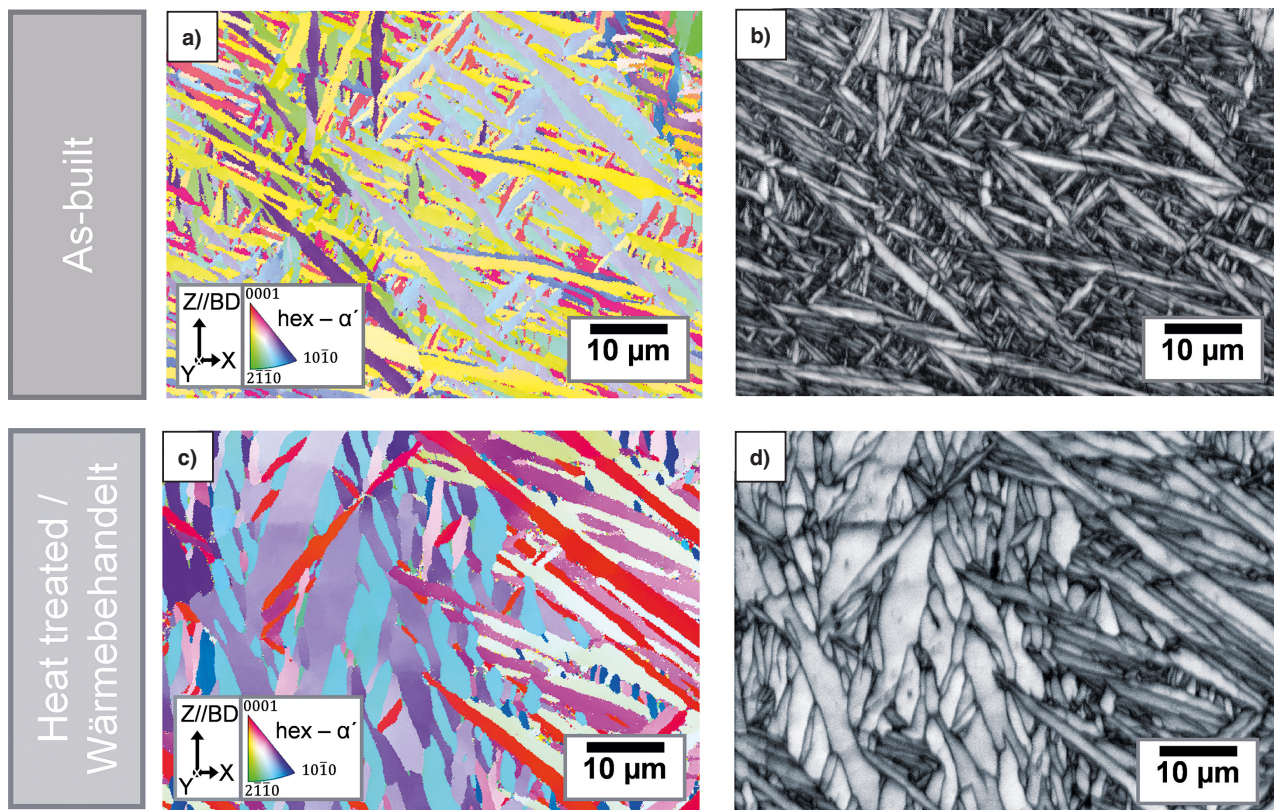
mentserfolg herangezogen. Höhere CI-Werte stehen bei gleichen Umfeldbedingungen für eine bessere Qualität der Probenoberfläche. Die Präparationsstudien ergaben, dass mit dem Elektrolyt A3, unter Verwendung einer Spannung von 30 V, einer Flussrate von 10 und einer Polierzeit von 40 s, die beste Oberflächenqualität erreicht wurde. Sowohl die as-built als auch die wärmebehandelten Proben zeigten bei diesen Parametern die höchsten CI-Werte.

### Vibrationspolitur

Neben den beschriebenen elektrolytischen Präparationsmethoden besteht auch die Möglichkeit mit einer Vibrationspolitur die Oberfläche einer Probe für eine EBSD-Messung vorzubereiten. Die Polierrate ist aber sehr gering, was in der Regel zu Polierzeiten von mehreren Stunden führt [16]. Bei einer Vibrationspolitur werden eingebettete Proben in einem Probenhalter eingespannt, welcher für die nötige Anpresskraft auf die Polierscheibe sorgt. Der Halter wird anschließend auf ein mit Poliersuspension befeuchtetes Poliertuch aufgesetzt und durch Vibrationen über das Tuch bewegt. Für die Vibrationspolitur wurde ein chemisch beständiges Poliertuch vom Typ MicroCloth der Fa. Buehler in Kombination mit einer OPS verwendet. Es stellte sich heraus, dass bei as-built Proben nach einer Polierzeit von 8 Stunden der höchste CI-Index erreicht wurde. Bei den wärmebehandelten Ti-6Al-4V-Proben reduzierte sich die Vibrationspolierzeit auf 4 Stunden, da diese Proben eine geringere Härte aufweisen.

### EBSD-Untersuchungen

Bilder 10 a) und b) zeigen die Kornorientierungs- und Qualitätsindex- (engl.: Image-Quality, IQ) Abbildung einer EBSD-Messung an einer as-built Probe nach einer Vibrationspolitur von 8 Stunden. Die Z-Achse des EBSD-Koordinatensystems ist parallel zu BD. Es sind deutlich die  $\alpha'$ -Nadeln der martensitischen Mikrostruktur und deren kristallographische Orientierungen zu erkennen. Im Vergleich dazu



**Figs. 10a to d:** EBSD grain orientation image of a a) martensitic and c) heat-treated Ti-6Al-4V sample with respective color coding according to the inverse pole figure; b) and d): EBSD IQ image (image quality index) of the same image sections.

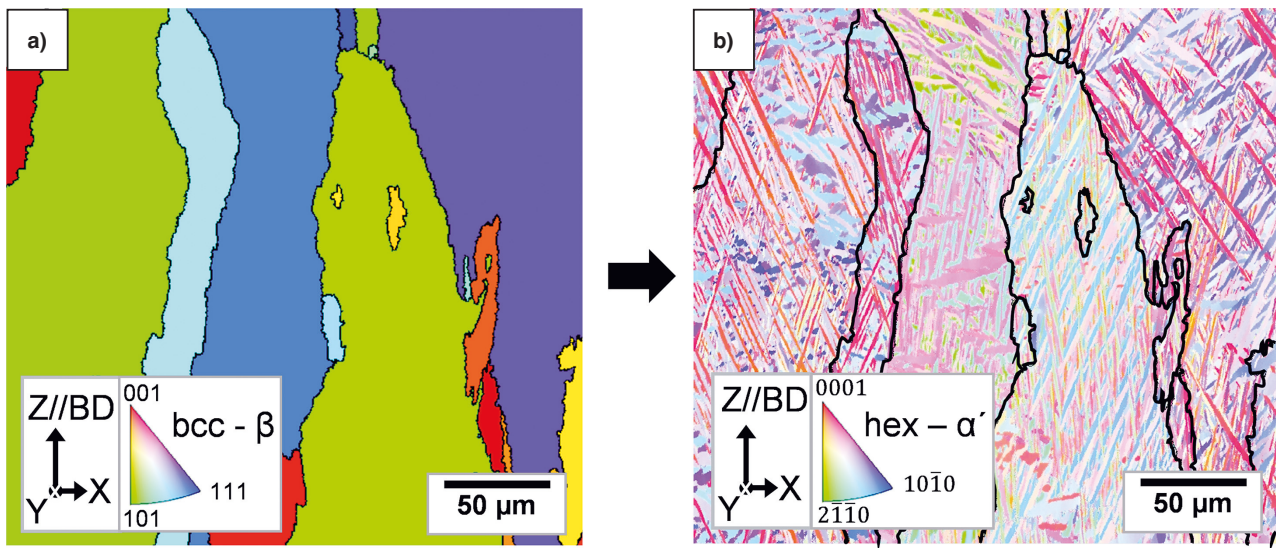
**Bilder 10a bis d:** EBSD-Kornorientierungsabbildung einer a) martensitischen und c) wärmebehandelten Ti 6Al 4V-Probe mit der zugehörigen Farbkodierung gemäß der inversen Polfigur; b) und d): EBSD-Qualitätsindexabbildung (IQ) derselben Bildausschnitte.

ment, the microstructure in the figs. 10 c) and d) appears considerably coarser suggesting a temperature-induced grain growth. As opposed to the grain interior presenting higher values, the areas in the IQ images appearing darker are grain boundaries with low CI values. The heat treatment induced low  $\beta$  phase fraction ( $< 5$  vol.%) is located at the  $\alpha$  grain boundaries. As the fraction is too low and the spatial resolution of the EBSD measurement is insufficient, it cannot be imaged.

Applying the optimized sample preparation procedure, it is now also possible to perform EBSD measurements of larger areas. Fig. 11 shows the result of an EBSD measurement of a heat-treated sample after 4 hour vibra-

erscheint die Mikrostruktur durch die Wärmebehandlung in den Bildern 10 c) und d) deutlich größer, was auf ein Kornwachstum aufgrund der verwendeten Temperatur schließen lässt. Die dunklen Bereiche in den IQ-Abbildungen sind Korngrenzen, an denen die CI-Werte, im Gegensatz zum Korninneren, gering sind. Der durch die Wärmebehandlung entstandene geringe  $\beta$ -Phasenanteil ( $< 5$  vol.%) befindet sich an den  $\alpha$ -Korngrenzen und kann aufgrund des geringen Anteils und einer zu geringen Ortsauflösung der EBSD Messung bildlich nicht erfasst werden.

Durch die optimierte Probenpräparation ist es nun möglich, auch EBSD-Messungen an größeren Bereichen durchzuführen. Bild 11 zeigt das Ergebnis einer EBSD-Messung einer wärmebehandelten Probe nach einer Vi-



**Figs. 11 a and b:** a)  $\beta$  grain structure of a heat-treated Ti-6Al-4V sample with Y orientation calculated using the software ARPGE [10, 11]; b) superposition of the calculated  $\beta$  grain structure and the respective EBSD grain orientation image indicating the respective orientation legends.

**Bilder 11 a und b:** a) Mit der Software ARPGE [10, 11] berechnete  $\beta$ -Kornstruktur einer wärmebehandelten Ti-6Al-4V-Probe mit Y-Ausrichtung; b) Überlagerung der berechneten  $\beta$ -Kornstruktur mit der zugehörigen EBSD-Kornorientierungsabbildung und der entsprechenden Orientierungslegenden.

tory polishing. As is apparent in Fig. 11a), the columnar  $\beta$  grain structure could be reconstructed based on the so-called Burger's orientation relationship using the software ARPGE [10, 11]. b) presents a superposition of the ARPGE file and the original file. This superposition reveals the  $\beta$  grain structure in the EBSD grain orientation image. In this way, not only an image detail can be examined. Crystallographic information of individual  $\beta$  grains can also be obtained by singling out and cutting along grain boundaries.

## 4. Conclusions

In this work, the sample preparation process for additively manufactured Ti-6Al-4V components was fundamentally analyzed. With this in mind, the entire process chain, from the preparation of powder samples to the sample preparation of SLM manufactured components, was outlined. An optimized sample preparation not just allows stand-

brationspolitur von 4 Stunden. Wie in Bild 11a) ersichtlich, konnte mit der Software ARPGE [10, 11] über die sogenannte Burgers Orientierungsbeziehung die kolumnare  $\beta$ -Kornstruktur rekonstruiert werden. In b) ist eine Überlagerung der ARPGE-Datei mit der Ursprungsdatei dargestellt. Durch diese Überlagerung wird die  $\beta$ -Kornstruktur in der EBSD-Kornorientierungsabbildung visualisiert. Diese Darstellung ermöglicht es nun, neben der Untersuchung eines Bildausschnittes, durch Herausheben und Zuschnitt entlang von Korngrenzen auch kristallographische Informationen über einzelne  $\beta$ -Körner zu erhalten.

## 4. Schlussfolgerungen

In dieser Arbeit wurde grundlegend die Probenpräparation für additiv gefertigte Ti-6Al-4V-Bauteile untersucht. Hierfür wurde die gesamte Prozesskette, beginnend bei der Präparation von Pulverproben bis hin zur Probenvorbereitung von SLM-gefertigten Bauteilen, beleuchtet. Eine optimierte Probenpräparation ermöglicht, neben den

ard examinations by LM and SEM. It also permits further crystallography investigations by EBSD of additively manufactured components. The preparations carried out on Ti-6Al-4V powder samples and AM components defined in this work lead to the following findings:

- During mounting, the hardness difference between a SLM manufactured solid material sample and the mounting material should be minimal in order to ensure an optimal preparation including the surface layer.
  - The parameters listed in Tab. 2 allowed the manufacture of reproducible sections providing an excellent surface quality – a requirement and thus a precondition for a variety of examination methods.
  - The  $\beta$  grain structures formed during the SLM process based on which the microstructural evolution can be interpreted can be contrasted by selective etching or electrolytic preparation methods. Another possibility to reveal the  $\beta$  grains is using a polarization filter in the LM.
  - Specific etching processes, such as etching by immersion according to Weck, do not only reveal the microstructure. They also visualize the layer structure and the molten pool boundaries in the SLM manufactured components.
  - High-resolution EBSD analyses presuppose an artifact and a deformation-free surface. Not only electrolytic polishing, but also vibratory polishing can be carried out to ensure a sufficient surface quality.
  - Superposing numerically calculated  $\beta$  grain structures and EBSD measurement data allows a targeted examination of the crystallography of individual  $\beta$  grains.
- Standarduntersuchungen mittels LM und REM, weiterführende Untersuchungen der Kristallographie mittels EBSD an additiv gefertigten Bauteilen durchzuführen. Die in dieser Arbeit definierten Präparationen an Ti-6Al-4V Pulverproben sowie AM-Bauteilen führten zu folgenden grundlegenden Erkenntnissen:
- Beim Einbetten von SLM-gefertigtem Vollmaterial sollte der Härteunterschied zwischen der Probe und dem Einbettmittel minimal sein, um eine optimale Präparation bis zur Randschicht zu ermöglichen.
  - Mit dem in Tab. 2 beschriebenen Verfahren konnten durchwegs reproduzierbar Schriffe mit hervorragender Oberflächenqualität hergestellt werden, was für eine Vielzahl von Untersuchungsmethoden notwendig ist und daher eine Voraussetzung ist.
  - Die zur Interpretation der Gefügeentwicklung während des SLM-Prozesses entstehenden  $\beta$ -Kornstrukturen können mittels selektiven Ätzungen oder elektrolytischen Präparationsmethoden kontrastiert werden. Eine weitere Möglichkeit, die  $\beta$ -Körner zu visualisieren, ist die Verwendung eines Polarisationsfilters im LM.
  - Mit speziellen Ätzungen, wie z.B. der Tauchätzung nach Weck, werden neben der Mikrostruktur auch die Schichtstruktur bzw. die Schmelzbadgrenzen in den SLM-gefertigten Bauteilen sichtbar.
  - Hochauflösende EBSD-Analysen setzen eine artefakt- und deformationsfreie Oberfläche voraus. Neben einer elektrolytischen Politur kann auch durch eine Vibrationspolitur für eine ausreichende Oberflächenqualität gesorgt werden.
  - Die Überlagerung von numerisch berechneten  $\beta$ -Kornstrukturen mit EBSD-Messdaten ermöglicht es, die Kristallographie einzelner  $\beta$ -Körner gezielt zu untersuchen.

## References / Literatur

- [1] DebRoy, T.; Wei, H.L.; Zuback, J.S.; Mukherjee, T.; Elmer, J.W.; Milewski, J.O.; Beese, A.M.; Wilson-Heid, A.; De, A.; Zhang, W.: *Prog. Mater. Sci.* 92 (2018), 112–224  
DOI: 10.1016/j.pmatsci.2017.10.001
- [2] Peters, M.; Leyens (Eds.), C.: *Titanium and Titanium Alloys: Fundamentals and Applications*, John Wiley & Sons, 2003  
DOI: 10.1002/3527602119
- [3] Uhlmann, E.; Kersting, R.; Klein, T.B.; Cruz, M.F.; Borille, A.V.: *Procedia Cirp.* 35 (2015), 55–60  
DOI: 10.1016/j.procir.2015.08.061
- [4] Barriobero-Vila, P.: *Phase transformation kinetics during continuous heating of  $\alpha+\beta$  and metastable  $\beta$  titanium alloys*, PhD Thesis, TU Vienna, Austria, 2015
- [5] Wimler, D.; Kardos, S.; Lindemann, J.; Clemens, H.; Mayer, S.: *Pract. Metallogr.* 55 (2018), 620–636  
DOI: 10.3139/147.110547
- [6] Frazier, W.E.: *J. Mater. Eng. Perform.* 23 (2014), Nr. 6, 1917–1928  
DOI: 10.1007/s11665-014-0958-z
- [7] Ter Haar, G.; Becker, T.: *Materials.* 11 (2018), Nr. 1, 146  
DOI: 10.3390/ma11010146
- [8] Liu, S.; Shin, Y.C.: *Mater. Des.* 164 (2019), 107552  
DOI: 10.1016/j.matdes.2018.107552
- [9] Neikter, M.; Huang, A.; Wu, X.: *Int. J. Adv. Manuf. Technol.* 104 (2019), Nr. 1–4, 1381–1391  
DOI: 10.1007/s00170-019-04002-8
- [10] Cayron, C.: *J. Appl. Crystallogr.* 40 (2007), Nr. 6, 1183–1188  
DOI: 10.1107/S0021889807048777
- [11] Cayron, C.; Artaud, B.; Briottet, L.: *Mater. Charact.* 57 (2006), Nr. 4–5, 386–401  
DOI: 10.1016/j.matchar.2006.03.008
- [12] Lachmayer, R.; Lippert, R.B.: *Additive Manufacturing Quantifiziert*, Springer-Verlag, Berlin, 2017  
DOI: 10.1007/978-3-662-54113-5
- [13] Neikter, M.; Åkerfeldt, P.; Pederson, R.; Antti, M.L.: *Microstructure characterisation of Ti-6Al-4V from different additive manufacturing processes*, in: *IOP Conf. Ser. Mater. Sci. Eng.*, IOP Publishing, 2017  
DOI: 10.1088/1757-899X/258/1/012007
- [14] Wimler, D.; Lindemann, J.; Gammer, C.; Spoerk-Erdely, P.; Stark, A.; Clemens, H.; Mayer, S.: *Mater. Sci. Eng. A.* 792 (2020), 139798  
DOI: 10.1016/j.msea.2020.139798
- [15] Vander Voort, G.F.: *Pract. Metallogr.* 48 (2011), 527–543  
DOI: 10.3139/147.110151
- [16] Vander Voort, G.F.: *Metallography, principles and practice*, ASM International, New York, 1999
- [17] Vander Voort, G.F.: *Metallographic preparation of titanium and its alloys*, in: *Buehler Tech-Notes* 3, Nr. 3, 1999
- [18] ASTM B964-16: *Standard Test Methods for Flow Rate of Metal Powders Using the Carney Funnel*, 2016
- [19] ASTM B212-17: *Standard Test Method for Apparent Density of Free-Flowing Metal Powders Using the Hall Flowmeter Funnel*, 2017
- [20] DIN ISO 9276: *Darstellung der Ergebnisse von Partikelgrößenanalysen: Deskriptive und quantitative Darstellung der Form und Morphologie von Partikeln*, 2012
- [21] Tang, H.P.; Qian, M.; Liu, N.; Zhang, X.Z.; Yang, G.Y.; Wang, J.: *JOM.* 67 (2015), Nr. 3, 555–563  
DOI: 10.1007/s11837-015-1300-4
- [22] Lütjering, G.; Williams, J.C.: *Titanium*, 1st ed., Springer Science & Business Media, 2007
- [23] Siemers, C.: *Maschinenbau.* 5 (2013), 44–46, Olympia Verlag, Zürich, Schweiz
- [24] Miley, D. V.; Calabra, A.E.: *A review of specimen mounting methods for metallography*, in: *Metallogr. Specim. Prep. Opt. electron Microsc.*, J.L. McCall, W.M. Mueller (Eds.), Plenum Press, London, 1974  
DOI: 10.1007/978-1-4615-8708-8\_1
- [25] Turk, C.; Kellezi, G.; Leitner, H.; Clemens, H.; Primig, S.: *Pract. Metallogr.* 52 (2015), Nr. 6, 323–333  
DOI: 10.3139/147.110344
- [26] Schumann, H.: *Metallografie*, 13. Auflage, Deutscher Verlag für Grundstoffindustrie GmbH, 1991
- [27] Vander Voort, G.F.: *Microstructure of titanium and its alloys*, in: *Ind. Heat.*, Nr. 73, 2006



- [28] Dutta, B.; Froes, F.H.: Additive manufacturing of Titanium alloys: state of the art, challenges and opportunities, Butterworth-Heinemann, 2016  
DOI: 10.1016/B978-0-12-804782-8.00003-3
- [29] Barnes, D.: Metallogr. Microstruct. Anal. 5 (2016), Nr. 6, 536-539  
DOI: 10.1007/s13632-016-0320-y
- [30] Schiebold, K.: Zerstörende Werkstoffprüfung: Metallographische Werkstoffprüfung und Dokumentation der Prüfergebnisse, Springer-Verlag, Berlin, 2018  
DOI: 10.1007/978-3-662-57803-2
- [31] Petzow, G.: Metallographisches, Keramographisches, Plastographisches Ätzen, 7. Auflage, Borntraeger Gebrueder, 2015

### Bibliography

DOI 10.1515/pm-2020-0001  
Pract. Metallogr. 58 (2021) 1; page 4–31  
© 2021 Walter de Gruyter GmbH,  
Berlin/Boston, Germany  
ISSN 0032-678X · e-ISSN 2195-8599

### Christian Fleißner-Rieger



was born 1993 in Innsbruck, Austria. He studied Materials Science at the Montanuniversität Leoben, Austria. Currently he is working on his PhD thesis at the Department of Materials Science, Montanuniversität Leoben. His

research work focuses on additive manufacturing of titanium alloys with a special focus on alloy development.

### Thomas Pogrietz



is master student in the field of Materials Science at the Montanuniversität Leoben. In his bachelor thesis at the Department of Materials Science he dealt with metallographic preparation methods for the application on additively manufactured titanium alloys.

## Article B

---

# Selective laser melting of a near- $\alpha$ Ti6242S alloy for high performance automotive parts

Christian Fleißner-Rieger <sup>1,\*</sup>, Tanja Pfeifer <sup>2</sup>, Tanja Jörg <sup>3</sup>, Thomas Kremmer <sup>4</sup>, Manfred Brabetz <sup>5</sup>, Helmut Clemens <sup>1</sup> and Svea Mayer <sup>1</sup>

<sup>1</sup> Department Werkstoffwissenschaft, Montanuniversität Leoben, Franz-Josef Straße 18, 8700 Leoben, Österreich

<sup>2</sup> Pankl Racing Systems AG, Additive Manufacturing Technologies, Industriestraße Ost 4, 8605 Kapfenberg, Austria

<sup>3</sup> voestalpine BÖHLER Edelstahl GmbH & Co KG, Mariazeller Straße 25, Kapfenberg 8605, Austria

<sup>4</sup> Chair of Nonferrous Metallurgy, Department Metallurgy, Montanuniversität Leoben, Franz-Josef Straße 18, Leoben 8700, Austria

<sup>5</sup> Alloy Development Group, Montanuniversität Leoben, Forschungszentrum Seibersdorf, Seibersdorf 2444, Austria

\* Corresponding author

Advanced Engineering Materials, **23**(12), 2001194, (2021)

<https://doi.org/10.1002/adem.202001194>

open access: CC BY-NC-ND 4.0



## FULL PAPER

# Selective Laser Melting of a Near- $\alpha$ Ti6242S Alloy for High-Performance Automotive Parts

Christian Fleißner-Rieger,\* Tanja Pfeifer, Tanja Jörg, Thomas Kremmer, Manfred Brabetz, Helmut Clemens, and Svea Mayer

This study aims to investigate additively manufactured Ti6242S specimens compared with the widely used Ti64 alloy with a special focus on microstructure and mechanical properties as well as the impact of subsequent heat treatments. As the Ti6242S alloy, which belongs to the family of near- $\alpha$  Ti-alloys, is often used at higher service temperatures, uniaxial tensile tests are performed at a room temperature up to 500 °C. By means of optical and electron microscopy, it is found that the as-built microstructure consists of acicular  $\alpha'$  martensite, which decomposes to  $\alpha + \beta$  during the subsequent heat treatment. A special focus on the prior microstructure shows that the Ti6242S alloy has a small  $\beta$  grain size, which influences the resulting  $\alpha'$  microstructure after the  $\beta \rightarrow \alpha'$  phase transformation. Furthermore, the mechanical properties at room temperature as well as elevated temperatures exceed the values for selective laser melted Ti64 and conventionally cast Ti6242 material. The heat-treated Ti6242S specimens exhibit an ultimate tensile strength of about 1213 MPa including a ductility of 11.3% at room temperature. These values may path the way to a substitution of the widely used Ti64 alloy by the near- $\alpha$  Ti6242S alloy, especially for highly loaded components at elevated temperatures.

## 1. Introduction

During the last decades, the development of Ti-based alloys, especially for powder metallurgical processing, has been of great interest. Although such Ti alloy parts processed by powder metallurgy are already used, their potential applications are still limited due to a small number of processable alloys.<sup>[1]</sup> Against the background of weight reduction and overall performance

improvements in terms of mechanical and thermal properties as well as the rising demand of the producing complex parts, the property profile of Ti-based alloys, especially for high-performance parts, e.g., in the automotive sector, has to be enhanced.

In contrast to the widely used  $\alpha + \beta$  alloy Ti-6Al-4V (Ti64) (m%, unless stated otherwise), the near- $\alpha$  alloy Ti-6Al-2Sn-4Zr-2Mo-Si (Ti6242S) implies enhanced mechanical properties, in particular an improved creep behavior. Therefore, the Ti6242S alloy is already used in high-temperature applications up to 540 °C, whereas the Ti64 alloy can only be used up to 400 °C.<sup>[2]</sup> Further key features of Ti6242S are a low density, high specific tensile strength combined with a good oxidation resistance.<sup>[3]</sup> In general, near- $\alpha$  and  $\alpha + \beta$  alloys contain two phases, namely, the hexagonal  $\alpha$  phase (space group  $P6_3/mmc^{[1]}$ ), which exhibits a higher strength, but a lower ductility when compared with the body-centered cubic (bcc)  $\beta$  phase (space group  $Im\bar{3}m^{[4]}$ ).<sup>[5]</sup> Unlike the  $\alpha + \beta$  Ti64 alloy, in the near- $\alpha$  Ti6242S alloy, the  $\beta$  stabilizing element V is replaced by Mo and limited to  $\leq 2$  m%.<sup>[6]</sup> In addition, Sn and Zr are added as the solid solution strengthening elements of the  $\alpha$  phase, and a minor amount of Si enhances the high-temperature properties due to the formation of  $\zeta$ -(Ti,Zr)<sub>5</sub>Si<sub>3</sub> silicides.<sup>[5,7]</sup> Besides standard production techniques, such as casting or forging, additive manufacturing (AM)

compared with the body-centered cubic (bcc)  $\beta$  phase (space group  $Im\bar{3}m^{[4]}$ ).<sup>[5]</sup> Unlike the  $\alpha + \beta$  Ti64 alloy, in the near- $\alpha$  Ti6242S alloy, the  $\beta$  stabilizing element V is replaced by Mo and limited to  $\leq 2$  m%.<sup>[6]</sup> In addition, Sn and Zr are added as the solid solution strengthening elements of the  $\alpha$  phase, and a minor amount of Si enhances the high-temperature properties due to the formation of  $\zeta$ -(Ti,Zr)<sub>5</sub>Si<sub>3</sub> silicides.<sup>[5,7]</sup> Besides standard production techniques, such as casting or forging, additive manufacturing (AM)


C. Fleißner-Rieger, Prof. H. Clemens, Prof. S. Mayer  
Chair of Physical Metallurgy and Metallic Materials  
Department of Materials Science  
Montanuniversität Leoben  
Franz-Josef Straße 18, Leoben 8700, Austria  
E-mail: christian.fleissner-rieger@unileoben.ac.at

T. Pfeifer  
Pankl Racing Systems AG  
Additive Manufacturing Technologies  
Industriestraße Ost 4, 8605 Kapfenberg, Austria

Dr. T. Jörg  
voestalpine BÖHLER Edelstahl GmbH & Co KG  
Mariazeller Straße 25, Kapfenberg 8605, Austria

Dr. T. Kremmer  
Chair of Nonferrous Metallurgy  
Department Metallurgy  
Montanuniversität Leoben  
Franz-Josef Straße 18, Leoben 8700, Austria

M. Brabetz  
Alloy Development Group  
Montanuniversität Leoben  
Forschungszentrum Seibersdorf, Seibersdorf 2444, Austria

 The ORCID identification number(s) for the author(s) of this article can be found under <https://doi.org/10.1002/adem.202001194>.

© 2021 The Authors. Advanced Engineering Materials published by Wiley-VCH GmbH. This is an open access article under the terms of the Creative Commons Attribution-NonCommercial-NoDerivs License, which permits use and distribution in any medium, provided the original work is properly cited, the use is non-commercial and no modifications or adaptations are made.

DOI: 10.1002/adem.202001194

became a state-of-the-art production technique for Ti alloys. Several research activities focused on AM of Ti64, particularly on powder-bed fusion techniques, such as selective laser melting (SLM) or electron beam melting (EBM).<sup>[8–12]</sup> The near net-shape manufacturing methods, such as SLM and EBM, provide multiple advantages, such as design freedom with the possibility of load-optimized geometries to increase the product customization and environmentally friendly use of materials. Furthermore, a decreasing material usage combined with reduced machining costs leads to production savings, especially for Ti-based components. Research results show that weight-optimized components have a lower environmental impact due to the reduced fuel consumption in the automotive sector as well as in aerospace industry.<sup>[13,14]</sup> Based on these results, it can be deduced that there is also a potential application field for AM Ti6242S in the automotive sector, as the alloy is commonly used in a cast, forged, and welded condition in the aerospace industry.<sup>[15,16]</sup>

Nonetheless, only a few articles concerning AM of Ti6242S are available to the best of authors' knowledge. Cui et al.<sup>[17]</sup> and Fujieda et al.<sup>[18]</sup> managed to produce boron-modified Ti6242S parts via EBM, whereas Fan et al.,<sup>[19]</sup> for the first time, successfully produced Ti6242 via SLM, resulting in a historically high ultimate tensile strength (UTS) of about 1437 MPa as well as 1510 MPa for the as-built and aged (595 °C for 8 h) specimens. These researchers also reported that this high UTS goes along with a reduced ductility of about 5% or rather 1.4% for the as-built and aged samples. The high tensile strength of the Ti6242 samples in the as-built condition already exceeds the values for related SLM Ti64 (UTS = 1137 – 1267 MPa<sup>[20–22]</sup>) and cast Ti6242 specimens (UTS = 970 MPa<sup>[23]</sup>). However, there is still a lack of scientific research activities regarding SLM of the Si variant Ti6242S together with appropriate post-process heat treatments to enhance the ductility. In general, an SLM process itself is associated with high cooling rates due to the small volume of the melt pool and the 3D thermal connectivity to the surrounding material.<sup>[24]</sup> High cooling rates, however, lead to non-equilibrium phases, pronounced residual stresses, and a diminished ductility. For example, in case of the  $\alpha + \beta$  two-phase Ti64 alloy, a solidification process with high cooling rate generates martensitic microstructures. During the SLM process, the material experiences a liquid  $\rightarrow \beta \rightarrow \alpha'$  phase transformation which leads to acicular  $\alpha'$  martensite embedded within the parent  $\beta$  grains.<sup>[25]</sup> The parent  $\beta$  grains typically form as elongated columnar grains in the SLM building direction (BD), resulting in anisotropic tensile properties. In addition, the mechanical properties of the alloy are strongly influenced by the final martensitic  $\alpha'$  microstructure, which has low ductility and reduced fracture toughness. Accordingly, subsequent heat treatments are applied after AM to transform the martensitic to an  $\alpha + \beta$

microstructure<sup>[24,25]</sup> with enhanced ductility and better fracture toughness. The realization of an appropriate heat treatment strongly depends on the required target properties. In many cases, SLM produced Ti64 is further processed by a sub-transus stress relief heat treatment in the temperature range of about 650–900 °C followed by air or furnace cooling to increase the ductility. For instance, this sub-transus heat treatment on the as-built samples lowers the UTS by about 20% and increases the elongation at fracture by about 43% on the other.<sup>[25–27]</sup> The enhancement of ductility properties is related to the precipitation of a certain amount of  $\beta$  phase along with a thermodynamic equilibrium material condition.<sup>[22]</sup>

The present study aims to investigate the commonly used Ti64 alloy in comparison with the near- $\alpha$  Ti6242S alloy for AM application. Among the automotive parts to be produced are turbochargers, flanges, and elements in the exhausting system such as manifolds, collectors,  $\alpha$ , and end pipes, which are exposed to the temperatures of up to 500 °C and are produced in limited quantities. Therefore, the determined tensile strength of the SLM Ti64 specimens is used as a benchmark and serves as target properties that should be exceeded by the Ti6242S samples, whereas the ductility of the newly produced Ti6242S samples has to be comparable for a possible use for AM applications. Furthermore, the microstructural evolution of the Ti6242S alloy based on SLM and sub- $\beta$  transus heat treatments is used to analyze the processing–microstructure–property relationships to produce a high quality, reliable component.

## 2. Materials and Methods

### 2.1. Starting Powder, SLM, and Post-Processing

The specimens investigated within this study were produced by SLM at Pankl Systems Austria GmbH, AM Technologies, on an EOS M290 AM facility. Besides Ti6242S specimens, also Ti64 reference specimens were produced. To achieve comparable results, both alloys were manufactured with the same processing parameters, i.e., with a volume energy density of about 60 J mm<sup>-3</sup>. These optimal production parameters, known as the process window, were optimized in terms of short processing times and a low porosity below 0.05 vol%.

The chemical composition of the gas atomized Ti6242S and the Ti64 powder is listed in **Table 1**.

During the SLM process, the materials also pick up interstitial elements, which resulted in an 0.03 m% and 0.01 m% increased O and N content. The elements, such as Al, Sn, Zr, Mo, V, and Fe, were determined via inductively coupled plasma atomic emission spectroscopy (ICP-AES), whereas Si, O, and N were determined via carrier gas hot extraction. The measurement of the

**Table 1.** Chemical composition of the investigated Ti6242S and Ti64 materials.

Element		Al	Sn	Zr	Mo	Si	V	Fe	O	N
Ti6242S [m%]	Powder	6.4	2.0	4.2	2.0	0.05		0.02	0.13	0.002
	As-built								+0.03	+0.01
Ti64 Grade 23 ELI [m%]	Powder	6.3					3.9	0.20	0.08	0.002
	As-built								+0.03	+0.01

**Table 2.** Sample geometries produced by SLM and investigated conditions.

Components	Build geometry [mm <sup>3</sup> ]	Investigated condition	Heat treatment	Atmosphere	Cooling media
Tensile samples	∅12 × 70	SRA	800–850 °C for 1–3 h	Vacuum	AC
Cuboid samples	22 × 22 × 25	As-built, SRA, and heat-treated	Up to 1020 °C	Vacuum and air	AC and WQ

particle size distribution was done by dynamic image analysis using a CAMSIZER from Retsch Technology GmbH and yielded D-values based on the volume ( $Q_3$ ) of about  $D_{10} = 17.4 \mu\text{m}$ ,  $D_{50} = 31.1 \mu\text{m}$ , and  $D_{90} = 43.3 \mu\text{m}$  for the Ti6242S powder, compared with  $D_{10} = 23.4 \mu\text{m}$ ,  $D_{50} = 37.2 \mu\text{m}$ , and  $D_{90} = 50.6 \mu\text{m}$  for the Ti64 powder.

**Table 2** shows an overview of the SLM manufactured samples, which were built and prepared for tensile testing and microstructural analysis. In the course of this, 12 specimens were produced for room temperature (RT) and high-temperature tensile testing, and each specimen was machined according to ISO 6892 ( $\emptyset$  6 mm inner sample diameter and a screw head M11). All tensile samples were built in the z-direction; i.e., the longitudinal axis was perpendicular to the building platform. To enable a certain amount of ductility, a stress relief annealing (SRA) heat treatment followed by air cooling (AC) was performed. The cuboid samples were built for microstructural investigations and were investigated in as-built and SRA sample condition. To determine phase fractions and phase transformation temperatures, additional isothermal heat treatments were performed at the temperatures of up to 1020 °C followed by water quenching (WQ).

## 2.2. Sample Preparation and Microstructural Investigations

The metallographic specimen preparation was performed by means of standard metallographic methods.<sup>[28]</sup> The etching process was done using a Kroll's reagent (100 mL distilled H<sub>2</sub>O, 2–6 mL HNO<sub>3</sub>-65%, and 1–3 mL HF-40%)<sup>[29]</sup> for 10–30 s. For transmission electron microscopy (TEM), the sample thinning of the 3 mm (diameter)-sized platelets was conducted electrolytically using a Tenu Pol-5 and an electrolyte A3 from Struers.

Light optical microscopy (LOM) was performed on a Zeiss Axio Imager.M2 equipped with a camera-based image acquisition program Zeiss AxioCam ICc5. Scanning electron microscopy (SEM) was done using a Versa 3D Dual Beam from Thermo Fisher (formerly FEI) armed with a field-emission gun dual focused ion beam device. For SEM microstructure analysis, secondary-electron (SE) and backscattered electron (BSE) imaging were utilized. To analyze the solidification behavior, the phase morphology, as well as the orientation relationship (OR), electron backscatter diffraction (EBSD) was performed on the previously mentioned SEM system with a Hikari XP EBSD camera from EDAX. The EBSD data were recorded and evaluated via TSL OIM Analysis 7. Besides low-angle grain boundaries, which are marked in color within the single grains, black lined high-angle grain boundaries reveal a grain deviation of >15° to the neighboring grains. The EBSD measurement parameters were 20 kV acceleration voltage, 350 nm step size, a spot size of 7, and 4 × 4 binning mode. As the material shows

a liquid → β → α' phase transformation sequence, it is important to investigate the β solidification process from the liquid phase. While the subsequent solid-state martensitic phase transformation conceals the parent β phase, the solidified microstructure was reconstructed from EBSD data using the program ARPGE from Cayron.<sup>[30,31]</sup> TEM investigations were performed using an FEI Tecnai F20 G2 from Thermo Fisher with an acceleration voltage of 200 kV. The images were recorded using bright field (BF), dark field (DF), or high-angle annular dark-field scanning TEM (HAADF-STEM) mode.

## 2.3. Phase Transformation Studies

The β-transus temperature was determined via differential scanning calorimetry (DSC) using a Labsys Evo from Setaram operating at the heating rates of 15, 20, and 30 K min<sup>-1</sup>. The X-ray diffraction (XRD) measurements were performed on a D8 Advance diffractometer from Bruker using a Cu-K<sub>α</sub> X-ray source with a wavelength of 0.154 nm. The measurements were performed in coupled 2-θ mode.

Thermodynamic simulations were performed using the Thermo-Calc 4.1 software,<sup>[32]</sup> utilizing the TCT12 database.

## 2.4. Tensile Testing

The stress-relieved Ti6242S and Ti64 tensile specimens produced by SLM were tested at RT in accordance with DIN EN 2002.<sup>[33]</sup> As the target parts are exposed to the temperatures of up to 500 °C in use, the tensile tests of the Ti6242S alloy were also performed at these temperatures to gain knowledge of the mechanical properties under these circumstances according to ISO 6892.<sup>[34]</sup>

The equipment used for tensile test was provided by Messphysik, namely, Systems 167 and 301 at RT, and 1008 and 1013 at elevated temperatures. To strengthen the statistical significance, all temperatures and sample conditions were tested at least three times. At the beginning of the tensile tests, low strain (LS) rates of about  $0.85 \times 10^{-4} \text{ s}^{-1}$  were applied until a certain strain ( $\epsilon > 0.2$ ) was reached. Thereafter, the strain rates were increased to  $8.5 \times 10^{-4} \text{ s}^{-1}$  to speed up the tensile test.

## 3. Results

### 3.1. As-Built Microstructure

**Figure 1** shows the LOM images of the etched as-built microstructure of a Ti6242S (Figure 1a,b) and Ti64 (Figure 1c,d) sample for comparison. The marked BD in Figure 1a is perpendicular to the building platform. Note that all following microstructure images were taken in the same orientation. It is shown that the images of the Ti6242S specimen show horizontal

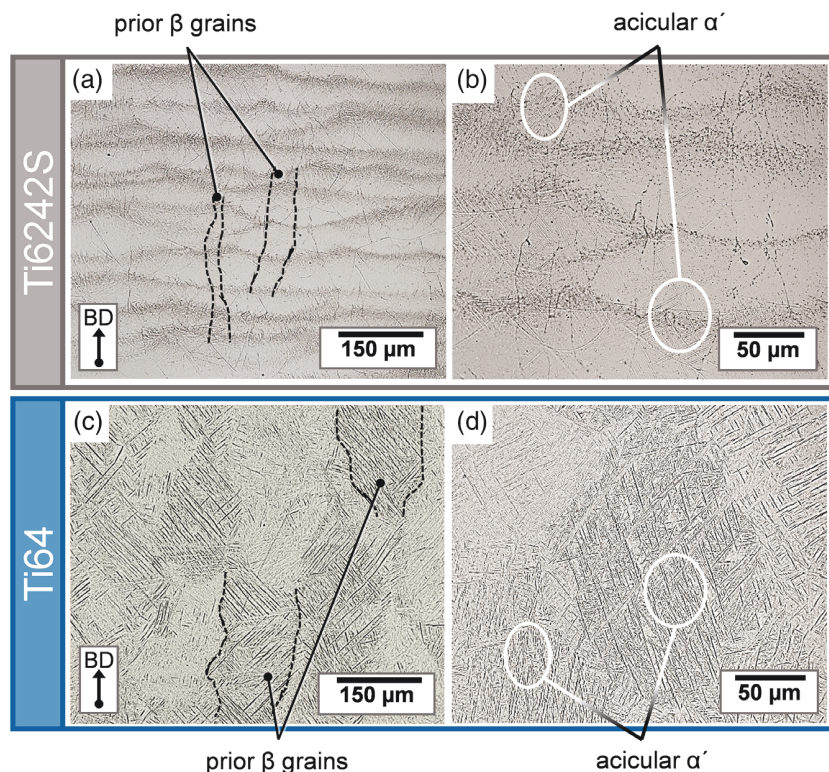


**Figure 1.** LOM images of the as-built microstructure of Ti6242S and Ti64: a,b) LOM images of the as-built microstructure revealing melt pool boundaries for the Ti6242S specimen and vertically orientated prior  $\beta$  grains. The LOM images with a higher magnification show prior  $\beta$  grains, which contain acicular-like martensitic  $\alpha'$  (encircled). c,d) The as-built microstructure of the reference Ti64 alloy is shown.

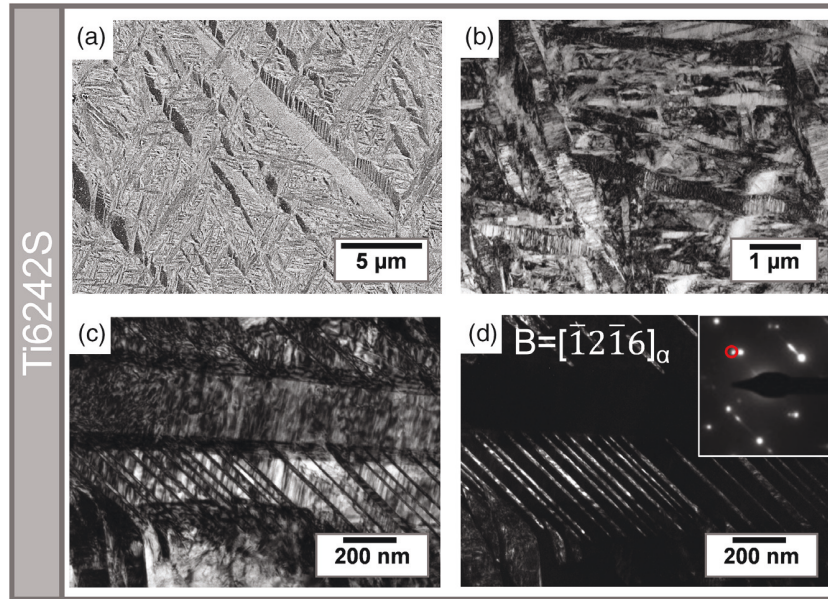
orientated dark bands. The occurrence of these so-called “layer bands”, which represent melt pool boundaries, is also reported in case of as-built Ti64 material by several authors.<sup>[25,35]</sup> According to this, Thijs et al.,<sup>[12]</sup> for example, measured an alternating Al content over several layers, which can be assigned to the cooling rate gradient within each melt pool. As a consequence, the layer bands show different chemical attack by the etchant. Figure 1a,b shows “layer bands” which typically occur in all Ti-based alloys manufactured by SLM. The absence of these layers in the images shown in Figure 1c,d can be attributed to the choice of the etching times, which were too short to contrast the slight chemical inhomogeneities of the Ti64 sample. The impact of these “layer bands” on the mechanical properties is comparatively small due to the applied post-process heat treatment, which reduces the inhomogeneities.

Prior  $\beta$  grain boundaries are indicated by dashed lines; see Figure 1a,c. The size of these prior  $\beta$  grains in the Ti6242S specimens as well as in the Ti64 material varies over a large scale, in length and width. Even though both specimens are produced with nearly the same processing parameters, the width of the prior  $\beta$  grains, which were measured with LOM, ranges from  $46 \pm 25 \mu\text{m}$  for the Ti6242S specimen to  $83 \pm 30 \mu\text{m}$  for the reference Ti64 material. More pronounced is the length deviation of these grains, which can reach several hundred micrometers. Within the prior  $\beta$  grains in case of the Ti6242S sample, acicular-like microstructural constituents occur (encircled in the

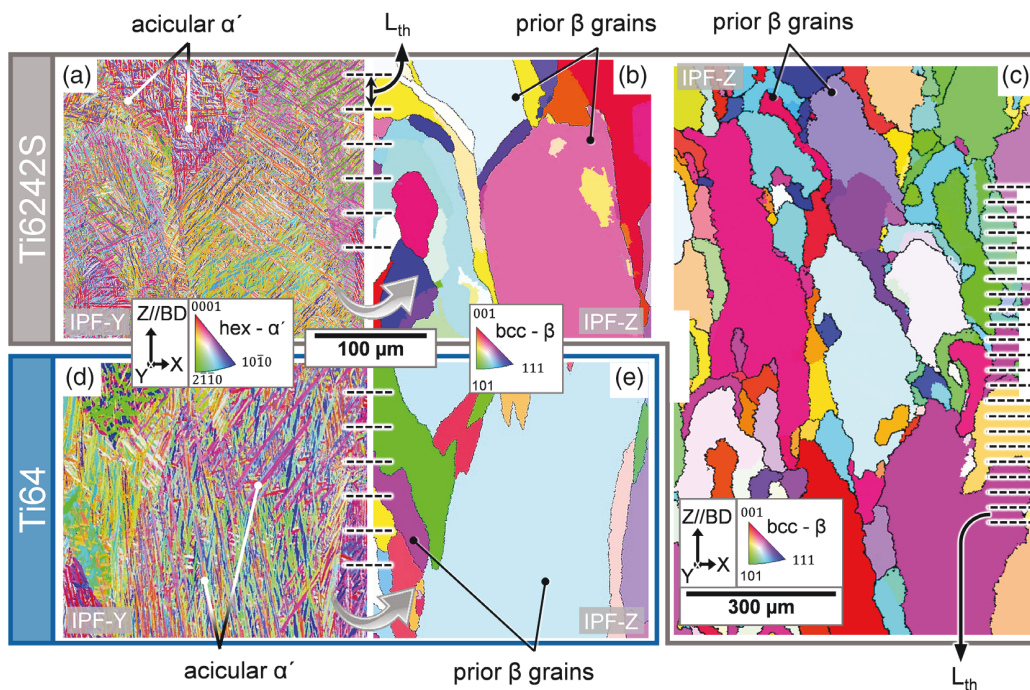
enlarged image in Figure 1b), which represent the martensitic  $\alpha'$  phase in the as-built condition. The martensitic  $\alpha'$  phase of the Ti64 specimen is more visible in Figure 1d, where the acicular microstructure arises from the  $\beta$  grains.

Figure 2a shows an SEM image of the as-built microstructure of the Ti6242S sample in BSE mode, revealing a fine acicular  $\alpha'$  microstructure. Furthermore, TEM investigations of the as-built microstructure shown in Figure 2b stated a high density of lattice defects and mechanical twins within the  $\alpha'$  needles. Such internal twinning in  $\alpha'$  is stated to occur during the martensitic transformation induced by a series of sharp thermal cycles during the SLM process.<sup>[36]</sup> A clear validation of the presence of mechanical twins is given in the selected area DF image of Figure 2c,d. It is shown that the selected spot (encircled in red) of the hexagonal  $[\bar{1}2\bar{1}6]_{\alpha}$  diffraction pattern only highlights twin features.

To gain knowledge of the microstructure formation during SLM, EBSD measurements were conducted on the as-built Ti6242 (Figure 3a–c) and Ti64 (Figure 3d,e). Figure 3a,d shows the inverse pole figure (IPF) maps of the fully hex SLM specimens. All prior  $\beta$  grains in Ti6242S and Ti64 contain martensitic  $\alpha'$  exhibiting an acicular-like morphology. A texture analysis reveals the occurrence of a crystal orientation, namely, the Burgers OR<sup>[6]</sup> for both, the Ti6242S and Ti64 samples. Therefore, the underlying crystallographic orientations within a single  $\beta$  grain are limited by this relationship, which governs



**Figure 2.** a) SEM image taken in BSE mode of the as-built Ti6242S microstructure showing the acicular  $\alpha'$  martensite. b) BF TEM image revealing a high density of lattice defects as well as mechanical twins. c) BF and d) DF images confirming the occurrence of mechanical twins. The insert shows the corresponding  $[\bar{1}2\bar{1}6]_{\alpha}$  diffraction pattern of the hexagonal structure and the selected spot (encircled in red) for the DF image (see text).



**Figure 3.** a–c) Results of EBSD analysis for the Ti6242S specimens and d,e) the reference Ti64 sample. IPF maps of the as-built martensitic microstructure of the Ti6242S and Ti64 specimens showing hexagonal  $\alpha'$  martensite within the prior  $\beta$  grains. b,e) Reconstructed prior  $\beta$  grain structure (with respect to the z-axis) of the area already shown using ARPGE,<sup>[30,31]</sup> representing the epitaxial growth of the grains over several deposited layers, where the thickness of the layers ( $L_{th}$ ) is drawn with dashed lines. c) Large-scale prior  $\beta$  grain structure (with respect to the z-axis) of the Ti6242S specimen.

the martensitic transformation  $\beta \rightarrow \alpha'$ . According to the Burgers OR,<sup>[6]</sup> the prior  $\beta$  grains of Figure 3b,c,e were reconstructed with the software ARPGE and displayed as IPF-Z maps; i.e., the EBSD maps were shown relative to the z-axis.<sup>[30,31]</sup> It appeared that the prior  $\beta$  grains show epitaxial growth during the SLM process, which occurs over several layers. Furthermore, the layer thickness  $L_{th}$  is related to the distances between the occurring layer bands parallel on the BD, shown in Figure 1. The large scale EBSD map in Figure 3c visualizes the dimensions of the growth of the  $\beta$  grain growth which reach more than 0.5 mm in length. This IPF-Z map (with respect to the z-axis) also shows the solidification direction of  $\beta$  grains. It can be shown that there is no indication for an overall [100] growth of  $\beta$  grains, i.e., no fiber texture, during the SLM process. Referring to Liu and Shin,<sup>[25]</sup> the size and morphology of these prior  $\beta$  grains are connected to anisotropic mechanical properties. These authors also reported that the prior  $\beta$  grain morphology can be controlled by the SLM process parameters.

Figure 4 shows the results of  $\alpha'$  grain size and grain morphology evaluation of the Ti6242S and Ti64 specimens. Due to the acicular shape of  $\alpha'$ , it is appropriate that the EBSD grain shape calculations via the TSL OIM Analysis 7 software are displayed as major and minor axes, i.e., the length of the longitudinal and lateral axis, as shown in Figure 4a. The density distribution  $q_2$  represents the fraction of grains within a class interval based on the area, whereas the cumulated values are shown as the cumulative distribution  $Q_2$ . As shown in Figure 4b,c, the major and minor axes of  $\alpha'$  in the Ti64 specimen are larger than those

**Table 3.** Average grain size of martensitic  $\alpha'$  in Ti6242S and Ti64 samples. The results shown in the following represent the  $d_{50}$  values of the cumulative fraction  $Q_2$ , see text.

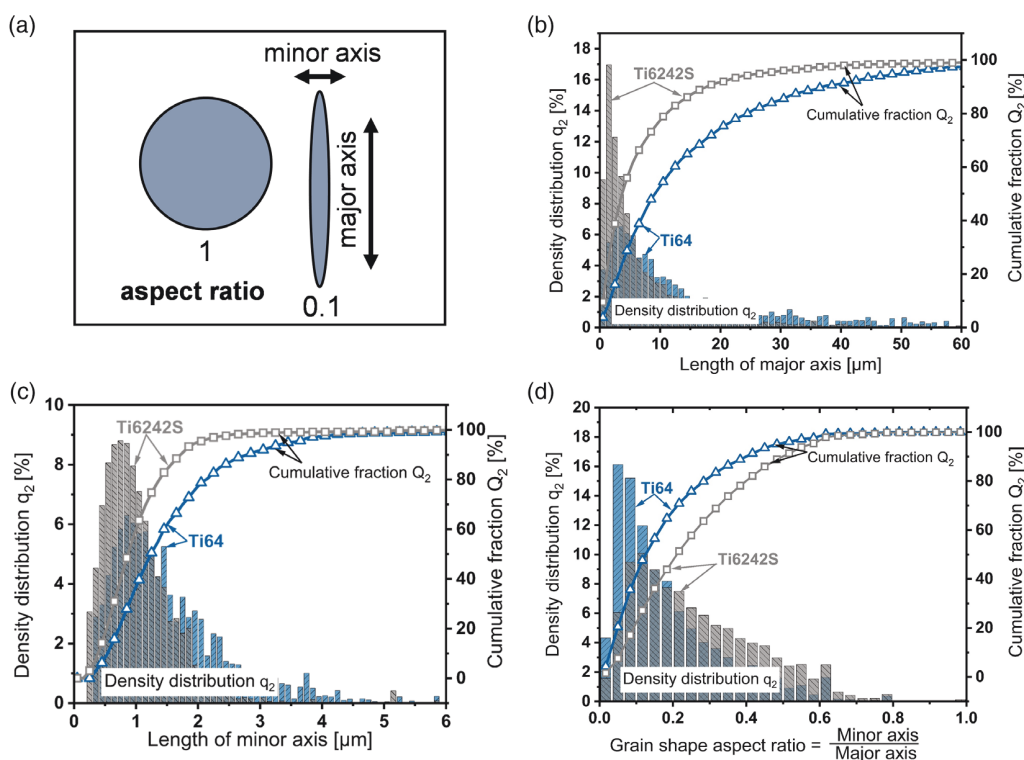
Alloy	Type	$d_{50}$ —major axis [ $\mu\text{m}$ ]	$d_{50}$ —minor axis [ $\mu\text{m}$ ]
Ti6242S	As-built	8.30	1.06
Ti64	As-built	16.13	1.53

of the grains of Ti6242S. A calculation of the average length of the major and minor axes, conducted over all grains, is given in Table 3. These results show that the average length of the major axis of the Ti64 alloy is nearly twice as large as the average length of the major axis of Ti6242S.

Moreover, the average length of the minor axis of the martensitic  $\alpha'$  in Ti6242S is about 1.06  $\mu\text{m}$  when compared with the average length of the minor axis of 1.53  $\mu\text{m}$  in the Ti64 reference material. The grain shape aspect ratio, which is defined as the length of the minor axis divided by the length of the major axis, is shown in Figure 4d. The relation between minor and major axes is more pronounced for the Ti64 material; i.e., the grain morphology for Ti6242S is more elliptical in shape.

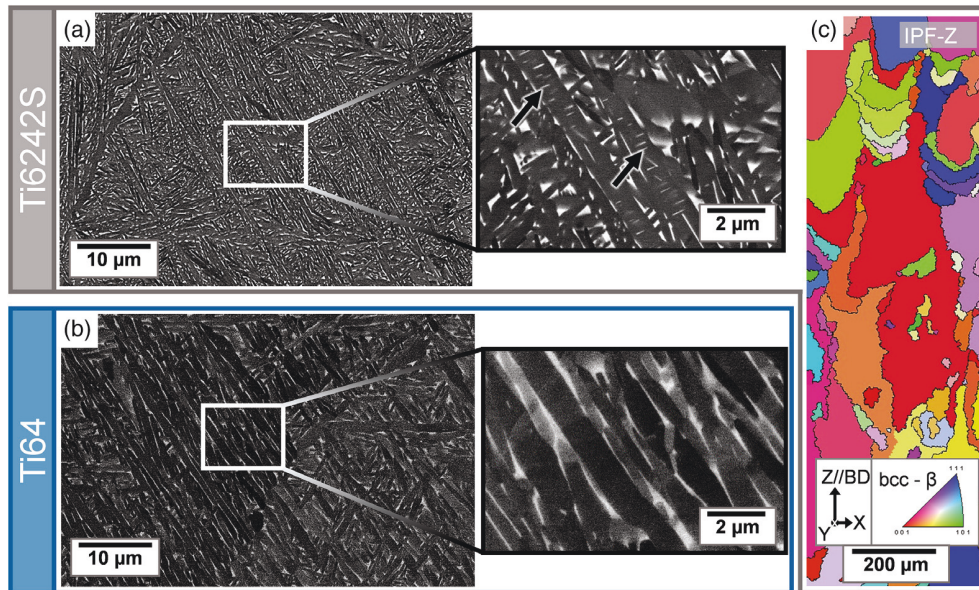
### 3.2. Heat-Treated Microstructure

Figure 5a,b shows the SEM-BSE images of the heat-treated microstructures, which were exposed to an SRA process



**Figure 4.** a) The acicular shape of  $\alpha'$  leads to the definition of major and minor axes as well as the aspect ratio as schematically drawn here. The EBSD  $\alpha'$  size evaluation shows that the length of the b) major and c) minor axes of the Ti6242S sample is smaller than that of the Ti64 reference material. d) The grain shape calculation reveals a higher aspect ratio for the acicular  $\alpha'$  grains in the Ti6242S specimen when compared with the Ti64 specimen.





**Figure 5.** SEM-BSE images of the SRA microstructures of the a) Ti6242S and b) Ti64 alloys showing an acicular microstructure. The precipitated  $\beta$  phase appears bright due to the high content of the  $\beta$  stabilizing elements (see text). The image of the Ti6242S specimen with a higher magnification shows small  $\beta$  precipitates (indicated by arrows) within the former  $\alpha'$  needles when compared with the Ti64 specimen in (b). c) Reconstructed prior  $\beta$  grain structure using ARPGE,<sup>[30,31]</sup> showing an overview image of the SRA Ti6242S sample.

(800–850 °C, 1–3 h). It is shown that the acicular-like appearance of the martensitic  $\alpha'$  phase remains but coarsens during the subtransus SRA treatment. In addition, the SRA process leads to the precipitation of the bcc  $\beta$  phase according to  $\alpha' \rightarrow \alpha + \beta$ , which appears bright due to the enrichment of heavier  $\beta$  stabilizing elements. For the Ti6242S sample, the  $\beta$  phase is enriched in Mo (see Chapter 3.4.) when compared with the V-enriched  $\beta$  phase in the Ti64 material. This precipitated  $\beta$  phase occurs mainly at  $\alpha$  grain boundaries. A closer observation at the higher magnification of Figure 5a reveals small rod-like  $\beta$  precipitates within enlarged  $\alpha$  grains, indicated by arrows. Figure 5c shows an overview image of the prior  $\beta$  microstructure reconstructed via ARPGE.<sup>[30,31]</sup> It is shown that the elongated parent microstructure still exists after the SRA treatment exhibiting similar sizes of prior  $\beta$  grains ( $47 \pm 13 \mu\text{m}$  in width). Figure 5b shows that for the Ti64 specimen, the  $\beta$  phase only occurs at former  $\alpha'$  needle boundaries, when compared with the Ti6242S sample.

To examine the characteristics of the present phases, TEM investigations of the SRA Ti6242S sample were conducted. **Figure 6a** shows an HAADF-STEM image of the microstructure revealing lattice defects, e.g., former twins, which act as nucleation sites for  $\beta$  phase precipitations within the hexagonal  $\alpha$  structure. The bright phase can be designated as  $\beta$  phase due to the enrichment in heavy elements, such as Mo,<sup>[37]</sup> which can be seen because of the atomic number (Z) contrast of the STEM in HAADF mode. According to Haubrich et al.,<sup>[38]</sup> 1D and 2D lattice defects act as potential sites for  $\beta$  phase nucleation, which can be seen via the occurrence of rod-like precipitations within the  $\alpha$  phase boundaries in the TEM-BF image of Figure 6b. The corresponding diffraction pattern, which is tilted in  $[0001]_{\alpha}$  zone axis of the matrix phase, reveals the reported

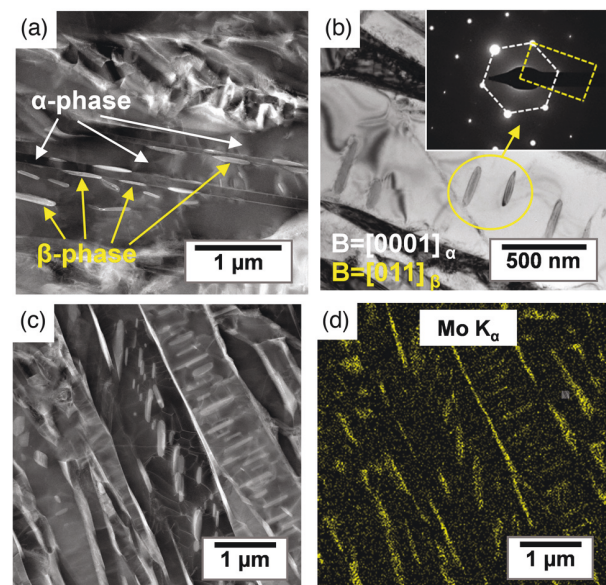


**Figure 6.** a) HAADF-STEM image of the SRA microstructure of the Ti6242S sample showing an  $\alpha$  needle and  $\beta$  precipitates forming along  $\alpha$  as well as lattice defects (twin boundaries). b) BF image of the SRA microstructure tilted in  $[0001]_{\alpha}$  zone axis of the matrix phase. The insert shows the corresponding diffraction pattern and reveals the  $\{0001\}_{\alpha} // \{110\}_{\beta}$ ,  $\langle 11\bar{2}0 \rangle_{\alpha} // \langle 111 \rangle_{\beta}$  Burgers OR.<sup>[6]</sup> c,d) Show a microstructure image taken in HAADF-STEM mode and the associated TEM-EDX map, respectively, which reveals a Mo enrichment in the  $\beta$  phase.

Burgers OR  $\{0001\}_{\alpha} // \{110\}_{\beta}$ ,  $\langle 11\bar{2}0 \rangle_{\alpha} // \langle 111 \rangle_{\beta}$ <sup>[6]</sup> between the  $\alpha$  matrix and the  $\beta$  precipitates of the Ti6242S alloy. In addition,

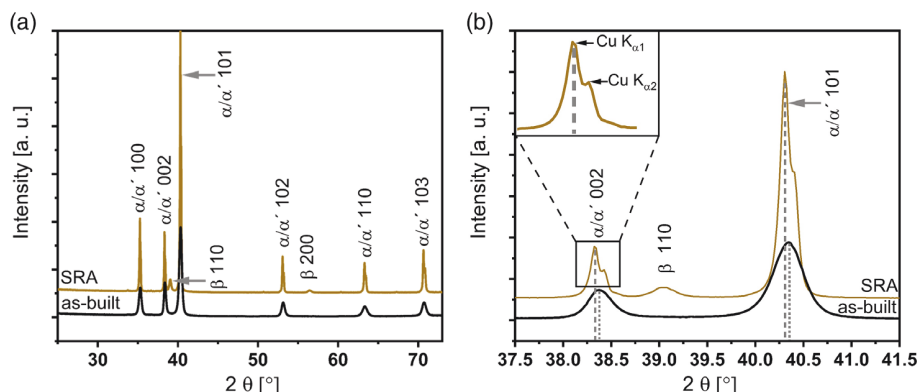


**Figure 7.** a) XRD plot of the Ti6242S material in as-built and heat-treated (SRA) condition. b) Selected section of the XRD plot, which reveals that the  $\alpha/\alpha'$  peaks are shifted to lower  $2\theta$  angles (indicated with dashed lines) in the cause of the heat treatment, which also causes the additional  $\beta$  peaks.

it has been shown that the density of lattice defects decreased after the SRA process for the Ti6242S specimen. STEM energy-dispersive X-ray spectroscopy (EDX) confirms the enrichment of Mo in the  $\beta$  phase, which is shown using the example of the HAADF-STEM image in Figure 6c and the associated STEM-EDX map in Figure 6d.

### 3.3. Phase Analysis via XRD

The identification of the phases in the as-built and the SRA condition was possible by means of XRD. The XRD pattern of as-built Ti6242S, as shown in Figure 7a, gives evidence that there is only a single hexagonal phase present. As both phases,  $\alpha$  and  $\alpha'$ , exhibit a hexagonal structure with almost similar lattice parameters,<sup>[39]</sup> it is not possible to distinguish between them, and thus, the results are designated as  $\alpha/\alpha'$ . In comparison, the SRA sample shows additional peaks linked to the bcc  $\beta$  phase. The section of the XRD spectra shown in Figure 7b also reveals that the peak positions of the SRA sample are shifted to lower  $2\theta$  angles (indicated with dashed lines) when compared with the as-built sample (dotted lines). According to Bragg's law ( $2 \cdot d_{hkl} \cdot \sin(\theta) = n \cdot \lambda$ ), the shift in peak position may be a consequence of diffusion processes and changed lattice parameters,<sup>[8]</sup> which will be discussed later in this article. An SRA treatment of an as-built sample leads to a relaxation of printing-induced non-equilibrium microstructures and associated microscale residual stresses in general.<sup>[8]</sup> Therefore, a smaller full width at half maximum in the SRA-treated condition is indicative of  $\alpha'$  decomposition followed by  $\alpha$  grain growth. As it is shown in the magnified spectra in Figure 7b, there are additional  $\text{Cu } K_{\alpha 2}$  peaks<sup>[40]</sup> in case of the SRA sample, which result out of the high peak intensities ( $>100\,000$  counts for the  $\alpha/\alpha'$ -101) peak). The  $\text{Cu } K_{\alpha 2}$  peak does not appear for the  $\beta$  phase in the SRA sample as well as for the as-built specimen due to the broaden peaks, which conceal the  $\text{Cu } K_{\alpha 2}$  features.

### 3.4. Determination of the $\beta$ -Transus Temperature

Before applying a post-process heat treatment on as-built samples, it is of great importance to know the exact temperature

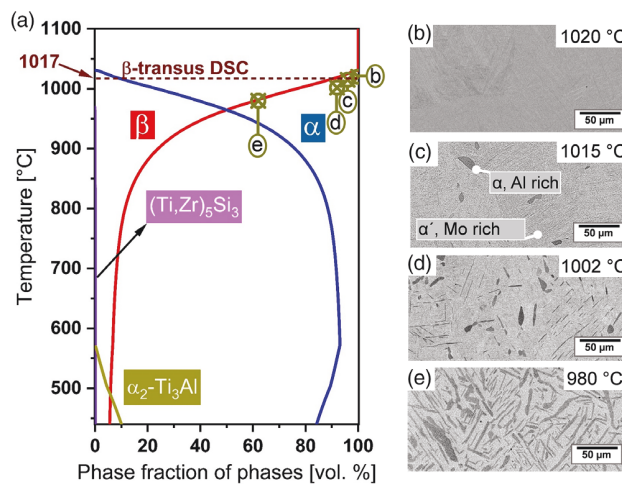


**Figure 8.** a) Thermo-Calc<sup>[32]</sup> phase fraction diagram based on the chemical composition of the Ti6242S as-built material with additional indications of the experimental measured phase fractions of the heat treatment study and DSC. SEM-BSE images of the microstructures after a post-process heat treatment at b) 1020 °C, c) 1015 °C, d) 1002 °C, and e) 980 °C with a dwell time of 8 h followed by WQ. The dark phase corresponds to the  $\alpha$  phase, whereas the light phase is martensitic  $\alpha'$  phase transforming from  $\beta$  during WQ (see text).

values of the occurring phase transformations, especially the  $\beta$ -transus temperature. Therefore, DSC measurements were conducted to determine this particular temperature of the AM Ti6242S alloy. It was found that the  $\beta$ -transus temperature is about  $1017 \pm 3$  °C, which matches with the results derived from heat treatment studies as well as Thermo-Calc<sup>[32]</sup> calculations; see Figure 8. As shown in Figure 8a, the thermodynamic calculation, based on the actual chemical composition of the Ti6242S as-built material, exhibits an equilibrium phase composition, including  $\alpha$ ,  $\beta$ , silicides as well as a certain amount of the intermetallic  $\alpha_2\text{-Ti}_3\text{Al}$  phase, depending on the temperature. Furthermore, these generated data via Thermo-Calc revealing a  $\beta$ -transus temperature, which is slightly higher, namely, 1030 °C. Figure 8b–e shows the microstructures of the

complementary heat treatment studies at 1020, 1015, 1002, and 980 °C, respectively, with a dwell time of 8 h, followed by WQ. During heating, the  $\beta$  phase content increases until the  $\beta$ -transus temperature is reached. Thus, microstructures exposed to the heat treatment followed by WQ consist of the coarse  $\alpha$  phase (dark) and martensitic  $\alpha'$  phase (bright). The martensitic  $\alpha'$  phase, which formed from the  $\beta$  phase due to high cooling rate during WQ, shows the same chemical composition as the parent  $\beta$  phase. Increasing temperatures, from 980 °C up to 1020 °C, raise the experimental measured  $\beta$  phase content (quantitative phase content analysis via LOM) from 62 vol% to 100 vol%, respectively, with a proportion of 92 vol% at 1002 °C and 96 vol% at 1015 °C. Quantitative EDX-SEM measurements on the sample (Figure 8c) show that the bright  $\alpha'$  phase contains almost the entire content of the  $\beta$  stabilizing element Mo (2.1 m% in  $\alpha'$  compared with 0.5 m% in  $\alpha$ ), whereas the dark  $\alpha$  phase is enriched with the  $\alpha$  stabilizing element Al (5.9 m% in  $\alpha'$  compared with 6.9 m% in  $\alpha$ ).

### 3.5. Mechanical Properties

Tensile tests were conducted to evaluate the mechanical properties of the Ti6242S material at RT as well as at high temperatures. All tests were performed on tensile test specimens in the heat-treated (SRA) condition. The stress–strain curves for the Ti6242S tensile tests at RT and elevated temperatures are displayed in Figure 9a. The results show that with increasing test temperature, the UTS and 0.2% yield strength (YS) decrease, whereas the ductility increases when compared with RT. Rising temperatures result in activation of additional slip systems and the reduction of the critical resolved shear stress (CRSS) as diffusion processes start to play a significant role in plastic deformation.<sup>[6,41]</sup> A comparison of mechanical properties and reference values from the literature<sup>[23]</sup> of cast and heat-treated Ti–6Al–2Sn–4Zr–2Mo is given in Figure 9b (right) and is summarized in Table 4. In addition, the mechanical properties of the reference SRA Ti64 material are added for comparison. At RT, SLM

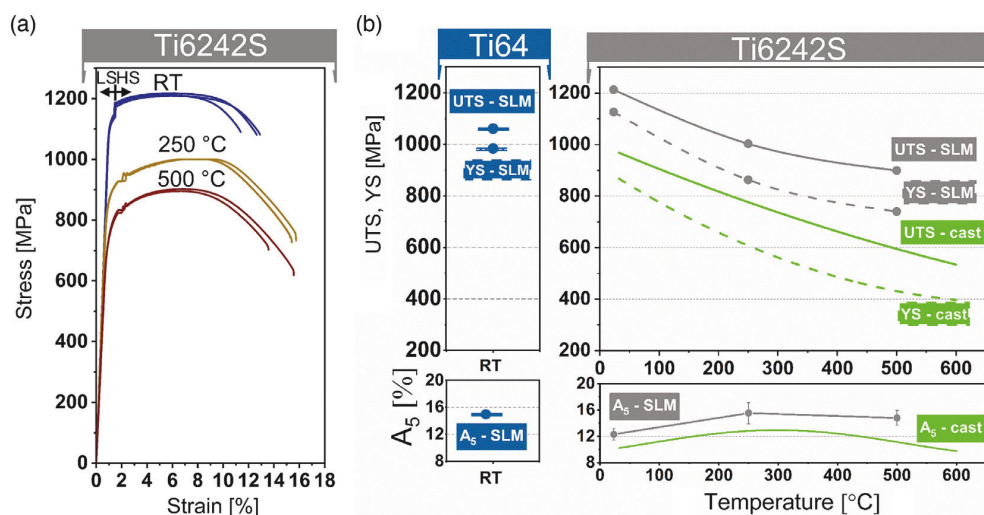


**Figure 9.** a) Stress–strain curves from tensile tests conducted at RT, 250 and 500 °C on heat-treated (SRA) SLM Ti6242S specimens. The strain rates were increased from LS rates, until a certain strain was reached, to high strain (HS) rates to accelerate the tensile test procedure. b) The mechanical properties reveal an increase in the strength of SLM Ti6242S specimens when compared with the SRA reference Ti64 material and literature<sup>[23]</sup> values of cast and heat-treated Ti6242. Moreover, at RT, SLM Ti64 specimens have the highest ductility followed by SLM Ti6242S and cast Ti6242.

**Table 4.** Mechanical properties of the investigated SLM manufactured Ti6242S and Ti64 specimens and values from reference studies for comparison.<sup>[19,23]</sup>

Specimen	T [°C]	UTS [MPa]	YS [MPa]	Elongation at fracture A <sub>5</sub> [%]	Reference
SLM Ti6242S—SRA	RT	1213 ± 4	1126 ± 9	11.3 ± 0.6	Present study
SLM Ti6242S—SRA	250	1003 ± 1	863 ± 5	14.8 ± 0.2	Present study
SLM Ti6242S—SRA	500	899 ± 5	740 ± 18	13.8 ± 1.0	Present study
Ti6242—cast + annealed	RT	968	867	10.2	[23]
Ti6242—cast + annealed	250	776	607	12.8	[23]
Ti6242—cast + annealed	500	594	430	11.1	[23]
SLM Ti64—SRA	RT	1061 ± 5	984 ± 10	14.6 ± 0.3	Present study
SLM Ti6242—as-built	RT	1381 ± 79	1293 ± 37	5.3	[19]
SLM Ti6242—annealed	RT	1438 ± 103	–	1.4	[19]

Ti6242S specimens exhibit higher UTS (1213 MPa) and YS (1126 MPa) values when compared with the reference SLM Ti64 (UTS = 1061 MPa, YS = 984 MPa). The higher strength of the SLM Ti6242S specimens goes along with a loss of ductility ( $A_5 = 11.3\%$ ) compared with the reference Ti64 samples ( $A_5 = 14.6\%$ ). The differences are even more pronounced when comparing with the cast and heat-treated Ti6242 from the literature.<sup>[23]</sup> The SLM produced Ti6242S samples have a UTS of about 899 MPa at 500 °C; see Figure 9b.

Donachie<sup>[23]</sup> also showed a difference in tensile properties between the Ti64 and Ti6242 alloys at elevated temperatures. Increasing the temperatures of up to 400 °C leads to a similar decrease in the tensile strength values for both alloys, T64 and T6242S. At the temperatures above 400 °C, a significant drop of tensile strength was found only for the alloy Ti64, which strongly limits the application potential at high temperatures.

## 4. Discussion

### 4.1. Evolution of the Microstructure

During SLM, the pre-alloyed powder is melted, solidified, and exposed to a cyclic heating procedure several times until the as-built sample obtains its final form.<sup>[24]</sup> As  $\alpha + \beta$  alloys solidify via the single  $\beta$  phase field region, size and morphology of the prior  $\beta$  grains are of great interest. The EBSD measurements and the following ARPE<sup>[30,31]</sup> calculations of the Ti6242S specimens show an epitaxial growth of the polycrystalline material, which results in elongated  $\beta$  grains over several layers. Orientation deviations of the prior  $\beta$  grains are the result of heat dissipation effects,<sup>[42]</sup> which are linked to processing parameters, such as scanning speed or laser power. In addition, the elongated grains might lead to a certain amount of anisotropy in terms of mechanical properties, as reported in the literature for SLM produced Ti64.<sup>[25]</sup> The  $\beta$ -transus temperature was determined via DSC investigations and complementarily evaluated by heat treatment experiments and thermodynamic calculations via Thermo-Calc.<sup>[32]</sup> The DSC obtained  $\beta$ -transus temperature ( $1017 \pm 3$  °C) fits very well with the complementary results of the heat treatment study, where the dissolution of the Al-rich  $\alpha$  phase is reached at 1020 °C and the thermodynamically calculated temperature value.

Cooling rates up to  $10^4$ – $10^6$  K s<sup>-1</sup> <sup>[43]</sup> lead to a martensitic transformation ( $\beta \rightarrow \alpha'$ ) of the  $\beta$  phase during SLM processing. As it is hard to distinguish between  $\alpha$  and  $\alpha'$  due to the similar lattice parameters, a differentiation is only possible in an indirect way. Therefore, SEM-BSE imaging and EBSD measurements were used to obtain complementary information about the present phases. The chemical homogeneity of the as-built Ti6242S material and the absence of the  $\beta$  phase in the EBSD evaluations leads to the conclusion that the hexagonal  $\alpha/\alpha'$  phase is predominant and supersaturated in the  $\beta$  stabilizing elements after the SLM process. Several researchers studied the occurrence of mechanical twins in Ti alloys produced via SLM.<sup>[8,27]</sup> They reported that mechanical twins mostly occur in martensitic microstructures, which were also observed in this study; see Figure 2. This leads to the assumption that the investigated SLM Ti6242S specimens consist mainly of  $\alpha'$  martensite.

Furthermore, the as-built microstructure is far from thermodynamic equilibrium when compared with the calculated Thermo-Calc<sup>[32]</sup> simulation results.

Regarding grain size examinations, it was shown that the acicular  $\alpha'$  microstructure is finer for the Ti6242S specimen, which is believed to be a result of expansion limitations during the martensitic phase transformation ( $\beta \rightarrow \alpha'$ ) caused by chemical differences of the two investigated alloys.<sup>[44]</sup> According to Figure 1, the prior  $\beta$  microstructure of the Ti6242S sample is smaller when compared with the reference material. Birmingham et al.<sup>[44]</sup> reported that the growth restriction factor is higher for the Ti6242S when compared with Ti64 and, thus, significantly influences the prior  $\beta$  grain size. As the prior  $\beta$  grain boundaries are insuperable barriers for the growth of  $\alpha'$ , a smaller parent  $\beta$  grain results in smaller  $\alpha'$  martensitic features, which were measured in this study; see Figure 4.

Texture analysis, which was also conducted by the evaluation of the EBSD data, confirms Burger's OR  $\{0001\}_\alpha // \{110\}_\beta$ ,  $\langle 11\bar{2}0 \rangle_\alpha // \langle 111 \rangle_\beta$ ,<sup>[6]</sup> which stands for the  $\beta$  to  $\alpha'$  transformation. Therefore, it limits the possible orientations of the hexagonal phase formed from a single parent  $\beta$  grain to 12 variants.<sup>[6]</sup> As the whole specimen consists of several prior  $\beta$  grains comprising similar crystallographic orientations, the behavior of the material is predominantly affected by the appearance of the parent  $\beta$  microstructure.

### 4.2. Heat Treatment

The requirement of a certain amount of ductility is often ensured by subsequent heat treatments below the  $\beta$ -transus temperature. It was shown that the acicular appearance of the  $\alpha$  grains still exists, after a sub-transus SRA process. Furthermore, the prior  $\beta$  microstructure, i.e., elongated  $\beta$  grains along the BD, has not changed in size during the heat treatment process. It can be assumed that remaining  $\alpha$  grains pin the  $\beta$  grain boundaries and suppress  $\beta$  grain growth in the cause of the SRA process.<sup>[45]</sup> In addition, a heat treatment temperature of about 800–850 °C provides a rather small driving force for fast grain growth. Nevertheless, a heat treatment of the martensitic  $\alpha'$  microstructure of the as-built specimens leads to the precipitation of the  $\beta$  phase, as shown in the XRD plot in Figure 7, and indicates the decomposition of the martensitic microstructure according to  $\alpha' \rightarrow \alpha + \beta$ . During the decomposition process of the martensitic  $\alpha'$  microstructure, Mo diffuses from the interior to the grain boundary. Mo has a smaller atomic radius of 0.139 nm compared with the atomic radius of Ti of 0.147 nm.<sup>[46,47]</sup> The precipitation of this Mo-enriched  $\beta$  phase shifts, therefore, the  $\alpha$  peak to lower  $2\theta$  angles due to the decrease in the Mo content in the  $\alpha$  phase. Besides the loss of Mo in the  $\alpha$  phase, the reduction of residual stresses and the reduced defect density due to the SRA process might also be a consequence of the changing lattice parameter.<sup>[48]</sup>

Fundamental investigations in the past<sup>[49]</sup> reported a quiet different diffusion coefficient of Mo ( $2.64 \cdot 10^{-15}$  cm<sup>2</sup> s<sup>-1</sup>) compared with V ( $3.91 \cdot 10^{-15}$  cm<sup>2</sup> s<sup>-1</sup>) in  $\alpha$ -Ti at 600 °C. Based on that, the occurrence of small  $\beta$  precipitates within  $\alpha$  grains (Figure 5) can be assigned to the lower diffusivity of Mo when compared with the  $\beta$  stabilizer V (atomic radius of about 0.132 nm) in the

reference Ti64 specimens. Furthermore, the  $\beta$  phase precipitation within the  $\alpha$  grains occurs along lattice defects, such as twin boundaries. Thermodynamic simulations predict a certain amount of  $\alpha_2$ -Ti<sub>3</sub>Al phase as well as silicides. However, neither  $\alpha_2$ -Ti<sub>3</sub>Al nor silicides were determined via XRD in the heat-treated condition. The formation of the  $\alpha_2$  phase, with  $2\theta$  superlattice diffraction positions at 26° and 31°, requires Al-rich areas, which can be a result of diffusion processes during sub-transus heat treatments in Ti alloys with an Al content above 6 m%.<sup>[6]</sup> Nonetheless, the thermodynamic calculations in Figure 8 suggest an  $\alpha_2$ -solvus temperature of about 540 °C, which lies significantly below the applied SRA temperature. Therefore, it is assumed that  $\alpha_2$  phase precipitation was suppressed. Although thermodynamic simulations also suggest silicides in Ti6242S even at the heat treatment temperatures of about 800–850 °C, there is no indication for the presence of this phase in XRD. For XRD, however, a certain volume fraction of a single phase is needed for detection. Therefore, it has to be considered that the potential silicide content was too small to be determined by means of XRD.

### 4.3. Mechanical Properties

Tensile tests were performed to investigate the mechanical properties of the SRA SLM Ti6242S alloy in comparison with the SRA reference SLM Ti64 material and literature results.<sup>[19,23]</sup> Figure 9 shows that the SLM Ti6242S alloy provides higher strength values than the SLM reference alloy Ti64 along with the Ti6242 cast and heat treated material.<sup>[23]</sup> High-temperature tensile tests at 250 and 500 °C revealed that the tensile strength of SLM manufactured Ti6242S also exceeded the values for cast and annealed Ti6242 specimens with a good balance of ductility. No significant drop in tensile strength was noted, as reported in the literature.<sup>[23]</sup> The enhanced mechanical properties of Ti6242S can be attributed to multiple reasons, such as grain refinement or the influence of alloying elements, in particular interstitials. The correlation between grain size and strength of polycrystalline materials can be described using the empirical equation of Hall–Petch according to  $\sigma \propto 1/\sqrt{D}$ ,<sup>[50,51]</sup> where  $D$  is the grain diameter. Thus, a decrease in grain size, as it was observed for SLM Ti6242S, results in a higher strength level. Furthermore, the alloying elements Sn and Zr are added, which both are solid solution strengtheners of the  $\alpha$  phase and, moreover, the interstitials O and N are also known to further strengthen the material.<sup>[6]</sup> As shown in the chemical composition, the Ti6242S alloy exhibits almost twice as much O than the reference alloy Ti64.

In this study, it has been shown that the SLM Ti6242S specimens reveal superior ductility properties than the literature values<sup>[23]</sup> of the cast Ti6242S material. Increasing strength in combination with increasing ductility is attributed to grain refinement<sup>[1]</sup> and, therefore, may be an explanation as reported for SLM Ti6242S material in this study.

## 5. Conclusion

This study pursued the opportunity to compare a commonly applied Ti64 alloy via the near- $\alpha$  alloy Ti6242S, both produced by the SLM process. Furthermore, it was aimed to obtain

fundamental understandings regarding the processing–microstructure–property relationship of SLM Ti6242S when compared with the reference Ti64 alloy in the conditions as-built as well as after a heat treatment. These results lead to the following conclusion.

SLM manufactured Ti6242S specimens reveal a defect-rich hexagonal  $\alpha'$  microstructure, which originated from the martensitic phase transformation ( $\beta \rightarrow \alpha'$ ) during solidification and the associated rapid cooling of the melted alloy powder. The microstructures in the as-built condition of both specimens, the Ti6242S as well as the Ti64 alloy, are thus far from thermodynamic equilibrium.

The prior  $\beta$  grain structure is smaller for the Ti6242S alloy when compared with the reference Ti64 alloy, despite the use of the same processing parameters as a volume energy density of about 60 J mm<sup>-3</sup>. The smaller  $\beta$  grain might also be the reason for the smaller acicular  $\alpha'$  grains, which are nearly half of the size (8.3  $\mu$ m major axis against 16.1  $\mu$ m) as observed for the Ti64 reference material.

The martensitic acicular  $\alpha'$  phase decomposes during a subsequent sub-transus SRA heat treatment toward thermodynamic equilibrium ( $\alpha' \rightarrow \alpha + \beta$ ). The resulting microstructure of the Ti6242S material contains a certain amount of  $\beta$  phase, precipitated at  $\alpha'$  grain boundaries. In addition, rod-like  $\beta$  precipitates occur along lattice defects, e.g., twin boundaries or dislocations, within the  $\alpha'$  grains.

The  $\beta$ -transus temperature was measured via DSC and complementary verified by heat treatment studies as well as thermodynamic calculations and is about 1017  $\pm$  3 °C.

The SLM produced Ti6242S alloy provides a UTS of about 1231 MPa with an elongation at a fracture of about 11.3% ( $A_5$ ). However, there is an increase in strength in the case of the SLM Ti6242S specimens when compared with SLM produced Ti64 samples (UTS = 1061 MPa,  $A_5$  = 14.6%) even though a small loss of ductility has to be considered. The difference is more pronounced when compared with cast Ti6242 and SLM manufactured Ti64, which show a significant drop in tensile strength at elevated temperatures. The high strength, especially at 500 °C, in combination with an additional enhanced tensile fracture strain is caused by an interplay of grain refinement along with the influence of the alloying elements Sn, Zr, and Si as well as the interstitials O and N.

## Conflict of Interest

The authors declare no conflict of interest.

## Keywords

additive manufacturing, heat treatment, high-temperature tensile properties, microstructural characterization, near- $\alpha$  titanium alloys, selective laser melting

Received: October 7, 2020  
 Revised: December 12, 2020  
 Published online:

- [1] *Titanium and Titanium Alloys: Fundamentals and Applications* (Eds: M. Peters, C. Leyens), John Wiley & Sons, Weinheim **2003**.
- [2] H. Chandler, *Heat Treater's Guide: Practices and Procedures for Ferrous Alloys*, ASM International **1996**.
- [3] W. J. Lu, D. Zhang, X. N. Zhang, R. J. Wu, T. Sakata, H. Mori, *Mater. Sci. Eng. A* **2001**, 311, 142.
- [4] E. G. Obbard, Y. L. Hao, R. J. Talling, S. J. Li, Y. W. Zhang, D. Dye, R. Yang, *Acta Mater.* **2011**, 59, 112.
- [5] A. Chamanfar, T. Pasang, A. Ventura, W. Z. Misiolek, *Mater. Sci. Eng. A* **2016**, 663, 213.
- [6] G. Lütjering, J. C. Williams, *Titanium*, Springer Science & Business Media, Berlin/Heidelberg **2007**.
- [7] H. Imai, G. Yamane, H. Matsumoto, V. Vidal, V. Velay, *Mater. Sci. Eng. A* **2019**, 754, 569.
- [8] G. Ter Haar, T. Becker, *Materials* **2018**, 11, 146.
- [9] W. E. Frazier, *J. Mater. Eng. Perform.* **2014**, 23, 1917.
- [10] B. Dutta, F. H. Froes, *Adv. Mater. Res. Trans. Tech. Publ.* **2014**, 1019, 19.
- [11] M. Simonelli, Y. Y. Tse, C. Tuck, *Metall. Mater. Trans. A* **2014**, 45, 2863.
- [12] L. Thijs, F. Verhaeghe, T. Craeghs, J. Van Humbeeck, J. P. Kruth, *Acta Mater.* **2010**, 58, 3303.
- [13] B. Dutta, F. H. Froes, *Additive Manufacturing of Titanium Alloys: State of the Art, Challenges and Opportunities*, Butterworth-Heinemann, Oxford, UK **2016**.
- [14] P. Barriobero-Vila, J. Gussone, A. Stark, N. Schell, J. Haubrich, G. Requena, *Nat. Commun.* **2018**, 9, 1.
- [15] T. K. Heckel, A. Guerrero Tovar, H. J. Christ, *Exp. Mech.* **2010**, 50, 483.
- [16] D. Ballat-Durand, S. Bouvier, M. Risbet, *Mater. Sci. Eng. A* **2019**, 766, 138334.
- [17] Y. Cui, K. Aoyagi, Y. Koizumi, T. Fujieda, A. Chiba, *Addit. Manuf.* **2020**, 31, 100971.
- [18] T. Fujieda, Y. Cui, K. Aoyagi, Y. Koizumi, A. Chiba, *Materialia* **2018**, 4, 367.
- [19] H. Fan, S. Yang, *Mater. Sci. Eng. A* **2020**, 788, 139533.
- [20] M. Simonelli, Y. Y. Tse, C. Tuck, *Mater. Sci. Eng. A* **2014**, 616, 1.
- [21] T. Vilaro, C. Colin, J. D. Bartout, *Metall. Mater. Trans. A. Phys. Metall. Mater. Sci.* **2011**, 42, 3190.
- [22] B. Vrancken, L. Thijs, J. P. Kruth, J. Van Humbeeck, *J. Alloys Compd.* **2012**, 541, 177.
- [23] M. J. Donachie, *Titanium – A Technical Guide*, ASM International, Materials Park, OH **2000**.
- [24] T. DebRoy, H. L. Wei, J. S. Zuback, T. Mukherjee, J. W. Elmer, J. O. Milewski, A. M. Beese, A. Wilson-Heid, A. De, W. Zhang, *Prog. Mater. Sci.* **2018**, 92, 112.
- [25] S. Liu, Y. C. Shin, *Mater. Des.* **2019**, 164, 107552.
- [26] M. Neikter, R. Woracek, T. Maimaitiyili, C. Scheffzük, M. Strobl, M. L. Antti, P. Åkerfeldt, R. Pederson, C. Bjerkén, *Addit. Manuf.* **2018**, 23, 225.
- [27] B. Vrancken, S. Buls, J.-P. Kruth, J. Van Humbeeck, in *Proc. 13th World Conf. Titanium*, John Wiley Sons, Inc., Hoboken, NJ **2016**, p. 1269.
- [28] C. Fleißner-Rieger, T. Pogrietz, D. Obersteiner, T. Pfeifer, H. Clemens, S. Mayer, *Pract. Metallogr.*, unpublished.
- [29] G. Petzow, *Metallographisches, Keramographisches, Plastographisches Ätzen*, Borntraeger Gebrueder, Stuttgart, Germany **2015**.
- [30] C. Cayron, B. Artaud, L. Briottet, *Mater. Charact.* **2006**, 57, 386.
- [31] C. Cayron, *J. Appl. Crystallogr.* **2007**, 40, 1183.
- [32] J. O. Andersson, T. Helander, L. Höglund, P. F. Shi, B. Sundman, *Calphad* **2002**, 26, 273.
- [33] DIN EN 2002-001, *Aerospace Series–Metallic Materials–Test Methods–Part 1: Tensile Testing at Ambient Temperature*, Beuth, Berlin **2006**.
- [34] ISO 6892-2, *Metallic Materials–Tensile Testing–Part 2: Method of Test at Elevated Temperature*, International Organization for Standardization, Geneva **2018**.
- [35] M. Neikter, A. Huang, X. Wu, *Int. J. Adv. Manuf. Technol.* **2019**, 104, 1381.
- [36] J. Yang, H. Yu, J. Yin, M. Gao, Z. Wang, X. Zeng, *Mater. Des.* **2016**, 108, 308.
- [37] P. D. Nellist, S. J. Pennycook, *The Principles and Interpretation of Annular Dark-Field Z-Contrast Imaging*, **2000**.
- [38] J. Haubrich, J. Gussone, P. Barriobero-Vila, P. Kürnsteiner, E. A. Jäggle, D. Raabe, N. Schell, G. Requena, *Acta Mater.* **2019**, 167, 136.
- [39] S. Malinov, W. Sha, Z. Guo, C. C. Tang, A. E. Long, *Mater. Charact.* **2002**, 48, 279.
- [40] J. J. De Rooi, N. M. Van Der Pers, R. W. A. Hendrikx, R. Delhez, A. J. Böttger, P. H. C. Eilers, *J. Appl. Crystallogr.* **2014**, 47, 852.
- [41] M. Tanaka, Y. Hayashi, Y. Okuyama, T. Morikawa, K. Higashida, *Mater. Trans.* **2019**, 60, 80.
- [42] A. A. Antonyamy, J. Meyer, P. B. Prangnell, *Mater. Charact.* **2013**, 84, 153.
- [43] P. K. Gokuldoss, S. Kolla, J. Eckert, *Materials* **2017**, 10, 672.
- [44] M. J. Bermingham, S. D. McDonald, M. S. Dargusch, D. H. St. John, *J. Mater. Res.* **2008**, 23, 97.
- [45] D. Ballat-Durand, S. Bouvier, M. Risbet, W. Pantleon, *Mater. Charact.* **2019**, 151, 38.
- [46] I. Shirovani, I. Kaneko, M. Takaya, C. Sekine, T. Yagi, *Phys. B: Condens. Matter* **2000**, 281, 1024.
- [47] S. X. Liang, M. Z. Ma, R. Jing, Y. K. Zhou, Q. Jing, R. P. Liu, *Mater. Sci. Eng. A* **2012**, 539, 42.
- [48] A. V. Dobromyslov, V. A. Elkin, *Mater. Sci. Eng. A* **2006**, 438, 324.
- [49] R. P. Elliott, Armour Research Foundation, Chicago **1962**.
- [50] E. O. Hall, *Proc. Phys. Soc. Sect. B* **1951**, 64, 747.
- [51] N. J. Petch, *J. Iron Steel Inst.* **1953**, 173, 25.

## Article C

# On the existence of orthorhombic martensite in a near- $\alpha$ titanium base alloy used for additive manufacturing

Christian Fleißner-Rieger<sup>1,\*</sup>, Matheus Araujo Tunes<sup>2</sup>, Christoph Gammer<sup>3</sup>, Tanja Jörg<sup>4</sup>,  
Tanja Pfeifer<sup>5</sup>, Michael Musi<sup>1</sup>, Francisca Mendez-Martin<sup>1</sup> and Helmut Clemens<sup>1</sup>

<sup>1</sup> Department Werkstoffwissenschaft, Montanuniversität Leoben, Franz-Josef Straße 18, 8700 Leoben, Österreich

<sup>2</sup> Materials Science and Technology Division, Los Alamos National Laboratory, 87545 Los Alamos, New Mexico, United States of America

<sup>3</sup> Erich Schmid Institute of Materials Science, Austrian Academy of Sciences, Jahnstraße 12, 8700 Leoben, Austria.

<sup>4</sup> voestalpine BÖHLER Edelstahl GmbH & Co KG, Mariazeller Straße 25, Kapfenberg 8605, Austria

<sup>5</sup> Pankl Racing Systems AG, Additive Manufacturing Technologies, Industriestraße Ost 4, 8605 Kapfenberg, Austria

\* Corresponding author

Journal of Alloys and Compounds, **897**, 163155 (2021)

<https://doi.org/10.1016/j.jallcom.2021.163155>

open access: CC BY-NC-ND 4.0





Contents lists available at ScienceDirect

## Journal of Alloys and Compounds

journal homepage: [www.elsevier.com/locate/jalcom](http://www.elsevier.com/locate/jalcom)

# On the existence of orthorhombic martensite in a near- $\alpha$ titanium base alloy used for additive manufacturing



Christian Fleißner-Rieger<sup>a,\*</sup>, Matheus Araujo Tunes<sup>b</sup>, Christoph Gammer<sup>c</sup>, Tanja Jörg<sup>d</sup>,  
Tanja Pfeifer<sup>e</sup>, Michael Musi<sup>a</sup>, Francisca Mendez-Martin<sup>a</sup>, Helmut Clemens<sup>a</sup>

<sup>a</sup> Department of Materials Science, Montanuniversität Leoben, Franz-Josef Straße 18, 8700 Leoben, Austria

<sup>b</sup> Materials Science and Technology Division, Los Alamos National Laboratory, 87545 Los Alamos, NM, United States

<sup>c</sup> Erich Schmid Institute of Materials Science, Austrian Academy of Sciences, Jahnstraße 12, 8700 Leoben, Austria

<sup>d</sup> voestalpine BÖHLER Edelstahl GmbH & Co KG, Mariazeller Straße 25, 8605 Kapfenberg, Austria

<sup>e</sup> Pankl Racing Systems AG, Additive Manufacturing Technologies, Industriestraße Ost 4, 8605 Kapfenberg, Austria

## ARTICLE INFO

### Article history:

Received 11 October 2021

Received in revised form 18 November 2021

Accepted 5 December 2021

Available online 8 December 2021

### Keywords:

Additive manufacturing

Laser powder bed fusion

Near-alpha

Titanium alloys

Orthorhombic martensite

## ABSTRACT

Additive manufacturing is a state-of-the-art production technology to produce tailor-made and highly complex parts. Among various other alloys, Ti base alloys are frequently used in this manufacturing technique due to their well-balanced properties and their wide range of applications. Allotropic phases and the occurrence of athermal phase transformations are the main reasons why these alloys hold a great development potential and are the basis of extensive use. High cooling rates during manufacturing lead to martensitic phases and the formation of nanometer-sized microstructures resulting in extraordinary strength. Simultaneously, such high cooling rates cause a high amount of lattice defects and the occurrence of residual stresses, which finally may result in delamination effects and cracks. Usually, a common approach to reduce residual stresses during additive manufacturing is to decrease thermal gradients by increasing the heat input or preheating the building platform. Instead of applying the typical approaches to lower thermal gradients, this study deals with the origin of the 'softer' orthorhombic martensite by accelerating the solidification process. The implementation of the orthorhombic phase in bulk components was inspired by a new phase transformation herein reported for the first time in the powder material, which also validates the possible occurrence of two martensitic phases in the same alloy. Various sophisticated characterization techniques like high energy and high-temperature X-ray diffraction, high-resolution transmission electron microscopy as well as atom probe tomography were applied to characterize this softer orthorhombic martensitic phase in detail aiming to highlight the opportunities accompanied by this new approach for additive manufacturing of titanium alloys.

© 2021 The Author(s). Published by Elsevier B.V.  
CC\_BY\_NC\_ND\_4.0

## 1. Introduction

Additive manufacturing (AM) – or 3D printing – as a key technology in modern industries paved the way for the manufacturing of complex structural parts faster and with less waste generation than conventional manufacturing techniques [1,2]. These great advantages follow the challenge to adapt and/or modify already established and well-investigated material systems, especially in the metal industry. Due to the nature of AM techniques, *i.e.* the layer-by-layer building of near net-shape components, it requires metallic powder as the starting material [3–5]. Typically, these powders are

produced via gas or plasma atomization [6]. The atomized particles should be chemically homogeneous and spherical to enable the formation of a homogeneous and dense layer and, subsequently, the production of pore-free components by AM [7]. Especially laser powder bed fusion (LPBF), is a state-of-the-art AM technique to produce Ti base components with complex geometries for the aerospace, automotive and biomedical industries, allowing the incorporation of inner channels for cooling fluids or topology optimization for stress-adjusted applications [8].

Ti base alloys typically contain primary phases with a hexagonal lattice structure which are designated as  $\alpha$ -Ti. To enable a certain amount of ductility, even at room temperature, alloying can be used to stabilize the body-centered cubic (bcc)  $\beta$  phase, generally known as the high-temperature phase of Ti and its alloys. The class of near- $\alpha$  Ti alloys, characterized by a small amount of  $\beta$  phase, is already

\* Corresponding author.

E-mail addresses: [christian.fleissner-rieger@unileoben.ac.at](mailto:christian.fleissner-rieger@unileoben.ac.at) (C. Fleißner-Rieger)



applied as lightweight materials for use at elevated temperatures, combining excellent creep resistance and high strength [9,10].

It is well known that phase transformations can be influenced by the cooling rate applied [11]. For near- $\alpha$  Ti alloys, relatively low cooling rates, e.g. furnace cooling during heat treatment, lead to an equilibrium microstructure consisting of a minor volume fraction of  $\beta$  phase and the predominant  $\alpha$  phase [9]. In contrast, high cooling rates can lead to the formation of non-equilibrium microstructures. During powder atomization, which generates high cooling rates, small melt drops rapidly solidify and generate a hexagonal martensitic microstructure, whereby the extremely high cooling rate (up to  $10^8 \text{ K}\cdot\text{s}^{-1}$ ) primarily depends on the particle diameter [12–14]. The LPBF process also leads to a supersaturated martensitic microstructure due to fast cooling, e.g., in the case of the LPBF process with cooling rates of  $\sim 10^4\text{--}10^6 \text{ K s}^{-1}$  within the small metal pool during solidification [15].

However, both production steps, powder atomization and LPBF, result in a martensitic phase transformation which is known to promote cracks and delamination during the additive manufacturing process [7,16].

In this study, the martensitic transformation is examined in a near- $\alpha$  Ti-6Al-2Sn-4Zr-2Mo-Si (Ti6242S, m.%) alloy used for additive manufacturing. This industrially relevant alloy, mainly produced via casting or forging, is already used in a variety of high temperature applications due to its enhanced mechanical properties and higher creep resistance in comparison to the commonly used Ti-6Al-4V (m.%) alloy [17].

Recent investigations of the Ti6242S alloy show that this alloy typically generates a  $\alpha'$  (hexagonal) martensitic microstructure as a consequence of rapid cooling during electron beam melting [18] or LPBF [19]. As both techniques require powder as starting material, investigations on the powder condition mainly focused on the sphericity and particle size distribution, which is why fundamental changes to the phase transformations and the occurring phases during rapid cooling may have been overlooked.

Consequently, within this study, we focus on the investigation of the initial powder and we are able to provide the experimental proof of a second type of martensite within one alloy system arising as a result of direct solidification without element partitioning. As the latter is an experimental confirmation resulting from the atomization process, we also investigated new routes to implement this type of martensite in a bulk sample by optimizing the LPBF process parameters. Fig. 1 summarizes the major findings of this study and shows, that the initial Ti6242S powder exhibits an orthorhombic crystal structure, whereas the as-built microstructure normally possesses a hexagonal crystal structure with respect to the fast cooling from  $\beta$  to  $\alpha'$ . By increasing the cooling rate during LPBF, the transformation changes and a 'softer' orthorhombic  $\alpha''$  type of martensite occurs. The basal plane atoms of the orthorhombic and hexagonal martensite in Fig. 1 are depicted as blue spheres, whereas green and purple atoms indicate central plane atoms. The atoms of a bcc {110} plane, which form the basal plane of the orthorhombic and hexagonal crystal structure during the phase transformation, are also depicted as blue spheres. A post-processing heat treatment was performed on the as-built samples, describing the evolution of the system towards thermodynamic equilibrium.

Various sophisticated tools, such as scanning electron microscopy (SEM), electron backscatter diffraction (EBSD), high-resolution transmission electron microscopy (HRTEM), synchrotron high energy X-ray diffraction (HEXRD), differential scanning calorimetry (DSC) and atom probe tomography (APT), helps to provide evidence of two variants of martensite occurring in the Ti6242S alloy, depending on the processing conditions and subsequent heat treatment parameters. The study is an important step to foster applications of Ti base alloys as-produced via AM processes.

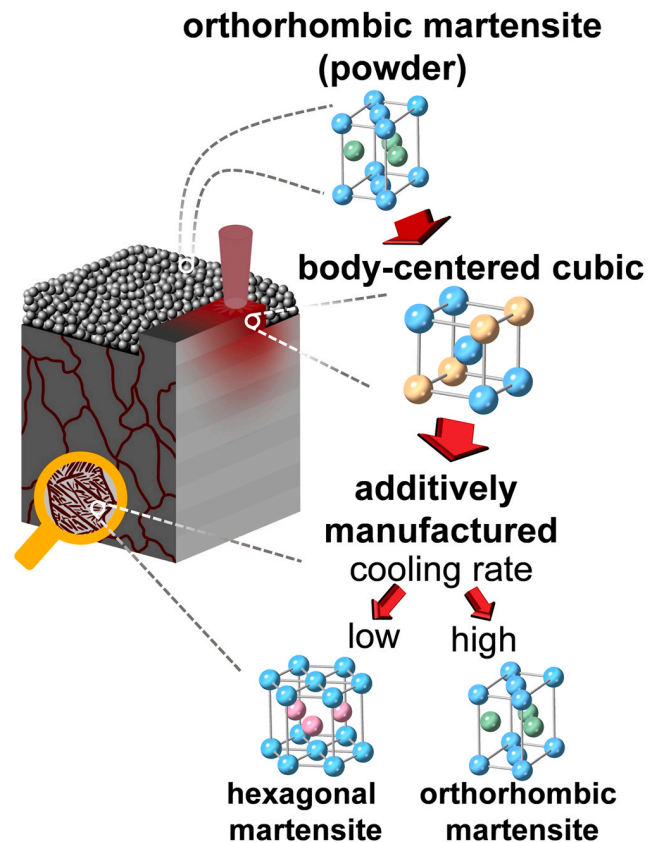


Fig. 1. Schematic representation of the powder-bed based additive manufacturing process. The initial orthorhombic crystal structure of the Ti6242S powder forms via a  $\beta \rightarrow \alpha''$  transformation pathway. During LPBF, the melted powder transforms due to rapid cooling into either a hexagonal  $\alpha'$  or an orthorhombic  $\alpha''$  martensite. The layer-by-layer building strategy results in an acicular shaped martensitic microstructure embedded in prior parent bcc  $\beta$  matrix grains.

## 2. Materials and methods

### 2.1. Material synthesis and heat treatment

The experimental investigations of the martensitic structures were done on EIGA (Electrode Induction Melting Inert Gas Atomization) atomized powder and as-built material of the Ti6242S alloy. After the atomization of the pre-alloyed rod, the powder was fractionated to a Gaussian particle size distribution between 15 and  $45 \mu\text{m}$  with a particle size of  $d_{10} = 17.6 \mu\text{m}$ ,  $d_{50} = 31.1 \mu\text{m}$  and  $d_{90} = 43.3 \mu\text{m}$ . The chemical composition of the powder is shown in Table 2. The elements such as Ti, Al, Sn, Zr, Mo, Si and Fe were determined via inductively coupled plasma atomic emission spectroscopy, and O and N via carrier gas hot extraction. The cuboid specimens ( $20 \times 15 \times 20 \text{ mm}^3$ ) were manufactured employing an EOS M290 AM unit at Pankl Racing Systems AG, Austria, using a volumetric energy density ( $E_d$ ) in the range from 35 to  $110 \text{ J}\cdot\text{mm}^{-3}$ , resulting in test samples with a porosity of less than 0.5 vol%, i.e., an absolute density of 99.5 vol%. The laser power during the process was set between 150 and 400 W and the scanning speed was continuously decreased from 2000 to  $800 \text{ mm}\cdot\text{s}^{-1}$  for reducing the  $E_d$  and thus generating high cooling rates. The building platform was pre-heated to  $100 \text{ }^\circ\text{C}$  and a  $67^\circ$  EOS scanning strategy was utilized. To avoid oxidization of the material, the building chamber was flooded by a constant Ar stream. The post-process heat treatment was performed in a cold-wall vacuum furnace (HTM Reetz GmbH, Germany) at  $800 \text{ }^\circ\text{C}$  for 12 h followed by furnace cooling to RT.

## 2.2. X-ray diffraction analysis

Synchrotron experiments were performed on the Synchrotron experiments were performed at beamline P07 at the synchrotron radiation source PETRA III at the Deutsches Elektronen-Synchrotron (DESY), Hamburg, Germany [20]. The energy of the monochromatic synchrotron beam was 70 keV, corresponding to a wavelength of 0.1773 Å and the beam cross-section was  $1 \times 1 \text{ mm}^2$ . Complete Debye-Scherrer diffraction rings of cuboid samples ( $5 \times 5 \times 9 \text{ mm}^3$ ) and powder were recorded in transmission geometry using a Perkin Elmer X-ray diffraction (XRD) 1621 flat panel area detector. The distance between the samples and the detector was 1564 mm, which was calibrated using  $\text{LaB}_6$ . The powder was enclosed in a custom-made Al holder with a threaded hole of  $\varnothing 4 \text{ mm}$ , in which the powder particles were initially mixed with isopropyl alcohol (that evaporates after assembly). The resulting HEXRD patterns were azimuthally integrated with the software program Fit2D [21]. The phases occurring and their respective volume fraction and lattice parameters were determined by Rietveld analysis of the integrated diffraction data using the software program MAUD [22].

The high-temperature XRD (HTXRD) measurements and the phase determination of samples manufactured with different  $E_d$  were performed on a D8 Advance diffractometer from Bruker AXS, Germany, equipped with a  $\text{Cu-K}\alpha$  X-ray source with a wavelength of 0.154 nm. The measurements were performed in locked coupled

mode (coupled  $\theta/2\theta$ ). For HTXRD, a vacuum chamber type HTK 1200 N by Anton Paar, Austria, was used. The diffractograms were recorded in  $50^\circ\text{C}$  steps from RT to  $800^\circ\text{C}$  with a heating rate of about  $7 \text{ K s}^{-1}$ . To reduce the time at elevated temperatures, i.e. to suppress surface oxidation, the measurements were conducted in a  $2\theta$  range between  $34^\circ$  and  $36^\circ$  in order to monitor the characteristic peak splitting associated with the orth crystal structure, applying a step size of  $0.02^\circ$  and a counting time of 2 s.

## 2.3. Microstructural characterization

The specimen preparation for SEM and EBSD analysis was carried out by using standard metallographic methods [23]. The characterization of the microstructure was performed on a FEI Versa 3D microscope from Thermo Fisher Scientific Instruments, United States. The microscope was equipped with a field emission gun and a gallium focused ion beam. The EBSD measurements were carried out with the HIKARI XP camera from EDAX, Germany. The EBSD data were recorded and evaluated using TSL OIM Analysis 7. Black-lined high-angle grain boundaries in Fig. 4b indicate a grain deviation of  $> 15^\circ$  from neighboring grains. The EBSD parameters were 20 kV acceleration voltage, 350 nm step size with a spot size of 7 and a  $4 \times 4$  binning mode.

Transmission electron microscopy (TEM) lamellas were using the focused-ion beam based preparation technique according to

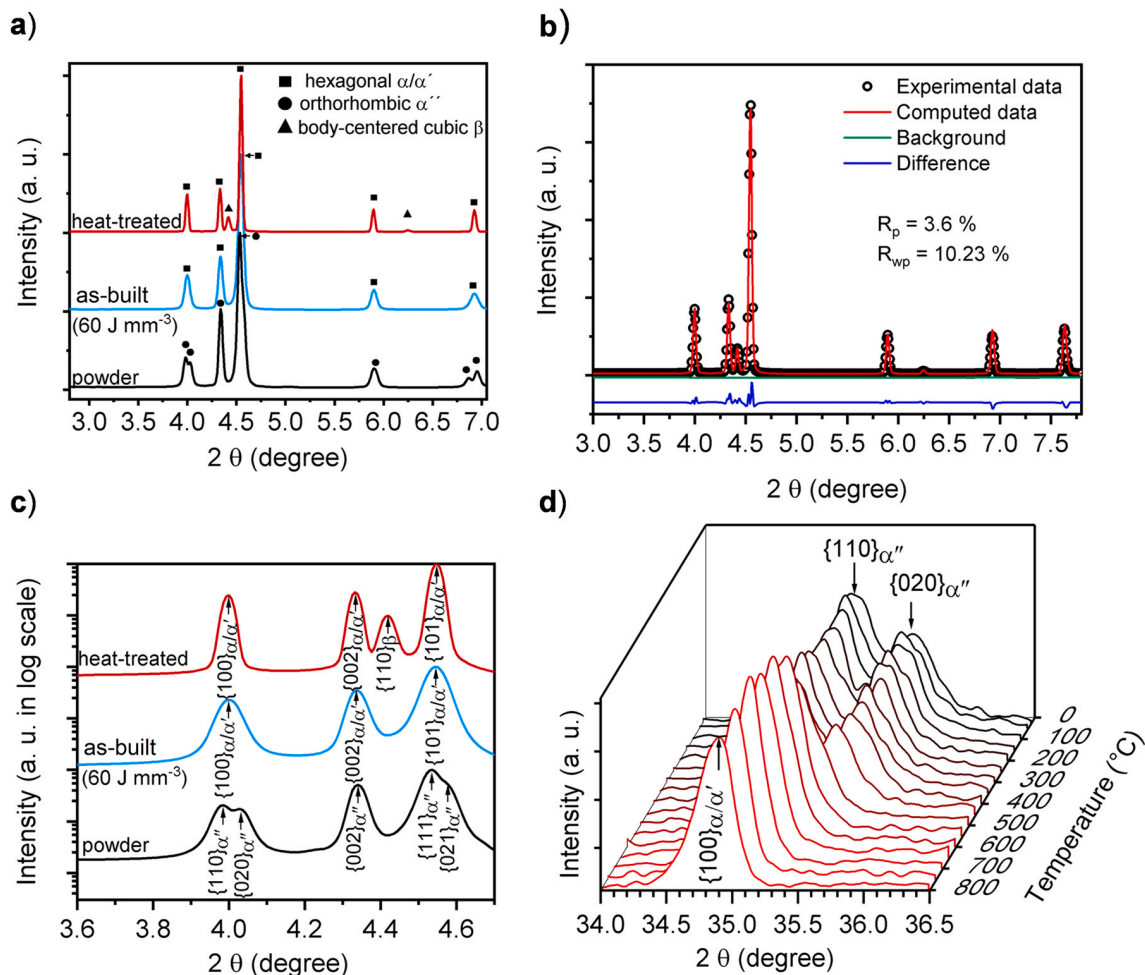


**Fig. 2.** Results of HEXRD experiments of the Ti6242S sample conditions. a) HEXRD pattern revealing the occurring phases in the alloy; b) Rietveld analysis of the heat-treated sample ( $800^\circ\text{C}$  for 12 h followed by furnace cooling); c) HEXRD spectra proving the occurrence of the orthorhombic  $\alpha''$  phase in the powder state and d) HTXRD measurements of a selected angular section for various temperatures demonstrating the transition of the powder towards thermodynamic equilibrium via the transformation orthorhombic  $\rightarrow$  hexagonal.

**Table 1**  
Experimentally determined lattice parameters of the three sample conditions analyzed.

Sample	Phase	Space group	a (nm)	b (nm)	c (nm)
powder	$\alpha''$ -orthorhombic	<i>Cmcm</i>	0.296	0.505	0.468
as-built (std. parameter)	$\alpha'$ -hexagonal	<i>P6<sub>3</sub>/mmc</i>	0.294	0.509 <sup>a</sup>	0.469
heat-treated	$\alpha$ -hexagonal	<i>P6<sub>3</sub>/mmc</i>	0.293	0.507 <sup>a</sup>	0.469
	$\beta$ -bcc	<i>Im<math>\bar{3}m</math></i>	0.325	0.460 <sup>a</sup>	0.460 <sup>a</sup>

<sup>a</sup> Note: calculated positions with respect to the orthorhombic symmetry.

Thompson et al. [24]. For the TEM investigations, a JEOL JEM2200 FS, Japan, with an acceleration voltage of 200 kV, was used. High-angle annular dark-field (HAADF) images were recorded by a JEOL HAADF TEM detector and the HRTEM images were taken with a TVIPS XF416 CMOS detector. Fast Fourier transformation (FFT) and inverse FFT (IFFT) analysis were applied to the HRTEM images. To evaluate the occurring phases and simulate their corresponding diffraction patterns, the software programs CrystalMaker and SingleCrystal from CrystalMaker Software Ltd, UK were used.

#### 2.4. Phase transformation and chemical composition analysis

The DSC measurements were performed with a LABSYS Evo from Setaram, France, by placing 50 mg of powder in an Al<sub>2</sub>O<sub>3</sub> crucible. The sample was first heated up from room temperature to 1150 °C and subsequently cooled down to 25 °C with a heating and cooling rate of 40 K min<sup>-1</sup>. The procedure was repeated a second time on the same and already heated powder material to study the phase transformation of the powder material in thermodynamic equilibrium.

To detect the elemental distribution at atomic scale, a local electrode atom probe 3000X HR system (LEAP) from Cameca, France was utilized. The APT tips were prepared by using the lift out technique following the standard procedure [24]. The measurements were performed in laser mode at 0.4 nJ, 40 K and 250 kHz. The reconstructions were done using IVAS 3.6.8 from Cameca.

#### 2.5. Hardness measurement

To evaluate the micro-hardness of the as-built samples, a Qness Q 60 A+ measuring device equipped with a Vickers indenter tip was used to carry out 30 single HV0.1 indents placed on a measurement grid.

### 3. Results and discussion

#### 3.1. Phase evolution by XRD: from powder to bulk samples

##### 3.1.1. Determination of occurring phases

The main challenge of this study is the differentiation between orthorhombic  $\alpha''$  martensite and hexagonal  $\alpha'$  martensite. From the employed complementary characterization techniques, XRD analysis is the most promising approach to distinguish between these both crystallographic structures, as their atomic positions are very similar. That means neither TEM diffraction analysis nor EBSD is suitable to distinguish both martensite phases due to low statistics in the case of TEM and the insufficient software-based phase determination with regard to EBSD.

For these reasons, HEXRD measurements were performed. This technique has a higher peak resolution and a better signal-to-noise ratio as well as more statistically relevant results, attributable to the larger sample volume analyzed when compared to a laboratory XRD, which is therefore needed for the present study [25]. The HEXRD results of three different sample conditions of the Ti6242S alloy are shown in Fig. 2a. The investigations were done on (i) as-atomized powder, (ii) the as-built condition, *i.e.* immediately after the LPBF

process, manufactured with standard process parameters and a volumetric energy density of about 60 J·mm<sup>-3</sup> and (iii) on the heat-treated variant. The heat treatment at 800 °C for 12 h followed by furnace cooling was conducted to bring the sample close to thermodynamic equilibrium. The Rietveld analysis was carried out using MAUD [26] and is presented in Fig. 2b in terms of the integrated intensities proportional to the calculated volume phase fraction. It can be seen that all diffraction peaks were indexed to the present phases and the refinement shows a good agreement [27] between the calculated and experimental data (weighted profile R-factor, R<sub>wp</sub> = 10.23%).

##### 3.1.2. Orthorhombic martensite in the atomized powder

The HEXRD spectra depicted in Fig. 2c show a defined angular range and the main peaks of the occurring orthorhombic, hexagonal and bcc phases in detail for the powder, as-built and heat-treated materials. By looking at the 2 $\theta$  position around 4.0°, the occurrence of only one phase in the Ti6242S powder material, namely the orthorhombic  $\alpha''$  is revealed. A characteristic of this phase is the occurrence of the {110} <sub>$\alpha''$</sub>  and {020} <sub>$\alpha''$</sub>  double peak when compared to the single {100} <sub>$\alpha/\alpha'$</sub>  peak present in the as-built and heat-treated sample conditions, where only the hexagonal phase occurs. Since the hexagonal {100} <sub>$\alpha/\alpha'$</sub>  peaks of the as-built and the heat-treated specimens are located in between the peak positions of the orthorhombic {110} <sub>$\alpha''$</sub>  and {020} <sub>$\alpha''$</sub>  phase peaks, it can be concluded that the powder does not reveal any  $\alpha/\alpha'$  constituents. The reason for the  $\alpha/\alpha'$  terminology is that  $\alpha$  and  $\alpha'$  exhibit the same hexagonal crystal structure with similar lattice parameters and only differ in their thermal history [28]. Therefore, it is impossible to differentiate between  $\alpha$  and  $\alpha'$  by means of XRD, so the peaks are designated as  $\alpha/\alpha'$ . Fig. 2d shows the results of the *in situ* HTXRD experiments which reveal the  $\alpha'' \rightarrow \alpha/\alpha'$  transformation in the Ti6242S powder. The HTXRD spectra selected points to a phase transformation temperature around 550 °C. Furthermore, the shift of the {110} <sub>$\alpha''$</sub>  and {020} <sub>$\alpha''$</sub>  peaks goes along with the atomic movement to form the hexagonal crystal structure as the material approaches the thermodynamic equilibrium.

##### 3.1.3. Additive manufacturing and thermodynamic equilibrium

The as-built sample (produced using standard LPBF parameters) [17] and the heat-treated sample, however, only show hexagonal  $\alpha/\alpha'$  phases. Additionally, the heat-treated variant reveals 5.59 vol% bcc  $\beta$  phase which occur due to the near-equilibrium material condition. The smaller full width at half maximum (FWHM) noticed in the XRD spectra of the heat-treated variant in Fig. 2c indicates a reduction in residual stress [29,30] as well as a decreasing defect density, *e.g.* dislocations, and larger grains when compared to the as-built sample condition.

The calculated lattice parameters of the present phases are given in Table 1. Due to symmetrical reasons, it is not necessary to assign the hexagonal and bcc system with all three lattice parameters. Nevertheless, atomic movements during the phase evolution can be better understood if all values are shown (unnecessary parameters are marked with a footnote an asterix). It can also be seen that the lattice parameters for both the orthorhombic and hexagonal phases are almost similar with respect to the resolution limit of the HEXRD

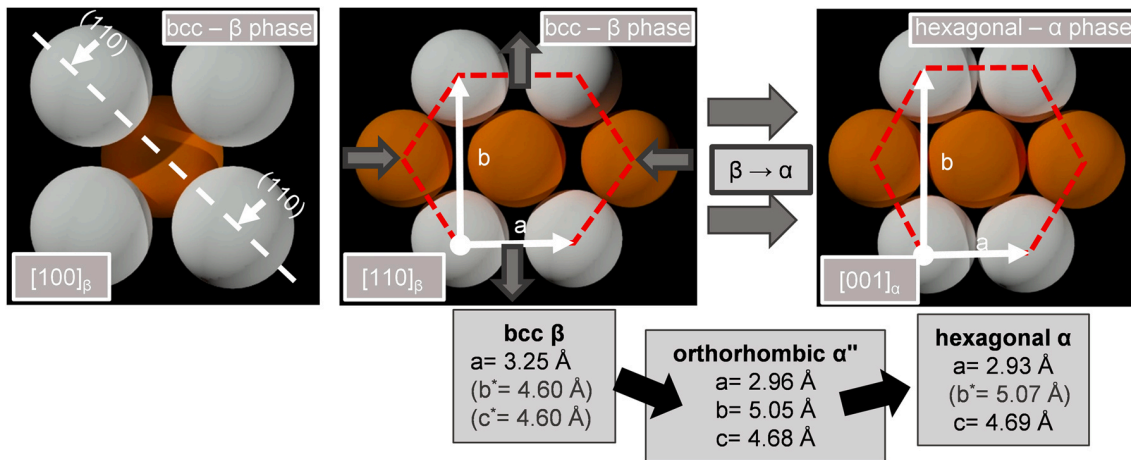


**Fig. 3.** Schematic representation of the  $\beta \rightarrow \alpha$  phase transformation. During fast solidification, as in the case of the atomized powder, the athermal shuffle of the basal plane atoms results in a decrease of  $a$  and increase of  $b$  lattice parameters. The orthorhombic  $\alpha''$  lattice structure represents an intermediate state (Unnecessary parameters, which are only shown for a better understanding of phase evolutions, are marked with an asterisk.) between the equilibrium phases.

measurement. The atomic positions follow a shift towards the thermodynamic equilibrium. This shift in the lattice parameters caused by the individual phase transformations (Fig. 1) can be better understood from the evolution of the lattice parameters given in Table 1.

### 3.1.4. $\beta \rightarrow \alpha'' \rightarrow \alpha$ phase transformation pathway

The allotropic phase transformation of the Ti6242S powder requires atomic movement from the bcc lattice structure to finally match the equilibrium hexagonal lattice structure, as schematically shown in Fig. 3. The athermal martensitic phase transformation involves a compression of the lattice cell along the  $a$  axis and an extension along the  $b$  axis in the basal plane. Furthermore, as long as the hexagonal equilibrium structure (induced by heat input) is not perfectly matched, the atoms are located in positions between the equilibrium crystal structures of the  $\alpha$  and  $\beta$  phase. The intermediate phase condition, i.e. the orthorhombic lattice structure, results in degenerated diffraction peaks according to Bragg's law ( $2 \cdot d_{hkl} \cdot \sin(\theta) = n \cdot \lambda$ ) and the periodic long-range order of the atoms along these lattice planes. The difference between the  $\beta \rightarrow \alpha'' \rightarrow \alpha$  and the  $\beta \rightarrow \alpha' \rightarrow \alpha$  pathways is that for the latter one, the atomic movement from  $\beta \rightarrow \alpha'$  is completed and a hexagonal crystal structure occurs.

## 3.2. Characterization of the Ti6242S powder material

### 3.2.1. Microstructure

The results of the microstructural investigations conducted on the Ti6242S powder material are summarized in Fig. 4. As depicted in the SEM image of Fig. 4a, taken with the secondary electron (SE) detector, the EIGA powder is of spherical shape and only few satellite particles are observed.

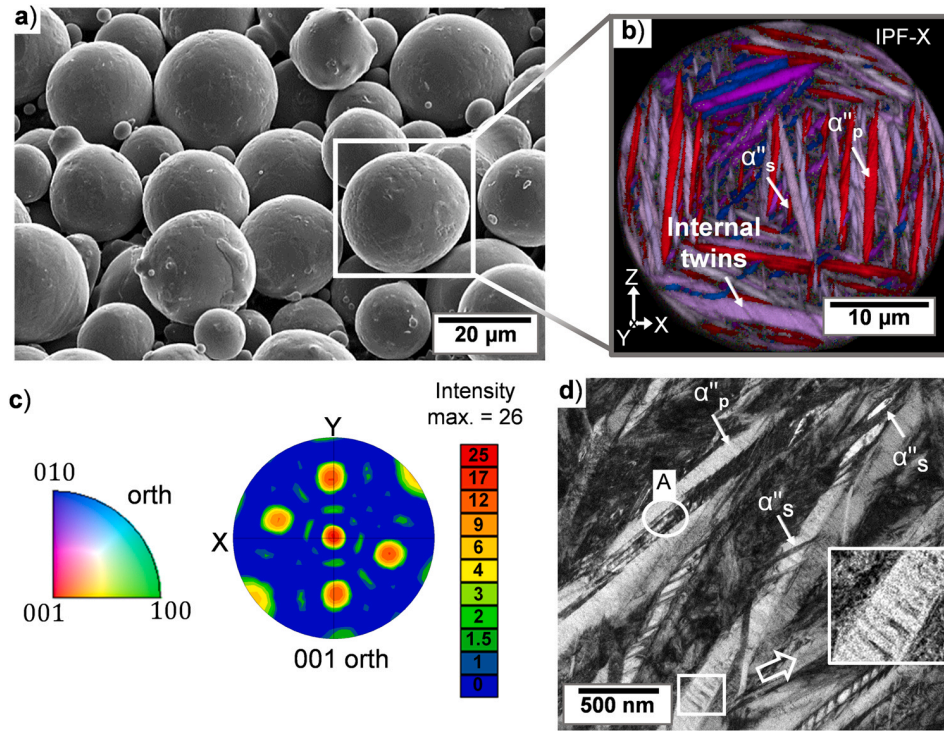
The crystallographic analysis of these particles is shown in Fig. 4b, where an EBSD assessment shows the nanometer sized martensitic microstructure. This EBSD measurement is displayed as an inverse pole figure (IPF) – X map, i.e. a map relative to the X-axis, thus making the acicular shape of the primary  $\alpha''_p$  and secondary  $\alpha''_s$  plates visible. In Fig. 4b, the IPF map is overlaid with the image quality of the EBSD measurement to enable a better look at other lattice defects, e.g. a twinning substructure, occurring within the  $\alpha''$  plates of the martensitic microstructure. Corresponding to the EBSD map, Fig. 4c shows the crystal orientation legend along with the  $\{001\}_{\alpha''}$  pole figure and intensity legend. The distribution of crystallographic orientations is clearly visualized in the EBSD pole figure and indicates the presence of six crystallographically preferred

$\{001\}_{\alpha''}$  orientations in the powder particle. In general, the occurrence of these preferred orientations in Ti alloys is often seen for  $\{0001\}_{\alpha/\alpha''}$  pole figures as a consequence of the  $\beta \rightarrow \alpha$  transformation and, therefore, this is linked to the parent  $\beta$  phase [31]. The crystal orientation relationship (OR) of the  $\alpha''$  and the parent  $\beta$  phase obtained in this study was determined to be  $\{110\}_{\beta} // \{001\}_{\alpha''}$  and  $\langle 111 \rangle_{\beta} // \langle 101 \rangle_{\alpha''}$  and agrees with results previously reported in literature [32]. According to the OR herein estimated, one can notice that all  $\alpha''$  grains in the investigated powder particle are linked to one parent  $\beta$  grain, i.e. the solidification took place by forming a single bcc crystal representing the whole powder particle studied.

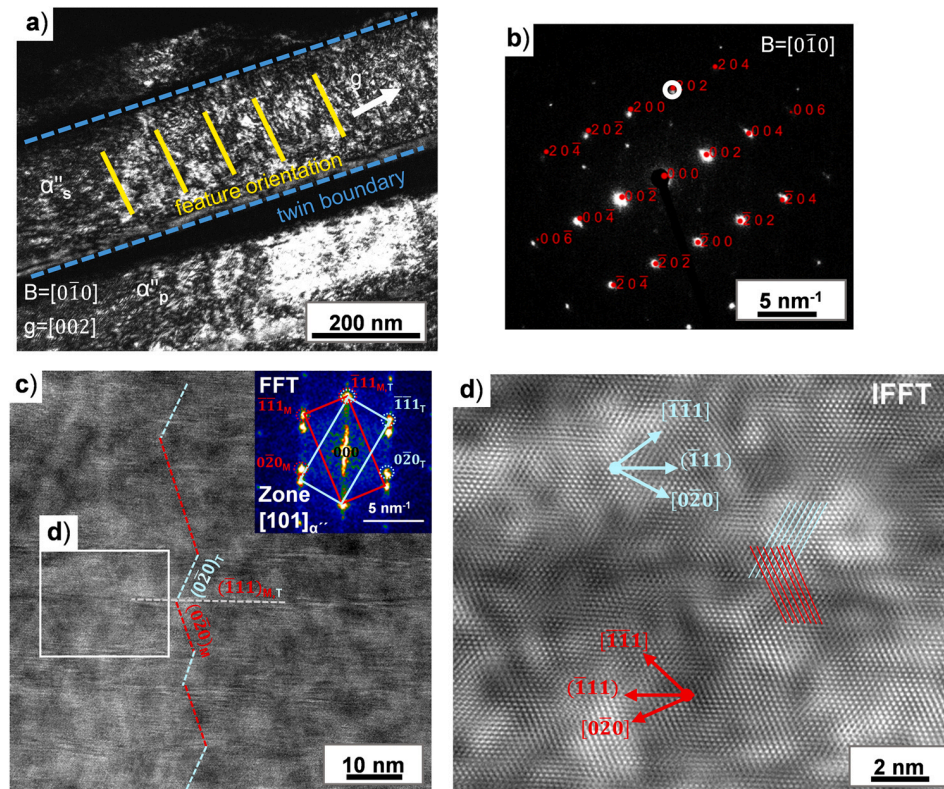
HAADF scanning-TEM (STEM) image in Fig. 4d shows the microstructure in more detail and reveals the presence of a hierarchical structures. During the initial stage of the martensitic transformation, the  $\alpha''_p$  structure forms, followed by thin  $\alpha''_s$  constituents that are nucleating in or adjacent to  $\alpha''_p$ . Area A marks a position with twin boundaries in which a follow-up HRTEM investigation was carried out later in Fig. 5. The enlarged area in the inset of Fig. 4d also reveals dark contrasted lines in the grain interior. These lines indicate the presence of lattice defects at specific lattice planes in the  $\alpha''$  crystal.

Fig. 5a displays a detailed image of these features conducted in TEM-SAED (selected area electron diffraction) mode by selecting a single spot indicated by the white circle in Fig. 5b. The image with  $\vec{B} = [0\bar{1}0]$  and  $\vec{g} = [002]$  shows that the lattice defects are allocated at  $(002)_{\alpha''}$  basal planes and according to Ref. [33], have been already validated as dislocations. These dislocations, arranged on the  $(002)$  basal plane, occur in  $\alpha''_p$  and  $\alpha''_s$  plates in a periodic way and at spacing distances of  $\sim 15$  nm. It is assumed that these dislocations, which also occur in bulk samples [17,34], act as nucleation sites for  $\beta$  phase precipitates. Fig. 5b also shows that, in contrast to the  $\alpha''_p$  plates,  $\alpha''_s$  plates are separated by twin boundaries.

The TEM results, as presented in Fig. 5c, indicate the atomic configuration of the Ti6242S in form of powder. The HRTEM image of the  $[101]_{\alpha''}$  zone axis shows a sequenced, twinned  $\alpha''$  structure with a twin thickness of approximately 8–16 nm. The red and cyan lines show the twinning direction, i.e. the deviation of twins and the matrix along the  $(0\bar{2}0)_{\alpha''}$  lattice plane. The FFT pattern of the corresponding detailed area (d) demonstrates, that in the case of the powder material, a  $(\bar{1}\bar{1}1)_{\alpha''}$  type twin is observed, which is in accordance with the results obtained on related alloys [35–37]. Fig. 5d shows an inverse FFT image and focuses on the internal structure of the twinned microstructure. The lattice plane distances of the  $(0\bar{2}0)_{\alpha''}$  and  $(\bar{1}\bar{1}1)_{\alpha''}$  marked in red and cyan are  $d_{(0\bar{2}0)M,T} = 0.256$  and  $d_{(\bar{1}\bar{1}1)M,T} = 0.225$  nm, respectively. The results agree with the obtained HEXRD values of about



**Fig. 4.** Microscopic characterization of the Ti6242S powder material. a) showing an SEM image (SE mode) of the analyzed powder. b,c) EBSD investigations revealing the internal acicular  $\alpha''$  microstructure including primary  $\alpha''_p$  and secondary  $\alpha''_s$  plates and the presence of mechanical twins. d) TEM analysis showing an HAADF image of the microstructure. Area A represents a position with twin boundaries in which a follow-up HRTEM investigation was conducted.



**Fig. 5.** TEM analysis of lattice defects in the Ti6242S powder material. a) TEM-DF image with  $B=[0\bar{1}0]$  and the corresponding SAED diffraction pattern in b) showing the orthorhombic  $\alpha''$  microstructure and revealing dislocations allocated at  $(002)$  basal planes and separated by twin boundaries. c) HRTEM investigation of twins displayed in the previous figure (Area A) and corresponding FFT observation. The  $(\bar{1}11)_{\alpha''}$  type twins are confirmed and the twinning sequence along the  $(020)_{\alpha''}$  lattice plane is displayed with red and cyan dashed lines. d) IFFT observation focusing on the atomic configuration of the mechanical twins occurring.

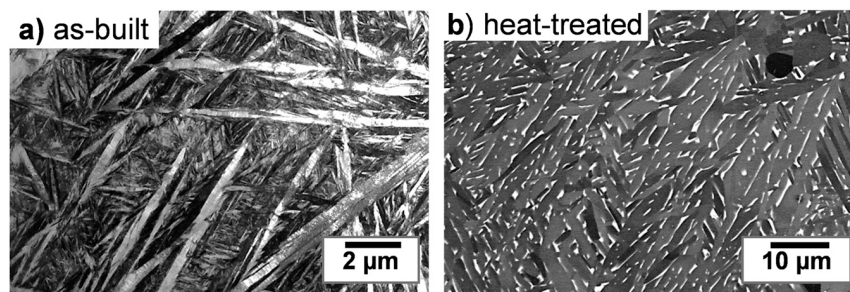


**Fig. 6.** TEM-BF image revealing the acicular  $\alpha'$  microstructure of the as-built component made by standard LPBF parameter ( $E_d$  of about  $60\text{ J}\cdot\text{mm}^{-3}$ ) in a) and the equilibrium microstructure of the heat-treated sample ( $800\text{ }^\circ\text{C} - 12\text{ h} - \text{FC}$ ) in b).

$d_{(020)} = 0.252$  and  $d_{(\bar{1}11)_{M,T}} = 0.224\text{ nm}$ . The occurrence of  $(\bar{1}11)_{\alpha'}$  type twins can be ascribed to the fundamental mechanism of a martensitic formation [31,38] to generate an invariant plane for the shear process. In addition, mechanical twinning is important for  $\beta$  phase precipitation because these interfaces also act as nucleation sites, as reported in Ref. [17].

The microstructures of the samples investigated with HEXRD are depicted in Fig. 6 and are presented as a bright field TEM image of the as-built sample in a) and a backscattered electron (BSE) – SEM image of the heat-treated specimen ( $800\text{ }^\circ\text{C} - 12\text{ h} - \text{FC}$ ) in b). The as-built component, produced with standard parameters and an  $E_d$  of about  $60\text{ J}\cdot\text{mm}^{-3}$ , reveals similarities with the powder material and reveals an acicular microstructure showing hierarchical  $\alpha'$  sub-structures. The heat-treated sample demonstrates the occurrence of equilibrium  $\beta$  phase constituents (bright phase) at  $\alpha$  grain boundaries and within larger  $\alpha$  grains, as reported in Ref. [17].

### 3.2.2. Phase transformation and elemental distribution

Fig. 7 shows the DSC measurement of the Ti6242S powder sample recorded during continuous heating. Phase transformations are indicated with square and circles for the respective exothermic and endothermic reactions. The measurements were performed starting with  $40\text{ K}\cdot\text{min}^{-1}$  and repeated a second time with the same and already heated powder material. The heat flow curve of the first heating cycle reveals an exothermic phase transformation at lower temperatures, suggesting the tempering of the martensite towards thermodynamic equilibrium ( $\alpha' \rightarrow \alpha$ ). Moreover, the temperature for the martensite relaxation of about  $600\text{ }^\circ\text{C}$  is in accordance with the HTXRD experiment

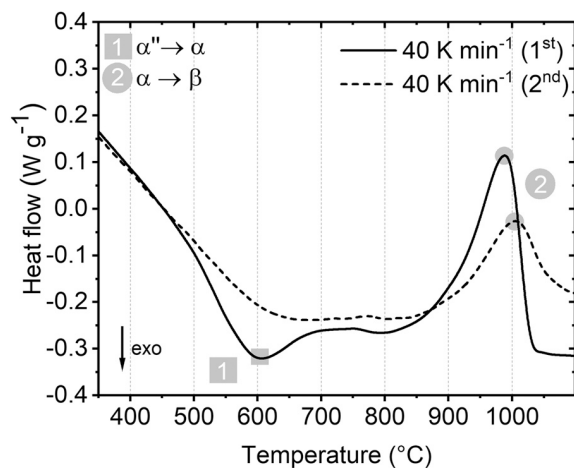


**Fig. 7.** DSC analysis. The heat flow curves of the Ti6242S powder are recorded during continuous heating at  $40\text{ K}\cdot\text{min}^{-1}$ . Only the heat flow of the first heating experiment with the virgin powder reveals an exothermic reaction during the martensite relaxation indicating the  $\alpha' \rightarrow \alpha$  transformation. The second heating experiment was performed on the already heated powder material.

shown in Fig. 2c. The second heating cycle only shows the  $\alpha \rightarrow \beta$  phase transformation and, therefore, confirms a thermodynamic equilibrium material condition of the powder after the first DSC heating cycle.

In general, a martensitic phase transformation in Ti base alloys depends on the chemical composition. The generated martensite with hexagonal lattice structure, designated  $\alpha'$ , appears in lean Ti base alloys with a certain amount of  $\beta$  stabilizing elements, e.g.  $V < 9\text{ m.}\%$  or  $\text{Mo} < 4\text{ m.}\%$  [39,40]. As the fraction of  $\beta$  stabilizing elements – which can be summarized as Mo equivalent (or simply  $[\text{Mo}]_{\text{eq}}$ ) – increases, the transformation to the hexagonal  $\alpha'$  cannot be fulfilled and the orthorhombic  $\alpha''$  martensite forms during quenching or deformation via stress-induced martensitic transformation [34,41–46]. Therefore, the orthorhombic structure represents an intermediate phase between  $\beta$  and  $\alpha$  phases. According to literature, the minimum amount of  $\beta$  stabilizing elements to generate an orthorhombic structure in the binary Ti-Mo system is  $6\text{--}8\text{ m.}\%$  Mo [47] or rather an  $[\text{Mo}]_{\text{eq}}$  of  $4.45\text{ m.}\%$  [34] in Ti base alloys quenched from the single  $\beta$  phase field region.

The chemical constitution of the Ti6242S alloy investigated is shown in Table 2 and displays a  $[\text{Mo}]_{\text{eq}}$  of about  $2.05\text{ m.}\%$ , which is significantly below the lowest value published in literature to generate martensite exhibiting a conventional orthorhombic structure. Previous experimental results reflect the occurrence of an orthorhombic  $\alpha''$  martensite in Ti alloys due to a heat treatment, i.e. enrichment of the  $\beta$  phase at high temperatures in  $\beta$  stabilizing elements, followed by quenching [46]. By increasing the solute content in the  $\beta$  phase, the hexagonal symmetry cannot be reached and the crystal gets distorted which is why the orthorhombic structure forms instead [9,48]. To exclude the hypothesis of elemental segregation, and thus a locally higher  $[\text{Mo}]_{\text{eq}}$  in the powder material, known to promote the orthorhombic  $\alpha''$  phase transformation, APT was performed. The results are presented in Fig. 8a and b. The region displayed measures  $60 \times 60 \times 100\text{ nm}^3$  and contains  $6.8 \cdot 10^6$  atoms. It can be seen that the elemental distribution for the powder material is homogeneous. For better visualization of the elemental distribution a video of the cylinder is shown in a **Supplementary Movie**. Fig. 8b presents a quantitative cluster analysis. The result confirms the homogeneous elemental distribution in the powder due to the almost perfect covering of the normal frequency distribution and the calculated cluster values (see Table 3) of the alloying elements Ti, Al, Sn, Zr, Mo and Si. The binomial distribution represents an ideal distribution within a homogenized alloy [49]. In addition, the homogeneous distribution of the powder indicates an athermal phase transformation, i.e. no diffusion has taken place during the atomization process.

**Table 2**

Chemical composition of the Ti-6Al-2Sn-4Zr-2Mo-Si powder investigated.

Element	Ti	Al	Sn	Zr	Mo
m.%	bal.	6.4	2.0	4.2	2.0
Element	Si	Fe	O	N	$[\text{Mo}]_{\text{eq}}$
m.%	0.05	0.02	0.13	0.002	2.05

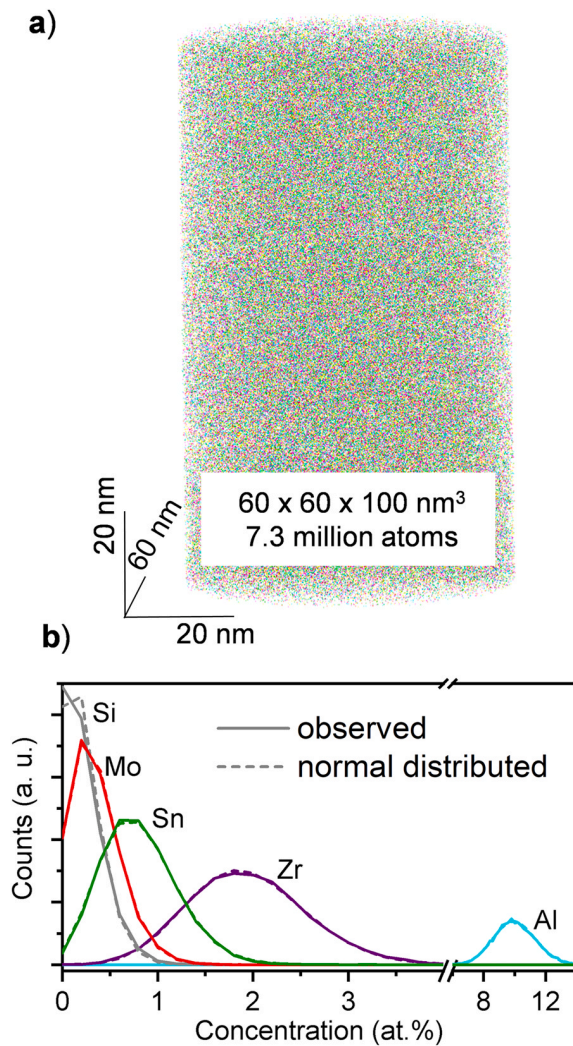


**Fig. 8.** APT analysis. a) APT elemental map in atomic scale showing a homogeneous distribution of the elements in the as-atomized powder; cluster analysis in b) reveals a normal distribution, i.e. ideally homogenized alloy composition in the powder condition.

**Table 3**

Quantitative cluster estimation of the as-atomized powder material investigated. The cluster value  $\mu$  ( $\mu = \sqrt{\chi^2 / (n + \chi^2)}$ ) describes whether the elements are randomly distributed ( $\mu = 0$ ) or accumulated ( $\mu = 1$ ).

Element	$\mu$ (Powder)
Ti	0.190
Al	0.060
Sn	0.029
Zr	0.036
Mo	0.030
Si	0.100

Supplementary material related to this article can be found online at [doi:10.1016/j.jallcom.2021.163155](https://doi.org/10.1016/j.jallcom.2021.163155).

### 3.3. Orthorhombic martensite in additively manufactured samples

As the orthorhombic type of martensite was found for the first time in the as-atomized Ti6242S powder in this study, we also investigated the opportunity to generate an orthorhombic martensite

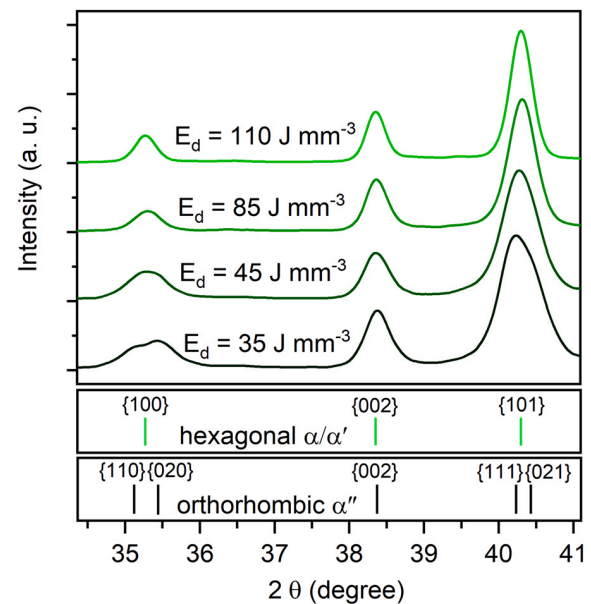


**Fig. 9.** XRD analysis of as-LPBF Ti6242S samples manufactured with varying  $E_d$ . The spectra reveal the occurrence of hexagonal  $\alpha/\alpha'$  martensite for higher  $E_d$  values. A reduction of  $E_d$  to  $35 \text{ J} \cdot \text{mm}^{-3}$  leads to the formation of orthorhombic  $\alpha''$  martensite.

phase in a bulk sample manufactured by LPBF. Since standard LPBF process parameters lead to hexagonal martensite, as seen in Fig. 2, and a variety of Refs. [19,50–52] report only the appearance of hexagonal martensite in the Ti6242S alloy, the LPBF parameters had to be changed accordingly. Gas atomization for producing metal powder involves cooling rates up to  $10^8 \text{ K s}^{-1}$  [12–14] when compared to slightly lower cooling rates of  $10^4$ – $10^6 \text{ K s}^{-1}$  in the case of the LPBF process [15]. Thus, it is obvious that higher cooling rates are needed to generate the orthorhombic  $\alpha''$  martensite.

The most important LPBF process parameter to be changed is the volumetric energy density  $E_d$ , which connects the main process variables like laser power and scanning speed. These parameters can also be stated as heat input during the manufacturing process. Decreasing the heat input leads to a finer microstructure and smaller melt pool as well as an increased cooling rate, needed for and also an increased cooling rate needed for the required adaptations of the additive manufacturing process [7]. Concerning the knowledge above, bulk components were manufactured by using different LPBF process parameters to increase the cooling rate and study the phases occurring. It should be addressed here, that a reduction of the heat input represents the direct opposite of the common knowledge to reduce thermal residual stresses by heat storage (reduction of thermal gradient) via preheating of the building platform or a higher heat input [7]. Inspired by the powder material in this study, higher cooling rates, however, lead to the formation of a different martensite with phase-specific benefits.

The results in Fig. 9 show the XRD spectra of as-built samples as a function of  $E_d$ . Here, the sample with the lowest  $E_d$  of about  $35 \text{ J} \cdot \text{mm}^{-3}$ , i.e. the highest cooling rate, clearly exhibits the orthorhombic  $\alpha''$  martensite. However, from XRD, it is not possible to exclude the simultaneous presence of  $\alpha'$  martensite constituents. A closer look at the peaks around  $35.5^\circ$  shows the broadening and final splitting of the peak with decreasing  $E_d$ , marking the change in the lattice structure from hexagonal  $\alpha'$  to orthorhombic  $\alpha''$ . It has been reported that only one type of martensite, either the hexagonal  $\alpha'$  or the orthorhombic  $\alpha''$ , can occur for a certain chemical composition of Ti base alloys [53] and both types cannot coexist in the same alloy. The XRD results in this study demonstrate that there is a possibility for controlling the occurrence of orthorhombic martensite by

changing the manufacturing parameters during the LPBF process, which had not been evidenced so far. Furthermore, the most significant difference in the martensitic transformation upon fast cooling to generate  $\alpha''$  orthorhombic is the softening of the material and increase in ductility as described in Refs. [46,54]. Softening of Ti6242S material during the LPBF might help to reduce residual stresses, which are known to promote cracks and delamination during the additive manufacturing process [7,16]. Hardness measurements of the as-built samples confirm the predicted softening of samples containing  $\alpha''$  martensite. The sample which was manufactured with an  $E_d$  of  $35 \text{ J}\cdot\text{mm}^{-3}$  and clearly reveals orthorhombic martensite that exhibits a reduced hardness of  $423 \pm 16 \text{ HV}0.1$  compared to  $456 \pm 11 \text{ HV}0.1$  for samples produced via standard LPBF parameters ( $E_d = 60 \text{ J}\cdot\text{mm}^{-3}$ ).

#### 4. Conclusion

Phase transformations in a near- $\alpha$  titanium base alloy for additive manufacturing applications were investigated in this study using cutting-edge HEXRD and a wide variety of electron microscopy characterization techniques to determine key constituents from micro to nanometer scale. A major discovery in the present work is the evidence of two types of martensite, namely orthorhombic  $\alpha''$  and hexagonal  $\alpha'$ , which are a function of the cooling rate for the same chemical composition of the engineering alloy Ti6242S and for Ti base alloys in general. Both martensitic phases are far from thermodynamic equilibrium due to the high cooling rate during the gas atomization and LPBF. The appearance of equilibrium phases can be controlled by transforming the metastable martensite into stable phases by a heat treatment subsequent to the LPBF process, which enables the synergistic interplay of high strength  $\alpha$  and ductile  $\beta$  phases.

HRTEM investigations in this work present the nanometer microstructure, governed by a hierarchical acicular martensite microstructure containing primary and secondary  $\alpha''$  constituents. The occurrence of lattice defects, such as mechanical twins and dislocations at the closed-packed lattice planes, may play a significant role in the precipitation morphology of the equilibrium  $\alpha + \beta$  microstructure in both the powder and as-built material.

The importance of this study can be better understood considering the softer nature of orthorhombic  $\alpha''$  martensite discovered in the Ti6242S alloy, which is important to addressing a long-standing problem of additive manufactured alloys, i.e. the vulnerability for cracks due to less residual stresses and enhanced ductility.

#### Funding

We acknowledge DESY (Hamburg, Germany), a member of the Helmholtz Association HGF, for the provision of experimental facilities. Parts of this research were carried out at PETRA III and we would like to thank Andreas Stark, Peter Staron and Norbert Schell for assistance. Beamtime was allocated for proposal I-20200691 EC. The authors would also like to thank Svea Mayer and Gloria Graf for her support during the editing and the APT evaluation of the present work. MAT is grateful to the European Research Council (ERC) excellent science grant "TRANSDESIGN" through the Horizon 2020 program under contract 757961 and also from the support from the Austrian Research Promotion Agency (FFG) in the project 3D nanoAnalytics (FFG-No 858040).

#### CRedit authorship contribution statement

C.F.R. performed the XRD and HTXRD analysis and conducted electron microscopy research including data acquisition. M.A.T. and C.G. performed the electron microscopy research including data evaluation. M.M. conducted HEXRD experiments including data evaluation. F.M.M. utilized APT investigations including data

acquisition. T.P. and T.J. designed and produced the additively manufactured Ti6242S components. H.C. enabled the funding for the present work. All authors contributed to the discussion and the editing of the manuscript.

#### Declaration of Competing Interest

The authors declare that they have no known competing financial interests or personal relationships that could have appeared to influence the work reported in this paper.

#### References

- [1] D. Zhang, D. Qiu, M.A. Gibson, Y. Zheng, H.L. Fraser, D.H. StJohn, M.A. Easton, Additive manufacturing of ultrafine-grained high-strength titanium alloys, *Nature* 576 (2019) 91–95, <https://doi.org/10.1038/s41586-019-1783-1>
- [2] T. DebRoy, T. Mukherjee, H.L. Wei, J.W. Elmer, J.O. Milewski, Metallurgy, mechanistic models and machine learning in metal printing, *Nat. Rev. Mater.* 6 (2021) 48–68, <https://doi.org/10.1038/s41578-020-00236-1>
- [3] C. Zhao, N.D. Parab, X. Li, K. Fezzaa, W. Tan, A.D. Rollett, T. Sun, Critical instability at moving keyhole tip generates porosity in laser melting, *Science* 370 (2020) 1080–1086, <https://doi.org/10.1126/science.abd1587>
- [4] A.J. Capel, R.P. Rimmington, M.P. Lewis, S.D.R. Christie, 3D printing for chemical, pharmaceutical and biological applications, *Nat. Rev. Chem.* 2 (2018) 422–436, <https://doi.org/10.1038/s41570-018-0058-y>
- [5] S.A. Khairallah, A.A. Martin, J.R.I. Lee, G. Guss, N.P. Calta, J.A. Hammons, M.H. Nielsen, K. Chaput, E. Schwalbach, M.N. Shah, M.G. Chapman, T.M. Willey, A.M. Rubenchik, A.T. Anderson, Y. Morris Wang, M.J. Matthews, W.E. King, Controlling interdependent meso-nanosecond dynamics and defect generation in metal 3D printing, *Science* 368 (2020) 660–665, <https://doi.org/10.1126/science.aay7830>
- [6] C.F. Yolton, F.H. Froes, *Conventional titanium powder production, Titanium Powder Metallurgy*, Butterworth-Heinemann, Waltham, MA, 2015, pp. 21–32.
- [7] T. DebRoy, H.L. Wei, J.S. Zuback, T. Mukherjee, J.W. Elmer, J.O. Milewski, A.M. Beese, A. Wilson-Heid, A. De, W. Zhang, Additive manufacturing of metallic components – process, structure and properties, *Prog. Mater. Sci.* 92 (2018) 112–224, <https://doi.org/10.1016/j.pmatsci.2017.10.001>
- [8] P. Barriobero-Vila, J. Gussone, A. Stark, N. Schell, J. Haubrich, G. Requena, Peritectic titanium alloys for 3D printing, *Nat. Commun.* 9 (1) (2018) 1–9, <https://doi.org/10.1038/s41467-018-05819-9>
- [9] C. Lütjering, J.C. Williams, *Titanium*, first ed., Springer Science & Business Media, Berlin, Heidelberg, 2007.
- [10] M. Peters, C. Leyens (Eds.), *Titanium and Titanium Alloys: Fundamentals and Applications*, first ed., John Wiley & Sons, Weinheim, 2003.
- [11] T. Ahmed, H.J. Rack, Phase transformations during cooling in  $\alpha + \beta$  titanium alloys, *Mater. Sci. Eng. A* 243 (1998) 206–211, [https://doi.org/10.1016/S0921-5093\(97\)00802-2](https://doi.org/10.1016/S0921-5093(97)00802-2)
- [12] K. Guo, C. Liu, S. Chen, H. Dong, S. Wang, High pressure EIGA preparation and 3D printing capability of Ti–6Al–4V powder, *Trans. Nonferrous Met. Soc. China* 30 (2020) 147–159, [https://doi.org/10.1016/S1003-6326\(19\)65187-3](https://doi.org/10.1016/S1003-6326(19)65187-3)
- [13] P. Fang, Y. Xu, X. Li, Y. Chen, Influence of atomizing gas and cooling rate on solidification characterization of nickel-based superalloy powders, *Rare Met. Mater. Eng.* 47 (2018) 423–430, [https://doi.org/10.1016/S1875-5372\(18\)30082-1](https://doi.org/10.1016/S1875-5372(18)30082-1)
- [14] Shiwen He, Liu Yong, Guo Sheng, Cooling rate calculation of non-equilibrium aluminum alloy powders prepared by gas atomization, *Rare Met. Mater. Eng.* 38 (2009) 353–356.
- [15] S. Liu, Y.C. Shin, Additive manufacturing of Ti6Al4V alloy: a review, *Mater. Des.* 164 (2019) 107552, <https://doi.org/10.1016/j.matdes.2018.107552>
- [16] G.M. Ter Haar, T.H. Becker, Low temperature stress relief and martensitic decomposition in selective laser melting produced Ti6Al4V, *Mater. Des. Process. Commun.* 3 (2021) e138, <https://doi.org/10.1002/mdp2.138>
- [17] C. Fleißner-Rieger, T. Pfeifer, T. Jörg, T. Kremmer, M. Brabetz, H. Clemens, S. Mayer, Selective laser melting of a near- $\alpha$  Ti6242S alloy for high performance automotive parts, *Adv. Eng. Mater.* 2001194 (2021), <https://doi.org/10.1002/adem.202001194>
- [18] M. Lopez, C. Pickett, E. Arrieta, L.E. Murr, R.B. Wicker, M. Ahlfors, D. Godfrey, F. Medina, Effects of postprocess hot isostatic pressing treatments on the mechanical performance of EBM fabricated Ti–6Al–2Sn–4Zr–2Mo, *Materials* 13 (2020), <https://doi.org/10.3390/ma13112604>
- [19] H. Fan, S. Yang, Effects of direct aging on near-alpha Ti–6Al–2Sn–4Zr–2Mo (Ti-6242) titanium alloy fabricated by selective laser melting (SLM), *Mater. Sci. Eng. A* 788 (2020) 139533, <https://doi.org/10.1016/j.msea.2020.139533>
- [20] N. Schell, A. King, F. Beckmann, T. Fischer, M. Müller, A. Schreyer, The high energy materials science beamline (HEMS) at PETRA III, *Mater. Sci. Forum* 772 (2014) 57–61, <https://doi.org/10.4028/www.scientific.net/MSF.772.57>
- [21] A.P. Hammersley, S.O. Svensson, M. Hanfland, A.N. Fitch, D. Häusermann, Two-dimensional detector software: from real detector to idealised image or two-theta scan, *High. Press. Res.* 14 (1996) 235–248, <https://doi.org/10.1080/08957959608201408>
- [22] L. Lutterotti, Maud: a Rietveld analysis program designed for the internet and experiment integration, 54–54, *Acta Crystallogr. Sect. A Found. Crystallogr.* 56 (2000), <https://doi.org/10.1107/s0108767300021954>



- [23] C. Fleißner-Rieger, T. Pogrietz, D. Obersteiner, T. Pfeifer, H. Clemens, S. Mayer, An additively manufactured titanium alloy in the focus of metallography, *Pract. Metallogr.* 58 (2021) 4–31, <https://doi.org/10.1515/pm-2020-0001>
- [24] K. Thompson, D. Lawrence, D.J. Larson, J.D. Olson, T.F. Kelly, B. Gorman, In situ site-specific specimen preparation for atom probe tomography, *Ultramicroscopy* 107 (2007) 131–139, <https://doi.org/10.1016/j.ultramicro.2006.06.008>
- [25] C. Laslau, B. Ingham, Z.D. Zujovic, P. Čapková, J. Stejskal, M. Trchová, J. Travas-Sejdic, Synchrotron X-ray scattering reveals early-stage crystallinity during the self-assembly of polyaniline nanotubes with rectangular cross-sections, *Synth. Met.* 161 (2012) 2739–2742, <https://doi.org/10.1016/j.synthmet.2011.10.012>
- [26] L. Lutterotti, Total pattern fitting for the combined size-strain-stress-texture determination in thin film diffraction, *Nucl. Instrum. Methods Phys. Res. Sect. B Beam Interact. Mater. At.* 268 (2010) 334–340, <https://doi.org/10.1016/j.nimb.2009.09.053>
- [27] B.H. Toby, R factors in Rietveld analysis: how good is good enough? *Powder Diffr.* 21 (2006) 67–70, <https://doi.org/10.1154/1.2179804>
- [28] S. Malinov, W. Sha, Z. Guo, C.C. Tang, A.E. Long, Synchrotron X-ray diffraction study of the phase transformations in titanium alloys, *Mater. Charact.* 48 (2002) 279–295, [https://doi.org/10.1016/S1044-5803\(02\)00286-3](https://doi.org/10.1016/S1044-5803(02)00286-3)
- [29] F.R. Kaschel, R.K. Vijayaraghavan, A. Shmeliov, E.K. McCarthy, M. Canavan, P.J. McNally, D.P. Dowling, V. Nicolosi, M. Celikin, Mechanism of stress relaxation and phase transformation in additively manufactured Ti-6Al-4V via in situ high temperature XRD and TEM analyses, *Acta Mater.* 188 (2020) 720–732, <https://doi.org/10.1016/j.actamat.2020.02.056>
- [30] M.T. Tsai, Y.W. Chen, C.Y. Chao, J.S.C. Jang, C.C. Tsai, Y.L. Su, C.N. Kuo, Heat-treatment effects on mechanical properties and microstructure evolution of Ti-6Al-4V alloy fabricated by laser powder bed fusion, *J. Alloy. Compd.* 816 (2020) 152615, <https://doi.org/10.1016/j.jallcom.2019.152615>
- [31] D. Banerjee, J.C. Williams, Perspectives on titanium science and technology, *Acta Mater.* 61 (2013) 844–879, <https://doi.org/10.1016/j.actamat.2012.10.043>
- [32] W. Elmay, S. Berveiller, E. Patoor, T. Gloriant, F. Prima, P. Laheurte, Texture evolution of orthorhombic  $\alpha''$  titanium alloy investigated by in situ X-ray diffraction, *Mater. Sci. Eng. A* 679 (2017) 504–510, <https://doi.org/10.1016/j.msea.2016.10.072>
- [33] S. Joseph, T.C. Lindley, D. Dye, Dislocation interactions and crack nucleation in a fatigued near-Alpha titanium alloy, *Int. J. Plast.* 110 (2018) 38–56, <https://doi.org/10.1016/j.jiplas.2018.06.009>
- [34] P. Barriobero-Vila, V. Biancardi Oliveira, S. Schwarz, T. Buslaps, G. Requena, Tracking the  $\alpha''$  martensite decomposition during continuous heating of a Ti-6Al-6V-2Sn alloy, *Acta Mater.* 135 (2017) 132–143, <https://doi.org/10.1016/j.actamat.2017.06.018>
- [35] K.A. Bywater, J.W. Christian, Martensitic transformations in titanium-tantalum alloys, *Philos. Mag.* 25 (1972) 1249–1273, <https://doi.org/10.1080/14786437208223852>
- [36] R. Davis, H.M. Flower, D.R.F. West, The decomposition of Ti-Mo alloy martensites by nucleation and growth and spinodal mechanisms, *Acta Met.* 27 (1979) 1041–1052, [https://doi.org/10.1016/0001-6160\(79\)90192-5](https://doi.org/10.1016/0001-6160(79)90192-5)
- [37] X. Ji, I. Gutierrez-Urrutia, S. Emura, T. Liu, T. Hara, X. Min, D. Ping, K. Tsuchiya, Twinning behavior of orthorhombic- $\alpha''$  martensite in a Ti-7.5Mo alloy, *Sci. Technol. Adv. Mater.* 20 (2019) 401–411, <https://doi.org/10.1080/14686996.2019.1600201>
- [38] S. Banumathy, R.K. Mandal, A.K. Singh, Structure of orthorhombic martensitic phase in binary Ti-Nb alloys, *J. Appl. Phys.* 106 (2009), <https://doi.org/10.1063/1.3255966>
- [39] R. Boyer, G. Welsch, E.W. Collings, *Materials Properties Handbook: Titanium Alloys*, fourth ed., ASM International, Materials Park, Novelty, Ohio, 1994.
- [40] H.M. Flower, R. Davis, D.R.F. West, *Martensite Formation and Decomposition in Alloys of Titanium Containing  $\beta$ -stabilizing Elements*, Titanium and Titanium Alloys, Springer, Boston, MA, 1982, pp. 1703–1715.
- [41] D. Ballat-Durand, S. Bouvier, M. Risbet, Contributions of an innovative post-weld heat treatment to the micro-tensile behavior of two mono-material linear friction welded joints using: The  $\beta$ -metastable Ti-5Al-2Sn-2Zr-4Mo-4Cr (Ti17) and the near- $\alpha$  Ti-6Al-2Sn-4Zr-2Mo (Ti6242) Ti-alloys, *Mater. Sci. Eng. A* 766 (2019) 138334, <https://doi.org/10.1016/j.msea.2019.138334>
- [42] W. Elmay, F. Prima, T. Gloriant, B. Bolle, Y. Zhong, E. Patoor, P. Laheurte, Effects of thermomechanical process on the microstructure and mechanical properties of a fully martensitic titanium-based biomedical alloy, *J. Mech. Behav. Biomed. Mater.* 18 (2013) 47–56, <https://doi.org/10.1016/j.jmbbm.2012.10.018>
- [43] K. Kapoor, P. Ravi, D. Naragani, J.S. Park, J.D. Almer, M.D. Sangid, Strain rate sensitivity, microstructure variations, and stress-assisted  $\beta \rightarrow \alpha''$  phase transformation investigation on the mechanical behavior of dual-phase titanium alloys, *Mater. Charact.* 166 (2020) 110410, <https://doi.org/10.1016/j.matchar.2020.110410>
- [44] K.K. Kharia, H.J. Rack, I. Introduction, Martensitic Phase Transformations in IMI 550, *Metall. Mater. Trans. A* 32 (2001) 671–679, <https://doi.org/10.1007/s11661-001-1002-0>
- [45] M.J. Lai, C.C. Tسان, D. Raabe, On the mechanism of {332} twinning in metastable  $\beta$  titanium alloys, *Acta Mater.* 111 (2016) 173–186, <https://doi.org/10.1016/j.actamat.2016.03.040>
- [46] N. Kazantseva, P. Krakhmalev, M. Thuvander, I. Yadroitsev, N. Vinogradova, I. Ezhov, Martensitic transformations in Ti-6Al-4V (ELI) alloy manufactured by 3D Printing, *Mater. Charact.* 146 (2018) 101–112, <https://doi.org/10.1016/j.matchar.2018.09.042>
- [47] R. Davis, H.M. Flower, D.R.F. West, Martensitic transformations in Ti-Mo alloys, *J. Mater. Sci.* 14 (1979) 712–722, <https://doi.org/10.1007/BF00772735>
- [48] A.V. Dobromyslov, V.A. Elkin, The orthorhombic  $\alpha''$ -phase in binary titanium-base alloys with d-metals of V-VIII groups, *Mater. Sci. Eng. A* 438–440 (2006) 324–326, <https://doi.org/10.1016/j.msea.2006.02.086>
- [49] M.P. Moody, L.T. Stephenson, A.V. Ceguerra, S.P. Ringer, Quantitative binomial distribution analyses of nanoscale like-solute atom clustering and segregation in atom probe tomography data, *Microsc. Res. Tech.* 71 (2008) 542–550, <https://doi.org/10.1002/jemt.20582>
- [50] H. Imai, G. Yamane, H. Matsumoto, V. Vidal, V. Velay, Superplasticity of metastable ultrafine-grained Ti-6242S alloy: mechanical flow behavior and microstructural evolution, *Mater. Sci. Eng. A* 754 (2019) 569–580, <https://doi.org/10.1016/j.msea.2019.03.085>
- [51] Y. Cui, K. Aoyagi, Y. Koizumi, T. Fujieda, A. Chiba, Enhanced oxidation resistance of a titanium-based alloy by the addition of boron and the application of electron beam melting, *Addit. Manuf.* 31 (2020) 100971, <https://doi.org/10.1016/j.addma.2019.100971>
- [52] T. Fujieda, Y. Cui, K. Aoyagi, Y. Koizumi, A. Chiba, Electron beam melting of boron-modified Ti-2Al-2Sn-4Zr-2Mo-0.1Si alloy with superior tensile strength and oxidation resistance at elevated temperatures, *Materials* 4 (2018) 367–372, <https://doi.org/10.1016/j.mtl.2018.10.013>
- [53] J.C. Williams, A.F. Belov (Eds.), *Titanium and Titanium Alloys: Scientific and Technological Aspects*, Volume 3 Springer Science & Business Media, New York, 1982.
- [54] Y. Guo, T. Jung, Y.L. Chiu, H. Li, S. Bray, P. Bowen, Microstructure and microhardness of Ti6246 linear friction weld, *Mater. Sci. Eng. A* 562 (2013) 17–24, <https://doi.org/10.1016/j.msea.2012.10.089>

## Article D

# Formation and evolution of precipitates in an additively manufactured near- $\alpha$ titanium base alloy

Christian Fleißner-Rieger<sup>1,†,\*</sup>, Hannah Schönmaier<sup>1,†</sup>, Michael Musi<sup>1</sup>, Christoph Turk<sup>2</sup>, Manfred Stadler<sup>2</sup>, Harald Gschiel<sup>2</sup>, Tanja Pfeifer<sup>3</sup> and Helmut Clemens<sup>1</sup>

<sup>1</sup> Department Werkstoffwissenschaft, Montanuniversität Leoben, Franz-Josef Straße 18, 8700 Leoben, Österreich

<sup>2</sup> voestalpine BÖHLER Edelstahl GmbH & Co KG, Mariazeller Straße 25, Kapfenberg 8605, Austria

<sup>3</sup> Pankl Racing Systems AG, Additive Manufacturing Technologies, Industriestraße Ost 4, 8605 Kapfenberg, Austria

\* Corresponding author

† These authors contributed equally to this work

Materialia, **12**, 101366 (2022)

<https://doi.org/10.1016/j.mtla.2022.101366>

open access: CC BY 4.0





Contents lists available at ScienceDirect

Materialia

journal homepage: [www.elsevier.com/locate/mtla](http://www.elsevier.com/locate/mtla)

## Formation and evolution of precipitates in an additively manufactured near- $\alpha$ titanium base alloy

Christian Fleißner-Rieger<sup>a,1,\*</sup>, Hannah Schönmaier<sup>a,1</sup>, Michael Musi<sup>a</sup>, Manfred Stadler<sup>b</sup>, Harald Gschiel<sup>b</sup>, Christoph Turk<sup>b</sup>, Tanja Pfeifer<sup>c</sup>, Helmut Clemens<sup>a</sup>

<sup>a</sup> Department of Materials Science, Montanuniversität Leoben, Franz-Josef Straße 18, 8700 Leoben, Austria

<sup>b</sup> voestalpine BÖHLER Edelstahl GmbH & Co KG, Mariázeller Straße 25, 8605 Kapfenberg, Austria

<sup>c</sup> Pankl Racing Systems AG, Additive Manufacturing Technologies, Industriestraße Ost 4, 8605 Kapfenberg, Austria

### ARTICLE INFO

#### Keywords:

Titanium alloys  
Atom probe tomography  
Synchrotron radiation  
Martensitic phase transformation  
Silicides

### ABSTRACT

Titanium base alloys are frequently used in laser powder bed fusion manufacturing processes and enable the production of lightweight and complex components. This study describes the influence of the heat input and various post-process heat treatments on the martensite formation and its decomposition in an additively manufactured Ti-6Al-2Sn-4Zr-2Mo-Si alloy. The change of the martensite crystal structure from orthorhombic to hexagonal, caused by additional heat input, was proven by high-energy X-ray diffraction. It is shown that the heat input of the laser affects the diffusion of alloying elements such as Mo and Si. This behavior was investigated by atom probe tomography, which confirms clustering of Mo and Si at dislocations and grain boundaries, and allows for linking the heat input during the manufacturing process with the morphology of the observed clusters. Moreover, particular emphasis is laid on explaining the formation mechanism of  $(\text{Ti,Zr})_6\text{Si}_3$  silicide particles during a subsequent heat treatment.

In general, near- $\alpha$  Ti base alloys are used for applications at elevated service temperatures up to 600 °C in the automotive and aerospace industry. This class of alloys combines a high creep resistance of  $\alpha$  alloys and the strength of  $\alpha+\beta$  alloys, such as the Ti-6Al-4V (m.%) alloy [1,2]. Although near- $\alpha$  Ti alloys had already been invented in the 1970s, up until today only a few research groups have focused on the processing of this alloy group by laser powder bed fusion (LPBF) additive manufacturing (AM) [3,4]. In contrast to traditional process routes such as casting and wrought processing, LPBF generates small melt pools, which undergo a martensitic transformation after solidification due to cooling rates of up to  $10^4$ – $10^6\text{Ks}^{-1}$  [5], thus leading to a non-equilibrium microstructure. Besides the  $\alpha'$  (hexagonal) or  $\alpha''$  (orthorhombic) martensite, near- $\alpha$  alloys also exhibit small amounts of the body-centered cubic  $\beta$  phase [6]. In contrast to the  $\alpha'/\alpha''$  phase, the formation of  $\beta$  phase is related to additional heat input during AM after solidification or post-process heat treatments [7,8]. Ti-6Al-2Sn-4Zr-2Mo-Si (Ti6242S, m.%) contains low amounts of Si, which enhances the creep resistance by means of forming silicide particles [2]. While the effect of Si alloying on the creep resistance is well understood, no investigations of the precipitation behavior of silicides in additively manufactured Ti6242S have been conducted thus far. Furthermore, the impact of heat input during

LPBF and post-processing on the  $\beta$  phase evolution has not been thematized for the near- $\alpha$  alloy Ti6242S.

This study deals with the investigation of LPBF manufactured Ti6242S by means of the correlative high-resolution methods atom probe tomography (APT), high-energy X-ray diffraction (HEXRD) and transmission electron microscopy (TEM). Particular emphasis is placed on determining the occurring phases as well as on the evolution of the sub-microstructure during the decomposition of the martensitic microstructure in the course of post-process heat treatments.

The initial Ti6242S powder material reveals a chemical composition of 6.4 m.% Al, 2.0 m.% Sn 4.2 m.% Zr, 2.0 m.% Mo, 0.05 m.% Si, and 0.13 m.% O. The Al, Sn, Zr, Mo, and Si contents were determined via inductively coupled plasma atomic emission spectroscopy, whereas the O content was determined via carrier gas hot extraction. The investigated cubic bulk specimens of the dimensions  $20 \times 15 \times 20\text{mm}^3$  were manufactured with an EOS M290 LPBF unit utilizing an energy density ( $E_d$ ) employing the range of 35 to 110  $\text{Jmm}^{-3}$ . The AM process was performed under constant Ar shielding gas environment and the building platform was pre-heated to 150 °C.

To assess local variations of the chemical composition, APT was performed on tips prepared via a standard focused ion beam technique [9] in a Versa 3D DualBeam workstation (FEI, OR, USA). The APT mea-

\* Corresponding author: Mr. Christian Fleißner-Rieger, Materials Science, Montanuniversität Leoben, 8700 Leoben, Austria.

E-mail address: [christian.fleissner-rieger@unileoben.ac.at](mailto:christian.fleissner-rieger@unileoben.ac.at) (C. Fleißner-Rieger).

<sup>1</sup> These authors contributed equally to this work.

<https://doi.org/10.1016/j.mtla.2022.101366>

Received 1 February 2022; Accepted 11 February 2022

Available online 14 February 2022

2589-1529/© 2022 The Author(s). Published by Elsevier B.V. on behalf of Acta Materialia Inc. This is an open access article under the CC BY license

(<http://creativecommons.org/licenses/by/4.0/>)

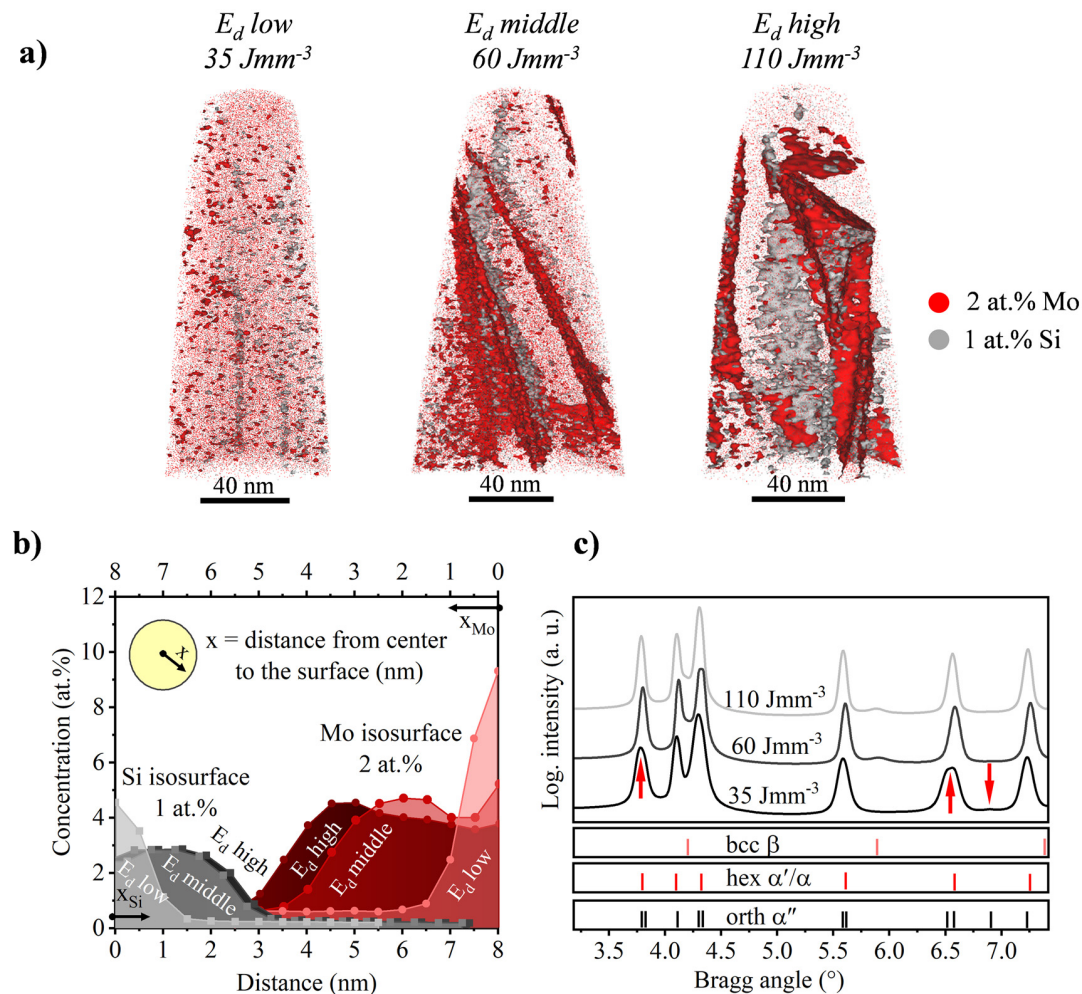


**Fig. 1.** (a) APT tips of the as-built samples fabricated with varying  $E_d$  (35, 60 and 110 Jmm<sup>-3</sup>), depicting the 2 at.% Mo and 1 at.% Si isosurfaces; (b) proxygrams of the 2 at.% Mo and 1 at.% Si isosurfaces of the three tips; (c) azimuthally integrated HEXRD curves of corresponding specimen conditions.

measurements were conducted using laser mode in a local electrode atom probe LEAP 3000X HR (Cameca, France). All tips were measured at a cryogenic temperature of 60 K, a laser energy of 0.4 nJ and a laser frequency of 250 kHz. For data evaluation, the APT reconstruction software IVAS 3.6 from Cameca was used.

**Fig. 1(a)** depicts three APT tips with 1 at.% Si and 2 at.% Mo isosurfaces, showing the as-built sub-microstructure of Ti6242S manufactured with  $E_d$  values of 35, 60 and 110 Jmm<sup>-3</sup>, respectively. In the as-built condition, only Si and Mo were inhomogeneously distributed. An  $E_d$  of 35 Jmm<sup>-3</sup> leads to linearly aligned slight segregations of Si, whereas Mo shows clustering and no significant segregations. This is assumed to be linked to the low solubility and the high diffusivity of Si when compared to Mo in the matrix phase [10,11].

An  $E_d$  of 60 and 110 Jmm<sup>-3</sup> results in plate- and rod-like Mo segregations in the  $\alpha'$  matrix phase. It can be assumed that a higher  $E_d$  leads to longer times at higher temperatures and, consequently, provides sufficient heat input to overcome the activation energy for Mo diffusion [10,11]. **Fig. 1(b)** provides the corresponding proxygrams, which show the change of the elemental concentration of the 2 at.% Mo and 1 at.% Si isosurfaces in the three tips. For a low  $E_d$  of 35 Jmm<sup>-3</sup>, the Si isosurfaces are smaller, yet more enriched in Si. For higher  $E_d$  of 60 and 110 Jmm<sup>-3</sup>, the Si isosurfaces are larger, but exhibit a lower core Si content (see  $x_{Si}$ -positions=0 nm). However, an  $E_d$  increase from 60 to 110 Jmm<sup>-3</sup> does not further decrease the core Si content. Similar to the Si isosurfaces, the mean size of the 2 at.% Mo isosurfaces also increases and the core

Mo content decreases substantially with higher  $E_d$  (see  $x_{Mo}$ -positions=0 nm) In addition, the Si and Mo segregations are not congruent. While all Mo segregations are enriched in Si, the Si segregations do not contain Mo in a similar manner. Areas where Mo and Si are present (Mo segregations) are considered to be an early stage of the  $\beta$  phase, while the areas solely enriched in Si (Si segregations) may be an early stage of silicide formation.

**Fig. 1(c)** depicts the HEXRD spectra for the samples manufactured with different energy densities. The HEXRD measurements were conducted at the beamline P07 at the synchrotron radiation source PETRA III at Deutsches Elektronen-Synchrotron (DESY, Hamburg, Germany). A Perkin Elmer X-Ray area detector 1621 (detector-specimen distance 1500 mm) and a radiation energy of 73.6 keV were used. Due to the high cooling rates, an orthorhombic  $\alpha''$  martensitic phase occurs when a low  $E_d$  of 35 Jmm<sup>-3</sup> is applied (see additional peaks marked with red arrows in the HEXRD spectrum). The presence of orthorhombic  $\alpha''$  martensite in the Ti6242S alloy manufactured by LPBF was recently proven and outlined in Ref [6]. Higher  $E_d$  of 60 and 110 Jmm<sup>-3</sup> lead to the formation of hexagonal  $\alpha'$  and early stages of  $\beta$  phase.

The following investigations concentrate on specimens manufactured with an intermediate  $E_d$  of 60 Jmm<sup>-3</sup>. **Fig. 2(a)** shows the HEXRD pattern with the respective  $\alpha'/\alpha$  and  $\beta$  peaks of the Ti6242S specimen in the as-built condition and after various subsequent heat treatments, revealing the decomposition of the martensitic microstructure. All heat

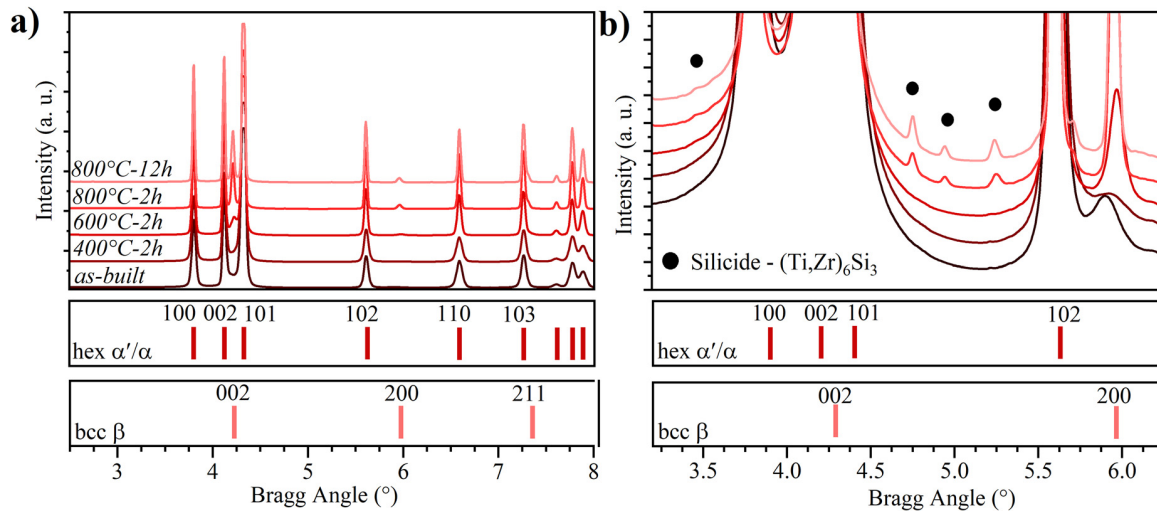


**Fig. 2.** (a) Azimuthally integrated HEXRD pattern of the microstructure in the as-built condition and after various heat treatments showing hexagonal  $\alpha'/\alpha$  and small bcc  $\beta$  peaks; (b) a section of the same HEXRD diffractograms revealing  $(\text{Ti,Zr})_6\text{Si}_3$  (silicide) peaks as well as the evolution of the  $\beta$  phase during various heat treatments.

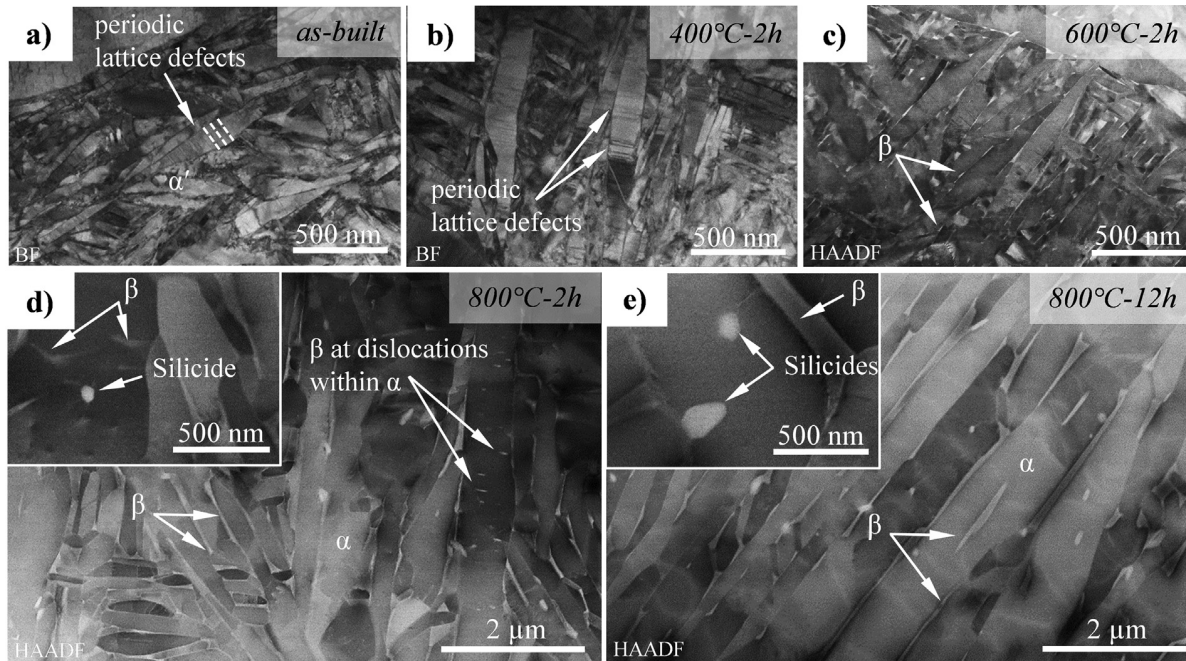


**Fig. 3.** STEM images taken in HAADF mode of the microstructure in (a) as-built condition and after subsequent heat treatments of (b) 2 h at 400 °C, (c) 2 h at 600 °C, (d) 2 h at 800 °C, and (e) 12 h at 800 °C followed by furnace cooling.

treatments were carried out in a cold-wall vacuum furnace (HTM Reetz GmbH, Germany) followed by furnace cooling.

As both the martensitic  $\alpha'$  and the equilibrium  $\alpha$  phase possess a hexagonal lattice structure, they cannot be distinguished and are therefore designated as  $\alpha'/\alpha$  in terms of HEXRD. Besides  $\alpha'/\alpha$ , heat treatments at increasing temperatures lead to higher  $\beta$  phase fractions according to the  $\alpha' \rightarrow \alpha + \beta$  decomposition. Furthermore, the full width at half maximum (FWHM) decreases with higher heat treatment temperature and longer holding time, indicating a reduction of the defect density as well as an increase in grain size [12,13]. The sections of the same HEXRD diffractograms in Fig. 2(b) reveal that already in the as-built condition, a small fraction of  $\beta$  (< 1 vol.%) is present. With increasing heat treatment temperature, the position of the  $\beta$ -200 peak shifts to higher Bragg

angles as the  $\beta$ -lattice parameter  $a_\beta$  decreases, indicating changes in the chemical composition. Additionally, the  $\beta$ -200 peak changes from as-built to 400 °C-2 h, which is typical for  $\alpha + \beta$  alloys and, for example, was experienced with an LPBF manufactured Ti-6Al-4V alloy [8]. The Rietveld analysis, performed with the software MAUD [14], revealed a  $\beta$  phase fraction of 7.5 vol.% for that sample condition, which was closest to thermodynamic equilibrium (800 °C-12 h). The samples heat-treated at 800 °C show slight amounts of an additional phase, identified to be silicides with an S2 type  $(\text{Ti,Zr})_6\text{Si}_3$  crystal structure [15–18].

Fig. 3(a) and (b) display scanning transmission electron microscopic (STEM) images of the microstructure recorded in bright-field (BF) mode and (c) to (e) display high-angle annular dark-field (HAADF) mode images of the as-built condition and after a heat treatment at 400, 600

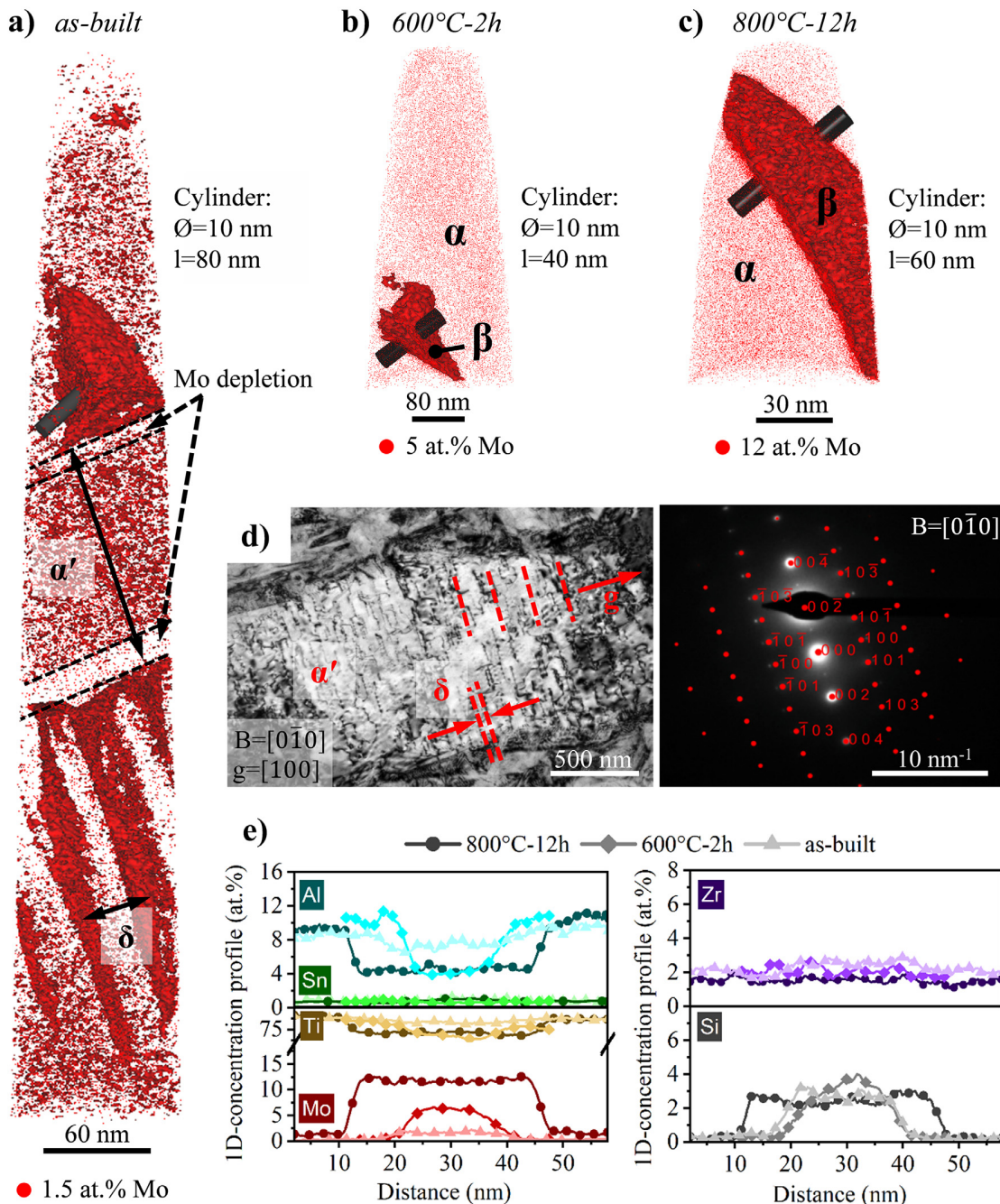


**Fig. 4.** APT tips of the (a) as-built condition with 1.5 at.% Mo isosurfaces, (b) after a heat treatment of 2 h at 600 °C with a 5 at.% Mo isosurface and (c) after heat treatment of 12 h at 800 °C with a 12 at.% Mo isosurface. (d) BF-TEM image of the microstructure in as-built condition and the corresponding diffraction pattern taken in  $[0\bar{1}0]$  zone axis; (e) 1D-concentration profiles along the ROI of the 1.5, 5 and 12 at.% Mo-isosurfaces of the three tips, displaying changes of the Ti, Mo, Al, Sn, Zr and Si concentrations.

and 800 °C followed by furnace cooling. The images were recorded using the previously mentioned Versa 3D DualBeam workstation operating with a STEM detector. In the as-built condition (Fig. 3(a)) and after 2 h at 400 °C (Fig. 3(b)), the microstructure appears acicular and is fine-grained ( $\sim 50\text{--}100\text{ nm}$  grain width). In addition, the  $\alpha'$  grains exhibit contrast variations in the form of lines perpendicular to the major grain axis, which are related to lattice defects as reported in [6,19]. Due to its low phase fraction,  $\beta$  is not visible in the STEM images although it has been confirmed by HEXRD. After 2 h at 600 °C, Fig. 3(c), the grain size is still small and, due to the increased phase fraction, thin  $\beta$  films are

visible along the grain boundaries. Due to the fineness of the structure, STEM does not enable a distinct differentiation between  $\beta$  and possibly present nanometer-sized  $(\text{Ti,Zr})_6\text{Si}_3$  silicides. The heat treatments at 800 °C (Fig. 3(d)) and (e) cause severe coarsening of the microstructure ( $\sim 500\text{--}1000\text{ nm}$  grain width) and the formation of continuous  $\beta$  films along  $\alpha$  boundaries. Furthermore,  $\beta$  precipitates and silicide particles with up to 250 nm in diameter are visible at the dislocations in the  $\alpha$  grains. In HAADF mode, the silicides appear brighter than  $\beta$  and qualitative EDS measurements of these particles confirmed enrichment of Zr and Si as well as a depletion in Mo.

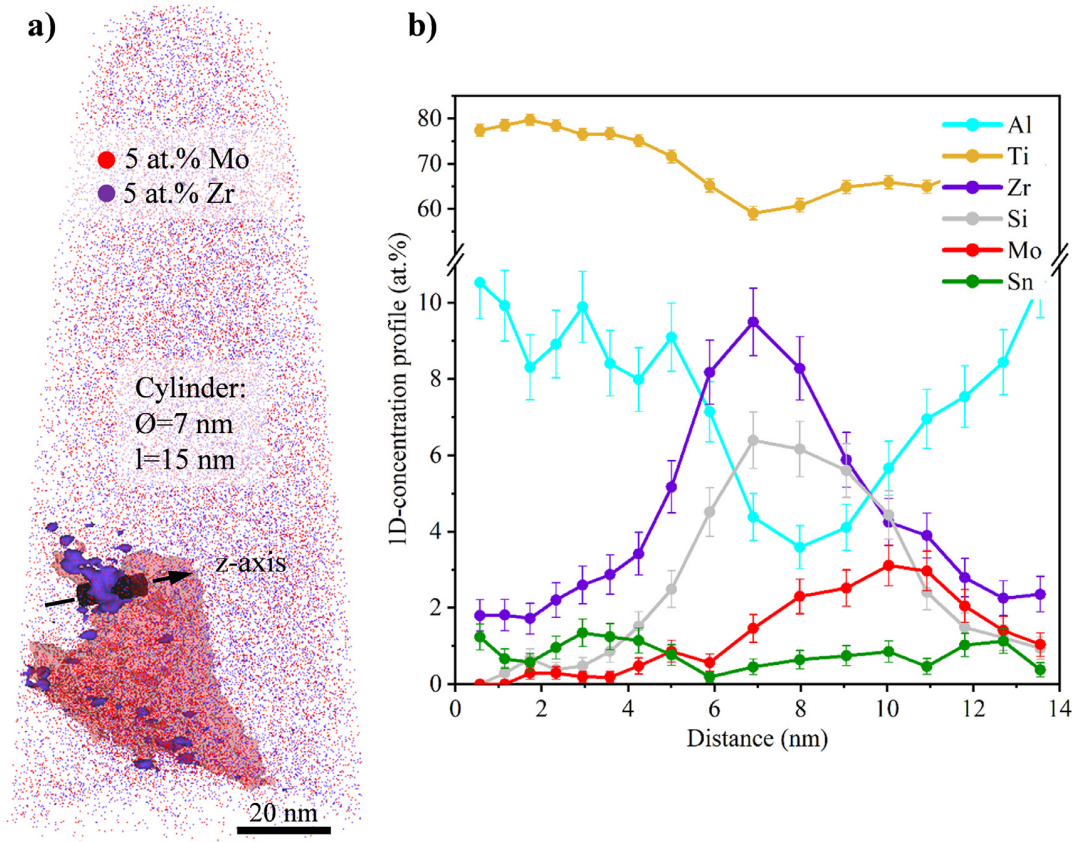


**Fig. 5.** (a) APT tip of the microstructure in 600 °C-2 h condition with 5 at.% Mo and 5 at.% Zr isosurfaces and (b) 1D-concentration profile along the ROI z-axis through a Zr isosurface.

**Fig. 4(a)** to **(c)** show APT tips with 1.5, 5 and 12 at.% Mo isosurfaces of the specimens in the as-built condition and after 600 °C-2 h and 800 °C-12 h heat treatments. The as-built APT tip in **Fig. 4(a)** displays Mo segregations along  $\alpha'$  grain boundaries as well as parallel rod-like Mo segregations within  $\alpha'$  grains. The Mo segregations are surrounded by a Mo depleted zone, respectively. The width of the  $\alpha'$  grains correlates with the grain size of the microstructure shown in **Fig. 3(a)** and the distance  $\delta$  between the rod-like Mo segregations in **Fig. 4(a)** is  $\sim 20$ – $50$  nm, which corresponds to the dimensions of the defect structure depicted in a corresponding bright-field (BF) TEM image in **Fig. 4(d)**. This BF-TEM image was recorded on an FEI Tecnai F20 G2 (Thermo Fisher, MA, USA) with an acceleration voltage of 200 kV. The respective diffraction pattern, with  $B = [0\bar{1}0]$  and  $g = [100]$ , reveals a  $\sim 20$ – $60$  nm distance between the dislocations situated on the prismatic (100) slip planes of the hexagonal lattice [2]. It is tempting to speculate that this dislocation structure acts as a nucleation site for  $\beta$  precipitates, which results in the occurrence of  $\beta$  within  $\alpha$  grains shown in **Fig. 3(d)**. This effect is more pronounced for specimens investigated in a previous work [4], pointing out that air cooling reduces Mo diffusion further and leads to a substantial accumulation of periodic  $\beta$  precipitates within the grain structure. In contrast to commonly used Ti-6Al-4V components, the occurrence of  $\beta$  precipitates within the grain structure leads to the enhanced tensile strength of the Ti6242S alloy reported in a previous study [4].

**Fig. 4(e)** shows the 1D-concentration profiles along regions of interest (ROI) through the Mo enriched regions of the three APT tips. The Mo concentration in Mo enriched zones increases from  $\sim 2$  at.% in the as-built condition to  $\sim 12$  at.% in the heat-treated 800 °C-12 h condition and explains the peak shift as observed in **Fig. 2**. A higher Mo concentration in  $\beta$  leads to a reduction of the lattice parameter caused by a difference in the atomic radii [20,21] and, consequently, an increase

in the Bragg angle. It can be derived from **Fig. 4(e)** that a broadening of the 1D-concentration profile was recognized after the heat treatment and the transition of the Mo enriched zones to the matrix became more defined. This indicates that the Mo enriched zones in the as-built condition are an early state of  $\beta$ , while in the 800 °C-12 h condition, the  $\beta$  phase is in stable equilibrium. The gradual transition of the Mo curve in the 600 °C-2 h condition is related to the ongoing Mo diffusion into  $\beta$  in order to reach the equilibrium composition. The depletion of the  $\alpha$ -stabilizing element Al in  $\beta$  is qualitatively similar to the enrichment of Mo, but the 4.5 at.% Al equilibrium concentration in  $\beta$  is already reached at the 600 °C-2 h condition. The equilibrium concentration of Si (2.5 at.%) is already fulfilled in the as-built sample condition (early stage of  $\beta$ ) due to the higher diffusivity of Si compared to other alloying elements [10,11]. Independent of the sample condition, the Mo enriched zones show no significant enrichment in Zr and Sn and are depleted of Ti.

**Fig. 5(a)** shows the same APT tip of the sample in the 600 °C-2 h condition showing 5 at.% Mo and 5 at.% Zr isosurfaces. The Zr enriched zones are closely arranged to  $\beta$ , indicating the precipitation of silicide particles at  $\alpha/\beta$  boundaries. The 1D-concentration profile along the ROI, provided in **Fig. 5(b)**, reveals a Zr concentration of maximum 10 at.%, an enrichment in Si and a depletion in Al. Furthermore, the Mo content is significantly lower than in  $\beta$ . This assumes that already in the condition 600 °C-2 h, fine  $(\text{Ti,Zr})_6\text{Si}_3$  silicides with a few nm in diameter are present, whereas no silicides were detected during multiple APT measurements of the as-built and 400 °C-2 h condition. Although Si clustering was already detected in the as-built (see **Fig. 1(a)**) and the 400 °C-2 h condition, the diffusivity of Zr was insufficient for the formation of silicides. According to literature, the enrichment of Zr [16], the lattice structure and lattice parameters [15], as well as the presence of

the  $\beta$  stabilizing element Mo [15] confirm the occurrence of a S2 type  $(\text{Ti,Zr})_6\text{Si}_3$  in the investigated alloy.

In conclusion, the chosen  $E_d$  during LPBF significantly affects the Mo diffusion and, in further consequence, the martensite type and morphology, ranging from orthorhombic  $\alpha''$  martensite with Si segregations at  $35 \text{ Jmm}^{-3}$  to hexagonal  $\alpha'$  and early stages of  $\beta$  phase formation at 60 and  $110 \text{ Jmm}^{-3}$ . The application of a low  $E_d$ , i.e., a high cooling rate, is determined as the key parameter for the formation of an orthorhombic crystal structure instead of the typically hexagonal one.

Investigations of specimens manufactured with an intermediate  $E_d$  of  $60 \text{ Jmm}^{-3}$  revealed that the nanometer-sized heterogeneities in the material affect the microstructure evolution during subsequent annealing. The  $\beta$  phase precursors with body-centered cubic structure precipitate along  $\alpha'$  grain boundaries and at dislocations on (100) prismatic slip planes of the  $\alpha'$  grains. Subsequent post-process heat treatment leads to coarsening of these  $\beta$  constituents and shifts the chemical composition of the segregated areas to equilibrium by means of Mo enrichment and Al depletion until stable  $\beta$  precipitates have formed. Silicide precipitates form at  $\alpha/\beta$  phase boundaries and exhibit sizes ranging from a few nm to  $0.25 \mu\text{m}$ . Although Si was found to segregate already during LPBF, it takes an additional heat treatment at temperatures of minimum  $600 \text{ }^\circ\text{C}$  for the formation of  $(\text{Ti,Zr})_6\text{Si}_3$  particles. This is assumed to be linked to the comparably low diffusivity of Zr atoms in the Ti6242S alloy.

#### Declaration of Competing Interest

The authors declare that they have no known competing financial interests or personal relationships that could have influenced the work reported in this paper.

#### Acknowledgments

The authors thank Francisca Mendez-Martin for her advice and help during the APT measurements and Manfred Brabetz for conducting TEM diffraction experiments. We acknowledge DESY (Hamburg, Germany), a member of the Helmholtz Association HGF, for the provision of experimental facilities. Parts of this research were carried out at PETRA III and

we would like to thank Andreas Stark and Peter Staron for their assistance. Beamtime was allocated for proposal I-20210846 EC. M. Musi is a recipient of a DOC Fellowship from the Austrian Academy of Sciences at the Department of Materials Science, Montanuniversität Leoben.

#### Supplementary materials

Supplementary data associated with this article can be found, in the online version, at doi:[10.1016/j.mta.2022.101366](https://doi.org/10.1016/j.mta.2022.101366).

#### References

- [1] C. Leyens, M. Peters, Titanium and Titanium Alloys: Fundamentals and Applications, 1st ed., Wiley-VCH, Weinheim, 2003.
- [2] G. Lütjering, J.C. Williams, Titanium, 1st ed., Springer Science & Business Media, Berlin Heidelberg, 2007.
- [3] H. Fan, S. Yang, Mater. Sci. Eng. A 788 (2020) 139533.
- [4] C. Fleißner-Rieger, T. Pfeifer, T. Jörg, T. Kremmer, M. Brabetz, H. Clemens, S. Mayer, Adv. Eng. Mater. 23 (2021) 2001194.
- [5] S. Liu, Y.C. Shin, Mater. Des. 164 (2019) 107552.
- [6] C. Fleißner-Rieger, M.A. Tunes, C. Gammer, T. Jörg, T. Pfeifer, M. Musi, F. Mendez-Martin, H. Clemens, J. Alloys Compd. 897 (2022) 163155.
- [7] G. Ter Haar, T. Becker, Materials (Basel) 11 (2018) 146.
- [8] J. Haubrich, J. Gussone, P. Barriobero-Vila, P. Kürnsteiner, E.A. Jäggle, D. Raabe, N. Schell, G. Requena, Acta Mater 167 (2019) 136–148.
- [9] M.K. Miller, K.F. Russell, K. Thompson, R. Alvis, D.J. Larson, Microsc. Microanal. 13 (2007) 428–436.
- [10] U. Zwicker, Titan Und Titanlegierungen, 1st ed., Springer, Berlin Heidelberg, 1974.
- [11] H. Nakajima, M. Koiwa, ISIJ Int 31 (1991) 757–766.
- [12] F.R. Kaschel, R.K. Vijayaraghavan, A. Shmeliov, E.K. McCarthy, M. Canavan, P.J. McNally, D.P. Dowling, V. Nicolosi, M. Celikin, Acta Mater 188 (2020) 720–732.
- [13] M.T. Tsai, Y.W. Chen, C.Y. Chao, J.S.C. Jang, C.C. Tsai, Y.L. Su, C.N. Kuo, J. Alloys Compd. 816 (2020) 152615.
- [14] L. Lutterotti, Acta Crystallogr. Sect. A Found. Crystallogr. 56 (2000) 54–54.
- [15] A.K. Singh, C. Ramachandra, J. Mater. Sci. 32 (1997) 229–234.
- [16] A. Popov, N. Rossina, M. Popova, Mater. Sci. Eng. A 564 (2013) 284–287.
- [17] H. Ba, L. Dong, Z. Zhang, X. Lei, Metals (Basel) 7 (2017) 286.
- [18] M. Antti, V.C. Ciprés, J. Mouzon, P. Åkerfeldt, R. Pederson, 14th World Conf, Titan (2020) 1–7.
- [19] S. Joseph, T.C. Lindley, D. Dye, Int. J. Plast. 110 (2018) 38–56.
- [20] I. Shirovani, I. Kaneko, M. Takaya, C. Sekine, T. Yagi, Phys. B Condens. Matter 281 (2000) 1024–1025.
- [21] S.X. Liang, M.Z. Ma, R. Jing, Y.K. Zhou, Q. Jing, R.P. Liu, Mater. Sci. Eng. A 539 (2012) 42–47.



## Article E

---

# Optimization of the post-process heat treatment strategy for a near- $\alpha$ titanium base alloy produced by laser powder bed fusion

Christian Fleißner-Rieger <sup>1,\*</sup>, Tanja Pfeifer <sup>2</sup>, Christoph Turk <sup>2</sup>, and Helmut Clemens <sup>1</sup>

<sup>1</sup> Department Werkstoffwissenschaft, Montanuniversität Leoben, Franz-Josef Straße 18, 8700 Leoben, Österreich

<sup>2</sup> Pankl Racing Systems AG, Additive Manufacturing Technologies, Industriestraße Ost 4, 8605 Kapfenberg, Austria

<sup>3</sup> voestalpine BÖHLER Edelstahl GmbH & Co KG, Mariazeller Straße 25, Kapfenberg 8605, Austria

\* Corresponding author

Materials, **15**(3), 1032 (2022)

<https://doi.org/10.1016/j.jallcom.2021.163155>

open access: CC BY 4.0





## Article

# Optimization of the Post-Process Heat Treatment Strategy for a Near- $\alpha$ Titanium Base Alloy Produced by Laser Powder Bed Fusion

Christian Fleißner-Rieger <sup>1,\*</sup> , Tanja Pfeifer <sup>2</sup>, Christoph Turk <sup>3</sup> and Helmut Clemens <sup>1</sup>

<sup>1</sup> Department of Materials Science, Montanuniversität Leoben, Franz-Josef Straße 18, 8700 Leoben, Austria; helmut.clemens@unileoben.ac.at

<sup>2</sup> Pankl Racing Systems AG, Additive Manufacturing Technologies, Industriestraße Ost 4, 8605 Kapfenberg, Austria; tanja.pfeifer@pankl.com

<sup>3</sup> Voestalpine BÖHLER Edelstahl GmbH & Co. KG, Mariazeller Straße 25, 8605 Kapfenberg, Austria; christoph.turk@bohler-edelstahl.at

\* Correspondence: christian.fleissner-rieger@alumni.unileoben.ac.at

**Abstract:** During the last decades, titanium alloys have been of great interest for lightweight applications due to their high strength in combination with a low material density. Current research activities focus on the investigation of near- $\alpha$  titanium alloys produced by laser powder bed fusion (LPBF). These alloys are known for their superior tensile strength and high creep resistance. This study focuses on the optimization of post-process heat treatments and the impact on tensile and creep strength of a LPBF produced Ti6242S alloy. Therefore, a variety of annealing steps were conducted to gain knowledge about the decomposition process of the non-equilibrium as-built microstructure and the arising influence on the mechanical properties. Components made of Ti6242S and produced by LPBF reveal an extraordinarily high ultimate tensile strength of about 1530 MPa at room temperature, but show a low elongation at fracture ( $A_5 = 4.3\%$ ). Based on microstructure-property relationships, this study recommends precise heat treatments on how to improve the desired mechanical properties in terms of strength, ductility as well as creep resistance. Moreover, this study shows a triplex heat treatment, which enhances the elongation at fracture ( $A_5$ ) to 16.5%, while the ultimate tensile strength is still at 1100 MPa.

**Keywords:** titanium alloys; additive manufacturing; characterization; electron microscopy; hardness; X-ray analysis; phase transformation



**Citation:** Fleißner-Rieger, C.; Pfeifer, T.; Turk, C.; Clemens, H. Optimization of the Post-Process Heat Treatment Strategy for a Near- $\alpha$  Titanium Base Alloy Produced by Laser Powder Bed Fusion. *Materials* **2022**, *15*, 1032. <https://doi.org/10.3390/ma15031032>

Academic Editor: Ludmila Kučerová

Received: 21 December 2021

Accepted: 26 January 2022

Published: 28 January 2022

**Publisher's Note:** MDPI stays neutral with regard to jurisdictional claims in published maps and institutional affiliations.



**Copyright:** © 2022 by the authors. Licensee MDPI, Basel, Switzerland. This article is an open access article distributed under the terms and conditions of the Creative Commons Attribution (CC BY) license (<https://creativecommons.org/licenses/by/4.0/>).

## 1. Introduction

Titanium base alloys are frequently used in the aerospace, automotive and medical sectors due to their beneficial strength-to-weight ratio, excellent corrosion resistance, biocompatibility, and high fatigue strength [1–4]. In particular, the group of the  $\alpha + \beta$  alloys is of great interest because of their well-balanced properties and the already available know-how in terms of producibility [5–7]. Recent research activities have focused on the investigation of near- $\alpha$  titanium base alloys, which reveal similarities to the popular  $\alpha + \beta$  alloys such as Ti-6Al-4V (m.%, Ti64), yet containing a lower fraction of  $\beta$  stabilizing elements [7–10]. Especially the near- $\alpha$  Ti-6Al-2Sn-4Zr-2Mo-Si (in m.%, Ti6242S) alloy produced by LPBF has gained attention due to several advantages such as higher tensile strength and superior creep resistance in comparison to the Ti64 alloy [11]. Additive manufacturing, e.g., LPBF, is regarded as a promising technology when compared to conventional manufacturing techniques, which is caused by less material waste via the direct production of highly complex geometries [12]. For example, titanium alloys are a popular choice for LPBF in industrial applications for producing biomedical implants [13], lightweight aerospace parts [14], as well as complex parts of the exhaust system in the automobile sector [11].

Choosing LPBF as a manufacturing technique can significantly improve the mechanical properties of components. Conventionally manufactured Ti6242S samples (casting and annealed) reveal an ultimate tensile strength (UTS) of 1000 MPa and an elongation at fracture of 10% [15]. The LPBF manufacturing process of Ti6242S components causes high cooling rates, leading to a martensitic microstructure and, in further consequence, to a significantly higher UTS of 1380 MPa and comparably low elongation at fracture of 5.3% [8]. The high cooling rates of this manufacturing process evoke a non-equilibrium material condition and promote a high density of lattice defects and residual stresses, which may lead to the formation of cracks and delamination during the LPBF process [16,17]. The microstructure of the Ti6242S components consists of long columnar parent  $\beta$ -grains ( $\sim 83 \mu\text{m}$  width), several hundred  $\mu\text{m}$  length which contain fine acicular  $\alpha'$  martensite ( $\sim 1 \mu\text{m}$  minor axis length and  $\sim 8 \mu\text{m}$  major axis length) as recorded in [11].

The martensitic microstructure is far from thermodynamic equilibrium and, therefore, unfavorable for industrial application as it causes low ductility and fracture toughness. Therefore, post-process heat treatments are well established for LPBF-produced titanium alloys [8,18]. These treatments focus on the reduction in residual stresses and enhancement of ductility. Simultaneously, the heat-treated specimens' tensile strength drops due to the change of a fully martensitic  $\alpha'$  microstructure into an  $\alpha + \beta$  microstructure which is closer to the thermodynamic equilibrium [19,20].

Fundamental investigations [21] on an LPBF-manufactured titanium base alloy show that the decomposition of the fully martensitic microstructure already begins at 400 °C. Annealing at this relatively low temperature increases the hardness in comparison to the initial sample condition. It is assumed that the presence of the intermetallic  $\alpha_2$ -Ti<sub>3</sub>Al phase and nanometer-sized  $\beta$  precipitates causes this hardness increase [16,22]. In contrast, heating to temperatures above 650 °C results in a higher  $\beta$  phase fraction as well as coarsened grains, leading to a hardness decrease [22]. After initial annealing, a final aging (stabilization) step is performed for elemental redistribution in the supersaturated phases, shifting the microstructure towards the thermodynamic equilibrium. For most Ti alloys, aging is typically performed in a temperature range of 500–600 °C, leading to a decomposition of unstable phases and a microstructure with enhanced hardness [23]. Furthermore, aging also promotes the formation of  $\alpha_2$  precipitates, which are known to further strengthen the material by means of stabilizing the dislocation structure by dislocation pinning [23,24].

Recent investigations on an-LPBF manufactured Ti6242S alloy have shown that the heat treatment response led to the precipitation of  $\beta$  particles at  $\alpha$ -grain boundaries and within  $\alpha$  grains. This behavior was ascribed to the low diffusivity of the  $\beta$ -stabilizing element Mo in this alloy [11]. The Ti6242S alloy is also known for its high creep resistance caused by its low self-diffusion coefficient [5,7]. Moreover, the alloying element Si promotes the formation of stable (Ti,Zr)<sub>6</sub>Si<sub>3</sub> silicide particles, which further decrease the dislocation movement [25].

This work aims to optimize the post-process heat treatment strategy of LPBF-manufactured Ti6242S samples with regard to balanced mechanical properties. Depending on the operating conditions, single or multi-step heat treatments are preferable. If the material is used at the upper-temperature limit (long term) at about 550 °C, then enhanced creep strength is required. In contrast, well-balanced ductility and strength are essential for room temperature (RT) application. Since the Ti6242S alloy was manufactured by LPBF for the first time only recently [8], appropriate annealing strategies have not yet been investigated in detail. Besides the impact of the heat treatment on the mechanical properties, additional focus is placed on the microstructural changes during the different steps of the post-process heat treatments. Particularly, the microstructure-property relationships concerning the tensile and creep strength will allow for identifying the proper heat-treatment strategy depending on the required mechanical properties. This may pave the way for a successful and more widespread use of the Ti6242S alloy produced by LPBF.

## 2. Materials and Methods

Microstructure analysis and mechanical testing were conducted on cylindrical specimens with a diameter of 15 mm and 85 mm length produced at Pankl Racing Systems AG, Additive Manufacturing Technologies, Kapfenberg, Austria on an M400 LPBF facility from EOS, Munich, Germany utilizing Ar shielding gas. The chosen volumetric energy density of the LPBF process was about  $60 \text{ J mm}^{-3}$  to ensure a high material density with a reduced pore content. The chemical analysis of the Ti6242S powder used for the manufacturing process was: 6.4 Al, 1.9 Sn, 3.9 Zr, 2.0 Mo, 0.09 Si, and 0.01 O (m.%). The chemical analysis of Al, Sn, Zr, Mo, Si was done via inductively coupled plasma atomic emission spectroscopy (ICP-AES), and the O concentration was determined via carrier gas hot extraction. Investigations on samples directly after the LPBF manufacturing process, i.e., on “as-built” samples, were conducted to analyze the reference condition and shed light on the starting microstructure. Dwell times, heat treatment temperatures and cooling conditions (air cooling, AC, furnace cooling, FC) were varied in order to learn about the microstructural evolution during the post-process treatments. Figure 1 displays the investigated one-step ( $\beta$ -annealing), two-step (duplex annealing) and three-step (triplex annealing) heat treatments investigated within this study. Based on thermodynamic calculations as reported in reference [11], a schematic diagram of the rising  $\beta$  phase fraction at higher temperatures is shown on the right of Figure 1.

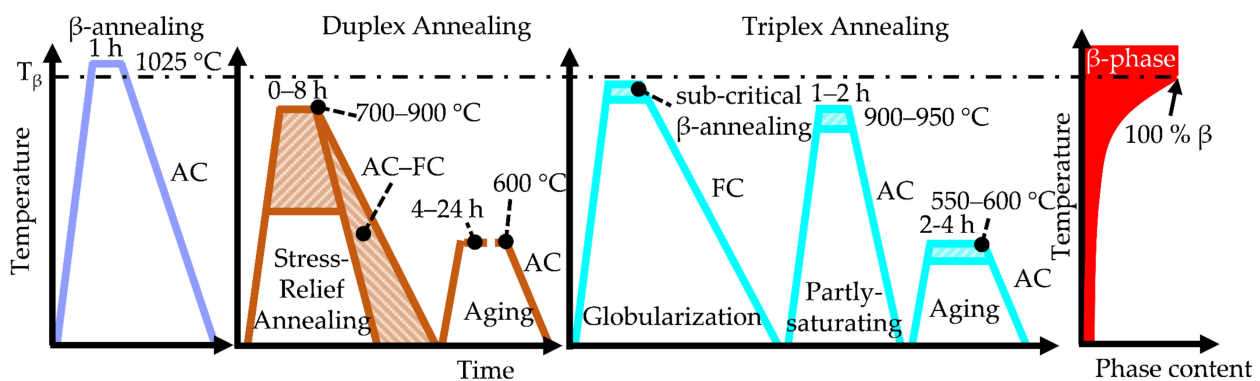


**Figure 1.** Schematic visualization of the investigated one-step, two-step and three-step post-process heat treatments conducted on as-built Ti6242S samples. The variation of temperatures, holding times and cooling conditions in terms of AC and FC was carried out to gain knowledge about the decomposition of the disequilibrium microstructure and to establish the optimum heat treatment parameters for the subsequent application. Additionally, schematically the course of the  $\beta$  phase fraction as function of temperature in thermodynamic equilibrium [11] is provided on the right side.

The  $\beta$  phase fraction is of great importance due to the differences in solubility of chemical elements in the  $\alpha$  and  $\beta$  phases [5]. Moderate annealing temperatures between  $700 \text{ }^\circ\text{C}$  and  $900 \text{ }^\circ\text{C}$ , which are significantly below the  $\beta$ -transus temperature ( $T_\beta$  for this alloy is  $1017 \text{ }^\circ\text{C}$ , [11]), are commonly used in the industry to reduce residual stresses and enhance ductility [11]. For this purpose, this investigation focuses on the differences in mechanical properties caused by the varying temperatures and holding times during the duplex annealing treatment. A  $\beta$ -annealing treatment was executed to investigate the high temperature properties. Furthermore, a novel three-step triplex annealing treatment was designed to test the fracture at elongation limits of this alloy. All heat treatments were conducted in temperature-calibrated Nabertherm N 11/HR box furnaces. The sample preparation of the metallographic specimens was performed using standard preparation techniques for titanium alloys according to reference [26]. X-ray diffraction (XRD) investigations with a D8 Advance diffractometer from Bruker, Billerica, USA in coupled  $2\theta$  mode using a  $\text{Cu-K}\alpha$  X-ray source with a wavelength of  $0.154 \text{ nm}$  were carried out to identify the occurring phases and the according volume fractions. Rietveld analysis [27] with the software TOPAS from Bruker was performed to analyze the phase fractions and lattice parameters of the phases

present. Light optical microscopy (LOM) with an AxioImager.M2 LOM from Zeiss, Jena, Germany was performed to determine the pore content of the as-built samples according to reference [26]. Fractography was conducted on a stereo-microscope, type DiscoveryV20 from Zeiss. Scanning electron microscopy (SEM) was done on a field-emission device Versa 3D Dual Beam from Thermo Fisher, Waltham, USA. This SEM was also used to investigate the specimens' phase morphology and grain size via electron backscatter diffraction (EBSD) analysis using a Hikari XP EBSD camera from EDAX, Mahwah, USA. The determination of the elemental composition of the individual phases was performed via energy-dispersive X-ray spectroscopy (EDS) on an Oxford Instruments Xmax 80 mm<sup>2</sup> EDS detector, which was mounted on a Clara SEM from Tescan, Brno, Czech Republic. Transmission electron microscopy (TEM) investigations were carried out on an FEI Tecnai F20 G2 TEM from Thermo Fisher by using an acceleration voltage of 200 kV. Micro-hardness measurements were performed to examine the influence of the various heat treatment parameters on the specimens' hardness. Therefore, a Qness Q 60 A+ measuring device from ATM Qness, Mammelzen, Germany equipped with a Vickers indenter tip was employed to perform 30 single HV0.1 indents per sample arranged on a measurement grid. Quasi-static tensile tests were conducted on heat-treated and machined tensile samples with gauge diameter of Ø 6 mm and a gauge length of 30 mm. The tensile specimens were mounted with a metric M10 screw head in accordance with DIN EN 2002 and deformed with a strain rate of  $0.8 \cdot 10^{-4} \text{ s}^{-1}$  on tensile test equipment provided by Messphysik. The listed elongation at fracture values A<sub>5</sub> within this study were determined according to DIN EN 2002. All temperatures and sample conditions were tested at least two times. Uniaxial creep testing was carried at a temperature of 550 °C under an applied load of 210 MPa, using TC30 and TC50 creep testing equipment of AET Technologies, Troy, MI, USA. The cylindrical samples used for creep testing had an inner sample diameter of Ø 6 mm and a gauge length of 30 mm. During the experiment, two extensometer bars were attached to the specimens for creep strain determination. The temperature was monitored and controlled via three thermocouples along the specimens' longitudinal axis.

### 3. Results

#### 3.1. As-Built Microstructure

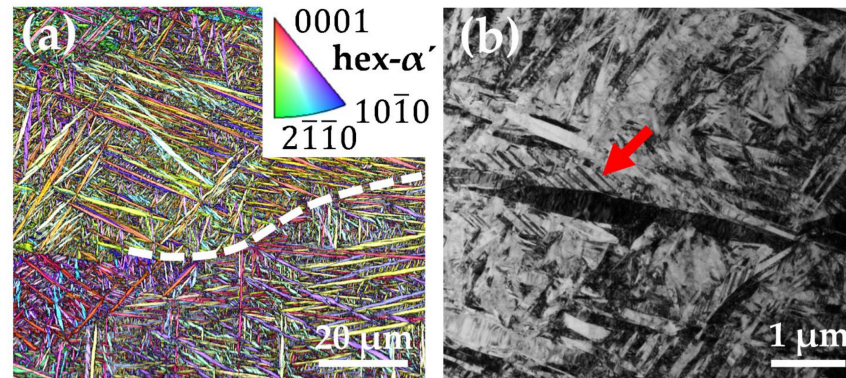
The results of the electron microscopic investigations of an as-built sample are shown in Figure 2. Figure 2a displays the EBSD image quality (IQ) and inverse pole figure (IPF) map. The image reveals the acicular morphology of the as-built microstructure. As the material fulfills a  $\beta \rightarrow \alpha'$  phase transformation after solidification of the melt pool, grain boundaries of the parent  $\beta$  grains are still visible and marked with a dashed line. According to reference [11], the crystal orientation of the  $\alpha'$  grains, located within the  $\beta$  grains, is linked to the Burgers orientation relationship. The pore analysis of the as-built samples reveals a very high density of the LPBF manufactured samples with a pore fraction of <0.05 vol.%.

Figure 2b shows a bright-field TEM (TEM-BF) image of the microstructure, which reveals a very fine  $\alpha'$  microstructure and a high density of defects like mechanical twins (red arrow).

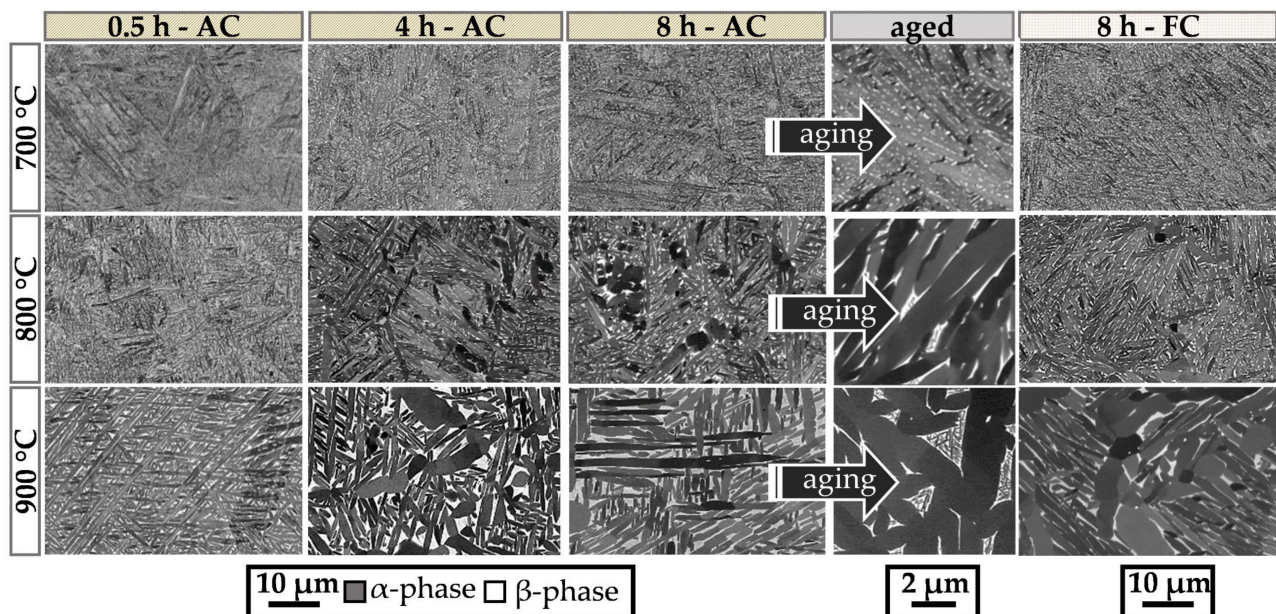
#### 3.2. Transformation during Duplex Annealing

Figure 3 shows SEM images of the microstructure recorded with a backscatter electron (BSE) detector to display the impact of different heat treatment temperatures and times on the evolution of the microstructure during the duplex annealing heat treatment. The images show the microstructure of the stress-relief annealed (SRA) samples at 700 °C, 800 °C and 900 °C from top to bottom and for dwell interval times of 0.5–8 h from left to right. Different cooling conditions in terms of AC and FC as well as a final aged microstructure are also added for comparison. As shown, the acicular morphology of the initial as-built sample condition remains for low annealing temperatures and short dwell times. Due to the decomposition of the supersaturated  $\alpha'$  martensite ( $\alpha' \rightarrow \alpha + \beta$ ) closer to thermodynamic equilibrium,  $\beta$  precipitates have formed in all heat-treated specimens. The appearance

of the  $\beta$  phase is bright in BSE contrast due to the enrichment with heavier elements like Mo [11]. An increase in the temperature to 900 °C and longer dwell times result in significant growth of  $\alpha$  and  $\beta$  grains as well as a globularization of the whole microstructure.



**Figure 2.** (a) EBSD IPF map with an IQ overlay shows the acicular morphology of the hexagonal martensitic microstructure after LPBF. A former parent  $\beta$  grain boundary is marked with a dashed line; (b) the TEM-BF image displays a high density of defects like mechanical twins (red arrow) in the nanometer-sized  $\alpha'$  microstructure of the as-built sample.



**Figure 3.** SEM images taken in BSE mode of the microstructure of LPBF-produced Ti6242S samples at different stages of the duplex annealing. Higher temperatures and longer dwell times lead to a significant increase in grain size. The additional aging treatment at 600 °C for 4 h results in a bi-lamellar morphology (see text).

In particular, the FC sample, which was annealed at 900 °C, reveals a much coarser microstructure originating from the low cooling rate. The  $\beta$  phase fraction in the FC samples is lower than in the AC condition, caused by the equilibrium condition of the material.

The effect of final aging (600 °C for 4 h) is visible when comparing the  $\beta$  phase before and after the aging treatment for the 8 h-AC sample in Figure 3. The aging step causes precipitation of fine  $\alpha$  phase within former  $\beta$  areas. This so-called bi-lamellar microstructure originates as the supersaturated  $\beta$  phase shifts to thermodynamic equilibrium. The aging effect is evident, especially for high temperatures where large  $\beta$  phase areas exist. For lower annealing temperatures, e.g., 700 °C, the microstructure consists of sub- $\mu$ m-sized  $\beta$  precipitates surrounded by  $\alpha$  constituents.

EBSD investigations were performed to analyze the influence of the dwell time on the microstructure during the 900 °C annealing treatments (Figure 4). The upper areas in the EBSD maps in Figure 4a show the IPF + IQ information of the hex  $\alpha$  phase, whereas the lower areas depict phase maps with an IQ overlay. The  $\alpha$  phase is colorized in grey, whereas the  $\beta$  constituents are highlighted in red. The acicular appearance of the fine grains coarsens with increasing dwell times and larger  $\alpha$  grains begin to split (white arrows). Furthermore, small  $\beta$  phase precipitates, as seen in the 1 h sample, accumulate and generate larger  $\beta$  grains in the 8 h treated samples. The EBSD grain size analysis in Figure 4b shows that an extension of the dwell time from 0.5 h to 8 h causes an increase in grain size. The average grain diameter  $d_{50}$  almost triples from 2  $\mu\text{m}$  (as-built) to 5.9  $\mu\text{m}$  (8 h-AC) due to the dissolution of smaller grains and the growth of the larger ones during the holding sequence. The evaluation of lattice parameters and phase fractions of the hexagonal (hex)  $\alpha$  and body-centered cubic (bcc)  $\beta$  phase was done via XRD measurements and is depicted in Figure 5 for the samples heat-treated at 900 °C. The results of the AC samples reveal an increase in the  $\beta$  phase fraction already after a dwell time of 0.5 h and an almost steady volume fraction of about 10 vol.% after 1 h. The evaluation of the lattice parameters shows that the hex  $\alpha$  lattice parameter ( $a_\alpha$  and  $c_\alpha$ ) and the bcc  $\beta$  lattice parameter ( $a_\beta$ ) remain unaltered after the SRA-AC treatments. Final aging at 600 °C for 2 h was conducted on 1 h and 8 h SRAAC samples, which showed a decrease in the  $\beta$  phase fraction after the aging treatment as well as for lower cooling rates (FC), when compared to the AC treatment. A lower  $\beta$  phase fraction is also visible in the microstructure images of the samples heat-treated at 900 °C as shown in Figure 3.

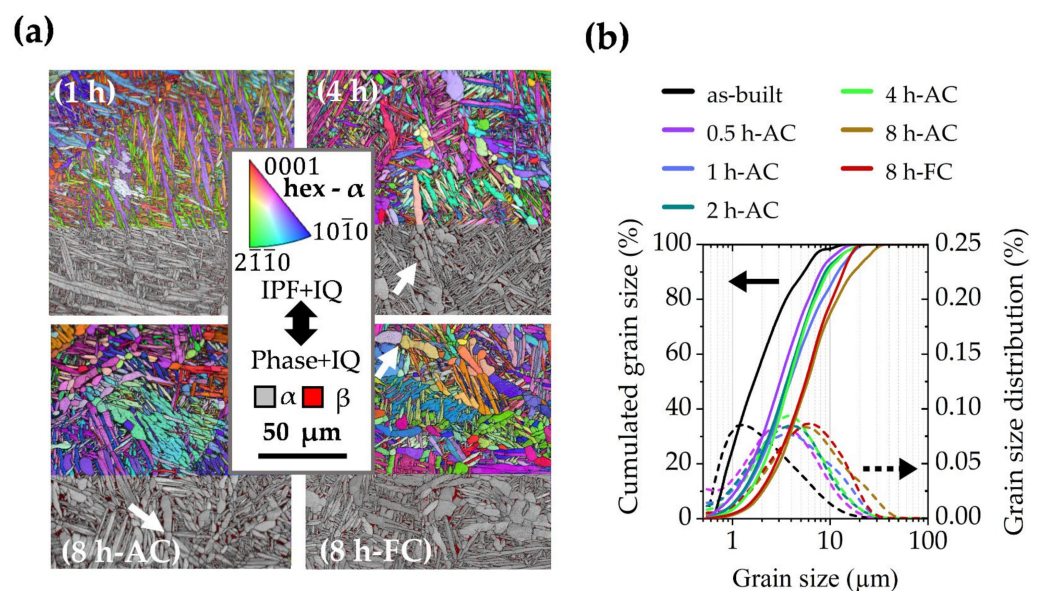


**Figure 4.** EBSD maps depicted as IPF + IQ maps on the upper side and as phase + IQ maps on the lower side of (a) showing the microstructure of the 900 °C heat-treated Ti6242S samples for different dwell times and cooling conditions. The EBSD grain size analysis in (b) reveals that the increasing grain size is linked to the prolonged dwell-time.

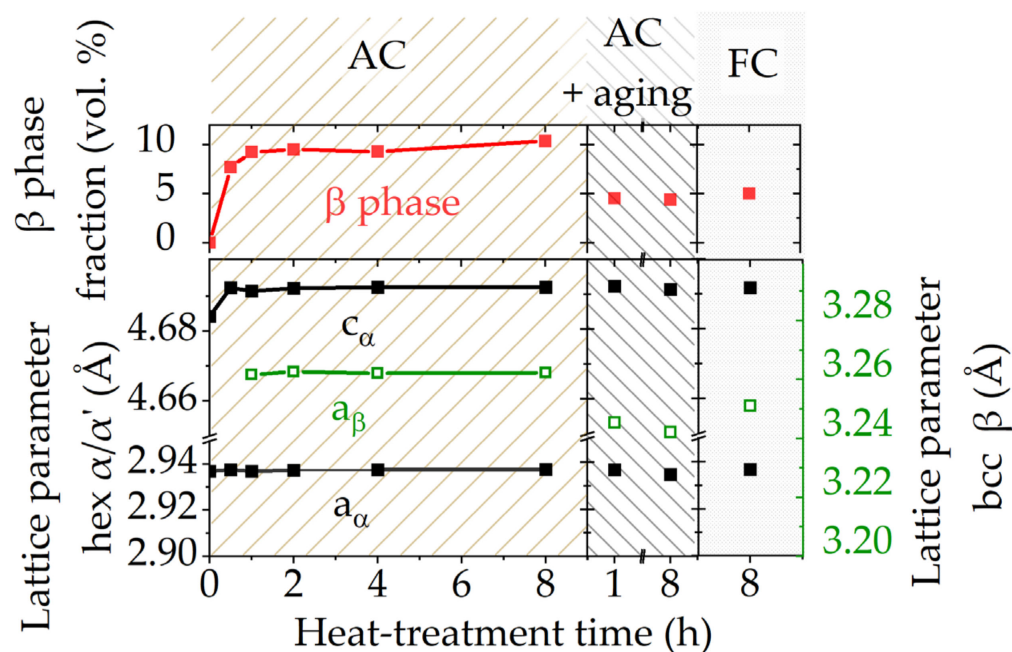


**Figure 5.** XRD results of the sample heat-treated at 900 °C showing the  $\beta$  phase volume fraction and lattice parameter of the  $\alpha$  and  $\beta$  phase for different SRA dwell times and cooling conditions. The final aging step (600 °C for 24 h) was carried out on 900 °C-1 h-AC and 900 °C-8 h-AC samples.

Moreover, from Figure 5 it is evident that only the lattice parameter of the bcc  $\beta$  phase decreases during aging or FC. The change in the  $\beta$  lattice parameter results from differences in chemical composition. As shown in Figure 6, EDS measurements reveal nearly constant Al, Sn and Zr concentrations in the  $\alpha$  phase, whereas the elements Mo and Fe completely diffuse into the  $\beta$  phase during the heat treatments. Obviously, the cooling rate severely influences the chemical composition of the  $\beta$  phase. While the FC sample is shifted closer to the thermodynamic equilibrium due to the lower cooling rate, the  $\beta$  phase is supersaturated in Al and depleted in Mo and Fe after the AC treatment. This is accompanied by a lower  $\beta$  phase fraction obtained in the specimens closer to equilibrium. The XRD diffractograms also suggest that no intermetallic  $\alpha_2$ -Ti<sub>3</sub>Al phase occurs in any of the investigated samples.

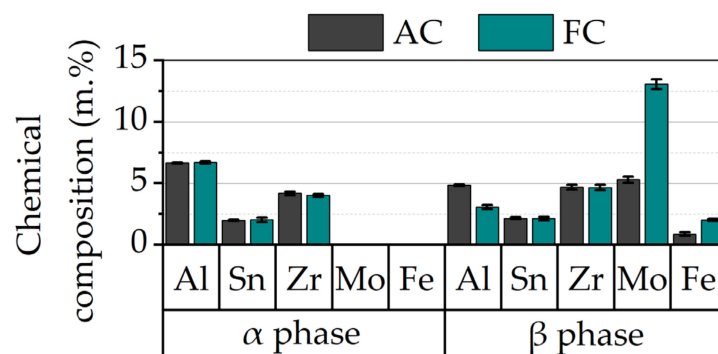


**Figure 6.** EDS measurements reveal the element partitioning between the  $\alpha$  and  $\beta$  phase depending on the applied cooling rate.

### 3.3. $\beta$ -Annealing and Triplex Annealing

As a lamellar microstructure results in improved creep resistance of Ti base alloys [5], a  $\beta$ -annealing treatment above the  $\beta$  transus temperature was utilized to diminish the as-built morphology and generate a more coarse-grained and lamellar microstructure. The impact of this treatment on the microstructure is shown in Figure 7a. The microstructure



consists of large primary  $\alpha$  colonies ( $\alpha_{col}$ ), grain boundary  $\alpha$  ( $\alpha_{GB}$ ) and a slight amount of basketweave substructures (encircled yellow) within a single parent  $\beta$  grain.

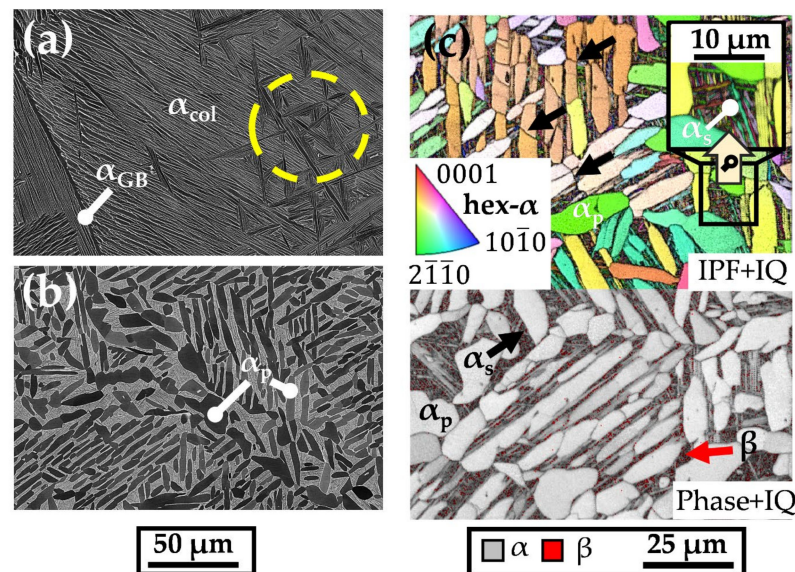


**Figure 7.** (a) SEM-BSE image shows the microstructure after  $\beta$ -annealing of an as-built Ti6242S sample. (b,c) demonstrate the effect of the triplex annealing heat treatment on the microstructure displayed in an SEM-BSE image and an EBSD map, respectively.

Triplex annealing was performed to enhance the ductility of the as-built condition. An SEM-BSE image of the microstructure after the triplex annealing is depicted in Figure 7b. It consists of darkly contrasted, partially globularized primary  $\alpha$  ( $\alpha_p$ ) grains and coarse  $\alpha_p$  lamellas which formed during the first stage of the three-step heat treatment, i.e., sub-critical annealing slightly below  $\beta$ -transus. In the second stage, the saturation annealing leads to approximately 30 vol.% of supersaturated  $\beta$  phase caused by the rapid cooling process. The black arrows indicate the splitting of  $\alpha_p$  grains, which originated during the first two annealing steps, better visible in the EBSD map shown in Figure 7c. In the third step of the triplex annealing, aging promotes secondary  $\alpha$  ( $\alpha_s$ ) and fine  $\beta$  precipitation. Here, the IPF + IQ map on the upper side shows these small  $\alpha_s$  constituents in between the  $\alpha_p$  grains. In the enlarged box, the grain size analysis reveals an  $\alpha$  grain size of about 1.0  $\mu\text{m}$  when compared to the overall grain size of the triplex annealed sample of about 13.6  $\mu\text{m}$ . Regarding the crystallographic orientation,  $\alpha_p$  and  $\alpha_s$  are both linked to the parent  $\beta$  phase via the Burgers orientation relationship [11]. Moreover, the EBSD Phase + IQ map on the lower side of Figure 7c presents the  $\beta$  phase (red arrow) occurring in the vicinity of  $\alpha_s$  grain boundaries.

#### 3.4. Impact of the Heat Treatments on the Mechanical Properties

The results of the micro-hardness tests of the duplex-annealed Ti6242S samples are displayed in Figure 8. The hardness of all AC samples decreases as both heat treatment temperature and time increase. The high hardness value of the as-built condition (486 HV0.1) significantly drops in the early stages of the heat treatment, which is more pronounced for the samples annealed at temperatures of 800  $^{\circ}\text{C}$  and 900  $^{\circ}\text{C}$  when compared to the 700  $^{\circ}\text{C}$  samples. In addition, the steady-state hardness is reached after a dwell time of 2 h for the investigated SRA temperatures in the range of 700–900  $^{\circ}\text{C}$ . The effect of the final aging treatment (600  $^{\circ}\text{C}$ ) during the last step of the duplex annealing is visible in the hardness depicted on the right of Figure 8. Aging was done on 1 h-AC (short SRA dwell time) and 8 h-AC (long SRA dwell time) samples and reveals an increase in micro-hardness, which is more pronounced for shorter SRA dwell times. It can be assumed that longer SRA dwell times lead to a more stable phase composition and, therefore, less pronounced

hardening during aging. Higher aging times (4 h → 8 h → 24 h) are also more effective for shorter SRA dwell times, whereas longer dwell times are not as favorable with regard to the obtained micro-hardness. Lower cooling rates, such as FC, result in an increase in hardness, especially for lower SRA temperatures. During the FC process, the microstructure shifts towards thermodynamic equilibrium when compared to AC, and the  $\beta$  phase fraction, which is lower after FC, is enriched with  $\beta$  stabilizing elements. Furthermore, the increased  $\alpha$  phase fraction also contributes to a higher micro-hardness after the FC process as, in general, the  $\alpha$  phase possesses higher strength than the  $\beta$  phase [28,29]. FC might also have a similar effect on the microstructure, especially at lower SRA temperatures, as seen for the aging treatment which leads to sub- $\mu\text{m}$  sized  $\beta$  precipitates.

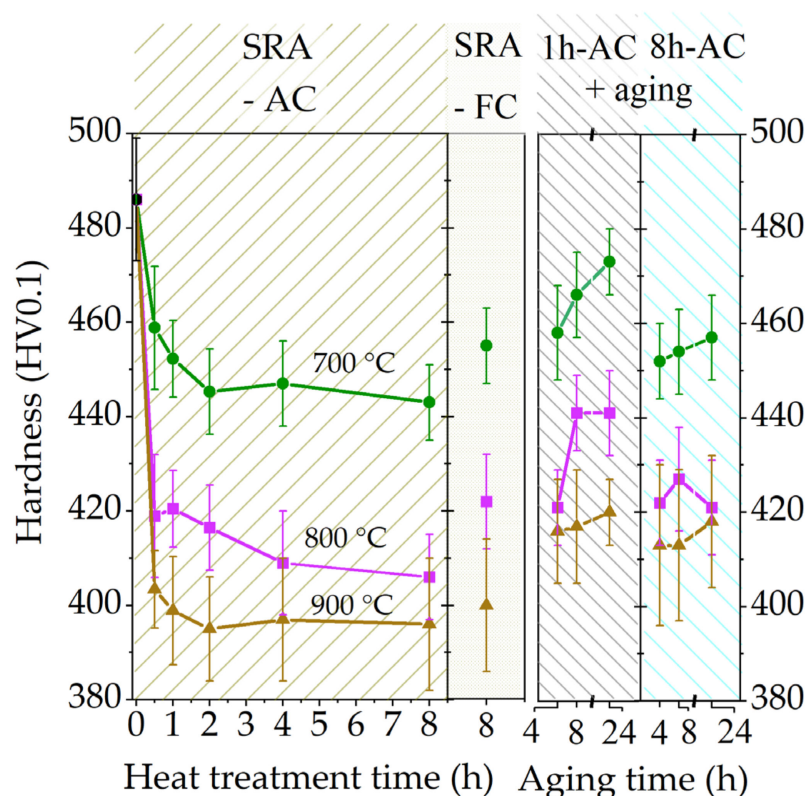


**Figure 8.** Micro-hardness tests performed on heat-treated Ti6242S specimens show a decreasing hardness with increasing heat treatment temperatures and times (left). Low cooling rates, such as FC and final aging at 600 °C, promote the hardness (right).

Tensile testing was conducted to validate the performance of samples with selected heat treatments, having a special focus on the elongation at fracture. The results of the tensile tests are compiled in Figure 9a and Table 1. They confirm that the UTS is highest for the as-built sample condition of around 1525 MPa. During the low-temperature duplex annealing (“duplex low” = 700 °C + aging), the strength and, interestingly, the strain to rupture decreases when compared to the as-built samples. Fractography analysis on the duplex low samples reveals crack initiation sites at LPBF typical defects, such as pores. As shown in the microstructure images, these duplex-annealed samples consist of a very fine  $\alpha + \beta$  microstructure with sub- $\mu\text{m}$ -sized  $\beta$  precipitates and, thus, are severely influenced by the possible movement and pile-ups of dislocations [8]. Therefore, stress concentrations at defects lead to cracks and cause early fracture events compared to the “duplex high” samples (=900 °C + aging). These samples show an elongation at break ( $A_5$ ) of about 16.0%, although the UTS is still at 1155 MPa. The  $\alpha + \beta$  microstructure within these samples can store continuously formed dislocations and offers sufficient space for dislocation movement in large  $\alpha_p$  grains leading to enhanced ductility. The triplex heat treatment leads to a slight

improvement of the ductility to  $16.5 \pm 0.3\%$  ( $A_5$ ), caused by a microstructure almost composed of large  $\alpha_p$  grains.

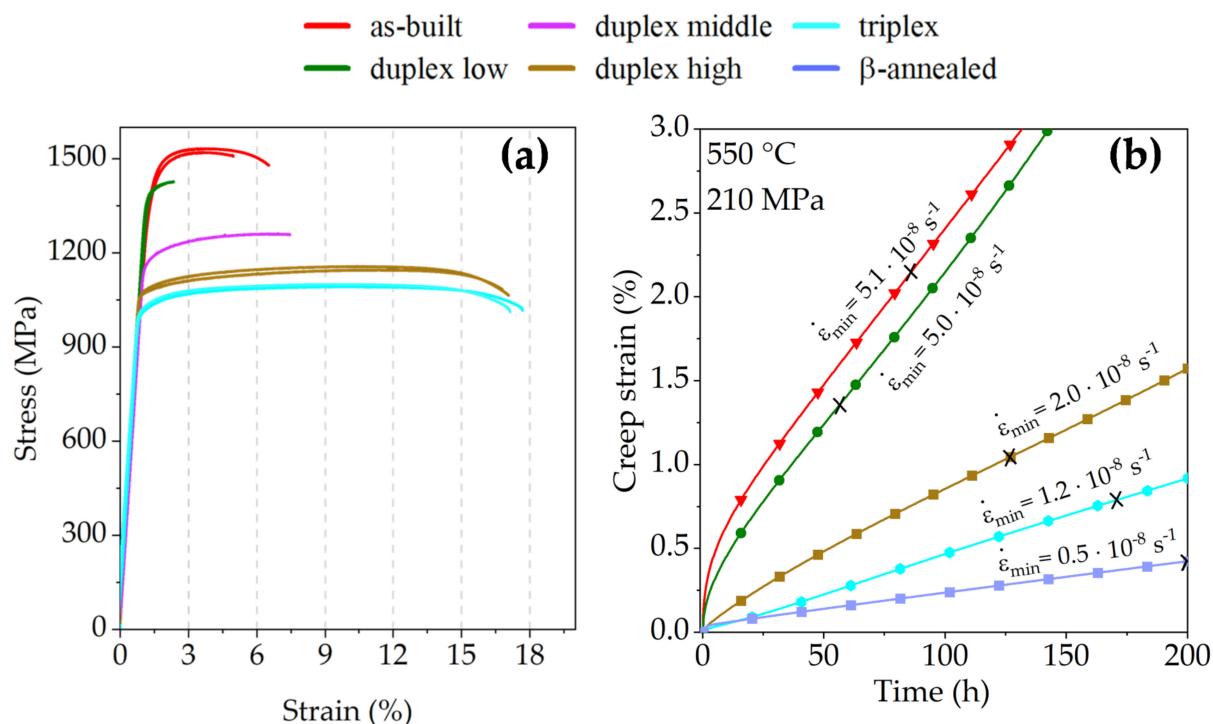


**Figure 9.** (a) Stress-strain curves obtained at RT show the tensile mechanical properties of the LPBF-produced Ti6242S specimens in as-built and heat-treated sample conditions; (b) creep strain as a function of time, which reveals the creep resistance as a function of the applied heat treatment. The cross (x) marks the time when the minimum creep rate ( $\dot{\epsilon}_{\min}$ ) was reached.

Besides the tensile properties, additional focus is placed on the impact of the heat treatment on the creep resistance of the LPBF-manufactured Ti6242S components. Therefore, creep tests were conducted at 550 °C under an applied load of 210 MPa on all variants. Figure 9b displays the creep strain as a function of the time as well as the minimum creep rate values ( $\dot{\epsilon}_{\min}$ ). The cross marks the time when the sample reached the minimum creep rate, also provided in Table 1. The as-built sample, which exhibits the highest tensile strength, reaches a creep strain  $\epsilon > 1\%$  already after 26 h and reveals a  $\dot{\epsilon}_{\min}$  of  $5.1 \cdot 10^{-8} \text{ s}^{-1}$  after 85 h. The minimum creep rate decreases for the duplex annealed samples with increasing annealing temperatures from  $\dot{\epsilon}_{\min} 5.0 \cdot 10^{-8} \text{ s}^{-1}$  (duplex low) to  $\dot{\epsilon}_{\min} 2.0 \cdot 10^{-8} \text{ s}^{-1}$  (duplex high). The respective  $\epsilon > 1\%$  creep strain is reached after 37 h and 120 h under the applied load of 210 MPa. The triplex annealed sample shows a further improvement of creep resistance and a  $\dot{\epsilon}_{\min}$  min of  $1.2 \cdot 10^{-8} \text{ s}^{-1}$ . For this sample condition, a creep strain of  $\epsilon > 1\%$  is only exceeded after 218 h. During  $\beta$ -annealing, the very fine  $\alpha'$  martensite transforms into a lamellar  $\alpha + \beta$  microstructure which is favorable for high creep resistance. This sample condition reveals the highest creep resistance, where  $\dot{\epsilon}_{\min}$  of  $0.5 \cdot 10^{-8} \text{ s}^{-1}$  is reached after 200 h, and the  $\epsilon > 1\%$  creep strain was not reached until the end of the creep test, in this case after 350 h.

**Table 1.** Comparison of mechanical properties and the influence of heat treatments on LPBF manufactured Ti6242S material.

Sample	Heat Treatment	UTS (MPa)	YS (MPa)	A <sub>5</sub> (%)	Min. Creep Rate $\dot{\epsilon}_{\min}$ ( $10^{-8} \text{ s}^{-1}$ )	Time (h) $\epsilon > 1\%$	Reference
as-built	-	1526 ± 6	1406 ± 17	4.3 ± 0.8	5.1 (85 h)	26	this study
duplex low	700 °C–1 h–AC 600 °C–24 h–AC	1421 ± 5	1390 ± 2	0.9 ± 0.3	5.0 (56 h)	37	this study
duplex middle	800 °C–1 h–AC 600 °C–24 h–AC	1263	1172	6.5	-	-	this study
duplex high	900 °C–8 h–AC 600 °C–4 h–AC	1155 ± 7	1075 ± 4	16.0 ± 0.1	2.0 (127 h)	120	this study
triplex	sub-critical $\beta$ -annealing–FC 900–950 °C–1–2 h–AC 550–600 °C–2–4 h–AC	1098 ± 4	1018 ± 5	16.5 ± 0.3	1.2 (170 h)	218	this study
$\beta$ -annealed	1025 °C–1 h–AC	-	-	-	0.5 (200 h)	>350	this study
as-built	-	1381	1293	5.3	-	-	[8]
cast + annealed	-	1006	910	10	-	-	[15]

#### 4. Discussion

The combination of the beneficial properties of Ti base alloys with the LPBF manufacturing process allows the production of light-weight structural parts with highly complex geometries. However, LPBF requires comprehensive know-how in the field of processing and in-depth knowledge of material-specific characteristics. Parts produced by LPBF reveal a non-equilibrium martensitic  $\alpha'$  microstructure, including a high amount of lattice defects and residual stresses [11]. Therefore, sub-transus post-process heat treatments are an effective way to shift the microstructure and the chemical composition of the constituting phases towards thermodynamic equilibrium, i.e.,  $\alpha' \rightarrow \alpha + \beta$ . Due to the relationship of mechanical properties and microstructural features, the applied heat treatments must be chosen carefully and should be explicitly adapted to the requirements for the final application. Concerning the wide range of available heat treatments for Ti base alloys, the following findings provide a guide for setting up a tailor-made heat treatment strategy:

##### 4.1. Heat Treatment to Achieve Higher Tensile Strength

In order to adjust a high tensile strength in a Ti6242S alloy, the as-built condition or duplex annealing is recommended. The tensile tests of the as-built samples show extraordinarily high tensile strength values of UTS = 1526 MPa, although the elongation at fracture A<sub>5</sub> is still at 4.3%, see Table 1. Therefore, the use of as-built samples should be considered if applications primarily focus on strength and low operating temperatures. It should be noted that as-built samples additionally reveal melt pool borders, which occur normal to the building direction and are caused by element segregations during the LPBF process. These melt pool borders, however, are of minor importance for mechanical properties as the total difference of element concentrations is comparably low [11].

Duplex annealing is recommended for applications with a need for well-balanced properties in terms of fracture at elongation and strength. During SRA, the overall decreasing hardness is determined by an interaction of decreasing defect density, grain coarsening and fine  $\beta$  phase precipitation. Additional aging is essential to increase the strength via element partitioning and precipitation of secondary  $\alpha$  features [23,24,30]. It is noteworthy that aging is only possible if the  $\alpha$  and  $\beta$  phases are not stable and under- or supersaturated in alloying elements. After AC, the  $\beta$  phase is supersaturated in Al and depleted in Mo and Fe and tends to shift towards thermodynamic equilibrium during aging. This leads to the precipitation of secondary  $\alpha_s$  and to a decrease in the  $\beta$  phase fraction. As a result, the

remaining  $\beta$  phase is heavily stabilized and a solid solution hardening with Mo and Fe is expected [5].

Regarding the SRA temperatures, duplex annealing at 700 °C causes sub- $\mu\text{m}$ -sized  $\beta$ -precipitates in combination with very fine  $\alpha$  constituents. This results in high strength but significantly decreases the ductility due to the lack of large plastic zones and dislocation pile-ups. Therefore, higher SRA temperatures, such as 800 °C and 900 °C, are favorable. The extension of SRA dwell times from 2 to 8 h does not affect the hardness, yet is important if an additional aging step is conducted. While shorter SRA dwell times lead to an increase in hardness during aging from 4 h to 24 h for the “duplex low” (700 °C) and “duplex middle” (800 °C) samples, the “duplex high” (900 °C) sample is not affected by longer SRA and aging dwell times. To summarize, the duplex annealing should either be performed with short dwell times for “duplex middle” treatment to the benefit of the strength enhancement during aging (800 °C-1 h-AC-600 °C-24 h-AC) or with a longer dwell time for “duplex high” heat treatment to gain additional ductility (900 °C-8 h-AC-600 °C-4 h-AC). The hardness of FC samples, in contrast, cannot further be enhanced by aging as these samples are already in thermodynamic equilibrium.

#### 4.2. Triplex Annealing to Obtain High Ductility

In general, a fine grained equiaxed microstructure is beneficial for higher ductility and can be achieved by thermo-mechanical processing (TMP) [5]. As TMP is not possible for AM components, a proper heat treatment strategy must be developed. Triplex annealing consists of a globularization treatment slight below  $\beta$ -transus followed by FC. During this stage, the globularization of primary  $\alpha_p$  grains occurs due to grain growth and so-called grain segmentation. The segmentation of primary grains results from the formation of subgrain boundaries caused by the minimization of the total free energy and the rearrangement of tangled dislocations into dislocation arrays as described in reference [31]. The large globularized  $\alpha_p$  grains contribute to the ductility and reveal enhanced local plasticity as they are capable of containing a large number of slip and shear bands and elongate under external load. The follow-up annealing between 900 and 950 °C generates approximately 30 vol.% of supersaturated  $\beta$  phase. This phase shift towards thermodynamic equilibrium during the final aging step and generates very fine secondary  $\alpha_s$ , contributing to the strength by hindering the dislocation motion via generation dislocation pile-ups at the  $\alpha/\beta$  phase boundaries. In addition, slip bands and dislocation walls in primary  $\alpha_p$  also enhance the strength by providing an effective barrier against dislocation movement [31].

In this context, it should be mentioned that also proper duplex annealing leads to enhanced fracture at elongation during tensile testing. In addition, duplex annealing would not need a third annealing step when compared to triplex annealing. On the downside, however, increasing dwell times at high temperatures must be considered as they are essential for superior ductility after duplex annealing.

#### 4.3. Enhanced Creep Resistance by Means of $\beta$ Annealing

The Ti6242S alloy is known for a superior temperature resistance when compared to the Ti64 alloy, especially at temperatures above 500 °C [15]. To enhance the creep resistance in the Ti6242 alloy, a minor amount of Si is added, which results in the precipitation of (Ti,Zr)<sub>6</sub>Si<sub>3</sub> silicide particles which decelerate the dislocation motion substantially [7,25,32]. According to previous investigations on a related alloy [33], creep in this alloy is governed by lattice diffusion-controlled dislocation climb. The coarse lamellar microstructure is beneficial for use at elevated temperatures [5], which was also confirmed in the creep investigations within this study. Therefore, this treatment should be used if applications primarily focus on temperature resistance. Unfortunately, the  $\beta$ -annealing treatment has to be performed above the  $\beta$ -transus temperature ( $T_\beta = 1017$  °C). However, these high temperatures diminish the typical LPBF microstructure and, in further consequence, decrease the superior tensile properties resulting from the LPBF process. Moreover, the newly formed  $\alpha$  phase at grain boundaries influences the mechanical properties negatively [5].

It is noteworthy that triplex annealed samples also show enhanced creep properties. With regard to the excellent creep resistance of the triplex annealed material, in combination with the well-balanced mechanical properties in terms of strength and ductility, this heat treatment strategy might also be applicable for the multifunctional usage of LPBF-manufactured Ti6242S parts.

## 5. Conclusions

This study sheds light on the process-microstructure-property relationship of an LPBF-manufactured Ti6242S alloy and provides recommendations for specific annealing strategies. The mechanical testing, in combination with a detailed microstructure investigation, utilizing a variety of high-resolution characterization techniques, led to the following conclusions:

- For high strength applications, it is recommended to use: (i) the as-built or (ii) the duplex annealing heat treatment (well balanced ductility-strength ratio).
- Engineering applications that require high ductility can be fulfilled if triplex or duplex annealing is performed. These treatments lead to a significant increase in the elongation at fracture.
- Annealing above the  $\beta$ -transus temperature  $T_{\beta}$  is recommended for long-term operating temperatures above 500 °C.

**Author Contributions:** Conceptualization, C.F.-R. and H.C.; investigation, C.F.-R.; writing—original draft preparation, C.F.-R.; writing—review and editing, H.C.; supervision, H.C.; funding acquisition, C.T. and T.P. All authors have read and agreed to the published version of the manuscript.

**Funding:** This research received no external funding.

**Institutional Review Board Statement:** Not applicable.

**Informed Consent Statement:** Not applicable.

**Data Availability Statement:** The datasets generated during and/or analyzed during the current study are available from the corresponding author on reasonable request.

**Conflicts of Interest:** The authors declare no conflict of interest.

## References

1. Liu, S.; Shin, Y.C. Additive manufacturing of Ti6Al4V alloy: A review. *Mater. Des.* **2019**, *164*, 107552. [[CrossRef](#)]
2. Sabban, R.; Bahl, S.; Chatterjee, K.; Suwas, S. Globularization using heat treatment in additively manufactured Ti-6Al-4V for high strength and toughness. *Acta Mater.* **2019**, *162*, 239–254. [[CrossRef](#)]
3. Niinomi, M. Mechanical biocompatibilities of titanium alloys for biomedical applications. *J. Mech. Behav. Biomed. Mater.* **2008**, *1*, 30–42. [[CrossRef](#)] [[PubMed](#)]
4. Wang, K. The use of titanium for medical applications in the USA. *Mater. Sci. Eng. A* **1996**, *213*, 134–137. [[CrossRef](#)]
5. Lütjering, G.; Williams, J.C. *Titanium*, 1st ed.; Springer Science & Business Media: Berlin/Heidelberg, Germany, 2007; ISBN 9783662132227.
6. Barriobero-Vila, P.; Gussone, J.; Stark, A.; Schell, N.; Haubrich, J.; Requena, G. Peritectic titanium alloys for 3D printing. *Nat. Commun.* **2018**, *9*, 1–9. [[CrossRef](#)]
7. Leyens, C.; Peters, M. *Titanium and Titanium Alloys: Fundamentals and Applications*, 1st ed.; Peters, M., Leyens, C., Eds.; Wiley-VCH: Weinheim, Germany, 2003; ISBN 9783527602117.
8. Fan, H.; Yang, S. Effects of direct aging on near-alpha Ti-6Al-2Sn-4Zr-2Mo (Ti-6242) titanium alloy fabricated by selective laser melting (SLM). *Mater. Sci. Eng. A* **2020**, *788*, 139533. [[CrossRef](#)]
9. Imai, H.; Yamane, G.; Matsumoto, H.; Vidal, V.; Velay, V. Superplasticity of metastable ultrafine-grained Ti-6242S alloy: Mechanical flow behavior and microstructural evolution. *Mater. Sci. Eng. A* **2019**, *754*, 569–580. [[CrossRef](#)]
10. Fujieda, T.; Cui, Y.; Aoyagi, K.; Koizumi, Y.; Chiba, A. Electron beam melting of boron-modified Ti-2Al-2Sn-4Zr-2Mo-0.1Si alloy with superior tensile strength and oxidation resistance at elevated temperatures. *Materialia* **2018**, *4*, 367–372. [[CrossRef](#)]
11. Fleißner-Rieger, C.; Pfeifer, T.; Jörg, T.; Kremmer, T.; Brabetz, M.; Clemens, H.; Mayer, S. Selective laser melting of a near- $\alpha$  Ti6242S alloy for high-performance automotive parts. *Adv. Eng. Mater.* **2021**, 2001194. [[CrossRef](#)]
12. Zhang, D.; Qiu, D.; Gibson, M.A.; Zheng, Y.; Fraser, H.L.; StJohn, D.H.; Easton, M.A. Additive manufacturing of ultrafine-grained high-strength titanium alloys. *Nature* **2019**, *576*, 91–95. [[CrossRef](#)]

13. Geetha, M.; Singh, A.K.; Asokamani, R.; Gogia, A.K. Ti based biomaterials, the ultimate choice for orthopaedic implants - A review. *Prog. Mater. Sci.* **2009**, *54*, 397–425. [[CrossRef](#)]
14. Dutta, B.; Froes, F.H. *Additive Manufacturing of Titanium Alloys: State of the Art, Challenges and Opportunities*; Butterworth-Heinemann: Oxford, UK, 2016; ISBN 9780128047828.
15. Boyer, R.; Welsch, G.; Collings, E.W. *Materials properties handbook: Titanium alloys*, 4th ed.; ASM International: Materials Park, OH, USA, 1994; ISBN 9780871704818.
16. Ter Haar, G.M.; Becker, T.H. Low temperature stress relief and martensitic decomposition in selective laser melting produced Ti6Al4V. *Mater. Des. Process. Commun.* **2021**, *3*, e138. [[CrossRef](#)]
17. DebRoy, T.; Wei, H.L.; Zuback, J.S.; Mukherjee, T.; Elmer, J.W.; Milewski, J.O.; Beese, A.M.; Wilson-Heid, A.; De, A.; Zhang, W. Additive manufacturing of metallic components – process, structure and properties. *Prog. Mater. Sci.* **2018**, *92*, 112–224. [[CrossRef](#)]
18. Ter Haar, G.; Becker, T. Selective laser melting produced Ti-6Al-4V: Post-process heat treatments to achieve superior tensile properties. *Materials* **2018**, *11*, 146. [[CrossRef](#)]
19. Zhang, X.Y.; Fang, G.; Leeflang, S.; Böttger, A.J.; Zadpoor, A.A.; Zhou, J. Effect of subtransus heat treatment on the microstructure and mechanical properties of additively manufactured Ti-6Al-4V alloy. *J. Alloys Compd.* **2018**, *735*, 1562–1575. [[CrossRef](#)]
20. Vrancken, B.; Thijs, L.; Kruth, J.P.; Van Humbeeck, J. Heat treatment of Ti6Al4V produced by selective laser melting: Microstructure and mechanical properties. *J. Alloys Compd.* **2012**, *541*, 177–185. [[CrossRef](#)]
21. Xu, W.; Sun, S.; Elambasseril, J.; Liu, Q.; Brandt, M.; Qian, M. Ti-6Al-4V additively manufactured by selective laser melting with superior mechanical properties. *JOM* **2015**, *67*, 668–673. [[CrossRef](#)]
22. Haubrich, J.; Gussone, J.; Barriobero-Vila, P.; Kürsteiner, P.; Jäggle, E.A.; Raabe, D.; Schell, N.; Requena, G. The role of lattice defects, element partitioning and intrinsic heat effects on the microstructure in selective laser melted Ti-6Al-4V. *Acta Mater.* **2019**, *167*, 136–148. [[CrossRef](#)]
23. Chandler, H. (Ed.) *Heat Treater's Guide Practices and Procedures for Nonferrous Alloys*; ASM International: Materials Park, OH, USA, 2006; ISBN 0871705656.
24. Donachie, M.J. *Titanium-A technical Guide*, 2nd ed.; ASM International: Materials Park, OH, USA, 2000; ISBN 978-953-51-0467-4.
25. Popov, A.; Rossina, N.; Popova, M. The effect of alloying on the ordering processes in near-alpha titanium alloys. *Mater. Sci. Eng. A* **2013**, *564*, 284–287. [[CrossRef](#)]
26. Fleißner-Rieger, C.; Pogrietz, T.; Obersteiner, D.; Pfeifer, T.; Clemens, H.; Mayer, S. An additively manufactured titanium alloy in the focus of metallography. *Pract. Metallogr.* **2021**, *58*, 4–31. [[CrossRef](#)]
27. Mccusker, L.B.; Von Dreele, R.B.; Cox, D.E.; Louër, D.; Scardi, P. Rietveld refinement guidelines. *J. Appl. Crystallogr.* **1999**, *32*, 36–50. [[CrossRef](#)]
28. Chong, Y.; Deng, G.; Yi, J.; Shibata, A.; Tsuji, N. On the strain hardening abilities of  $\alpha + \beta$  titanium alloys: The roles of strain partitioning and interface length density. *J. Alloys Compd.* **2019**, *811*, 152040. [[CrossRef](#)]
29. Wang, K.; Yan, Z.; Zhou, Y.; Wei, S.; Wang, X.; Xin, R.; Liu, Q. Slip initiation in interlayered  $\beta$  and corresponding slip transfer during compression of a lamellar-structure titanium alloy. *Results Phys.* **2020**, *18*, 103276. [[CrossRef](#)]
30. Gheysarian, A.; Abbasi, M. The effect of aging on microstructure, formability and springback of Ti-6Al-4V titanium alloy. *J. Mater. Eng. Perform.* **2017**, *26*, 374–382. [[CrossRef](#)]
31. Zhao, Z.; Chen, J.; Tan, H.; Zhang, G.; Lin, X.; Huang, W. Achieving superior ductility for laser solid formed extra low interstitial Ti-6Al-4V titanium alloy through equiaxial alpha microstructure. *Scr. Mater.* **2018**, *146*, 187–191. [[CrossRef](#)]
32. Singh, A.K.; Ramachandra, C. Characterization of silicides in high-temperature titanium alloys. *J. Mater. Sci.* **1997**, *32*, 229–234. [[CrossRef](#)]
33. Hayes, R.W.; Viswanathan, G.B.; Mills, M.J. Creep behavior of Ti-6Al-2Sn-4Zr-2Mo. I. The effect of nickel on creep deformation and microstructure. *Acta Mater.* **2002**, *50*, 4953–4963. [[CrossRef](#)]